

ANALYSIS OF EXPERIMENTAL BEHAVIOR OF PRETENSIONED
CONCRETE BENT CAPS USING MOTION CAPTURE SYSTEMS

A Thesis

by

CODI DAVID MCKEE

Submitted to the Office of Graduate and Professional Studies of
Texas A&M University
in partial fulfillment of the requirements for the degree of

MASTER OF SCIENCE

Chair of Committee, Anna C. Birely
Committee Members, John B. Mander
Mohammed E. Haque

Head of Department, Robin Autenrieth

May 2018

Major Subject: Civil Engineering

Copyright 2018 Codi David McKee

ABSTRACT

Precast, pretensioned concrete (PSC) bent caps allow for accelerated bridge construction while reducing, or eliminating, cracks typically seen in reinforced concrete (RC) bent caps. When cracks do form in PSC caps, they occur at internal discontinuities such as those created by emulative cap-to-column connections and interior voids for weight reduction. To assess the behavior of PSC bent caps, an experimental test program was conducted of six full-scale bent cap sub-assemblages. This Thesis focuses on the behavior of the specimens with interior voids and monitoring of initial cracking using an Optotrak Certus motion capture system.

Visual observations of the tests indicate that interior voids significantly decrease the cracking shear strength of the caps. Void detailing did not appear to have a significant impact on the onset of shear cracking, but did impact the orientation and extent of shear cracking at design loads. Beyond design loads, differences in the behavior were negligible. Failure occurred in the negative bending region with spalling of concrete in the compression zone for the specimens with varied void details. A more abrupt failure occurred in the bent cap with a voided overhang due to additional spalling of concrete along a compression strut along the overhang interior void.

The Optotrak Certus system provided displacement data for a dense grid-like array of light-emitting diodes (LEDs). LED displacements were validated using traditional instrumentation and treated as nodal displacements in a mesh of four-node isoparametric quadrilateral elements to establish strains. Regions of concentrated principal tensile

strains indicated the regions and orientation of observed cracks, indicating the promise of motion capture systems as a tool for assessing the development of cracking in PSC members.

DEDICATION

I dedicate this work to my niece Avah, whose phone calls, video chats, and paintings brighten my days. One day your favorite Uncle will be done with school, but until then I look forward to every chance that I get to see you.

ACKNOWLEDGEMENTS

I would like to thank my committee chair, Dr. Anna Birely, and my committee members, Dr. John Mander, and Dr. Mohammed Haque, for their guidance and support throughout the course of this research.

Thank you to TxDOT personnel Darrin Jensen, Christopher Miller, Courtney Holle, Graham Bettis, Todd Speck, Jason Tucker, Manuel Pardon Jr., Susana Ceballos, Frank Estrada III, Dennis Johnson, and Roger Lopez for serving as the project monitoring committee for this research. Thank you to Bexar Concrete Works in San Antonio, Texas for fabricating the pretensioned bent caps. I would like to thank the Texas A&M High Bay Structural and Materials Testing Laboratory personnel Dr. Peter Keating, Charles Droddy, and Matthew Potter for their guidance and assistance with fabrication and experimental testing.

I would like to thank my colleagues Usha Rani Barooah, Kevin Yole, and Judong Lee for their hard work, dedication, and contribution to this research. Thank you to all the other graduate and undergraduate students involved with this research for their hard work and support with fabrication, testing, and demolition. Completing this research would not be possible without this help and support. Special thanks to all my friends and colleagues that have made my time at Texas A&M such an unforgettable experience. Thank you to Nick Danney and Emily Miller for your friendship and support, and for keeping me positive through the process of writing this Thesis.

I am deeply thankful to my family and friends for their love and support throughout this journey. The words of encouragement and reminders of home from my mother Marie Mangan, father David McKee, step-father Eric Mangan, step-mother Shauna McKee, and all my grandparents, aunts, uncles, and siblings has made my transition to Texas and journey through graduate school possible. Thank you to my “Texas family” Mark, Shaun, Angela, and Nick Danney for making Texas feel like home.

CONTRIBUTORS AND FUNDING SOURCES

This work was supervised by a Thesis committee consisting of advisor Dr. Anna Birely and committee member Dr. John Mander of the Zachry Department of Civil Engineering, and committee member Dr. Mohammed Haque of the Department of Construction Science.

All work for this Thesis was completed by the student, under the advisement of Dr. Anna Birely and Dr. John Mander of the Zachry Department of Civil Engineering, and Dr. Mohammed Haque of the Department of Construction Science.

Funding was provided by the Texas Department of Transportation, Project 0-6863 “Develop Strong and Serviceable Details for Precast, Prestressed Concrete Bent Cap Standards That Can Be Implemented on Everyday Bridge Construction Projects”, Darrin Jensen Project Manager.

TABLE OF CONTENTS

	Page
ABSTRACT	ii
DEDICATION	iv
ACKNOWLEDGEMENTS	v
CONTRIBUTORS AND FUNDING SOURCES.....	vii
TABLE OF CONTENTS	viii
LIST OF FIGURES.....	x
LIST OF TABLES	xvii
1. INTRODUCTION.....	1
1.1. Research Motivation	2
1.2. Research Objectives	3
1.3. Overview of Thesis	3
2. LITERATURE REVIEW.....	6
2.1. Usage of Precast Concrete Bridge Elements.....	6
2.2. Reinforced Concrete Bent Caps	8
2.3. Precast Prestressed Bent Caps.....	16
2.4. Precast Beam-To-Column Connections	20
2.5. Voids in Concrete Bridge Structures.....	25
2.6. Motion Capture Systems	31
2.7. Research Questions Arising from Literature Review	41
3. EXPERIMENTAL TEST PROGRAM.....	43
3.1. Experimental Test Program Overview	43
3.1.1. Overview	44
3.1.2. Specimen Design.....	45
3.1.3. Test Matrix	52
3.1.4. Experimental Test Setup	53
3.2. Test Specimen Construction.....	61
3.3. Instrumentation	74
3.3.1. Traditional Instrumentation.....	74
3.3.2. Advanced Instrumentation	77
3.4. Material Properties	80
3.4.1. Concrete Material Properties.....	80
3.4.2. Steel Material Properties	85
3.5. Experimental Testing	86
3.5.1. Specimen Loading.....	86
3.5.2. Summary of Observed Results.....	95

3.5.3.	Impact of Design Variables	110
4.	DATA ANALYSIS	122
4.1.	Overview	122
4.2.	Post-Processing	122
4.2.1.	Data Synchronization	122
4.2.2.	Coordinate System Transformation	123
4.2.3.	Marker Naming	126
4.3.	Data Comparison.....	129
4.4.	Analysis of Experimental Data	132
4.4.1.	Deformed Shape	132
4.4.2.	Strain Fields.....	139
4.5.	Summary and Discussion of Data Analysis	156
4.5.1.	Post-Processing	156
4.5.2.	Data Comparison.....	157
4.5.3.	Analysis of Experimental Data	157
5.	SUMMARY, CONCLUSIONS, AND RECCOMENDATIONS.....	159
5.1.	Summary	159
5.2.	Conclusions	161
5.2.1.	Optotrak Certus Motion Capture System Measurement	161
5.2.2.	Interior Void Details.....	163
5.2.3.	Overhang Geometry	164
5.3.	Recommendations	165
5.4.	Areas of Future Work.....	165
	REFERENCES.....	167

LIST OF FIGURES

	Page
Figure 2.1. Pierce Elevated Precast Concrete Bent Cap and Beam-Column Connection (Jones and Vogel 2001).	8
Figure 2.2. Retrieval Location of Specimens from Niagara Parkway Bridge.....	9
Figure 2.3. Experimental Test Setup (Young et al. 2002).....	11
Figure 2.4. Example Strain Gauge Placement Plan (Bracci et al. 2000).....	12
Figure 2.5. Longitudinal Reinforcement Strain Profile for Specimen 1A (Young et al. 2002).	13
Figure 2.6. Instrumentation of Pier Cap Specimens (Bechtel 2011).....	15
Figure 2.7. Load vs. Deflection Plot Example (Bechtel 2011).	15
Figure 2.8. Top/Bottom Strand Configuration (left) and Side Strand Configuration (right) (Barooah 2016).....	17
Figure 2.9. Nominal Strength vs. Area of Prestressing for Top/bottom and Side Strand Configurations (Barooah 2016).....	19
Figure 2.10. Prototype Bridge Shear (left) and Moment (right) Diagrams (Yole 2017).	19
Figure 2.11. Specimen Shear (left) and Moment (right) Diagrams (Yole 2017).	19
Figure 2.12. Pullout Test Setup (Matsumoto et al. 2001).	22
Figure 2.13. Load-Slip Behavior during Pullout Tests (Matsumoto et al. 2001).	22
Figure 2.14. Connection Test Setup (Matsumoto et al. 2001).	23
Figure 2.15. Experimental Test Setup (Restrepo et al. 2011).	24
Figure 2.16. Lateral Hysteretic Response of Column (Restrepo et al. 2011).	25
Figure 2.17. Experimental Test Setup (Schnittker and Bayrak 2008).	26
Figure 2.18. Load-Deflection Plot Example (Schnittker and Bayrak 2008).....	27
Figure 2.19. 4B28 Box Beam Shear Test Setup (Valderrama 2011).	29

Figure 2.20. Shear Deformation Monitoring Instrumentation (Valderrama 2011).	30
Figure 2.21. Shear Demand versus Shear Strain Plot Example (Valderrama 2011).	30
Figure 2.22. Structural Wall Test Setup (Lowes et al. 2011).	32
Figure 2.23. Krypton CMM Measurement Volume (Lowes et al 2011).	33
Figure 2.24. Typical Krypton CMM LED Target Layout (Lowes et al. 2011).	33
Figure 2.25. Photogrammetry Target Placement Example (Hart 2012).	34
Figure 2.26. Krypton LED Displacements Comparison with Traditional String Pot Measurements (Birely 2012).	35
Figure 2.27. Displacement Profile Example (Birely 2012).	36
Figure 2.28. Unsmoothed and Smoothed Strain Field Plot Example (Birely 2012).	37
Figure 2.29. Pretensioned Bulb-Tee Girder Test Setup (Hawkins and Kuchma 2007).	38
Figure 2.30. LED Krypton Targets and Zurich Gauge Targets Layout (Hawkins and Kuchma 2007).	39
Figure 2.31. Horizontal Strain Profile Example (Hawkins and Kuchma 2007).	40
Figure 2.32. Average Horizontal Strain versus Applied Load Example (Hawkins and Kuchma 2007).	40
Figure 3.1. Prototype Shear and Moment Diagrams. (Adapted with permission from Birely et al. 2018a).	45
Figure 3.2. Specimen Shear and Moment Diagrams. (Adapted with permission from Birely et al. 2018a)	45
Figure 3.3. Prototype Bridge Configurations. (Adapted with permission from Birely et al. 2018a)	47
Figure 3.4. Prestressing Strand Layout. (Adapted with permission from Birely et al. 2018a)	48

Figure 3.5. End Region Detailing. (Adapted with permission from Birely et al. 2018a).....	50
Figure 3.6. Pocket Connection Details. (Adapted with permission from Birely et al. 2018a).....	51
Figure 3.7. General Experimental Test Setup 3D Rendering. (Adapted with permission from Birely et al. 2018a).....	55
Figure 3.8. Phase 1 Experimental Test Setup. (Adapted with permission from Birely et al. 2018a).....	56
Figure 3.9. Phase 2 Experimental Test Setup. (Adapted with permission from Birely et al. 2018a).....	57
Figure 3.10. Rocker Foundation (stability pegs were removed prior to testing). (Adapted with permission from Birely et al. 2018a).....	58
Figure 3.11. Vertical Reaction Frame. (Adapted with permission from Birely et al. 2018a).....	58
Figure 3.12. Horizontal Reaction Frames. (Adapted with permission from Birely et al. 2018a).....	59
Figure 3.13. Horizontal Actuator Connections. (Adapted with permission from Birely et al. 2018a).....	60
Figure 3.14. Bearing Pad Locations. (Reprinted with permission from Birely et al. 2018a).....	60
Figure 3.15. Vertical Actuator Load Assembly. (Adapted with permission from Birely et al. 2018a).....	61
Figure 3.16. Prestressing Bed Layout. (Reprinted with permission from Birely et al. 2018a).....	62
Figure 3.17. Initial (black) and Final (red) Prestressing Strand Layout. (Adapted with permission from Birely et al. 2018a).....	63
Figure 3.18. Placement of Initial Strands and End Formwork. (Reprinted with permission from Birely et al. 2018a).....	63
Figure 3.19. Actuator Load Assembly. (Reprinted with permission from Birely et al. 2018a).....	65

Figure 3.20. Corrugated Steel Pipe Installation. (Reprinted with permission from Birely et al. 2018a).....	66
Figure 3.21. PSV-28B Polystyrene Forming Block. (Reprinted with permission from Birely et al. 2018a).....	66
Figure 3.22. Polystyrene Forming Blocks Installed. (Reprinted with permission from Birely et al. 2018a).....	67
Figure 3.23. PVC Drain Pipe Installation. (Reprinted with permission from Birely et al. 2018a).....	67
Figure 3.24. Interior Void Polystyrene Forming Block Hold Downs. (Reprinted with permission from Birely et al. 2018a)	68
Figure 3.25. Strands through Pocket Connection. (Reprinted with permission from Birely et al. 2018a).....	68
Figure 3.26. Strain Gauged Reinforcement. (Reprinted with permission from Birely et al. 2018a).....	69
Figure 3.27. PSV-28B Mild Steel Hoop Installation. (Reprinted with permission from Birely et al. 2018a).....	69
Figure 3.28. Thermocouple Plan. (Reprinted with permission from Birely et al. 2018a).....	70
Figure 3.29. Concrete Batch Distribution. (Reprinted with permission from Birely et al. 2018a).....	72
Figure 3.30. Concrete Placement and Consolidation. (Reprinted with permission from Birely et al. 2018a).....	72
Figure 3.31. PSV-28B Polystyrene Block Shifting. (Reprinted with permission from Birely et al. 2018a).....	73
Figure 3.32. Concrete Finishing and Curing. (Adapted with permission from Birely et al. 2018a).....	73
Figure 3.33. Strand Release. (Adapted with permission from Birely et al. 2018a).....	74
Figure 3.34. LVDT Locations. (Reprinted with permission from Birely et al. 2018a).....	76
Figure 3.35. Optotrak LED Marker Layouts with Typical Grid Spacings.....	79

Figure 3.36. Concrete Compressive Strength vs Age. (Reprinted with permission from Birely et al. 2018a).....	83
Figure 3.37. 28-Day Bent Cap Concrete Stress-Strain Curves. (Reprinted with permission from Birely et al. 2018a).....	85
Figure 3.38. Location of Actuator Forces. (Reprinted with permission from Birely et al. 2018a).....	88
Figure 3.39. Load Pattern Moment Diagrams. (Reprinted with permission from Birely et al. 2018a).....	89
Figure 3.40. Visual Observation at Failure (Back Face). (Reprinted with permission from Birely et al. 2018a).....	97
Figure 3.41. Visual Observation at Failure (Failed region). (Reprinted with permission from Birely et al. 2018a).....	98
Figure 3.42. Cracking of Phase 1 and Phase 2 Specimens After Failure.....	99
Figure 3.43. Cracking of Phase 1 Specimens under Pattern A SLS.....	102
Figure 3.44. Cracking of Phase 1 Specimens under Pattern A 140% ULS.....	103
Figure 3.45. Cracking of Phase 1 Specimens under Pattern B (Max. Positive Moment) and Pattern E (Max. Negative Moment).	104
Figure 3.46. Cracking of Phase 2 Specimens under Pattern A SLS.....	107
Figure 3.47. Cracking of Phase 2 Specimens under Pattern A 140% ULS.....	108
Figure 3.48. Cracking of Phase 2 Specimens under Pattern B (Max. Positive Moment) and Pattern E (Max. Negative Moment).....	108
Figure 3.49. Comparison of Shear Cracks in Span Region of PSV-28A and PSV-28B at ULS and 140% ULS Demands. (Reprinted with permission from Birely et al. 2018a).....	112
Figure 3.50. Comparison of Formation of Shear Cracks in Square End of PSV-28A and PSV-28B under V_{max} of Square End. (Reprinted with permission from Birely et al. 2018a)	113
Figure 3.51. Comparison of Damage at Failure in Negative Moment Region of PSV-28A and PSV-28B. (Reprinted with permission from Birely et al. 2018a).....	115

Figure 3.52. Loss of Concrete in Negative Moment Region of Phase 2 Specimens during Maximum Negative Moment Demands. (Reprinted with permission from Birely et al. 2018a)	116
Figure 3.53. Comparison of Cracking in Negative Moment Region of Pretensioned Specimens with Different Pocket Connection Details under ULS and 140% ULS Demands. (Reprinted with permission from Birely et al. 2018a)	117
Figure 3.54. Comparison of Damage in Overhangs with Different Lengths and Void Details under ULS and 140% ULS Demands. (Reprinted with permission from Birely et al. 2018a)	119
Figure 3.55. Comparison of Overhang Damage of Solid (PSV-28A) and Voided (PSV-28B) Overhang at Negative Moment Region Failure. (Reprinted with permission from Birely et al. 2018a)	120
Figure 4.1. 3-D Euler Rotations. (Source: Optotrak User Manual)	125
Figure 4.2. Optotrak Coordinate Rotation (units in mm) Showing Original and Transformed Position of Bent Cap Specimen.....	125
Figure 4.3. General LED Marker Naming – Phase 1.....	127
Figure 4.4. General LED Marker Naming – Phase 2.....	128
Figure 4.5. Comparison of Vertical Displacement Measured by String Pot 13 and LED Marker BM-28 During Pattern A for PSV-16-12.....	130
Figure 4.6. Comparison of Horizontal Displacement Measured by String Pot 6 and LED Marker CE-23 During Pattern A for PSV-16-12.....	131
Figure 4.7. Demonstration of Specimen Rotation Influence on Vertical and Horizontal Displacement Measurements.	131
Figure 4.8. Comparison of Vertical Displacement Measured by String Pot 13 and LED Marker BM-28 During Pattern A to Pattern D for PSS-16-12. (Note: LED BM-28 Shown in Green in Figure 4.7).....	132
Figure 4.9. Comparison of Deformation of LED Marker Rows under Pattern A (SLS & ULS) Demands for PSV-28A & PSV-28B (deformation exaggerated x100).....	134
Figure 4.10. Comparison of Deformation of LED Marker Columns under Pattern A ULS Demands for PSV-28A & PSV-28B (deformation exaggerated x100).....	135

Figure 4.11. Vertical Displacement of the Bent Cap vs Applied Load at Key Locations along Span Region Interior Voids for PSV-28A & PSV-28B under Pattern A Demands.....	137
Figure 4.12. Vertical Displacement of the Bent Cap vs Applied Load at Key Locations along Overhang for PSV-28A & PSV-28B under Pattern A Demands.	138
Figure 4.13. General Transformation for Mapping LED Markers from Physical Space to ζ - η Space for Isoparametric Quadrilateral (Q4) Formulation.....	141
Figure 4.14. Smoothing Elementwise Nodal Strains based on LED Tributary Area.....	143
Figure 4.15. Comparison of Unsmoothed and Smoothed Shear (γ_{xy}) Strain Fields.....	143
Figure 4.16. Horizontal, Vertical, & Shear Strain Fields (ϵ_x , ϵ_y , & γ_{xy}) under Pattern A ULS Demands for PSV-28A.....	145
Figure 4.17. Horizontal, Vertical, & Shear Strain Fields (ϵ_x , ϵ_y , & γ_{xy}) under Pattern A ULS Demands for PSV-28B.....	146
Figure 4.18. Principal Tensile, Compressive, & Shear Strain Fields (ϵ_1 , ϵ_2 , & γ_{max}) under Pattern A ULS Demands for PSV-28A.....	148
Figure 4.19. Principal Tensile, Compressive, & Shear Strain Fields (ϵ_1 , ϵ_2 , & γ_{max}) under Pattern A ULS Demands for PSV-28B.....	149
Figure 4.20. Comparison of Principal Tensile Strains and Observed Damage under Pattern A Demands for PSV-28A.....	152
Figure 4.21. Comparison of Principal Tensile Strains and Observed Damage under Pattern A Demands for PSV-28B.....	153
Figure 4.22. Comparison of Principal Tensile Strains and Observed Damage for PSV-28B for Both Applications of Pattern A ULS Demands.....	154
Figure 4.23. Principal Tensile Strain versus Applied Shear Demand at Nodes Adjacent to Observed Shear Cracks in the Voided Span Region of PSV-28A During Pattern A Loading.....	155

LIST OF TABLES

	Page
Table 3.1. Summary of Prototype Bridge Details. (Adapted with permission from Birely et al. 2018a).....	46
Table 3.2. Experimental Test Matrix. (Adapted with permission from Birely et al. 2018a).....	53
Table 3.3. Summary of Strain Gauges. (Adapted with permission from Birely et al. 2018a).....	75
Table 3.4. Concrete Compressive Strength Results. (Adapted with permission from Birely et al. 2018a).....	82
Table 3.5. Modulus of Elasticity, Indirect Tensile, and Modulus of Rupture Results. (Adapted with permission from Birely et al. 2018a).....	84
Table 3.6. Steel Tensile Test Results. (Adapted with permission from Birely et al. 2018a).....	86
Table 3.7. Actuator Control Pattern. (Reprinted with permission from Birely et al. 2018a).....	90
Table 3.8. Summary of Demands Phase 1.	91
Table 3.9. Summary of Demands Phase 2.	92
Table 3.10. Summary of Crack Formation and Widths: Phase 1. (Reprinted with permission from Birely et al. 2018a)	105
Table 3.11. Summary of Crack Formation and Crack Widths: Phase 2. (Reprinted with permission from Birely et al. 2018a)	109

1. INTRODUCTION

The development of precast bridge substructures is an instrumental step to further the advancement and use of accelerated bridge construction techniques. Part of this advancement includes the development of precast, pretensioned bent caps. Precast, pretensioned bent caps are similar to other prestressed bridge elements in that they offer the ability for more rapid, economical, safer construction, and enhanced resistance to cracking under service loads.

The utilizing pretensioned concrete over traditional reinforced concrete allows for the construction of longer span bent caps with equal, or greater, performance. However, the construction of precast bent caps can bring forward issues related to transportation and placement. Such issues can be mitigated by including internal voids during fabrication. To implement the use of pretensioned bent caps in the State of Texas, experimental testing is necessary to understand the behavior and performance results.

In this research, six full-scale experimental tests of bent cap sub-assemblages of TxDOT standard bridge designs were tested under realistic load cases. Sub-assemblages included one reinforced concrete, two solid pretensioned, and three voided pretensioned. Fabrication and experimental results are presented. As a part of this study, the behavior of different design variables including the use of interior voids, differing amounts pretensioning and shear reinforcement, and detailing options were investigated. Measurements made with traditional and non-contact systems are compared, to assess the ability of the non-traditional measurements to aid in the better understanding of bent cap

behavior. Conclusions and recommendations regarding the design, construction, testing, and experimental performance measurements will be provided.

1.1. Research Motivation

The use of precast, pretensioned bent caps is being increasingly implemented in the State of Texas. At the time of this research, conventional bridge bents utilize either cast-in-place or precast reinforced concrete bent caps. The Texas Department of Transportation (TxDOT) has begun to expand their use of precast, pretensioned concrete bent caps leading to the release of the Prestressed, Precast Bent Cap Option for Round Columns standards sheets into their bridge standards inventory. To fully understand the benefits of using pretensioned concrete bent caps over the conventional reinforced concrete bent caps, experimental testing must be performed. Beneficial capabilities permitted by utilizing precast, pretensioned bent caps include the use of interior voids for weight reduction and the use of longer bent cap span lengths coupled with superior flexural and shear performance and reduced cracking under normal bridge demands. To aid in the understanding of how these design variables impact the performance of the bent caps, the use of an Optotrak Certus motion capture system can be applied during experimental testing to measure displacements and strains where traditional measurement systems may be limited. To confidently present conclusions drawn using the data collected by the Optotrak Certus motion capture system, measurements shall be validated and compared to traditionally collected data. Furthermore, assumptions made during the design of pretensioned bent caps should be evaluated for applicability and the experimental performance of the bent caps shall be compared to the expected performance.

1.2. Research Objectives

This research seeks to evaluate the experimental performance of pretensioned concrete bent caps with varied designs by use of motion capture system measurements. The investigation will aim to evaluate the impact of interior voids, interior void details, and overhang geometry and details on the overall performance of the bent cap system. An additional objective is to validate the motion capture system as a method to measure the response of pretensioned concrete beams.

1.3. Overview of Thesis

Section 2 presents a literature review of previous research relating to the experimental testing of bent caps and methods of measuring experimental performance. Information from the literature demonstrates the past and present methods of collecting data during experimental tests. Specific areas of focus include the historical and state-of-the-art uses of bent caps, cap-to-column connections in precast bent cap systems, use of voids in concrete, and use of motion capture systems to collect reliable measurements in experimental testing.

Section 3 presents an overview of an experimental test program conducted as part of Texas Department of Transportation (TxDOT) research Project 0-6863. This research was performed to develop standard flexure and shear design provisions for precast, prestressed concrete bent caps intended for use with everyday bridges. As part of the experimental testing, six precast concrete bent caps were designed, constructed, and tested in two phases. In this Thesis, an overview of the full experimental test program is presented, with a summary of Phase 1 and Phase 2 specimen design, test matrix, and discussion of the experimental test setup. Details on the fabrication of Phase 2

pretensioned specimens are discussed. Details of both traditional and advanced instrumentation methods are provided. Material properties of all concrete and steel components are presented. Details of experimental testing are discussed, including the specimen loading, summary of observed results and impact of design variables.

The bent cap specimens were instrumented with internal and external instruments such as traditional strain gauges, linear variable differential transformers (LVDT), string potentiometers, and the more advanced Optotrak motion capture sensors. Data collected from these instruments, along with visual observation of damage, aided in the understanding of the behavior of each bent cap and how the design variable influenced the performance.

To better estimate the expected performance of the specimens, material properties of the concrete and the reinforcing steel were collected for each component. Using this information, the expected behavior of the bent caps were compared to the actual performance.

Section 4 presents analysis of the experimental performance of the prestressed bent caps using collected Optotrak Certus motion capture data for Phase 2 test at service and design loads. Details of post-processing are presented, as well as validation of Optotrak measurements by comparison to string potentiometer measurements. The Optotrak data is used to analyze the deformed shape of the specimens and to assess the development of cracking using principal tensile strains.

Section 5 presents a summary of the findings of the experimental test program, including visual observations and data collected using the Optotrak Certus motion capture

system. The potential of data analysis using the high-fidelity data is assessed, and any recommendations to aid in the future use of this measurement technology are presented and discussed. Needs for further analysis of collected in TxDOT Project 0-6863 are identified.

2. LITERATURE REVIEW

This section summarizes previous research related to the objectives of this Thesis. Section 2.1 discusses a brief history of the use of precast and prestressed bridge components in the State of Texas. Experimental research related to precast reinforced concrete bent caps and pretensioned bent caps is discussed in section 2.2 and section 2.3. Section 2.4 discusses research conducted to aid in the development of the cap-to-column connections for precast concrete bent cap systems, while previous research conducted to investigate the use of voids in bridge structures is presented in section 2.5. Section 2.6 discusses previous experimental research conducted with the collection of measurement with motion capture systems. Questions that arose from conducting this literature review are presented in section 2.7.

2.1. Usage of Precast Concrete Bridge Elements

Like many state transportation agencies, the Texas Department of Transportation (TxDOT) had begun using precast superstructure elements in the 1950s, following the signing of the 1956 Federal Aid Highway Act that created a necessity for economical transportation structures (Ralls et al. 1993). The first use of precast elements in the State of Texas were precast concrete beams on the Corpus Christi Harbor Bridge in 1956 (Cox et al. 2007). Since the initial introduction of precast bridge superstructure elements, TxDOT has developed an inventory of standard precast, pretensioned I-girders, X-beams, U-beams, and slab beams for use in conventional bridges (Jones and Vogel 2001).

To take advantage of the economic benefits of utilizing precast bridge elements TxDOT began the use of precast substructure elements in replacement of the Pierce

Elevated section of Interstate Highway 45 in Houston, Texas in 1996 (Jones and Vogel 2001). The project required the replacement of 113 spans of the elevated highway structure, with an estimated user daily delay cost of \$100,000. Using conventional TxDOT bridge construction techniques, the replacement project was estimated to take more than a year and half to complete. The final design for the structure replacement included the use of precast reinforced concrete bent caps to minimize the overall project length and the economic impact on commuters. The TxDOT engineers incorporated a beam-to-column connection (shown in Figure 2.1) that allowed for the minimal deviation from conventional reinforcement layout of the bent caps. The success of the Pierce Elevated project, and input from industry, lead to a push by TxDOT for research and development of precast reinforced concrete bent caps (Jones and Vogel 2001).

Prior to the Pierce Elevated replacement project, TxDOT had, as part of its bridge design inventory, a collection of standard cast-in-place reinforced concrete interior bent designs for prestressed concrete X-beam, prestressed concrete I-girder, prestressed slab beam, and prestressed box beam superstructure configurations with roadway widths ranging from 24-ft to 44-ft with skews of 0 degrees to 45 degrees. Following the success of the 1996 Pierce Elevated project, a set of companion standards allowing for the use of a precast reinforced concrete bent cap option was developed.



Figure 2.1. Pierce Elevated Precast Concrete Bent Cap and Beam-Column Connection (Jones and Vogel 2001).

2.2. Reinforced Concrete Bent Caps

Mander et al. (1996) investigated the behavior of 30-year old bridge piers that had not been designed for ductile behavior. Destructive experimental testing was performed on a 1960s era concrete pier that was designated for demolition. The bridge pier was retrieved from the Niagara Parkway Bridge (shown in Figure 2.2), originally constructed in downtown Niagara Falls, New York. As common with bridge structures designed and constructed in that era, this bridge pier was not designed for seismic activity. A non-retrofitted and a retrofitted specimen were inverted, and instrumented with sonic transducers, linear resistance potentiometers, shear gauges, and load cells. Through applying cyclic load reversals with increasing amplitudes, the behavior of the bridge piers was studied. The primary deficiency of the non-retrofitted bridge pier was noted to be the lack of adequate transverse reinforcement in the joint and column. The retrofitted

specimen was able to successfully transfer the failure zone from the knee joint to the column.

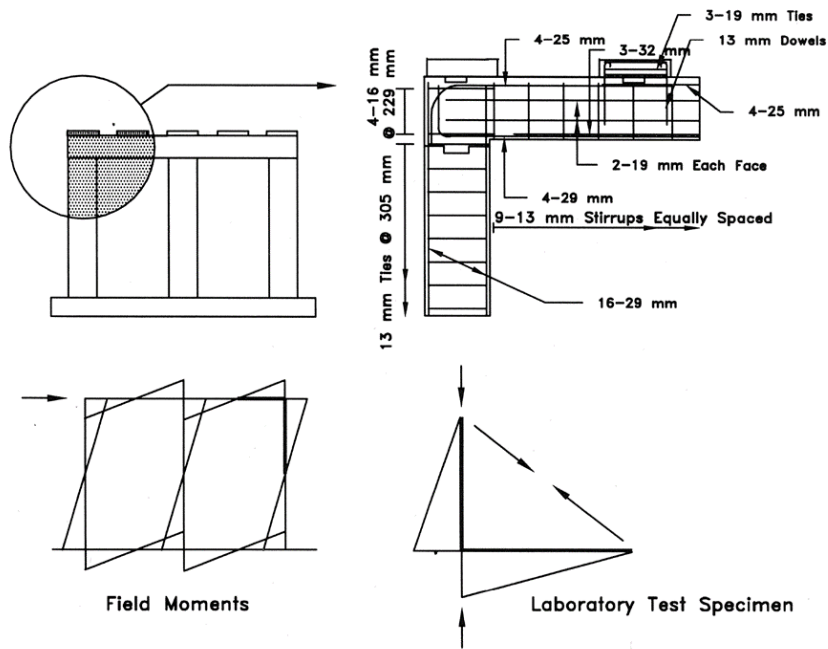


Figure 2.2. Retrieval Location of Specimens from Niagara Parkway Bridge.

Young et al. (2002) investigated unexpected shear cracking in reinforced concrete bent caps designed with existing standards. Researchers investigated bent cap design requirements and detailing arrangements that were common at the time of the research, including service stress in flexural reinforcement, the reinforcing bar layout, and location of critical flexural design sections.

Full-scale experimental testing of 16 reinforced concrete bent cap specimens focused primarily on the negative bending region at the exterior column location. The experimental test setup is shown in Figure 2.3. The researchers placed strain gauges along

the main tensile, compressive, side-face, and transverse reinforcing bars similar to that shown in Figure 2.4. Strains were plotted along the length of the bent cap specimens for each loading stage, as seen in the example in Figure 2.5. To understand the behavior of the bent caps, experimental strain was compared to the expected strain from analytical modeling at key locations (the face of the column and column centerline).

Based on the results of experimental testing, researchers recommended that the column centerline should be used as the critical design section for flexure, effectively providing a slight over strength at the effective column face section. To limit the extent of flexural cracking, the researchers recommended that the service stress in the flexural reinforcement be limited to 36 ksi and 30 ksi for moderate and severe exposure conditions, respectively. The researchers validated that the current skin reinforcement requirements in the American Association of State Highway and Transportation Officials (AASHTO) and American Concrete Institute (ACI) 318 codes were appropriate to assist in crack control. The influence of these recommendations can be seen in the current TxDOT standard interior bent cap design sheets.

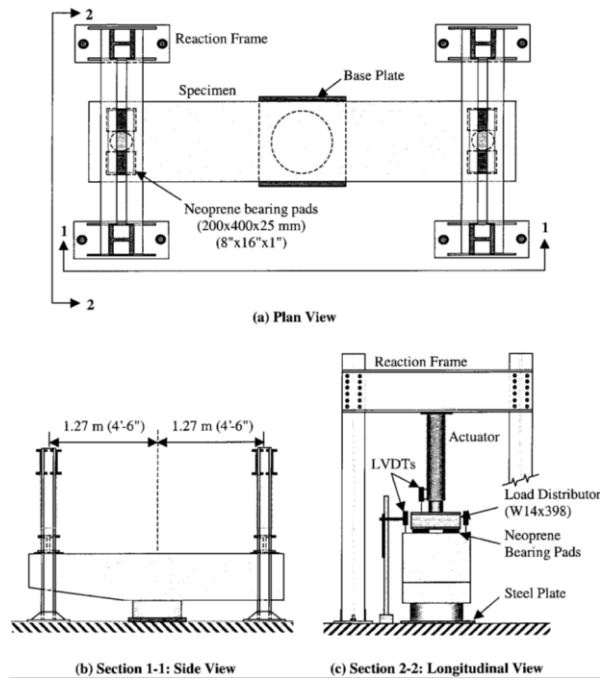


Figure 2.3. Experimental Test Setup (Young et al. 2002).

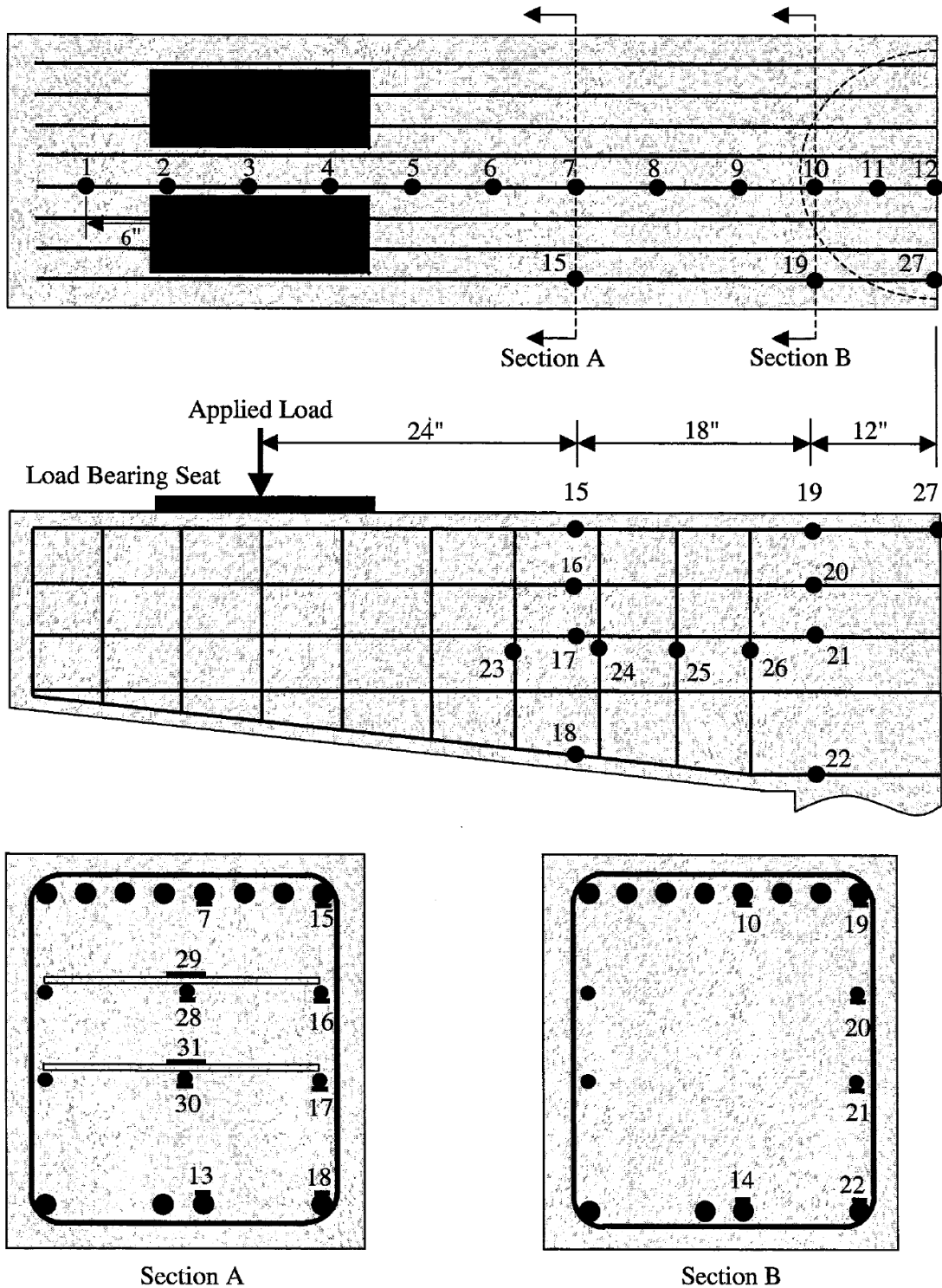


Figure 2.4. Example Strain Gauge Placement Plan (Bracci et al. 2000).

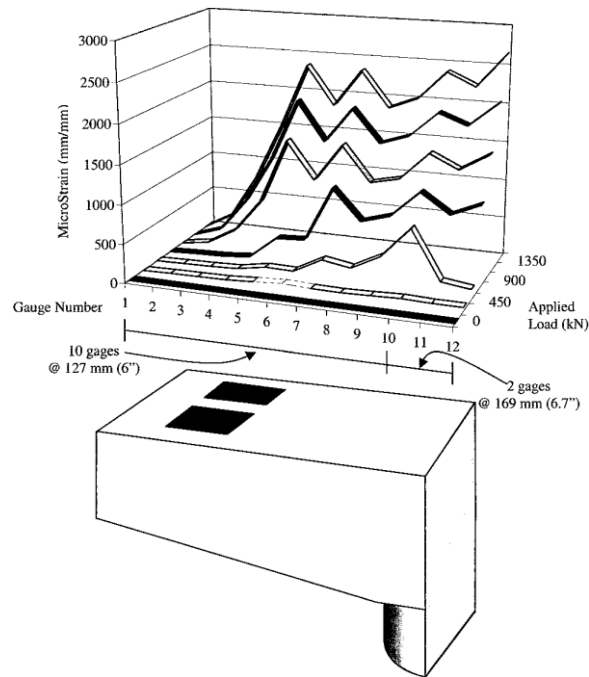


Figure 2.5. Longitudinal Reinforcement Strain Profile for Specimen 1A (Young et al. 2002).

Bechtel (2011) investigated methods of external strengthening of reinforced concrete pier caps that were shown to be susceptible to premature shear cracking. The test program was developed based on the pier caps from bridge 085-0018 in Dawson County, Georgia. The behavior of these reinforced concrete bridge pier caps was studied up to their ultimate capacity. The results of the analytical and experimental study were used to develop an external strengthening system.

A finite element model (FEM) was created to determine the maximum shear force that could be applied to the pier cap under normal loading conditions. Both full-scale and half-scale specimens were tested to understand how size effects influence the behavior of the beams. Specimens were instrumented, as seen in Figure 2.6, with strain gauges attached to reinforcing bars, linear variable differential transformers (LVDT), string

potentiometers, and load cells. From testing the specimens, strain gauge and LVDT data was used to calibrate the FEM. The calibrated FEM aided in. During the tests, the deflection of the beam under the loading point was measured and correlated with the applied load, shown in Figure 2.7. The loads at which significant shear cracks formed were marked on the plots; an obvious change in the behavior of the cracked beams is noted by the researchers.

Based on the experimental testing and finite element modeling, researchers noted that the stress concentration induced by the column was an important factor in dictating the failure mode and principal compression strut angle. Also, increases in the tension longitudinal reinforcement was shown to increase the ultimate capacity of the beams by way of increasing the capacity of the tension tie. By increasing the capacity of the tension tie, the shape of the tied arch changed, which decreased the effects of the stress concentration at the beam-column connection. It was concluded that a size effect was only evident when the ultimate strength of the beams was governed by splitting failure of the concrete.

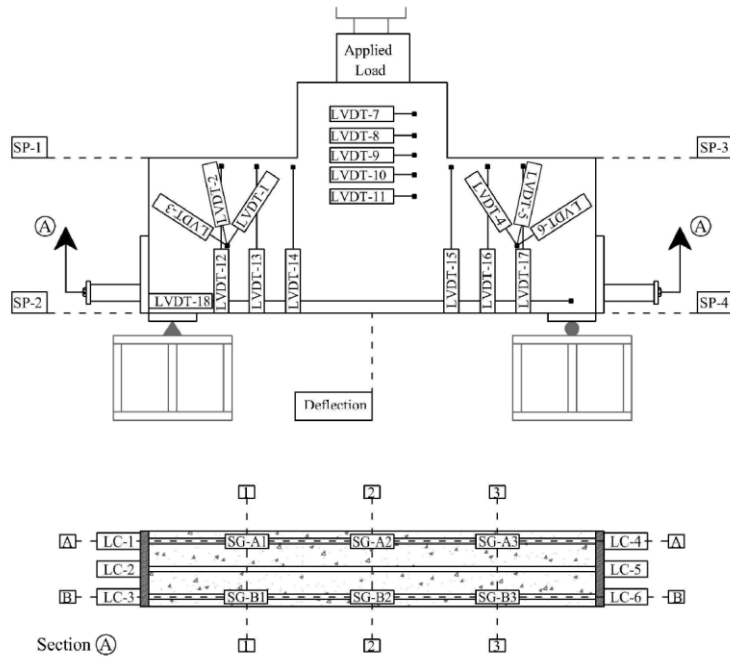


Figure 2.6. Instrumentation of Pier Cap Specimens (Bechtel 2011).

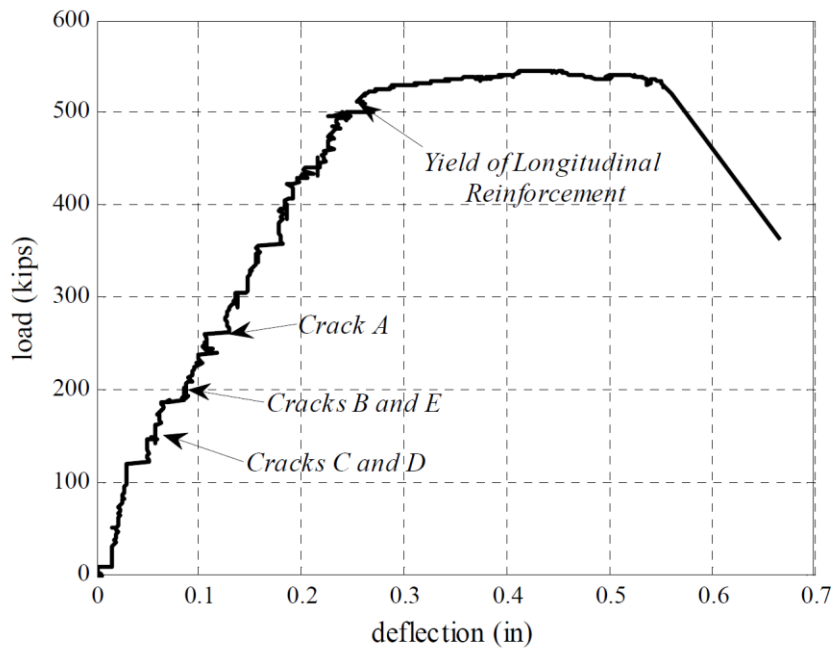


Figure 2.7. Load vs. Deflection Plot Example (Bechtel 2011).

2.3. Precast Prestressed Bent Caps

To aid the Texas Department of Transportation (TxDOT) in developing and implementing precast, pretensioned bent caps, research was performed at Texas A&M University and is presented in [Birely et al. \(2018a\)](#) and [Birely et al. \(2018b\)](#). Portions of this research are documented by [Barooah \(2016\)](#) and [Yole \(2017\)](#). [Barooah \(2016\)](#) developed a flexure design procedure and design recommendations for engineers to easily integrate pretensioned bent caps into new projects. As part of this study, maximizing the benefits of utilizing pretensioning was a focus. The design concept of maintaining zero tensile stresses under dead load demands was imposed to ensure that any cracks that had formed would close upon removal of the live load. To allow for the field connection of the precast cap beam and the cast-in-place columns, a side strand configuration was recommended (shown in Figure 2.8). Through comparison of top/bottom and side strand configurations, it was concluded that the capacity of the bent caps was not significantly affected by using the side strand configuration- with a reduction in capacity of less than 5% (Figure 2.9). Through analysis of both reinforced concrete and pretensioned concrete bent cap designs with demands representative of the entire TxDOT bridge inventory, it was shown that the expected behavior and performance of the pretensioned bent caps was satisfactory in achieving the design objectives. For most bridge layouts, cracking was not expected in pretensioned bent caps even under the ultimate load cases. For these same bridge configurations, it was shown that cracking could be expected at the service load level in the reinforced concrete bent caps.

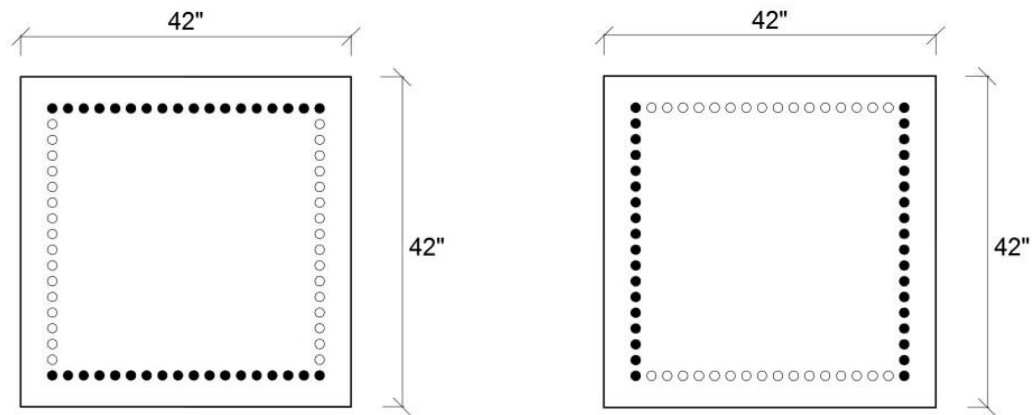


Figure 2.8. Top/Bottom Strand Configuration (left) and Side Strand Configuration (right) (Barooah 2016).

The work of [Yole \(2017\)](#) built upon the work of [Barooah \(2016\)](#) with the experimental testing of reinforced concrete and pretensioned concrete bent cap specimens. Based on the capacity of the laboratory equipment, bent cap test specimens representing a standard TxDOT three column, four-girder BIG32 bridge configuration were designed and constructed (Figure 2.10 and Figure 2.11). The pretensioned bent cap was designed following the design procedures recommended by [Barooah \(2016\)](#). To accurately compare the effects of pretensioning on the bent caps, a reinforced concrete specimen was designed to closely replicate the capacity and reinforcement configuration of the pretensioned bent cap.

The specimens were tested by applying demands representing realistic bridge demands, maximum positive and negative moment demands based on the experimental test setup, joint opening/closing demands, and a final load case to initiate failure of the beams. The bent cap specimens were instrumented with strain gauges placed on the

longitudinal (reinforced concrete specimen only), transverse reinforcement, and beam-column connection components, linear variable differential transformers (LVDT), and string potentiometers. During experimental testing, loading was paused at key load cases to examine, measure, and mark cracks and damage. The research presented in Birely et al. (2018a) and Yole (2017) did not present significant analysis of collected instrument data- this was preserved for future publications.

Based on visual observations, it was shown that the pretensioned bent cap specimen performed significantly better than the reinforced concrete specimen did. The pretensioned bent cap showed a delay in the onset of cracking and a significant decrease in the amount and size of cracks under realistic bridge demands. It was also shown that most cracks that appeared in the pretensioned specimen under service loads closed, or nearly closed, upon the removal of live loads. While cracking unexpectedly appeared at the service load level in the pretensioned specimen, the flexural design objectives of zero tension under dead load and ductile behavior were satisfied. The premature onset of flexural cracking is discussed further in Birely et al. (2018a).

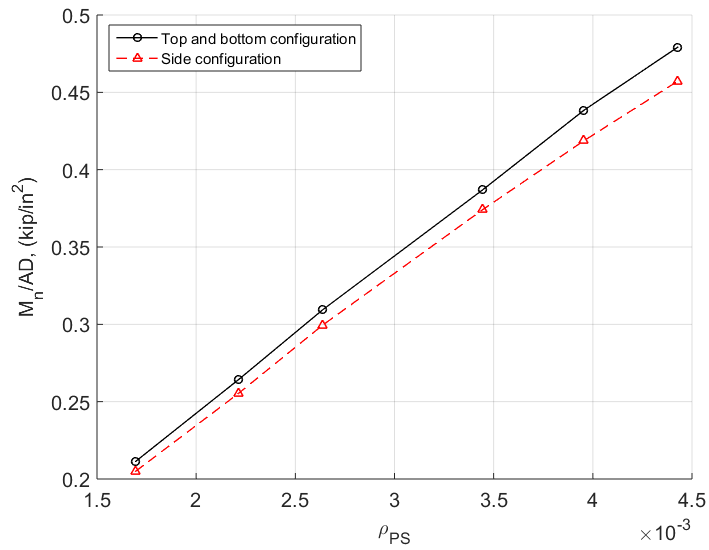


Figure 2.9. Nominal Strength vs. Area of Prestressing for Top/bottom and Side Strand Configurations (Barooh 2016).

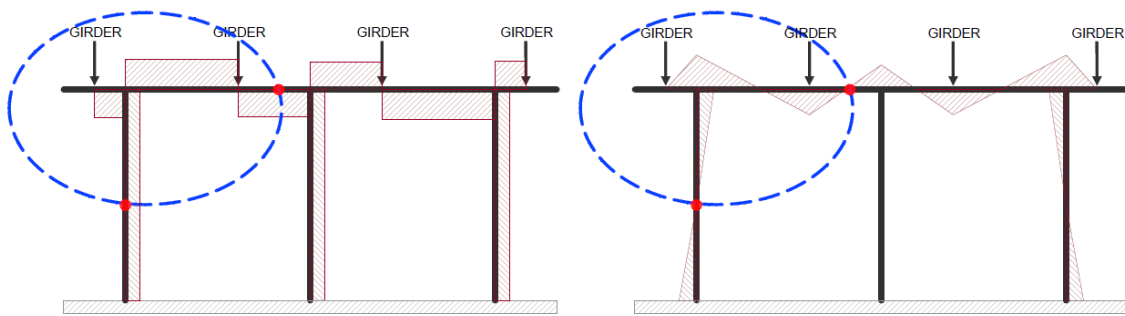


Figure 2.10. Prototype Bridge Shear (left) and Moment (right) Diagrams (Yole 2017).

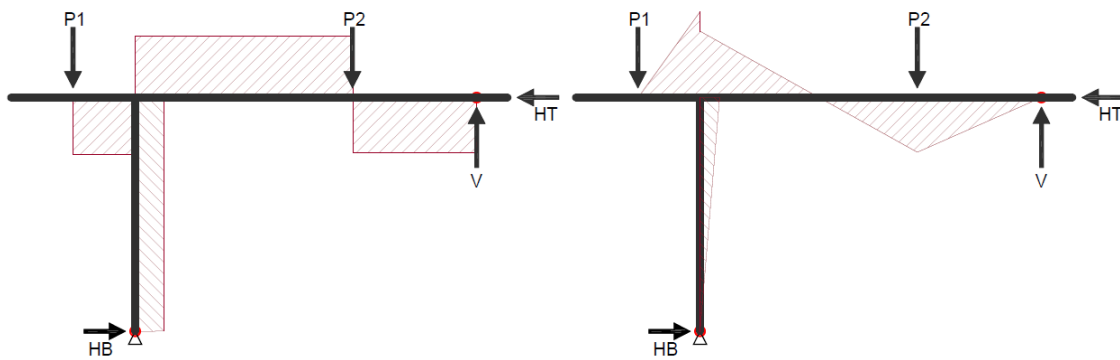


Figure 2.11. Specimen Shear (left) and Moment (right) Diagrams (Yole 2017).

2.4. Precast Beam-To-Column Connections

One of the challenges of producing standards for precast reinforced concrete bent caps was developing an adequate beam-to-column connection that would cause the least interference with the reinforcement layout in the existing standards for easy integration. Matsumoto et al. (2011) conducted a three-phase test program to ultimately develop a precast reinforced concrete bent cap system for conventional bridge systems in non-seismic regions.

Details for candidate connections were developed in Phase 1. These connections included single line grout pocket, double line grout pocket, vertical duct, and a bolted connection. Experimental testing was performed in Phase 2 to address the uncertainties uncovered during the development of the details in Phase 1 and to investigate the performance of each connection type. These uncertainties included bar anchorage in grout, interlock of pockets and ducts in the cap, failure modes, and the influence of confining reinforcement.

To address the bar anchorage concerns, a series of pullout tests were conducted. Researchers varied the bar anchorage type, bar size, embedment depth, number of bars per pocket, bar configuration, confining reinforcement, grout type, and grout brand. Pullout tests were conducted with the test setup shown in Figure 2.12. Data was collected from strain gauges placed along the length of the bars and on the vertical ducts, string potentiometers attached to the bottom the bars (through a tube in the grout) and to the concrete beam, and with linear potentiometers attached to the lead bar. The strain profile in the bars was correlated with the applied load to show the distribution of stress in the straight and headed bars. In tests with the vertical ducts, strains in the ducts were measured

to help understand the confining behavior of the vertical ducts. The vertical displacement of the bars was measured to monitor load-slip behavior, as shown in Figure 2.13.

Tests on the complete candidate connections were conducted with the test setup shown in Figure 2.14. The specimens were instrumented similar to the methods during the pullout tests, with the addition of string potentiometers to measure the beam deflection. The same measurements were analyzed from the connection tests as the pullout test. This allowed a comparison of the behavior in the full-scale connection under realistic loading to the behavior during the pullout tests. Load-deflection behavior of the beam and column base fixity were also studied.

Phase 3 tests aimed to assess the constructability of the different connection types by having a contractor fabricate and assemble precast bents with the different candidate connection type and details. The bents were also subjected to in-field proof load testing, where the load-deflection behavior was measured. Damage was marked and tracked during testing. Limited damage during the testing indicated that the connections behaved as expected. Using the results from the Phase 2 and Phase 3 testing, the researchers produced recommendations for a design procedure and for construction. The influence of these recommendations are seen in the TxDOT precast reinforced concrete bent cap option standard drawings that were released after the completion of this research.

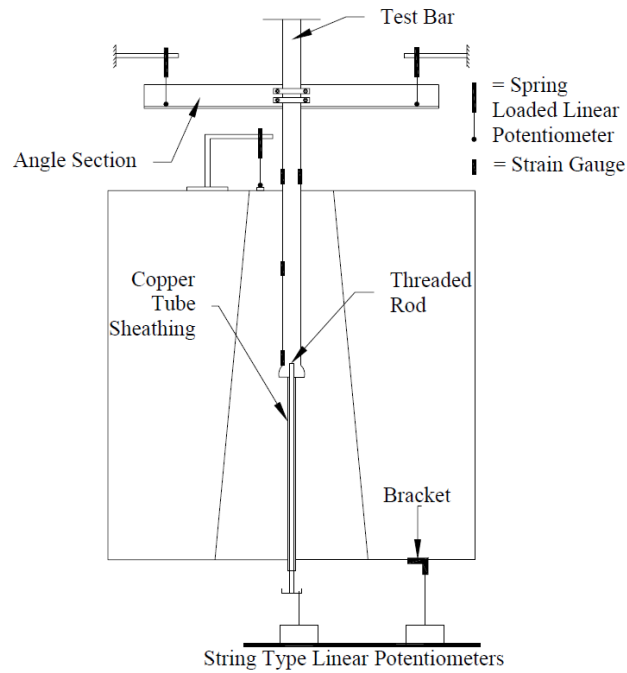


Figure 2.12. Pullout Test Setup (Matsumoto et al. 2001).

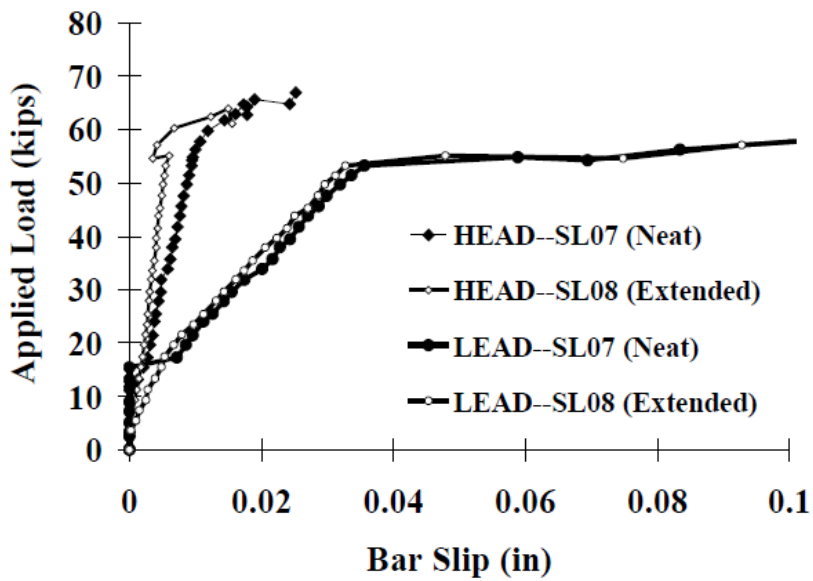


Figure 2.13. Load-Slip Behavior during Pullout Tests (Matsumoto et al. 2001).

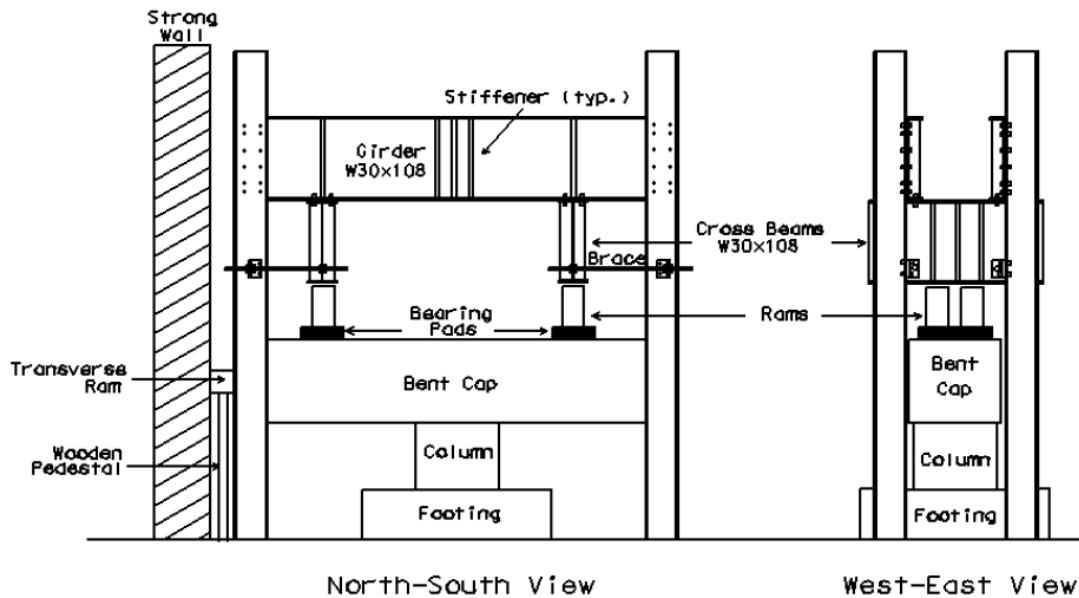


Figure 2.14. Connection Test Setup (Matsumoto et al. 2001).

Research on precast beam-to-column connections was continued by Restrepo (2011) with the experimental testing of seven 42% scale precast bent cap sub-assemblages with different cap-to-column connection types, such as grouted vertical ducts, cap pockets, and concrete filled pipe hybrid connections. The aim of this research was to investigate the performance of the precast bent cap connections under seismic loading to aid in the development of using precast bent cap system in seismic regions.

The experimental test setup, shown in Figure 2.15, applied cyclic loading to the column. Specimens were instrumented with strain gauges on the internal reinforcement, linear potentiometers, and inclinometers. The lateral displacement of the column was plotted against the applied lateral load to show the hysteretic response of the column, as shown by the example in Figure 2.16. The predicted response was plotted over the experimental response to show the correlation of the stiffness and ductility. Transverse

reinforcement strain profiles were plotted to show the behavior of the shear reinforcement outside and inside of the joint region.

From experimental testing, the cap pocket (full ductility) was shown to perform similarly to the monolithic cast-in-place connection, and thus satisfactory for use in seismic applications. Researchers used the results of experimental testing to aid in the development of design specifications and to propose changes to the AASHTO Guide Specifications for LRFD Seismic Bridge Design and AASHTO LRFD Bridge Design Specifications.

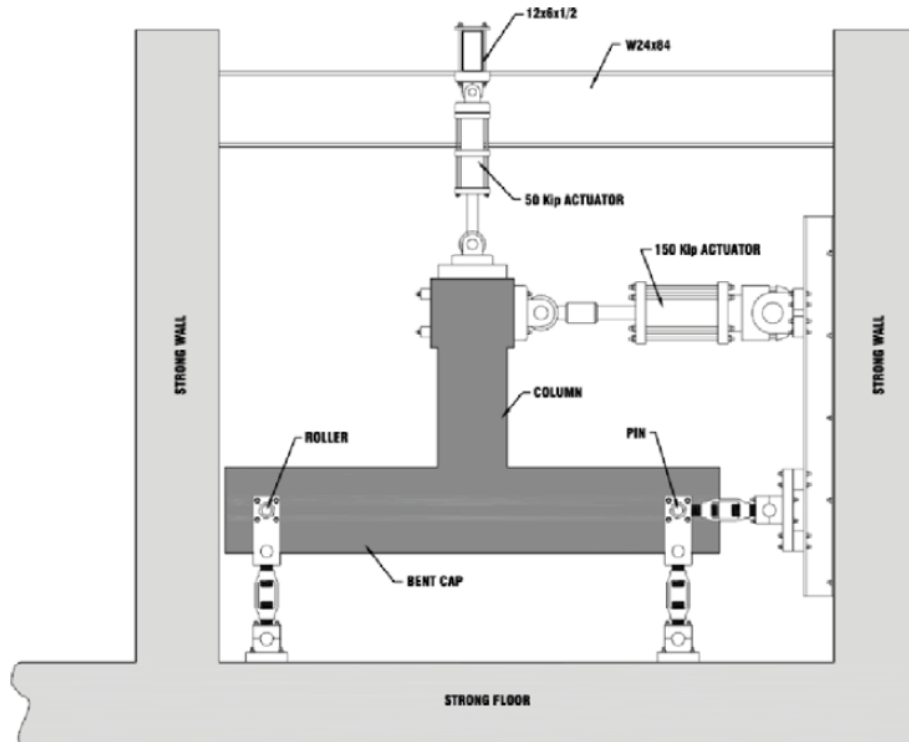


Figure 2.15. Experimental Test Setup (Restrepo et al. 2011).

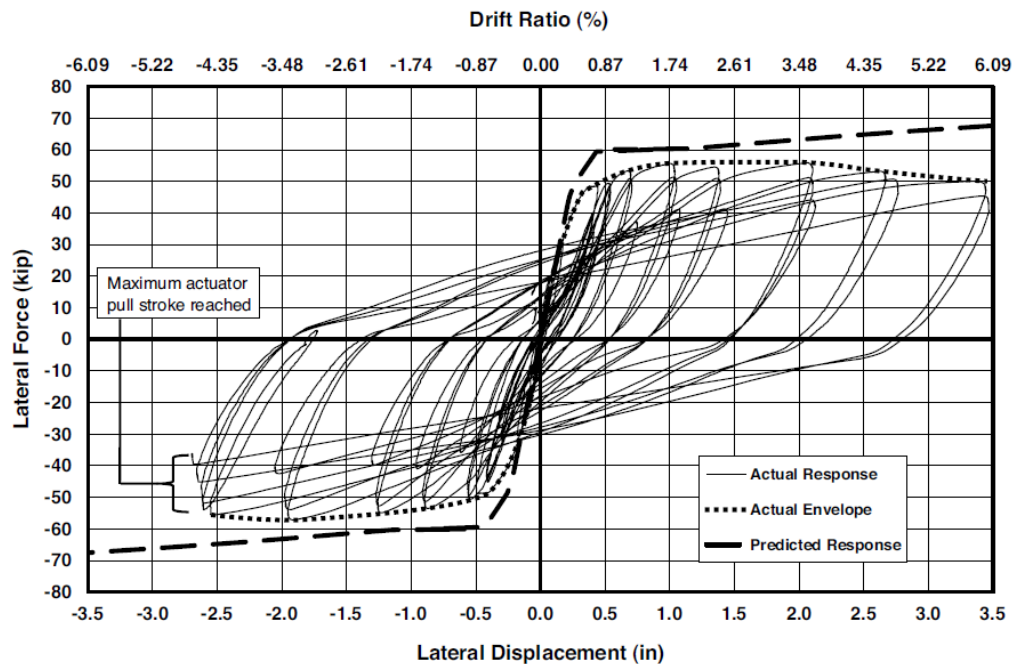


Figure 2.16. Lateral Hysteretic Response of Column (Restrepo et al. 2011).

2.5. Voids in Concrete Bridge Structures

Some of the most commonly used voided concrete elements in the State of Texas are pretensioned box beam bridge girders. Box beams are similar in nature to voided bent caps in that the cross-section is primarily hollow, leaving a thin web along the sides of the beam.

Schnittker and Bayrak (2008) performed full-scale experimental testing on 45 pretensioned concrete TxDOT Type-C beams (I-beams) and 10 pretensioned concrete box beams to investigate the effects of exceeding the allowable compressive stress at the release of pretensioning strands. The test girders were constructed by several different fabricators, to provide variation in techniques, mix designs, consolidation methods (vibration or self-consolidating), and material properties. The pretensioned girders were designed and constructed with intentional at-release overstressing by up to 10%.

The girder specimens were tested in flexure in the test setup shown in Figure 2.17. Girders were instrumented with linear potentiometers to measure the displacement at the ends and mid-span. Box beam specimens were loaded incrementally to 20% beyond the observed cracking load. Loading was paused to mark and measure cracking. Using the collected data, load-deflection relationships were plotted and used to determine the apparent cracking moment capacity. It was recommended by the researchers that the allowable compressive stress at release be increased no more than 5% from the current limit.

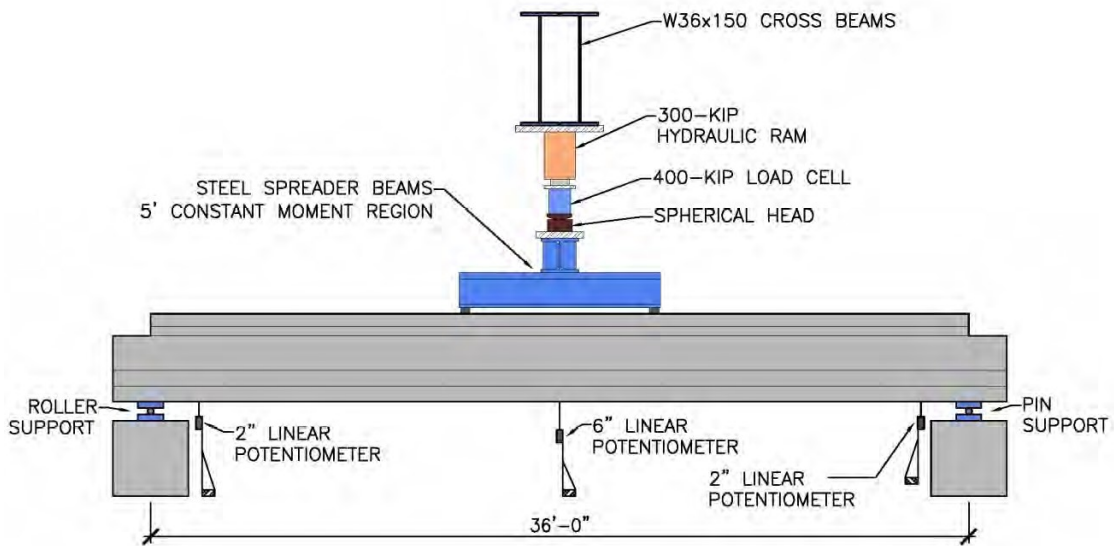


Figure 2.17. Experimental Test Setup (Schnittker and Bayrak 2008).

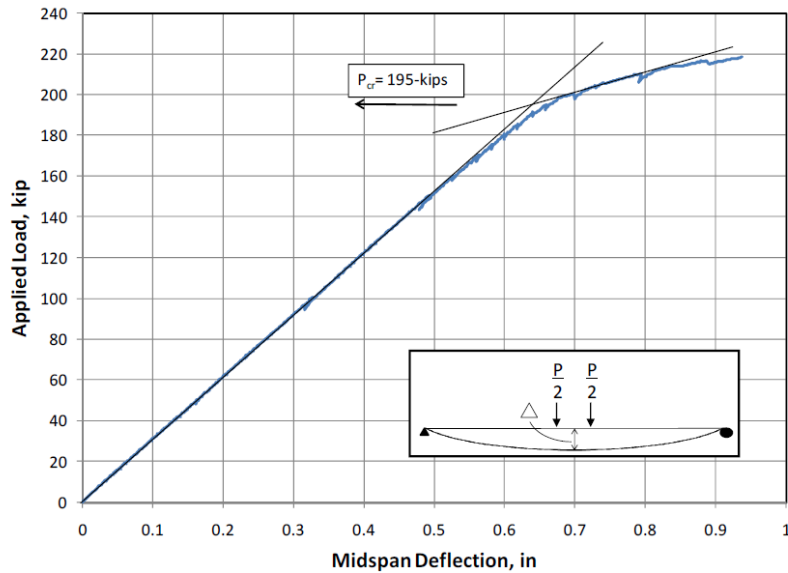


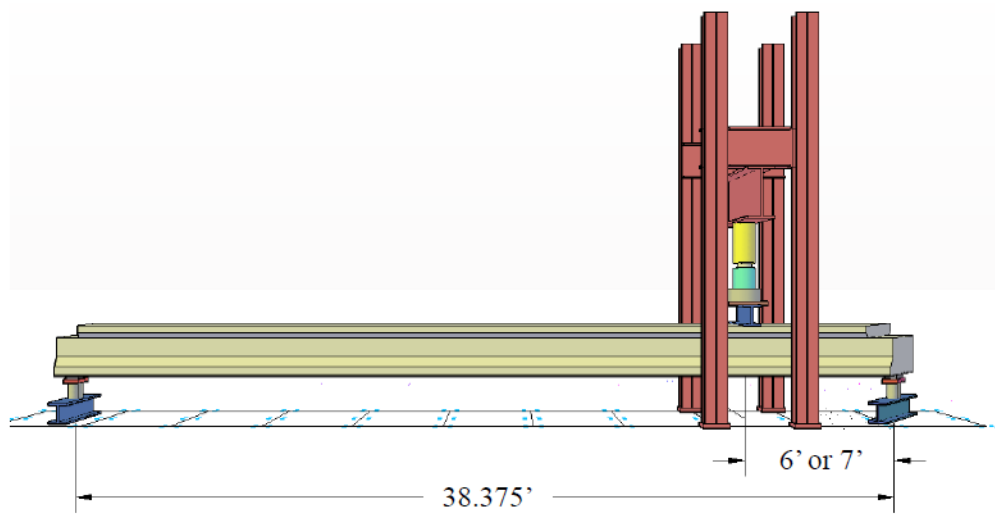
Figure 2.18. Load-Deflection Plot Example (Schnittker and Bayrak 2008).

Valderrama (2011) tested ten 4B28 (4-ft wide, 28-inches deep) and five 5B40 (5-ft wide, 40-in. wide) box beam girders to understand how the characteristics of box beams influence their behavior. Additional shear tests were performed on the 4B28 girders tested by Schnittker and Bayrak (2008), with the addition of five 5B40 box beam specimens cast. A variation to the internal void geometry in one specimen was included to investigate the influence of void geometry on shear performance. Since the 4B28 box beam girders were not previously failed and testing was focused primarily on pure flexure at the mid-span, shear testing the ends of the beams remained feasible. Each 4B28 box beam was tested twice, once on each end, with the test setup shown in Figure 2.19. The test setup for the 5B30 beams was similar in nature to that of the 4B28 tests.

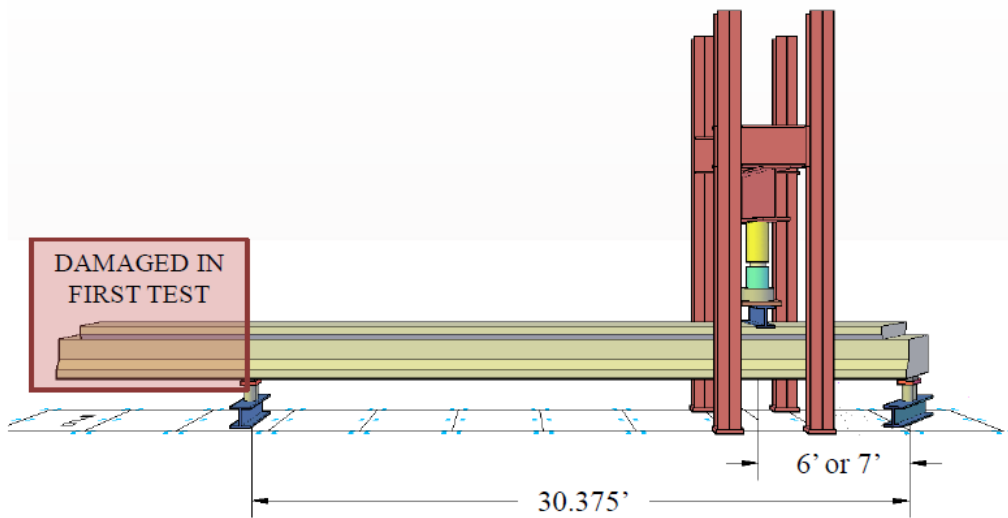
Girders were instrumented with linear potentiometers under the supports and at mid-span to measure the displacement and placed between the load point and the support

(as shown in Figure 2.20) to measure shear deformations. The 5B50 girders were also instrumented with internal strain gauges on the reinforcing steel.

During testing, the onset of shear cracks was recorded. Plotting measured average diagonal strain in the test area versus applied shear demand, as shown in Figure 2.21, showed a distinct change in behavior of the beams after initial cracking. The strain profiles of transverse reinforcement in the test region were plotted against the normalized applied shear. The load at which diagonal cracks first appeared correlated with a clear change in measured strain in the transverse reinforcement near the crack location. The researchers noted that the theoretical shear capacity and experimental shear capacity of the pretensioned concrete box beams varied no more than a comparison of results from similar experimental tests performed on pretensioned I-girders, suggesting that the current methods of shear design developed for thin-webbed I-girder are applicable to wide, hollow box beams. No discernable differences in behavior of the box beams with different interior void details were observed.



(a) First Shear Test Setup



(b) Second Shear Test Setup

Figure 2.19. 4B28 Box Beam Shear Test Setup (Valderrama 2011).

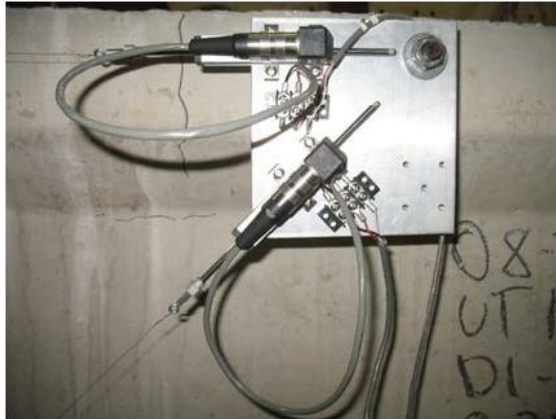


Figure 2.20. Shear Deformation Monitoring Instrumentation (Valderrama 2011).

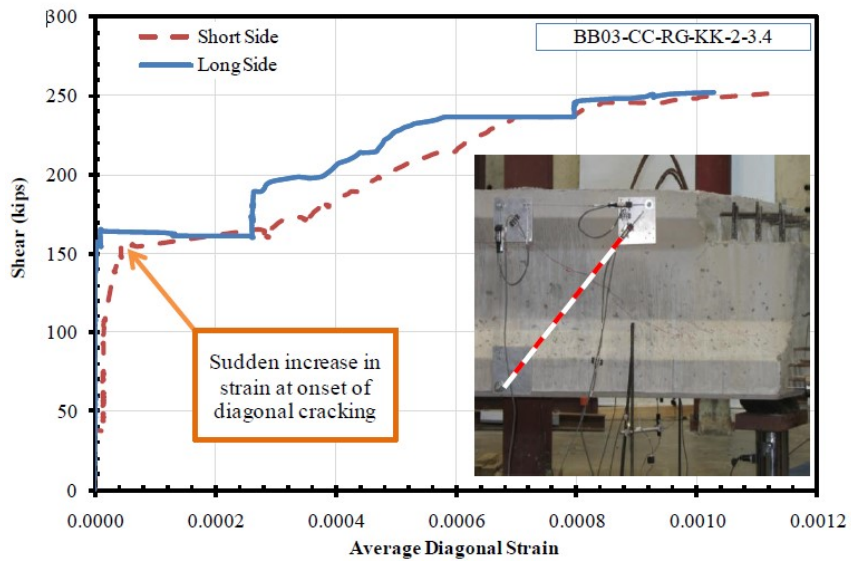


Figure 2.21. Shear Demand versus Shear Strain Plot Example (Valderrama 2011).

2.6. Motion Capture Systems

The use of motion capture systems to collect measurements in experimental testing of concrete structures has gained popularity in recent years.

Experimental testing was conducted at the University of Illinois at Urbana-Champaign on eight 1/3-scale structural concrete walls, as documented by [Lowes et al. \(2011\)](#), [Lowes et al. \(2012\)](#), [Hart \(2012\)](#), and [Birely \(2012\)](#). The walls replicated the lower three stories of a 10-story prototype building and were subjected to simulated seismic loading with the test setup shown in Figure 2.22. Experimental testing investigated the impact of reinforcement layout, shear demand, and lap splices at the base of the wall.

Researchers instrumented the walls with a variety of traditional sensors, including internal and external strain gauges, linear potentiometers, string potentiometers, and linear variable differential transformers. Advanced measurement methods including the use of a non-contact Nikon Metrology K-Series (Krypton) Optical Coordinate Measuring Machine (CMM) and high-resolution photogrammetry.

Traditional measurements were heavily collected during the tests. Strain gauges were placed on reinforcement and on the surface of the concrete. Linear potentiometers measured the average strain over relatively large gauge lengths. String potentiometers and LVDTs were used to measure the absolute displacement of the walls.

Advanced measurements methods were used to collect high-resolution data over a large area. The non-contact Krypton CMM system was used to collect data from only the bottom two stories of the wall, due to the limitations of the collection volume (Figure 2.23). Light emitting diode (LED) markers were attached in a 6-inch grid pattern

(Figure 2.24) to the walls, and a single Krypton CMM camera was used to collect data. The photogrammetry technique utilized eight high-resolution cameras to take photos of the walls throughout testing. Photogrammetry targets (Figure 2.25) were attached to the walls to aid in the combining and processing of the photographic data. Processing and analysis of the data collected with the Krypton CMM and photogrammetry is presented in detail in [Birely \(2012\)](#) and [Hart \(2012\)](#).

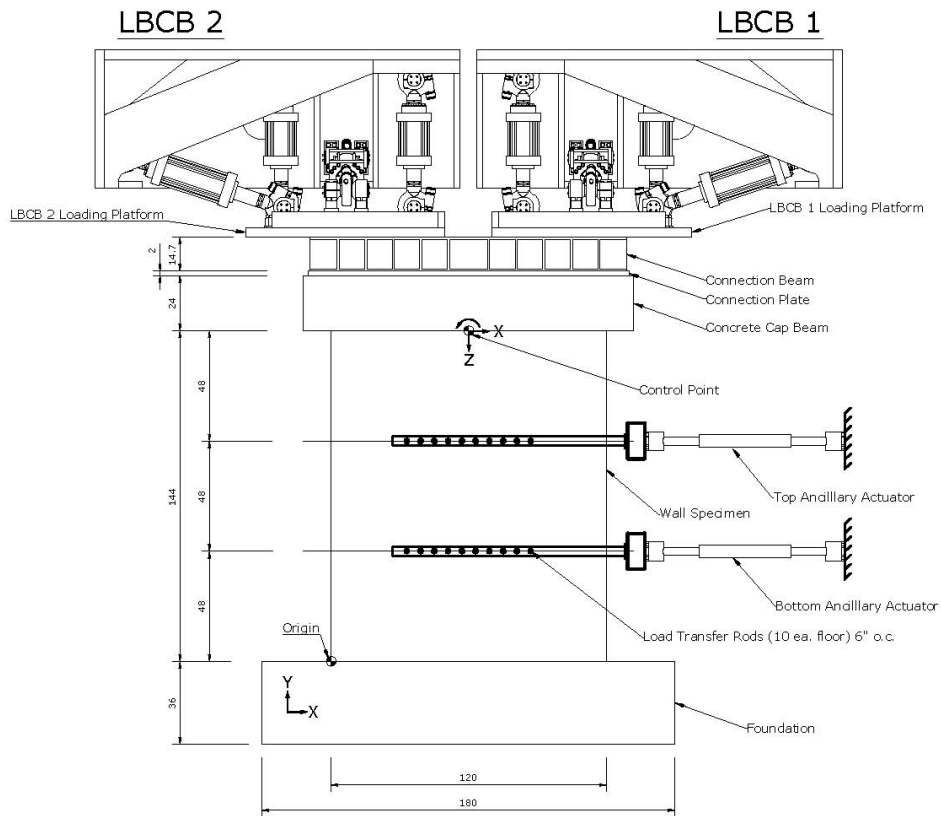


Figure 2.22. Structural Wall Test Setup (Lowes et al. 2011).

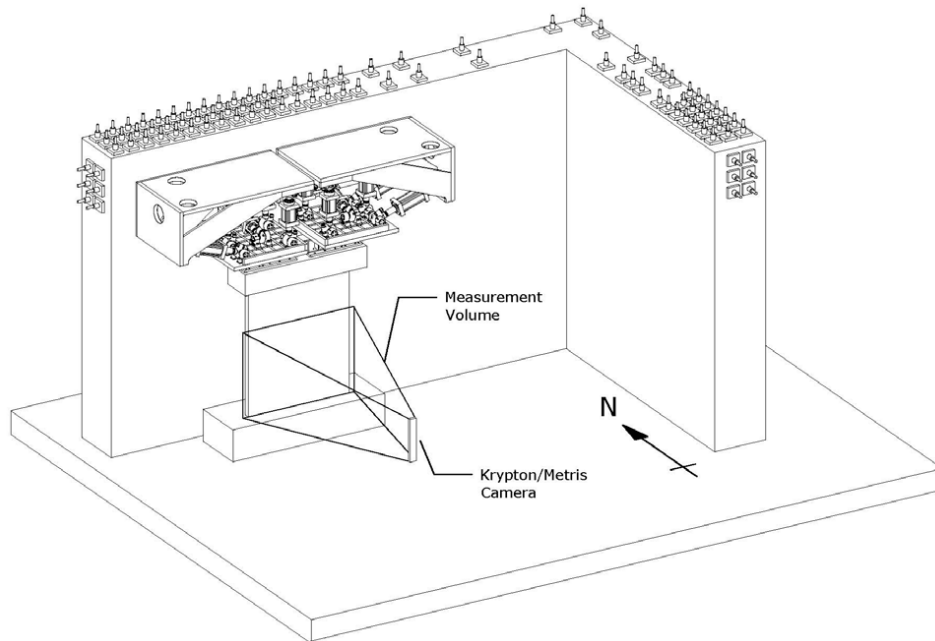


Figure 2.23. Krypton CMM Measurement Volume (Lowe et al 2011).

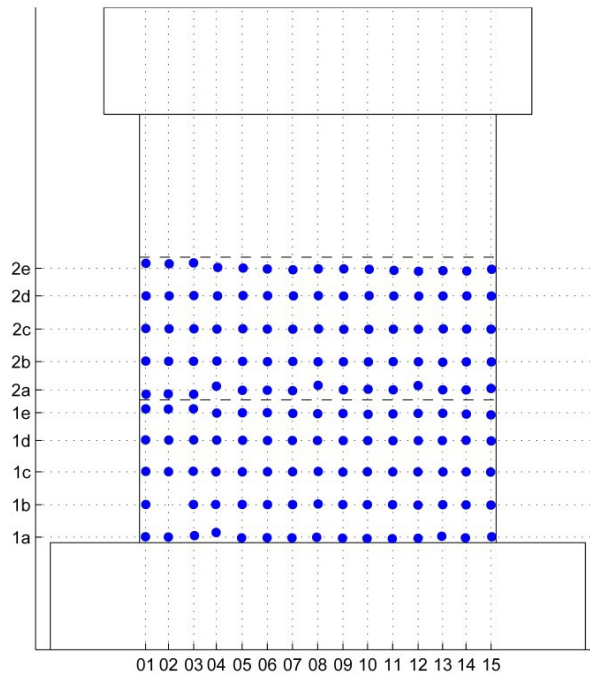


Figure 2.24. Typical Krypton CMM LED Target Layout (Lowe et al. 2011).

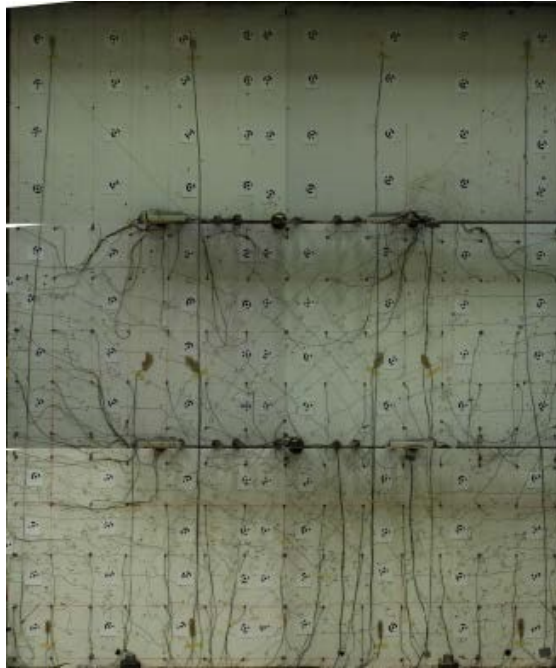


Figure 2.25. Photogrammetry Target Placement Example (Hart 2012).

Birely (2012) presented the seismic performance of the slender structural walls; with significant analysis performed using the Krypton CMM data. Parameters such as displacements and rotations, effective stiffness, drift, strain fields, and deformation were calculated using the Krypton measurements.

Displacement measurements from the Krypton CMM system were compared to traditional measurements where possible. It was shown that lateral displacements measured with the Krypton CMM matched closely to the displacements measured by the traditional string potentiometers (Figure 2.26). With the Krypton CMM system only used on the first and second story of the wall specimen, the lateral displacement of the third story was measured with a control string pot located at the center-top of the wall. It was shown that the average lateral displacement of an entire row of LED targets matched

closely to the displacement of the single LED target located at the center of the row. Using the average lateral displacement of the rows of LED targets on the first and second story in addition to the lateral displacement measured with the control string pot, displacement profiles of the wall specimens at different stages of testing were plotted; an example is shown in Figure 2.27.

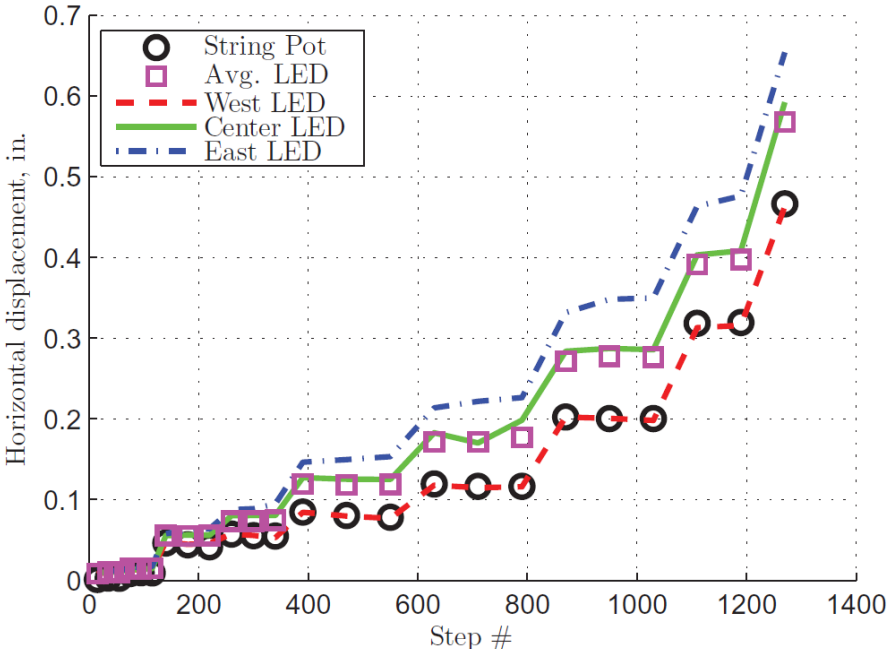


Figure 2.26. Krypton LED Displacements Comparison with Traditional String Pot Measurements (Birely 2012).

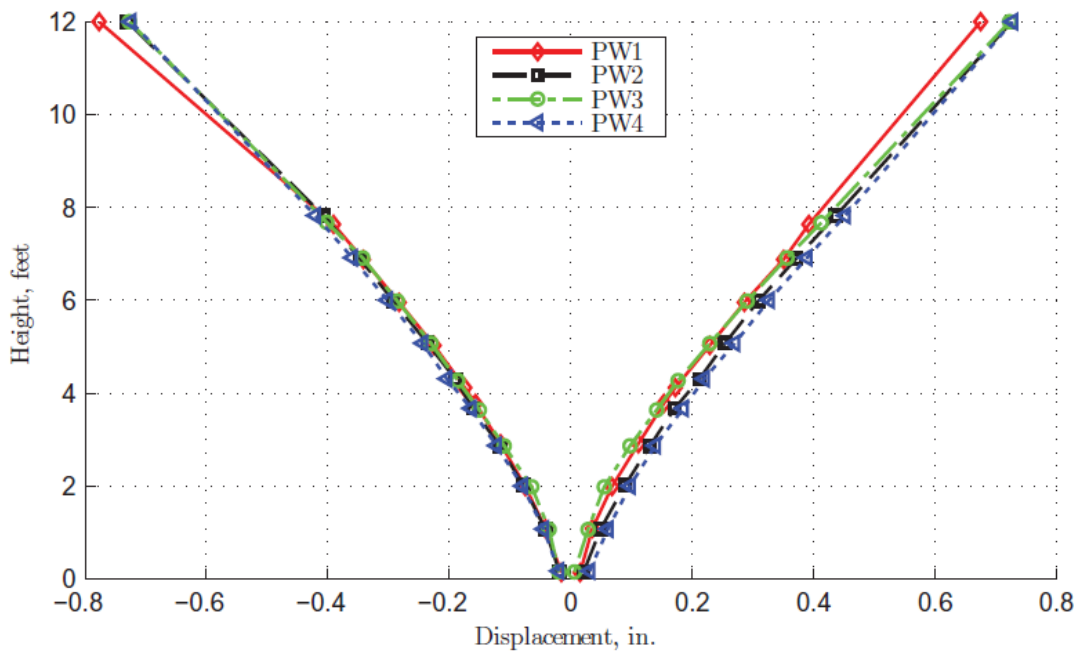


Figure 2.27. Displacement Profile Example (Birely 2012).

The dense grid of Krypton LED targets resembled a grid mesh from a finite element analysis. Using the Krypton CMM data, strains fields were created for the first and second story of the wall specimens. Two methods were used to calculate strain from the Krypton CMM data. The first used the displacement of each Krypton target as the nodal displacement in a finite element mesh. The second method used the displacement of a Krypton target relative to its original position to determine strain.

The first method of calculating strains used four-node isoperimetric quadrilateral finite element formulation. Strain was determined at each corner and at the center of the “element”. The strain values were used to plot strain fields and to determine principal strains. The weighted average of the strain values determined for the “node” common to adjacent “elements” were used to smooth the strain field plots. An example is shown in

Figure 2.28. Where data for all four corners of the “element” were not available and where Krypton CMM data was not collected, strains were calculated using the second method by utilizing the relative change in geometry between points. The strain field plots were used to show the difference in behavior of the wall specimens with the varied designs.

The relative distribution and magnitude of horizontal, vertical, shear, and principal strains led to conclusion about the influence of the design variables on the behavior of the walls. The locations of maximum tensile and compressive strains corresponded with the locations of observed crushing and cracking. Evaluating the compressive and tensile strains at the extreme fiber of the walls indicated that the walls were tension-controlled at the nominal state.

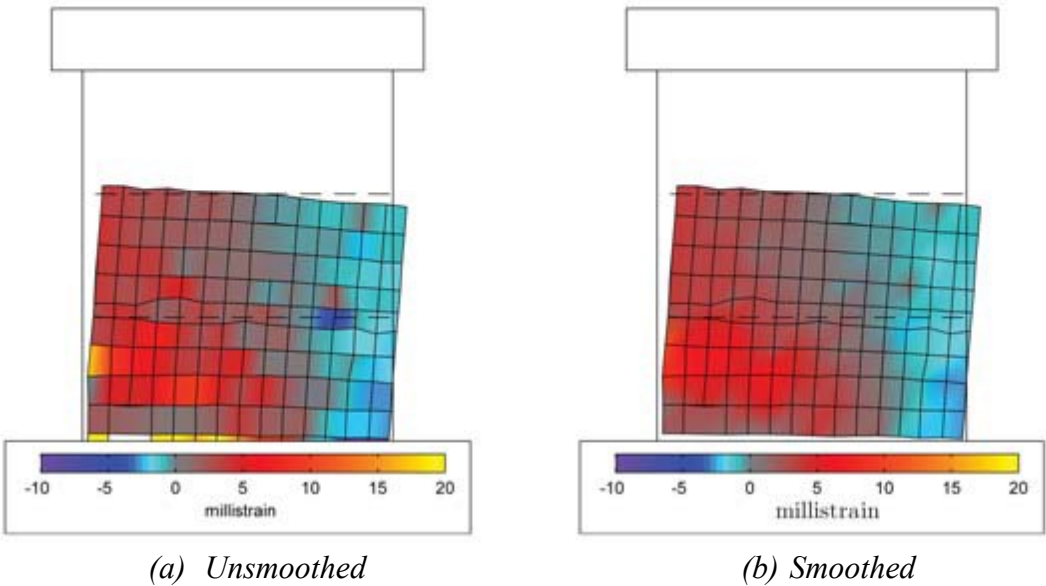


Figure 2.28. Unsmoothed and Smoothed Strain Field Plot Example (Birely 2012).

Hawkins and Kuchma (2007) explored the application of the existing AASHTO LRFD Bridge Design Specifications shear provisions to high-strength structural concrete members through experimental testing. Testing was performed on ten pretensioned bulb-tee bridge girders with variations in concrete strength, design shear stress, strand anchorage details, and end reinforcement details. The girders were tested by simulating a uniformly distributed load with hydraulic loading jacks spaced evenly along the length, as shown in Figure 2.29.

Girder specimens were instrumented with traditional sensors, such as internal and external strain gauges and LVDTs. Portable measurement tools were used, such as Whittimore Gauges and Zurich Gauges, to measure the displacement of targets attached to the girders. The Krypton CMM system was used to collect data in the end-regions of the girders. The LED Krypton targets and Zurich Gauge targets layouts are shown in Figure 2.30.

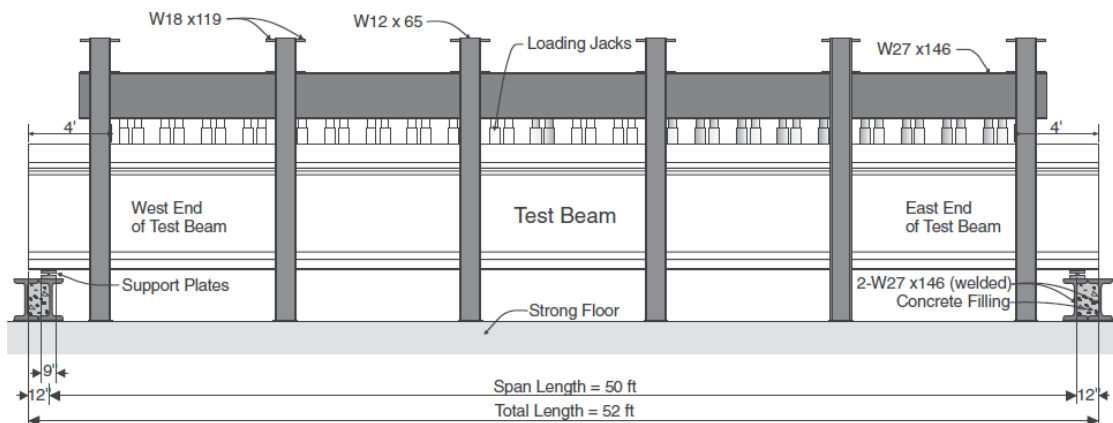


Figure 2.29. Pretensioned Bulb-Tee Girder Test Setup (Hawkins and Kuchma 2007).

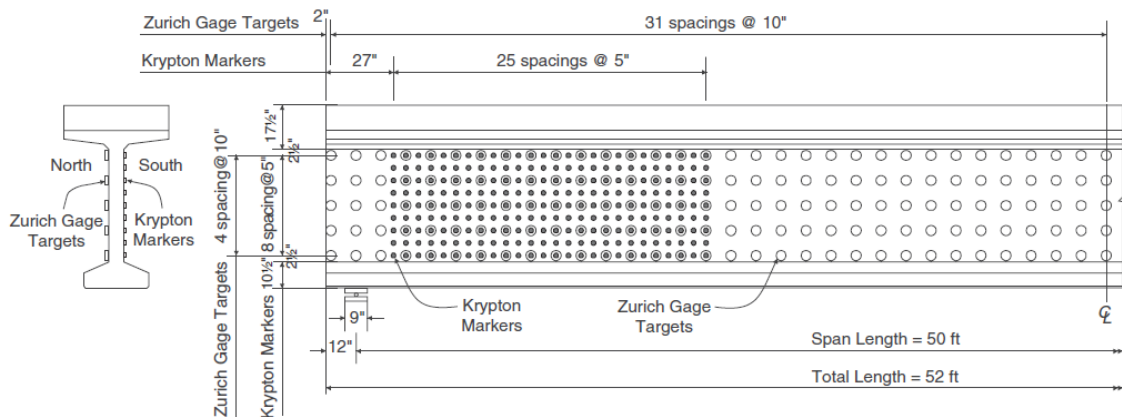


Figure 2.30. LED Krypton Targets and Zurich Gauge Targets Layout (Hawkins and Kuchma 2007).

Vertical, horizontal, and diagonal strains were computed along the length and height of the girder end-regions. Strain profiles were plotted for each row and column of LED Krypton targets, along with the average horizontal and vertical strain of each row and column versus the applied load; an example is shown in Figure 2.31 and Figure 2.32.

From the detailed strain measurements, researchers showed that the average vertical strain at a location of 15-inches from the support was essentially zero, confirming the design assumption that the design shear reinforcement at the critical design section is adequate for use in the region between the support and the critical section. Results showed that the horizontal strain distributions 20-inches from the support significantly increased prior to failure the girder, supporting the claim that the loss of the prestress and significant damage along the longitudinal reinforcement precedes the shear failure of the girders.

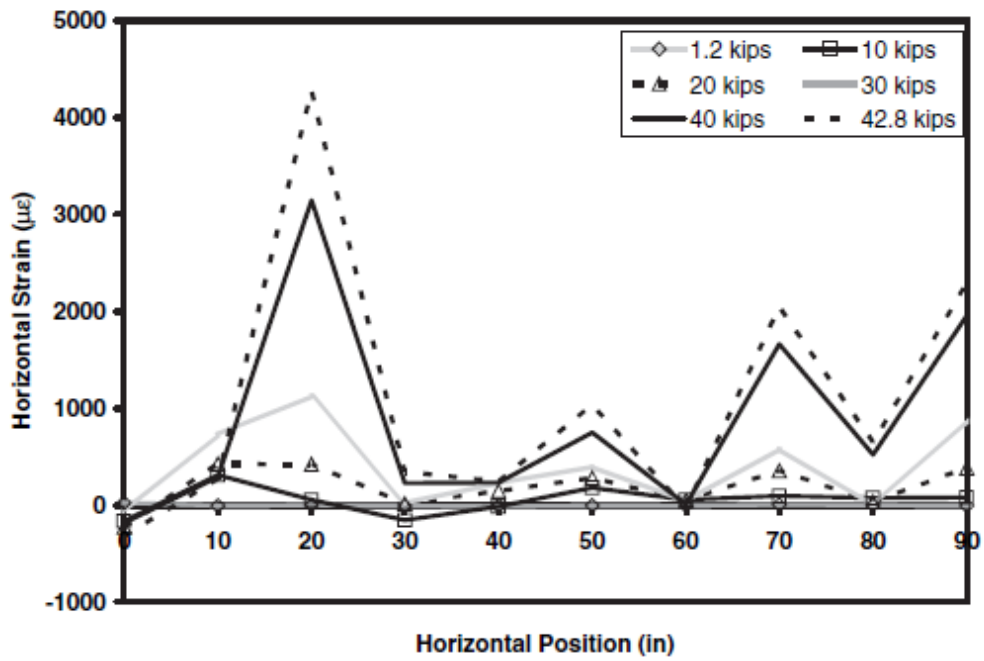


Figure 2.31. Horizontal Strain Profile Example (Hawkins and Kuchma 2007).

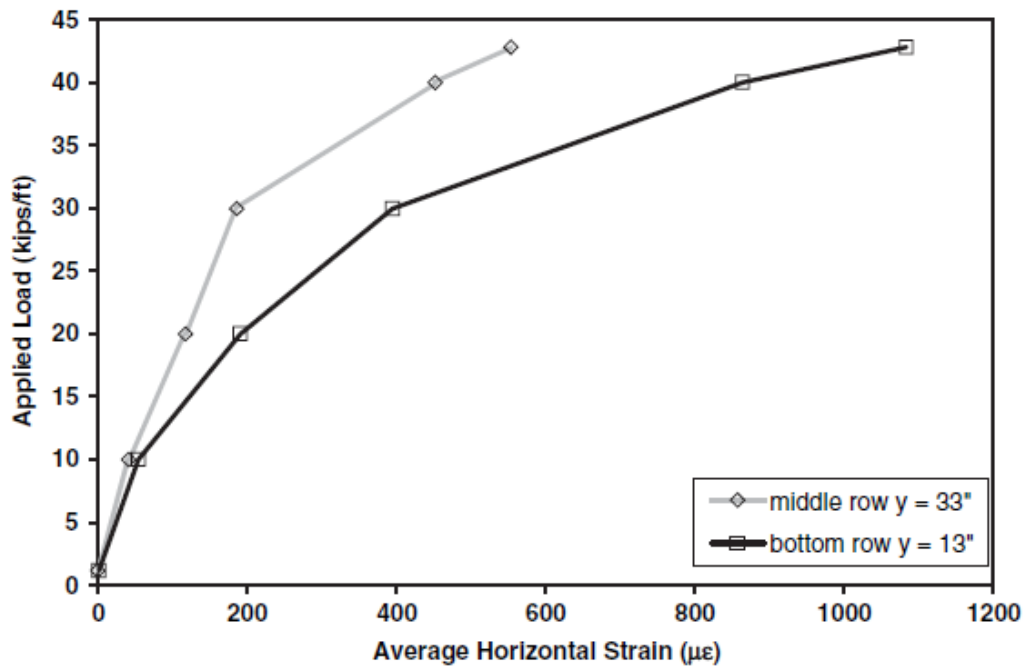


Figure 2.32. Average Horizontal Strain versus Applied Load Example (Hawkins and Kuchma 2007).

2.7. Research Questions Arising from Literature Review

The following questions arise based the previous research studied in the literature review:

- *Can the Optotrak Certus motion capture system measure the small displacements expected in the experimental testing of the pretensioned bent caps?*

Research conducted by Birely (2012) validated the use of a motion capture system to measure the large displacements typical of experimental seismic testing of reinforced concrete. The pretensioned concrete bent caps studied in this Thesis were subjected to primarily low-rate static load patterns. Combined with the inherent decrease in deformation due to the nature of pretensioned concrete, the ability of the motion capture system to measure some displacements is questioned. This research looks to validate the Optotrak system as useful method of collecting experimental data.

- *Can the Optotrak Certus motion capture data be used to verify and expand upon the observations and conclusions drawn in the research documented in Birely et al. (2018a) and Birely et al. (2018b)?*

The research data studied in this Thesis originated from the full test program documented by Birely et al. (2018a) and Birely et al. (2018b). The conclusions drawn on the behavior of pretensioned bent caps were primarily based on visual observations of damage that occurred during experimental testing. This research looks to correlate the visual observations with analysis of experimental data.

- *Can the Optotrak Certus motion capture data be utilized to quantify the behavior of the pretensioned concrete bent caps and show the influence of design variables?*

Previous research utilized an assortment of traditional measurement methods to collect data at discrete locations on test specimens. Bracci et al. (2000) used strain gauges placed along the length of reinforcing steel in different locations of the bent cap geometry to create behavior profiles. These profiles were used to compare experimental and expected performance of reinforced concrete bent caps and to show the influence of varied design parameters on the experimental behavior. This research looks to apply the advanced data analysis techniques achievable with motion capture system data, as shown by Birely (2012) and Hawkins and Kuchma (2007), to provide a more detailed insight on the behavior of the pretensioned bent caps and to show how variations in detailing influence the performance.

3. EXPERIMENTAL TEST PROGRAM*

3.1. Experimental Test Program Overview

Experimental testing was performed by the Texas A&M Transportation Institute (TTI) at the Texas A&M University High Bay Structural and Materials Testing Laboratory (SMTL) on six full-scale precast concrete bent cap specimens. This research was supported by Texas Department of Transportation (TxDOT) research Project 0-6863 titled “Develop Strong and Serviceable Details for Precast, Prestressed Concrete Bent Cap Standards That Can Be Implemented on Everyday Bridge Construction Projects.” Full details and documentation of the project are presented in [Birely et al. \(2018a\)](#) and [Birely et al. \(2018b\)](#). This section provides an overview of the project as relates to this Thesis.

The objectives were to validate the proposed design procedure, assess performance at service and ultimate demands, and establish failure modes with the experimental testing of full-scale sub-assemblages of standard TxDOT I-girder bridge bents. Design variables investigated included the influence of shear reinforcement, amount of prestressing, and the use of interior voids to reduce the bent cap weight.

The experimental test program consisted of six full-scale sub-assemblages, tested in two phases. The phases were distinguished by the specimen geometry and the amount of prestressing. Phase 1 tested one reinforced concrete bent cap as a reference test and three 16 strand pretensioned bent caps. The pretensioned bent caps included an equivalent

*Parts of this chapter are adapted and reprinted from [Birely et al. 2018a](#) (see References) with permission from Texas A&M Transportation Institute.

strength design to the reinforced concrete design, a variation in the shear reinforcement spacing, and use of an interior void. Phase 2 consisted of two longer specimens, both with 28 strands and interior voids. The Phase 2 specimens investigated the impact of void detailing.

This Thesis will focus primarily on construction of Phase 2 specimens and results of Phase 1 and Phase 2 pretensioned bent cap specimens. A detailed comparison of the experimental performance of the reinforced concrete bent cap and the equivalent pretensioned concrete bent cap was discussed in Yole (2017).

3.1.1. Overview

The bent cap test specimens were limited by the capacity of the available laboratory equipment. The overhead crane capacity was a major limiting factor in determining the maximum size of the sub-assemblages. To replicate more closely the indeterminate structure that the prototype bents represented, the test specimens were designed as a subassembly of a full bent consisting of the bent cap from the overhang to the second inflection point in the first span and the column from the bent to the inflection point. This region, indicated by a blue oval in Figure 3.1, allows for experimental evaluation of the performance under both positive negative moment demands and the transfer of forces from the bent cap to the column. Figure 3.2 shows a schematic of the subassembly and the shear and moment demands produced by the loads.

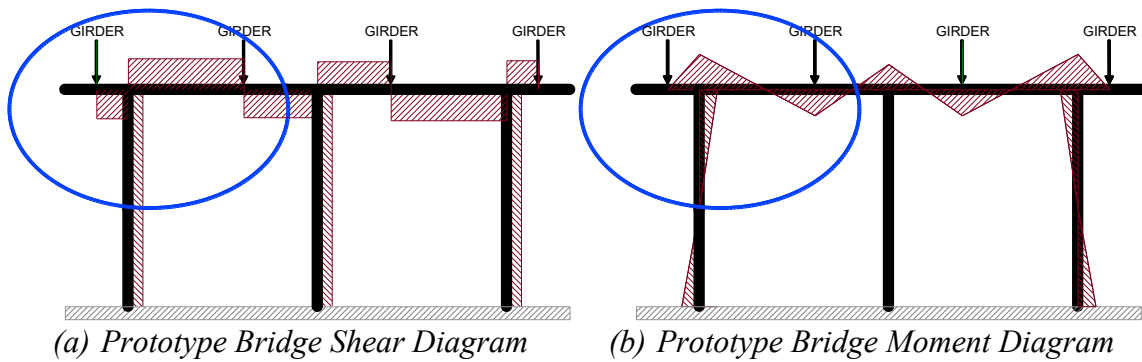


Figure 3.1. Prototype Shear and Moment Diagrams.
 (Adapted with permission from Birely et al. 2018a)

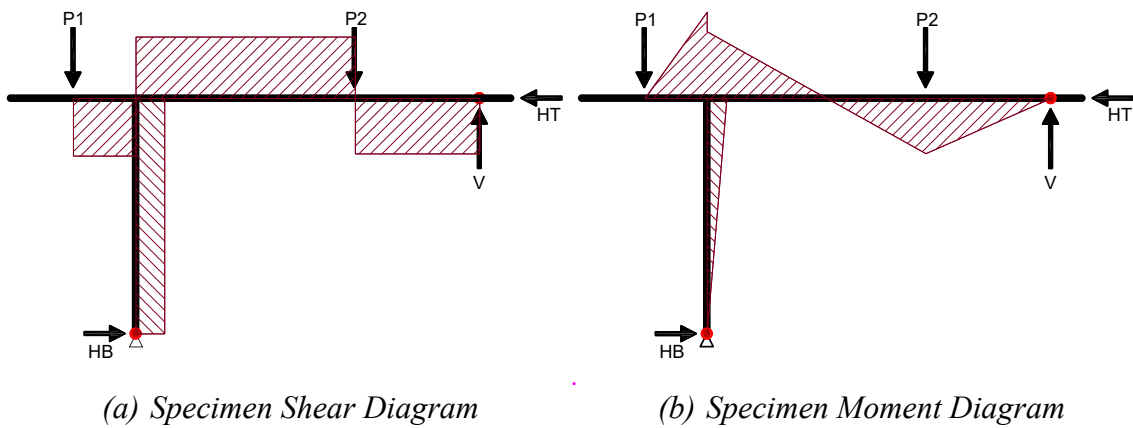


Figure 3.2. Specimen Shear and Moment Diagrams.
 (Adapted with permission from Birely et al. 2018a)

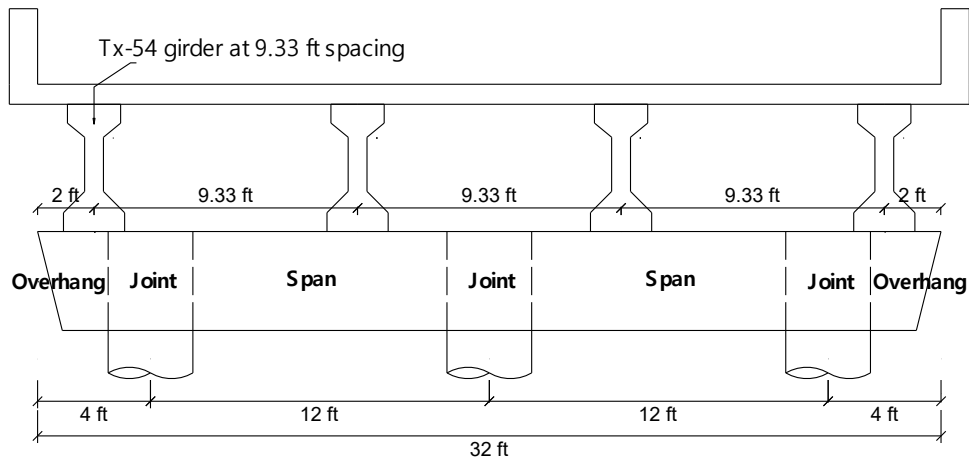
3.1.2. Specimen Design

To ensure that the full-scale specimens could be adequately tested, they were designed such that the expected flexural capacity of the bent cap did not exceed the moment capacity of the experimental test setup. Using the known actuator capacities and maximum moment demands that could be achieved with the test setup, a prototype bridge that had similar bridge demands was selected from the TxDOT bridge inventory. During Phase 2, the length of the bent cap specimens was increased which allowed for a higher

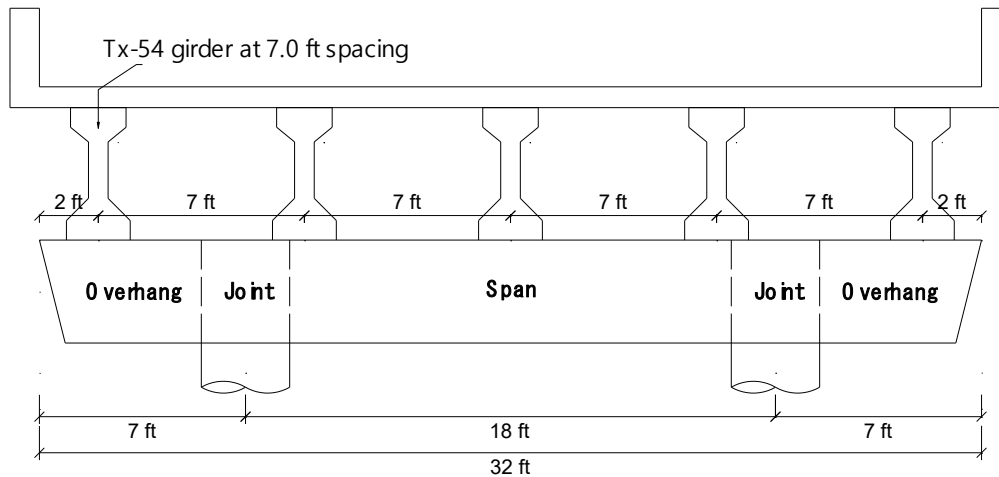
moment demand from the test setup. This change allowed the design to incorporate more prestressing strands than in Phase 1. The selected prototype bridges are summarized in Table 3.1, and shown in Figure 3.3.

Table 3.1. Summary of Prototype Bridge Details. (Adapted with permission from Birely et al. 2018a)

Property	Phase 1	Phase 2
Identifier	BIG-32	Modified BIG-32
Span Length (feet)	66	80
BC Length (feet)	32	32
BC Height (inch)	42	42
BC Width (inch)	42	42
Girder Types	Tx28 – Tx54	Tx28 – Tx54
Number of Girders	4	5
Girder Spacing (feet)	9.33	7
Column Diameter (feet)	3	3
Column Spacing (feet)	12	18
Number of Columns	3	2
Overhang (feet)	4	7



(a) Phase 1 - BIG-32



(b) Phase 2 - Modified BIG-32

Figure 3.3. Prototype Bridge Configurations.
(Adapted with permission from Birely et al. 2018a)

3.1.2.1. Flexural Design

The flexural design of the specimens followed the design procedure recommended by Barooah (2016) and is summarized in detail in Birely et al. (2018a). The number of strands were selected following the “zero tension under dead load” philosophy. A side strand configuration was chosen to allow for the pocket connection. Based on this approach, 16 strands were selected for Phase 1 and 28 strands were selected for Phase 2. Due to the significantly higher negative moment demand compared to the positive moment

demand in Phase 2 specimens, an eccentricity of -2.57-in. (above center) was selected. Figure 3.4 shows the strand layout for Phase 1 and Phase 2 specimens.

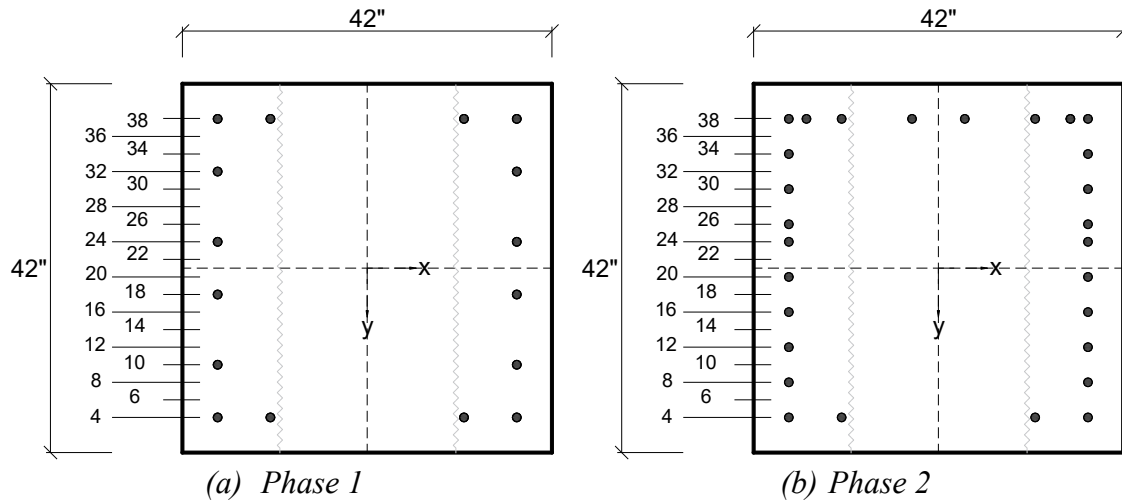


Figure 3.4. Prestressing Strand Layout.
(Adapted with permission from Birely et al. 2018a)

3.1.2.2. Shear Design

The shear design of the bent cap specimens followed the AASHTO LRFD Bridge Design Specifications (2014) general procedure of sectional design from Appendix B5. This method is appropriate for components where assumptions of beam theory are valid, and therefore was applied to the span region between the columns. Details of this design are discussed in [Birely et al. \(2018a\)](#) and are summarized below.

The design concrete compressive strength (f'_c) was 6 ksi, and two legs of #5 was chosen as the transverse reinforcement for both Phase 1 and Phase 2. Based on the critical sections for shear design, transverse reinforcement spacing of 12-in. was selected. In Phase 1, one specimen was designed to not satisfy the AASHTO minimum area of steel

requirement and instead satisfy the maximum spacing requirement. For this specimen, a spacing of 24-in. was selected.

Specimens with interior voids were designed to allow for the reduction of bent cap dead load. For these specimens, a 26-in. square void was selected to allow for equal concrete cover on the exterior and interior of the prestressing strands. Due to the decreased cross-sectional area in the voided region, the required transverse reinforcement spacing was 9-in. To allow for a direct comparison between the solid and voided specimens, the transverse reinforcement spacing was kept consistent at 12-in.

3.1.2.3. End Region

The end region detailing took into consideration the spalling reinforcement from the AASHTO LRFD 5.10.10.1 and included bursting reinforcement immediately after spalling reinforcement from $D/4$ to the transfer length. Details of this design are discussed in [Birely et al. \(2018a\)](#). Individual C-Bars (#5 bars) were used at $D/4$ for the spalling reinforcement. C-Bar and S-Bar pairs were used for the bursting reinforcement up to the transfer length. During Phase 2, one specimen used end region detailing from standard drawings released by TxDOT during the completion of Phase 1. The end region detailing of the square ends was the same as the battered ends, except modified to account for the non-sloped face. Figure 3.5 shows the end region reinforcement for Phase 1 and Phase 2.

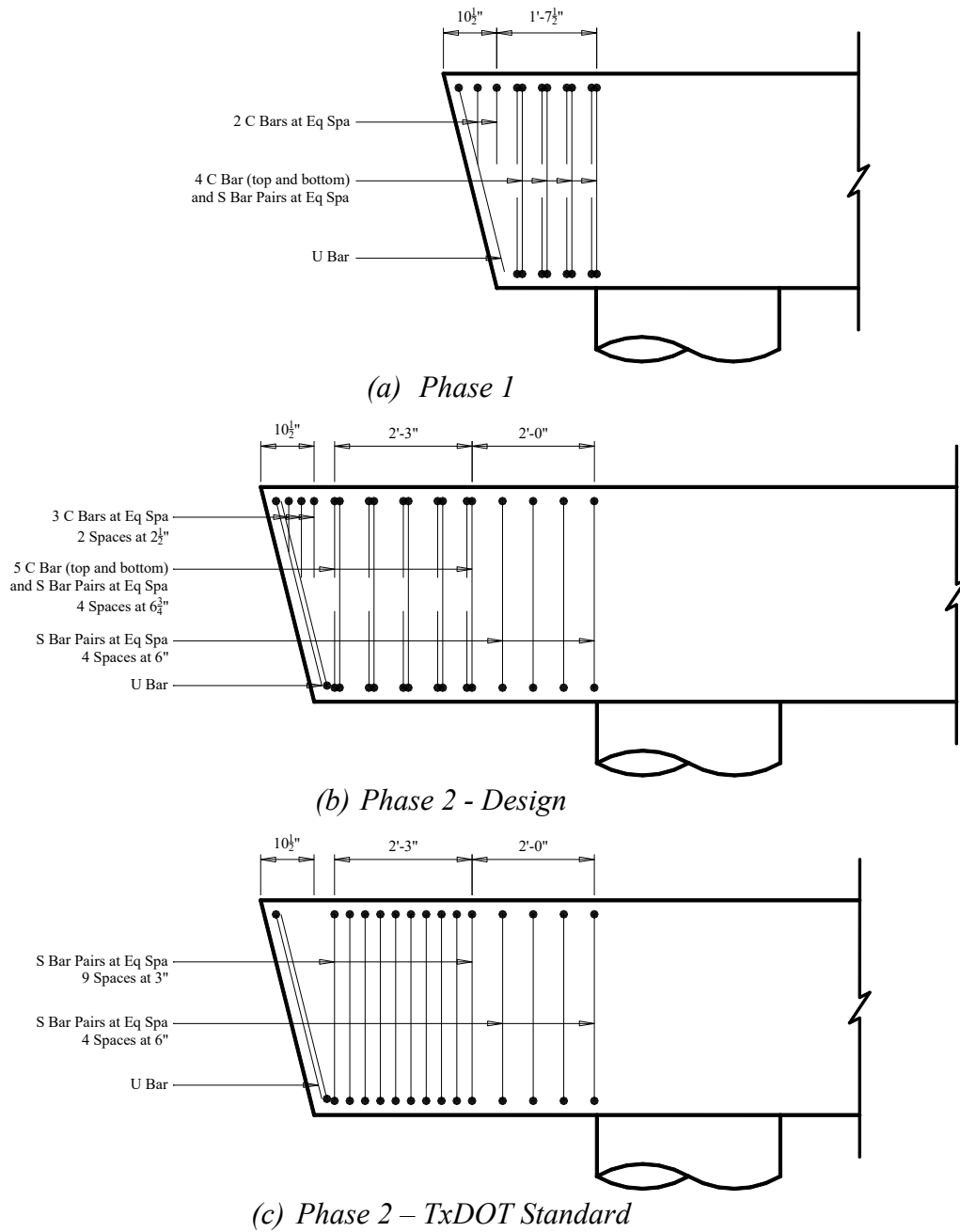


Figure 3.5. End Region Detailing.
 (Adapted with permission from Birely et al. 2018a)

3.1.2.4. Column and Connection

The design of the column longitudinal and spiral reinforcement was the same as current TxDOT design standards for prestressed concrete girder bridges. The column diameter was 3-ft with 10-#9 longitudinal reinforcing bars and #4 deformed spiral reinforcement.

A pocket connection was chosen to connect the precast bent caps to the columns. The pocket connection emulates a monolithic connection by utilizing a single large pocket that encloses the dowel bars extending from the column. This connection replaced the 4-in. diameter vertical ducts in the current TxDOT Precast Bent Cap Option for Round Columns standard sheet. Following the recommendations of [Barooah \(2016\)](#), the spacing of 6-#11 bars detailed in the current connection standard was decreased to maximize the ease of constructability. A 21-in. diameter 12 gage corrugated steel pipe was selected to form the pocket. Figure 3.6 shows details of the pocket connection.

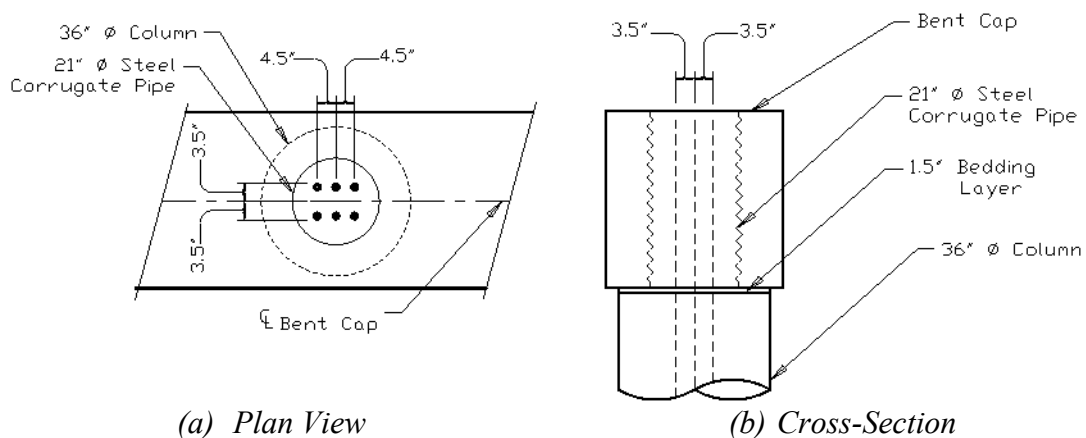


Figure 3.6. Pocket Connection Details.
(Adapted with permission from Birely et al. 2018a)

3.1.3. *Test Matrix*

The objective of the test matrix was to compare a pretensioned concrete design to an equivalent reinforced concrete design and to investigate the impact of differing shear reinforcement, number of strands, inclusion of interior voids, and different interior void details. Table 3.2 shows a summary of each bent cap specimen tested. The naming of the specimens has the first set of characters showing the type of specimen (RCS = Reinforced Concrete Solid, PSS = Pretensioned Solid, PSV = Pretensioned Void). The second set of characters shows the number of reinforcement bars or strands. The third set of characters indicates the spacing of the shear reinforcement in inches. The two specimens in Phase 2 have the same number of strands and shear spacing but different details, with names distinguished by A and B without using the third set of characters.

Table 3.2. Experimental Test Matrix. (Adapted with permission from Birely et al. 2018a)

Phase Specimen	Flexural Reinf.	Shear Spacing	Void	Overhang	Description
Phase 1					
RCS-16-12	16-#8 Bars	12 in.	N	Standard*	RC design
PSS-16-12	16-0.6 in ϕ	12 in.	N	Standard	PSC design
PSS-16-24	16-0.6 in ϕ	24 in.	N	Standard	Reduced shear reinf.
PSV-16-12	16-0.6 in ϕ	12 in.	Y	Standard	Interior void
Phase 2					
PSV-28A	28-0.6 in ϕ	12 in.	Y	Long**	Longer specimen with void
PSV-28B	28-0.6 in ϕ	12 in.	Y	Long w/ void	Longer specimen with two voids & modified void geom.

* Current TxDOT design (4-ft); ** Longer overhang (7-ft)

3.1.4. Experimental Test Setup

Figure 3.7 shows a 3D rendition of the experimental setup in the Texas A&M High Bay Structural and Materials Testing Laboratory (SMTL). The Phase 1 specimens had a bent cap length of 16-ft and a column height of 6.3-ft (8 ft to center of bent cap), shown in Figure 3.8. The Phase 2 specimens had a bent cap length of 22-ft and utilized the same column configuration as Phase 1, shown in Figure 3.9.

The column rested on a rocker foundation, shown in Figure 3.10, bolted to a 10-ft x 7-ft steel foundation plate. Two top vertical actuators (P1, P2) supported on 9-ft headers between the vertical reaction towers, shown in Figure 3.11, simulated the girder loads. The bottom vertical actuator (V) acted as the shear at the bent cap inflection point and connected to the strong floor by a 4-ft x 4-ft steel foundation plate. Horizontal

actuators (HT, HB) attached to horizontal load reaction frames, shown in Figure 3.12, provided stability.

The test setup up was located directly above strong floor foundation wall to accommodate the large forces acting during testing. Reaction frames and foundation plates were secured to the SMTL strong floor by 2-1/2-in. post-tensioned threaded bars tensioned to 3,000 psi

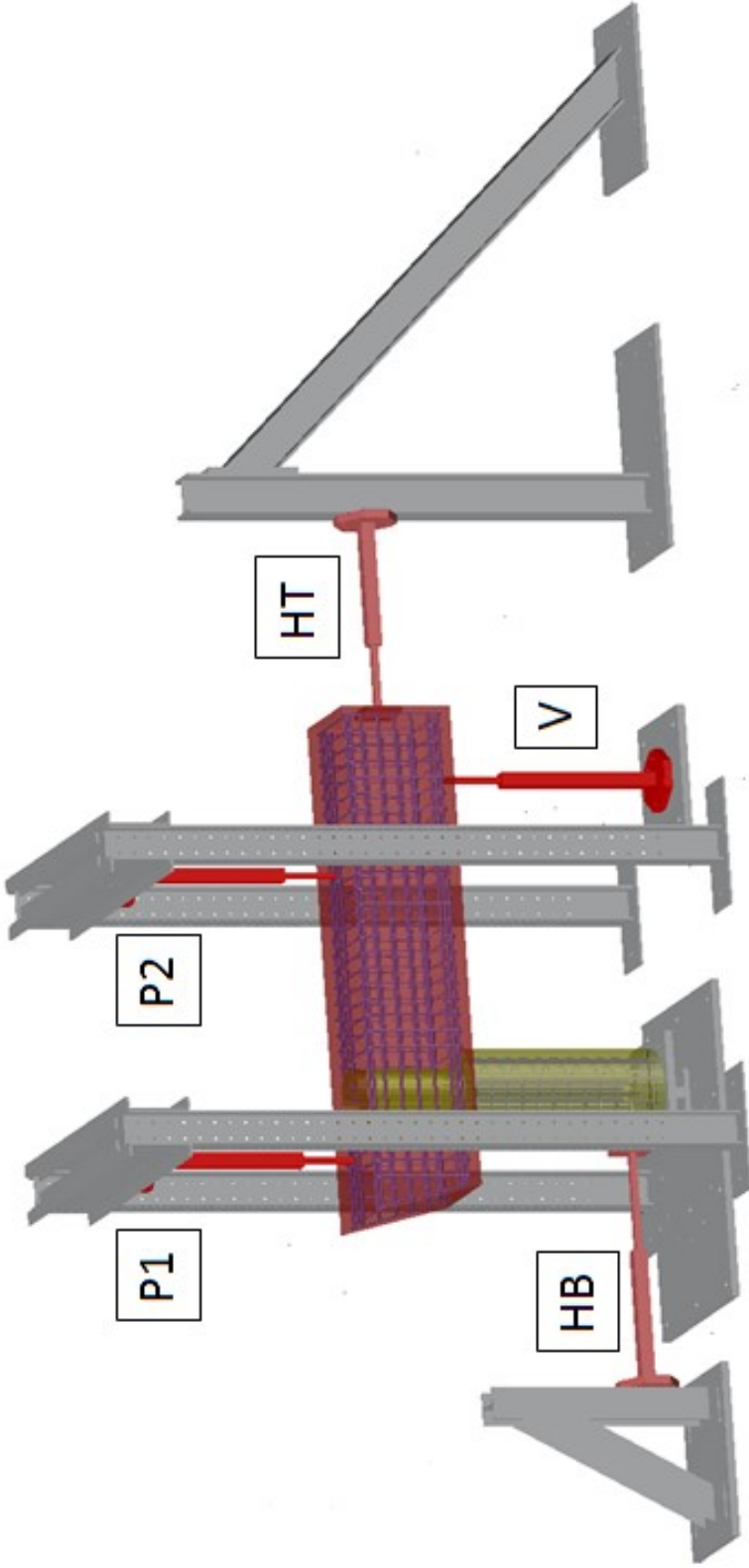


Figure 3.7. General Experimental Test Setup 3D Rendering. (Adapted with permission from Birely et al. 2018a)

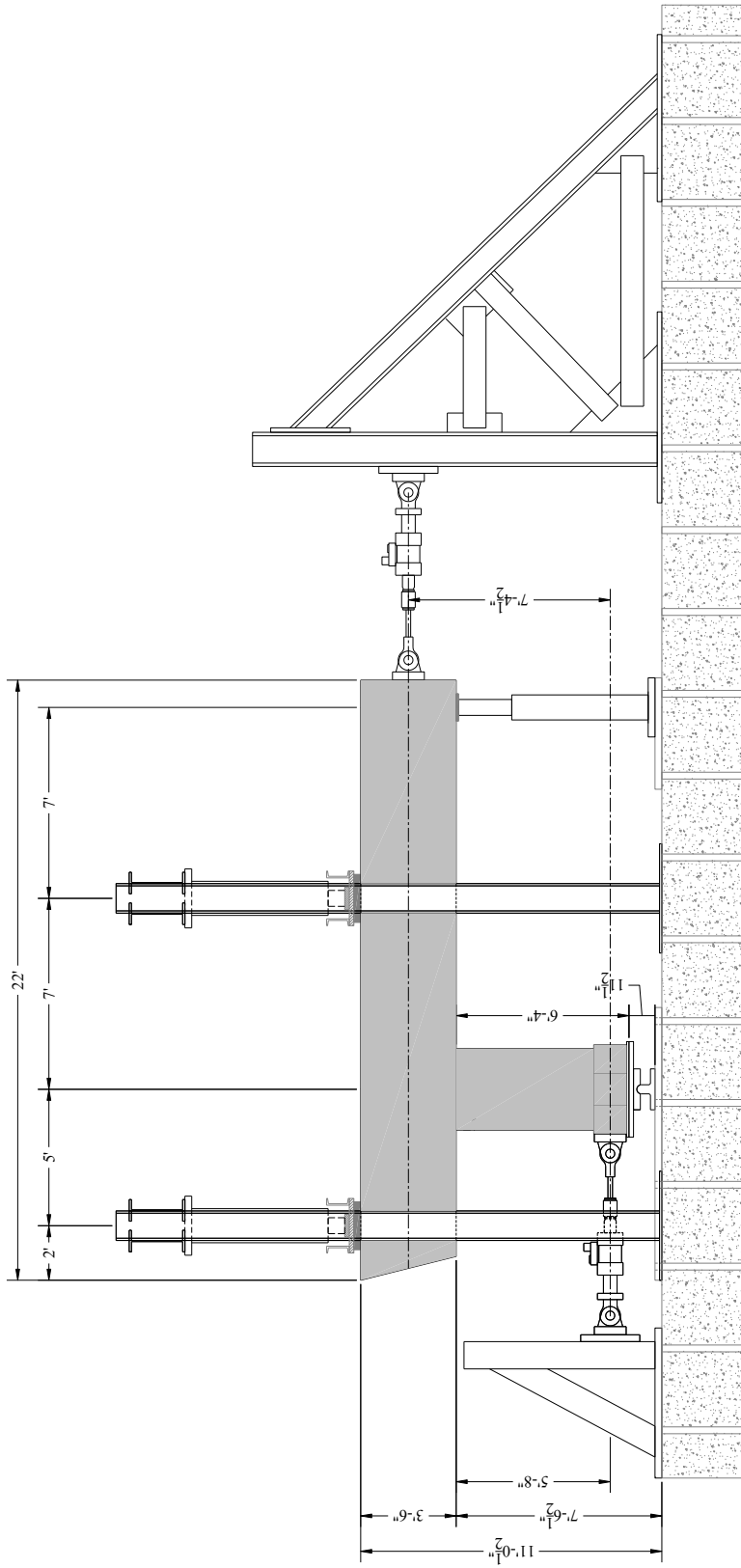
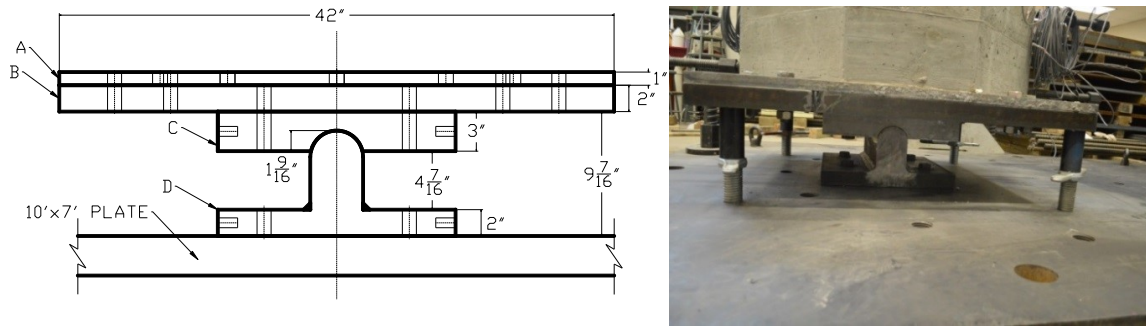


Figure 3.9. Phase 2 Experimental Test Setup. (Adapted with permission from Birely et al. 2018a)



**Figure 3.10. Rocker Foundation (stability pegs were removed prior to testing).
(Adapted with permission from Birely et al. 2018a)**



**Figure 3.11. Vertical Reaction Frame.
(Adapted with permission from Birely et al. 2018a)**



(a) *Bottom Horizontal Actuator (HB)
Reaction Frame*

(b) *Top Horizontal Actuator (HT)
Reaction Frame*

Figure 3.12. Horizontal Reaction Frames. (Adapted with permission from Birely et al. 2018a)

The top and bottom horizontal 110-kip actuators (HT and HB) were attached to the specimens with threaded rods that were installed during casting, shown in Figure 3.13. The actuators were installed on the horizontal reaction frames. The two vertical 600-kip actuators, simulating girder loads, were mounted to the 9-ft headers between the vertical reaction towers. Load was applied to the bent cap through TxDOT approved bearing pads placed as shown in Figure 3.14. Actuator load assemblies were designed to distribute the load from the single vertical actuator ram to the two bearing pads representing the individual girders, shown in Figure 3.15. Additional 2-in. steel plates were added to stiffen the assembly.



(a) HT Actuator Connection Rods

(b) HB Actuator Connection Rods

Figure 3.13. Horizontal Actuator Connections.
 (Adapted with permission from Birely et al. 2018a)

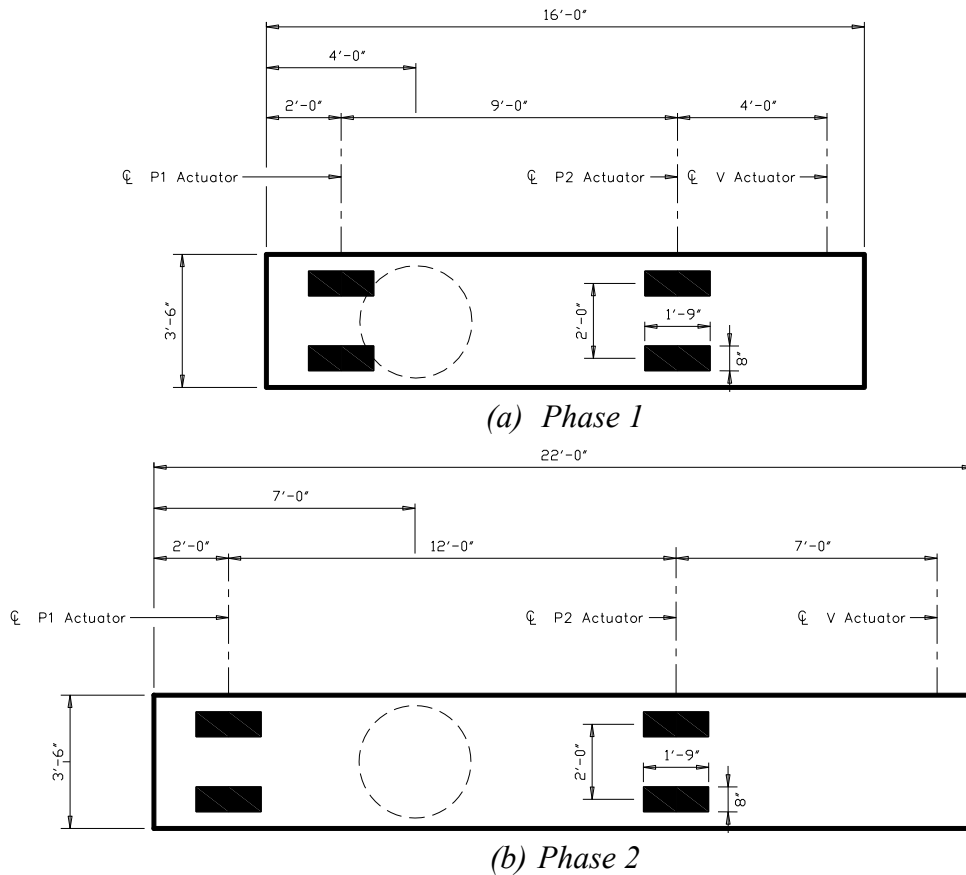
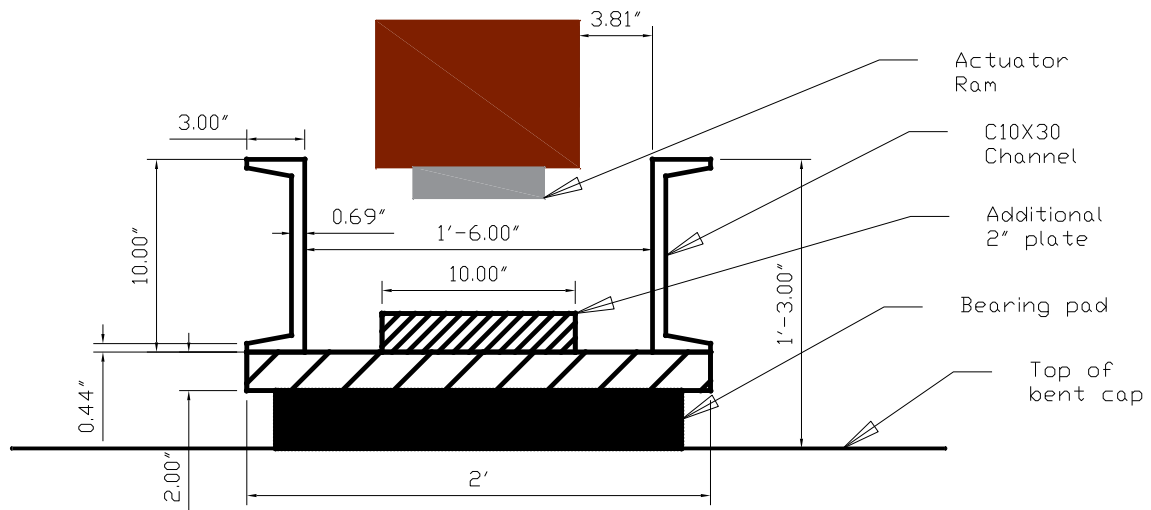


Figure 3.14. Bearing Pad Locations.
 (Reprinted with permission from Birely et al. 2018a)



(a) Actuator Load Assembly Plan



(b) Vertical Actuators Installed



(c) Additional 2-in. Plate

Figure 3.15. Vertical Actuator Load Assembly.
 (Adapted with permission from Birely et al. 2018a)

3.2. Test Specimen Construction

The precast support column was constructed in the Texas A&M High Bay Structural and Materials Testing Laboratory (SMTL), while the pretensioned bent caps were fabricated at Bexar Concrete Works under the inspection and supervision of Texas Department of Transportation (TxDOT) and Texas A&M Transportation Institute (TTI) personnel. The construction of Phase 1 pretensioned bent cap specimens and precast support columns are detailed in Yole (2017).

The fabrication of Phase 2 pretensioned bent caps PSV-28A and PSV-28B occurred on prestressing line BB at Bexar Concrete Works (same as Phase 1). The specimens were positioned approximately at the middle along the length of the prestressing bed; the orientation of the prestressing line is shown in Figure 3.17.

Prestressing strands were fed through the wooden square end formwork and metal battered end formwork. Due to the geometry of the bent caps, details of the pocket connection, and size/location of the polystyrene voids, only 22 of the 28 strands were stressed at the start of fabrication. All prestressing strands were stressed to a force equivalent to $0.75f_{pu}$ of the 0.6-in. diameter Grade 270 7-wire strands (44 kips). The six strands located at the top of the strand pattern (B 38, F 38, and H 38 in Figure 3.17) were placed after pocket and interior void placement. After the initial strands were pulled through the header plates, the headers were spread to the correct positions along the prestressing bed. The headers were secured with metal plates welded to the base of the prestressing bed to prevent any movement.

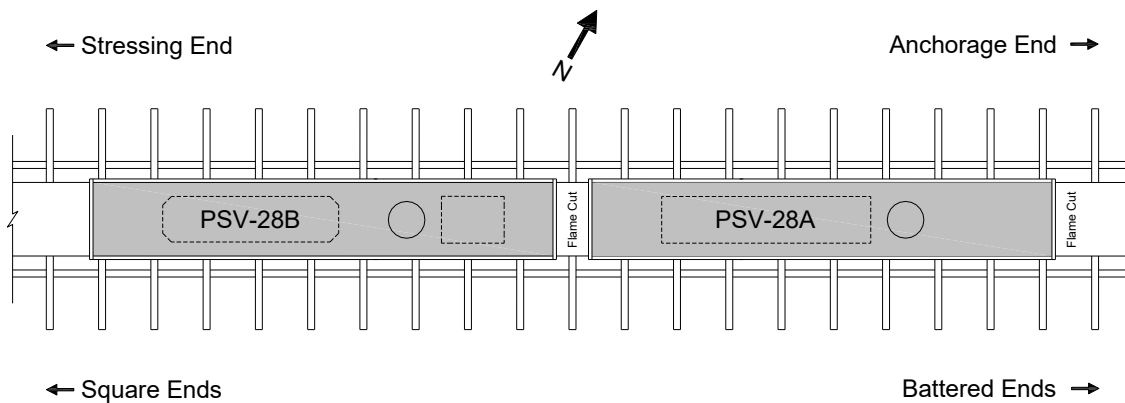


Figure 3.16. Prestressing Bed Layout.
(Reprinted with permission from Birely et al. 2018a)

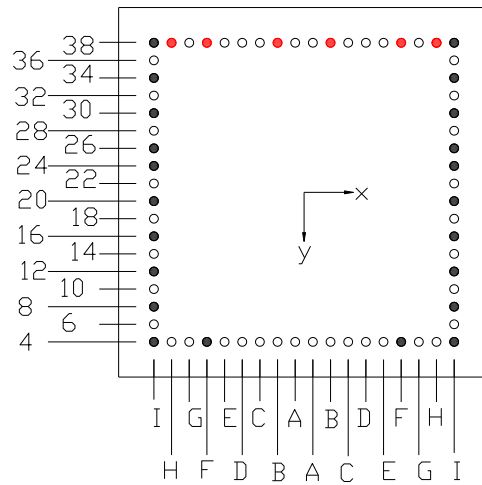


Figure 3.17. Initial (black) and Final (red) Prestressing Strand Layout.
 (Adapted with permission from Birely et al. 2018a)



(a) Prior to spreading headers

(b) Prior to stressing first group of strands

Figure 3.18. Placement of Initial Strands and End Formwork.
 (Reprinted with permission from Birely et al. 2018a)

Following the stressing of the initial 22 strands, workers placed the interior components of the bent caps. The all-thread actuator load assemblies (Figure 3.19) were

placed in the wooden formwork of the square ends of both specimens, as required for experimental testing and shown in the construction plans.

The corrugated steel pipes were installed into the formwork. Due to the differences in pocket connection details, different methods of securing the corrugated steel pipe were used for each specimen. The corrugated steel pipe for specimen PSV-28A was secured on top of a 6-in. polystyrene forming plug using a threaded rod (Figure 3.20a). For specimen PSV-28B, the corrugated steel pipe extended to the bottom of the formwork and welded metal tabs were used to prevent movement of the corrugated steel pipe during concrete placement (Figure 3.20b). A polystyrene forming plug was placed at the top of each corrugated steel pipe to seal the pocket connection during concrete placement.

The geometry, size, and quantity of the interior voids differed between PSV-28A and PSV-28B. The interior voids were formed with polystyrene blocks. The longitudinal 5-in. chamfer on the polystyrene blocks for PSV-28B were precut at the time of manufacturing, while the transverse 5-in. chamfer was field cut after the block was cut to the appropriate length (Figure 3.21 and Figure 3.22). The polystyrene blocks were held in place with #3 rebar tied to the prestressing strands. PVC drain pipes were installed at the bottom corners of the polystyrene blocks (Figure 3.23). Polystyrene blocks were restrained from floating during concrete placement with rectangular plywood held down with threaded rods secured to the transverse formwork bracing. Due to the geometry of interior void in specimen PSV-28B, adjustments were made to the hold down mechanism. Instead of a single piece of plywood held with two threaded rods, two pieces of plywood

were held in place with individual threaded rods. These differences can be seen in Figure 3.24.

After the interior void forming blocks and corrugated steel pipes were installed, the last six strands were fed through the formwork and the pocket connection (Figure 3.25). The prestressing strands were passed through holes in the corrugated steel pipe in specimen PSV-28B (Figure 3.25b). In both specimens, the strands were passed through the polystyrene plugs at the top of the corrugated steel pipes; holes were formed in the polystyrene using a heated piece of strand (Figure 3.25a).



(a) All-thread Actuator Load Assembly

(b) Actuator Load Assembly Installed

**Figure 3.19. Actuator Load Assembly.
(Reprinted with permission from Birely et al. 2018a)**



(a) PSV-28A Corrugated Pipe Secured to Prestressing Bed



(b) PSV-28B Welded Metal Tabs Securing Corrugated Pipe



(c) PSV-28A Polystyrene Plug Secured with All-Thread Rod



(d) PSV-28B Top Polystyrene Plug

Figure 3.20. Corrugated Steel Pipe Installation.
(Reprinted with permission from Birely et al. 2018a)



(a) PSV-28B Interior Void Polystyrene Block (span) - Elevation



(b) PSV-28B Interior Void Polystyrene Block (span) - Side

Figure 3.21. PSV-28B Polystyrene Forming Block.
(Reprinted with permission from Birely et al. 2018a)



(a) PSV-28A Interior Void Polystyrene Block – In Place



(b) PSV-28B Interior Void Polystyrene Block – In Place

Figure 3.22. Polystyrene Forming Blocks Installed.
(Reprinted with permission from Birely et al. 2018a)



(a) PSV-28A PVC Drain Pipes



(b) PSV-28B PVC Drain Pipes

Figure 3.23. PVC Drain Pipe Installation.
(Reprinted with permission from Birely et al. 2018a)



(a) PSV-28A



(b) PSV-28B

Figure 3.24. Interior Void Polystyrene Forming Block Hold Downs.
(Reprinted with permission from Birely et al. 2018a)



(a) Strands Placed Through PSV-28A
Forming Plug



(b) Workers Feeding Strands Through
PSV-28B Pipe

Figure 3.25. Strands through Pocket Connection.
(Reprinted with permission from Birely et al. 2018a)

Mild steel reinforcement was placed after all strands had been stressed. Transverse shear reinforcing bars gauged for monitoring during experimental testing were provided by the research team (Figure 3.26). Two #5 mild steel hoops were placed around the top of the corrugated steel pipe in PSV-28B (Figure 3.27). The hoops were secured to the reinforcing cage using tie wire and #3 reinforcing bars where necessary to maintain the correct position. Thermocouples were installed in both specimens, as seen in the

thermocouple plan shown in Figure 3.28. Prior to placing concrete, TxDOT and TTI personnel inspected the reinforcement cages. Adjustments were made where necessary. The metal formwork was placed to close the formwork and transverse bracing was attached along the length of both specimens.



(a) PSV-28A Strain Gauged Mild Steel Shear Reinforcement and Corrugated Steel Pipe



(b) PSV-28B Strain Gauged Mild Steel Shear reinforcement, Mild Steel Hoops, and Corrugated Steel Pipe

Figure 3.26. Strain Gauged Reinforcement.
(Reprinted with permission from Birely et al. 2018a)

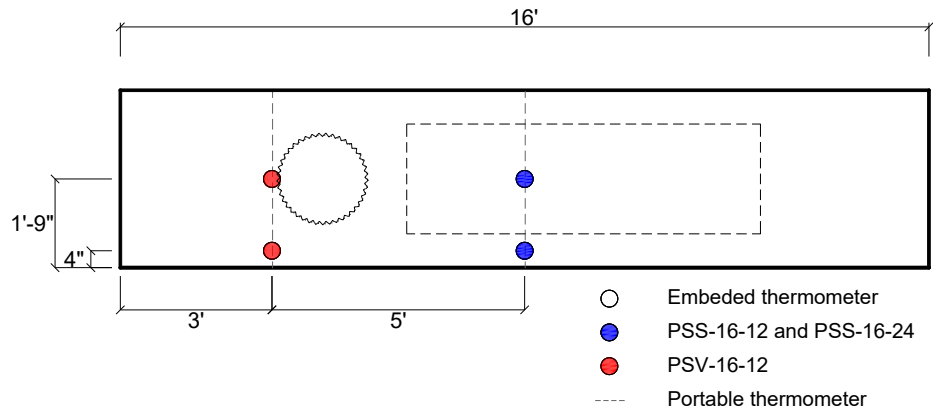


(a) Elevation View

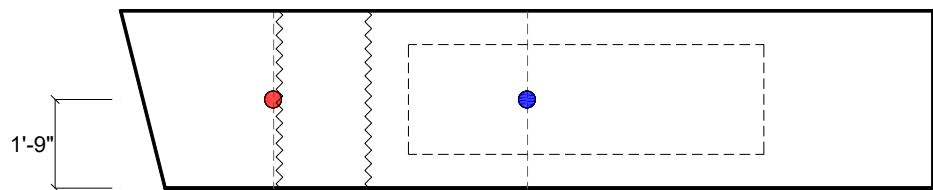


(b) Hoops at Top of Steel Pipe

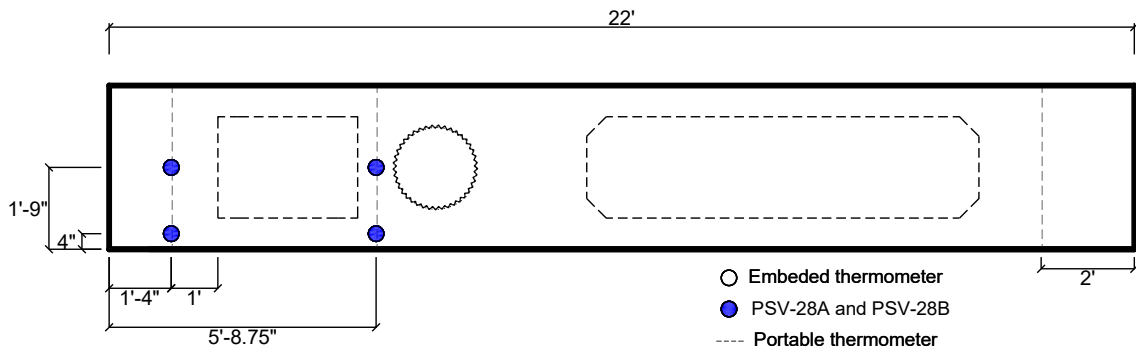
Figure 3.27. PSV-28B Mild Steel Hoop Installation.
(Reprinted with permission from Birely et al. 2018a)



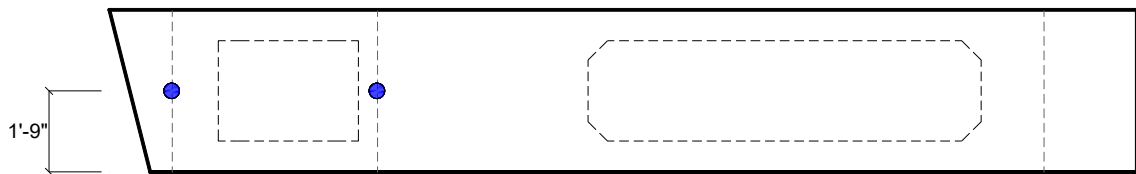
(a) Phase 1 – Plan View



(b) Phase 1 – Elevation View



(c) Phase 2 – Plan View



(d) Phase 2 – Elevation View

Figure 3.28. Thermocouple Plan.
 (Reprinted with permission from Birely et al. 2018a)

Concrete was placed in 4 cubic yard batches from the onsite plant. Five batches were used to cast the Phase 2 specimens. These batches are referred to as batches J, K, L, M, and N. For each concrete batch, slump was recorded and test cylinders were made. Each concrete batch had a slump ranging between 7 to 7-1/2 inches. Batch L was used in both specimens, so additional material testing specimens (cylinders and beams) were made. PSV-28A consisted of batches J, K, and L, while PSV-28B consisted of batches L, M, and N. The approximate distribution of the concrete (by batch) in each of the specimens is shown in Figure 3.29. The concrete was placed in approximately equal lifts in each specimen. Workers used vibrators to consolidate the concrete (Figure 3.30). During the placement of concrete near the square end of PSV-28B, the interior void was shifted out of place. Workers adjusted the polystyrene block back to within 3/8-inches from the correct position and resumed the concrete placement (Figure 3.31). After completing the concrete placement, workers removed the threaded rods holding down interior void forming blocks, finished the surface with metal and wooden trowels, and installed a water irrigation system. The specimens were covered with black plastic to retain heat and moisture during the initial curing process (Figure 3.32).

Concrete compressive strength was tested each day. The morning of the 3rd day after casting the concrete had reached the specified compressive strength of 4 ksi. The black plastic covers were removed, and the formwork was removed from the specimens. The prestressing strands were released with the hydraulic jacks at the stressing end of the prestressing bed. Using a flame torch, strands were cut at the anchorage end of the prestressing bed (Figure 3.33a). Strands were released in a circular symmetric pattern, as

seen in Figure 3.33b. At the time of strand release, no initial cracking was noted. The specimens were lifted from the prestressing beds and moved to another location for the removal of the header plates. No cracking was noted on the end faces of the specimens after the removal of the header plates.

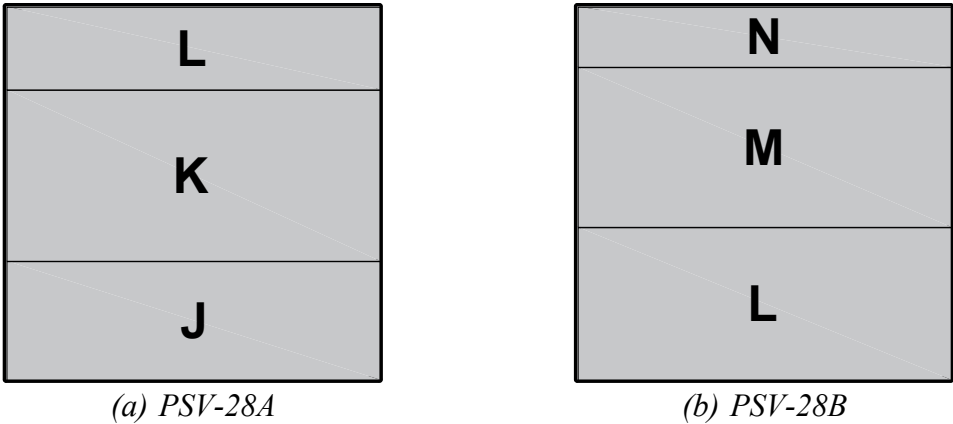


Figure 3.29. Concrete Batch Distribution.
(Reprinted with permission from Birely et al. 2018a)



Figure 3.30. Concrete Placement and Consolidation.
(Reprinted with permission from Birely et al. 2018a)



(a) Shifted

(b) Correcting the Shift

Figure 3.31. PSV-28B Polystyrene Block Shifting.
(Reprinted with permission from Birely et al. 2018a)



(a) Trowel Finishing



(b) Irrigation System



*(c) Removing All-Thread Rods
 Securing Polystyrene Voids*

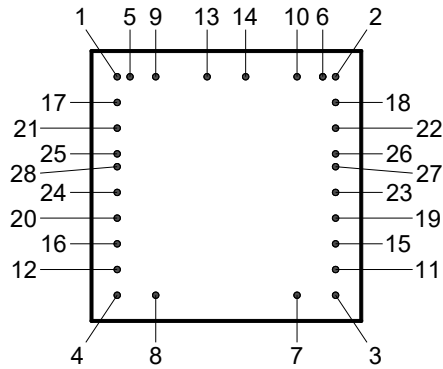


(d) Black Plastic Covering

Figure 3.32. Concrete Finishing and Curing.
(Adapted with permission from Birely et al. 2018a)



(a) Torch Cutting Strands



(b) Strand Release Pattern

Figure 3.33. Strand Release. (Adapted with permission from Birely et al. 2018a)

3.3. Instrumentation

To monitor the experimental performance, the bent cap specimens were instrumented with internal and external instrumentation. Traditional measurement techniques were used along with an advanced motion capture system method. Details of the different instrumentation methods are discussed below.

3.3.1. Traditional Instrumentation

To obtain the desired data, different types of instruments and their locations were carefully chosen. The instruments can be categorized into internal and external instrumentation. The internal instrumentation includes strain gauges while external instrument contains linear string potentiometers, and linear variable differential transformers (LVDT). Detailed instrumentation plans are provided in Appendix A.

Strain gauges were placed on the bent cap transverse reinforcement, corrugated steel pipe, column longitudinal bars, and column dowel bars. The number of strain gauges are summarized in Table 3.3. Gauges were placed longitudinally at mid-height of the bent cap transverse reinforcement. In the columns, gauges were placed on the longitudinal

flexural reinforcing bars located at the two quadrants positioned in the direction of bending. The dowel bar strain gauges were placed on the outer most bars in the pattern and positioned at center height of the bent cap, above/below the bedding layer, and aligned with the column longitudinal gauge. Gauges placed on the corrugated steel pipes varied based on the specimen. For Phase 1 specimens, a set of vertical and horizontal gauges were placed towards the bottom of the pipe aligned with the dowel bar gauges. For all specimens, a set of vertical and horizontal gauges were placed at center height of the bent cap. For Phase 2 specimens, vertical and horizontal gauges were placed at the four quadrants of the steel pipes. PSV-28B had strain gauges placed at center height of the J-Bar located at the centerline of the column and at the four quadrants of the additional #4 hoops placed at the top of the corrugated steel pipe.

Table 3.3. Summary of Strain Gauges. (Adapted with permission from Birely et al. 2018a)

Phase Specimen	Bent Cap	Column	Connection		Total
	Transverse	Flexural	Dowel	Pipe	
Phase 1					
All PSC	7	4	8	4	23
Phase 2					
PSV-28A	12	4	8	8	32
PSV-28B	17*	4	8	8	37

*4 strain gauges placed on #4 hoop

During Phase 1, a total of six of LVDTs were installed in horizontal, vertical, and diagonal directions in the joint region to measure relative vertical, horizontal, and diagonal

displacement to monitor joint shear deformations (Figure 3.34a). In all tests, two LVDTs were placed vertically under the bent cap adjacent to column to measure opening of the bedding layer. On PSV-28B, two additional LVDTs (Figure 3.34b) were placed vertically under the bent cap adjacent to the column in the location of the outer dowel bars to determine the strain in the dowel bars during loading. LVDTs within bent cap-column connection measured relative vertical, horizontal, and diagonal displacement to monitor joint shear deformations. Two vertical LVDTs under the bent cap adjacent to the column measured opening at the bedding layer.



(a) Phase I Joint Region LVDTs

(b) Dowel Bar (PSV-28B only) and Bedding Layer LVDTs

Figure 3.34. LVDT Locations. (Reprinted with permission from Birely et al. 2018a)

Twenty-eight linear string potentiometers were used to measure horizontal and vertical displacement of the specimens. In Phase 1, 13 were placed vertically along the centerline of the bottom of the bent cap, and 11 were placed horizontally on the bent cap and column. Four string potentiometers placed at corners were used to check whether torsion occurred. Based on observations during experimental testing of Phase 1 specimens, string potentiometers to monitor torsion were excluded from the instrumentation plan and added to the vertical string potentiometers for Phase 2. For Phase 2, 17 were placed vertically along the centerline of the bottom of the bent cap. For both Phase 1 and Phase 2, nine string potentiometers were placed horizontally on the bent cap and column to measure displacement. Two on the east end monitored displacement at the top horizontal actuator. Two string potentiometers at the column base were installed to check whether slip occurred at the column support.

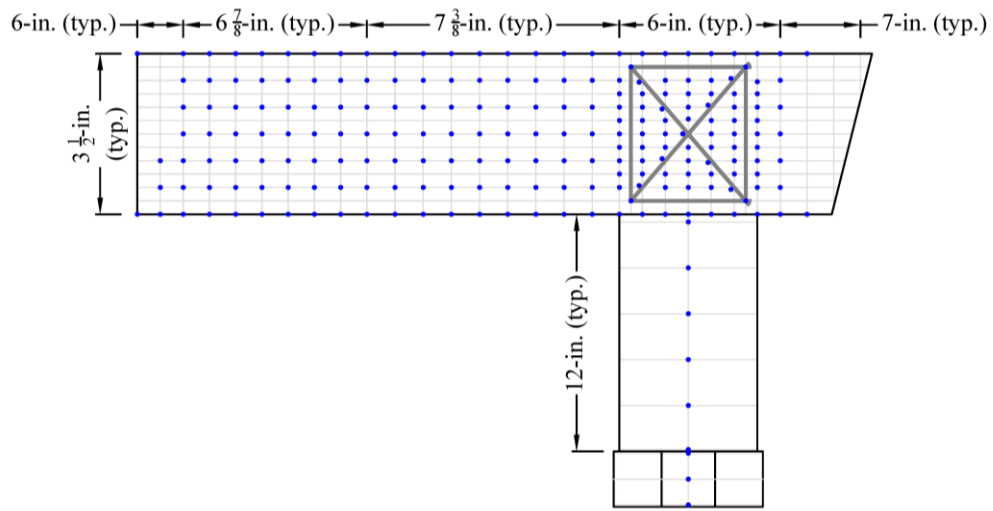
3.3.2. Advanced Instrumentation

An Optotrak Certus motion capture system was used to collect displacement data during the experimental tests. The Optotrak systems uses position sensors that contain three individual infrared cameras that track the motion of light emitting diode (LED) markers. The Optotrak system can track up to 512 LED markers with a maximum marker frequency of 4600 Hz, depending on the configuration used.

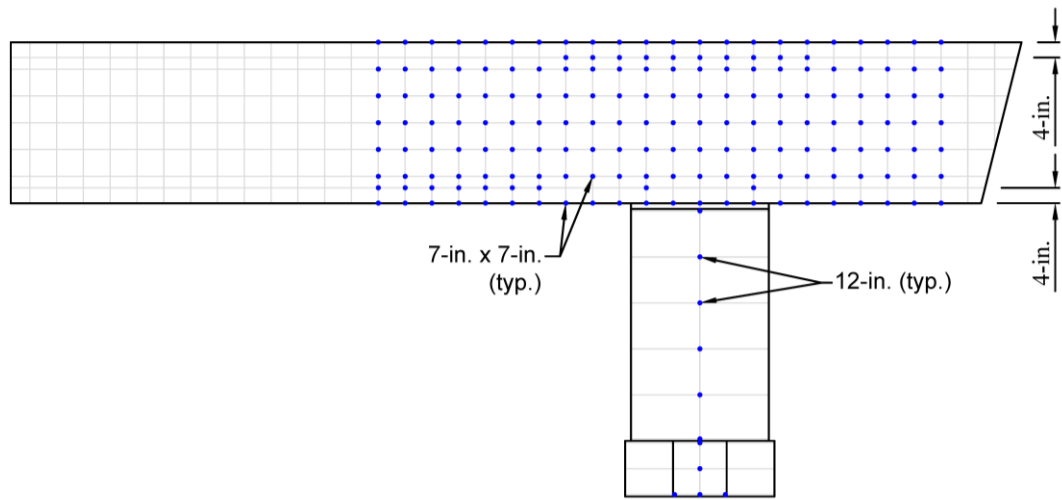
Two position sensors were used inline, and were registered to a common, arbitrary coordinate system prior to each test. LED marker layouts for Phase 1 and Phase 2 varied based on the limits of the position sensors measurement volume and the test setup. LED markers were placed on the back face of the bent cap specimens in a grid pattern, and were

placed on the column along the centerline. Markers were placed at the end of the embedded threaded rods for the LVDTs in the joint region during Phase 1 to allow for potential comparisons of measurements. In Phase 2, a row of LED markers was placed along the outermost tension steel layer in the positive and negative moment regions of the bent cap specimens. Figure 3.35 shows the general LED marker layout for Phase 1 and Phase 2.

The collection rate and marker frequency depended on the number of LED markers used during the tests. For the first test, the maximum number of markers for the configuration used (256) were used. A marker frequency of 250 Hz and a collection rate of 1 Hz were used. For consistency, the same settings were applied to subsequent tests regardless of the actual number of LED markers used.



(a) Phase 1



(b) Phase 2

Figure 3.35. Optotrak LED Marker Layouts with Typical Grid Spacings.

3.4. Material Properties

The following section presents the concrete and steel material properties results gathered from samples obtained during fabrication of the specimens.

3.4.1. Concrete Material Properties

To obtain measured material properties, each concrete batch was sampled to perform the following material properties tests: slump, compressive strength, modulus of elasticity, indirect tensile strength, and modulus of rupture. The fresh concrete was sampled following ASTM C172/C172M standards. Molded cylinder and beam specimens were sampled following ASTM C31/C31M standards.

Slump tests were performed on every batch of concrete following ASTM C143/C143M standards to determine the consistency and flowability of the concrete. The slump tests were performed to ensure compliance with TxDOT specifications for hydraulic cement concrete and to ensure that the fresh concrete would easily consolidate within the tight confines of the steel reinforcing cage and pocket connection. Results of the slumps tests are shown in Table 3.4.

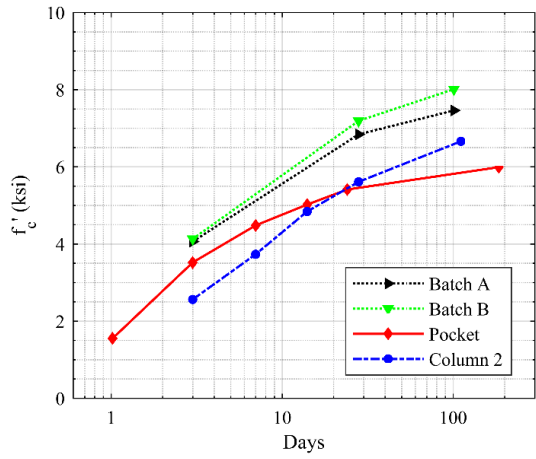
Concrete compressive tests were performed for every batch according to the sampling plan following ASTM C39/C39M standards. During Phase 1 the results of three 6-in. x 12-in. cylinder specimens were averaged, and during Phase 2 the results of three 4-in. x 8-in. cylinder specimens were averaged to indicate the representative compressive strength (f'_c). Results of the concrete strength tests are summarized in Table 3.4. Deviation from the target testing dates are noted where applicable in Table 3.4. Plots comparing the concrete compressive strength (f'_c) versus age are shown in Figure 3.36.

Modulus of elasticity (E_c), indirect tensile (f_{ct}), and modulus of rupture (f_r) tests were conducted in conjunction with the 28-day compressive strength tests. These tests were performed following ASTM C469/C469M, ASTM C496/C496M, and ASTM C78/C78M standards respectively. Additional indirect tensile tests were conducted on, or close to, the date of experimental testing for each specimen. The results of the modulus of elasticity, indirect tensile, and modulus of rupture for each batch of concrete are summarized in Table 3.5. Stress versus strain curves for concrete batches used in the fabrication of the reinforced concrete bent cap and the pretensioned bent caps are shown in Figure 3.37. During Phase 1, only Batch C was tested for 28-Day E_c , f_r , and f_{ct} . During Phase 2, all batches (J-N) were tested for 28-Day E_c , f_r , and f_{ct} .

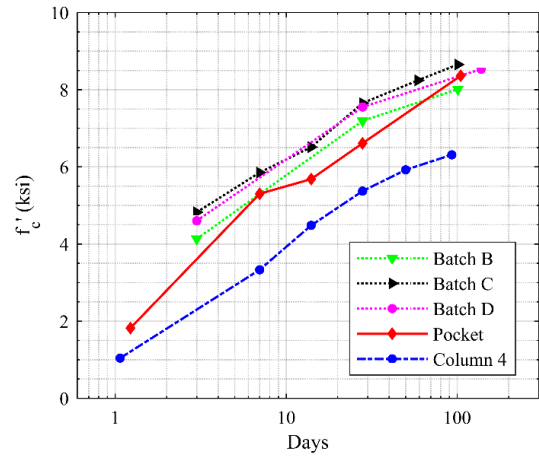
Table 3.4. Concrete Compressive Strength Results. (Adapted with permission from Birely et al. 2018a)

Specimen	Component	Slump (in)	f'_c (ksi)					Test Day
			1 Day	3 Day	7 Day	14 Day	28 Day	
PSS-16-12	Column 2	7.00	-	2.56	3.73	4.84	5.61	6.66
	Pocket	5.50	1.55	3.52	4.48	5.02	-	5.41
	Batch A	7.00	-	4.06	-	-	6.84	7.46
	Batch B	7.00	-	4.13	-	-	7.19	8.01
PSS-16-24	Column 4	8.00	1.04	-	3.33	4.48	**5.37	6.34
	Pocket	6.50	1.82	-	5.30	5.68	6.61	6.61
	Batch B	7.00	-	4.13	-	-	7.19	-
	Batch C	7.00	-	4.82	5.85	6.51	7.65	-
	Batch D	7.00	-	4.60	-	-	7.55	-
PSV-16-12	Column 3	8.00	1.04	-	3.33	4.48	**5.37	5.92
	Pocket	5.50	0.91	2.48	-	3.78	**4.79	4.72
	Batch E	7.00	-	3.85	-	-	7.90	8.82
	Batch F	7.00	-	4.04	-	-	7.65	8.38
PSV-28A	Column 5	-	0.77	-	4.28	5.27	5.81	7.01
	Pocket	8.00	-	*3.86	4.52	5.18	5.56	-
	Batch J	7.00	-	-	5.64	-	6.91	8.28
	Batch K	7.50	-	-	5.37	-	6.94	8.03
	Batch L	7.50	-	4.24	4.70	5.45	6.32	7.19
PSV-28B	Column 6	-	0.77	-	4.28	5.27	5.81	7.37
	Pocket	8.50	1.67	*5.12	5.83	†6.96	7.29	6.96
	Batch L	7.50	-	4.24	4.70	5.45	6.32	7.85
	Batch M	7.25	-	-	4.54	-	6.25	7.50
	Batch N	-	-	-	4.92	-	6.44	8.01

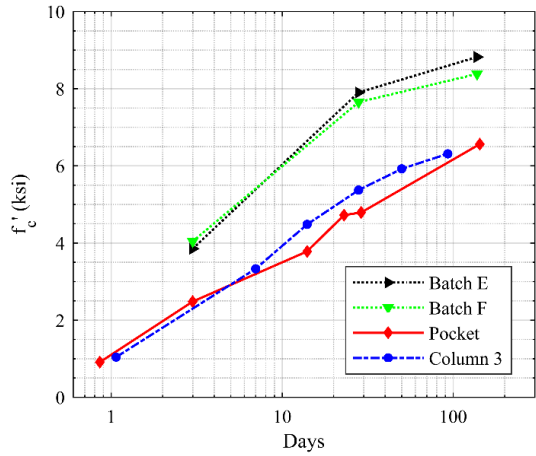
*4 day, †15 day, **29 day



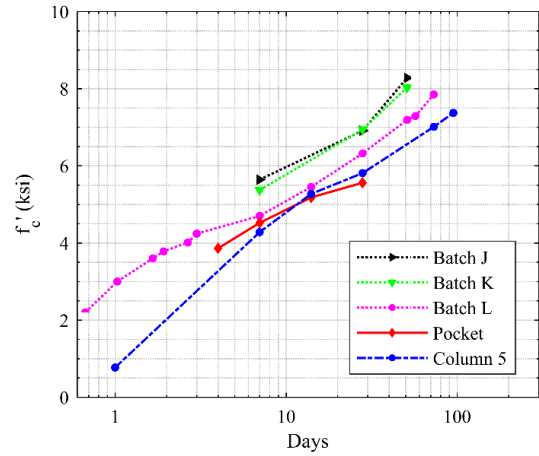
(a) PSS-16-12



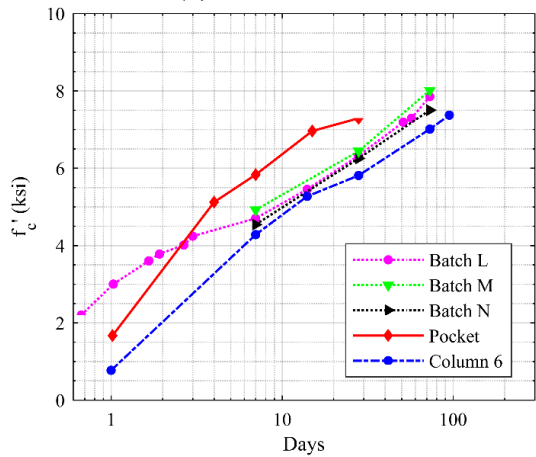
(b) PSS-16-24



(c) PSV-16-12



(d) PSV-28A



(e) PSV-28B

Figure 3.36. Concrete Compressive Strength vs Age.
(Reprinted with permission from Birely et al. 2018a)

Table 3.5. Modulus of Elasticity, Indirect Tensile, and Modulus of Rupture Results. (Adapted with permission from Birely et al. 2018a)

Specimen	Component	E_c (ksi)		f_{ct} (ksi)		f_r (ksi)	
		28 Day	Test	28 Day	Test	28 Day	Test
PSS-16-12	Column 2	5447	6340	0.77	0.77	0.93	0.92
	Pocket	-	5840	-	0.79	-	0.85
	Batch A	-	4920	-	0.95	-	-
	Batch B	-	3914	-	0.87	-	-
PSS-16-24	Column 4	**5447	-	**0.93	-	**0.77	-
	Pocket	5610	5610	0.78	0.78	0.96	0.96
	Batch B	-	-	-	-	-	-
	Batch C	3976	-	0.83	-	0.85	-
	Batch D	-	-	-	-	-	-
PSV-16-12	Column 3	-	5333	**0.72	0.72	**0.84	0.92
	Pocket	**5027	4696	**0.71	0.63	**0.74	0.77
	Batch E	-	-	-	0.91	-	-
	Batch F	-	-	-	0.90	-	-
PSV-28A	Column 5	5290	-	0.75	0.91	0.86	-
	Pocket	5447	-	0.78	0.78	0.88	-
	Batch J	4066	-	-	0.97	-	-
	Batch K	3837	-	-	0.90	-	-
	Batch L	3764	-	0.79	0.86	0.86	-
PSV-28B	Column 6	5290	-	0.75	-	0.86	-
	Pocket	5848	-	0.93	0.81	0.87	-
	Batch L	3764	-	0.79	0.89	0.86	-
	Batch M	3941	-	-	0.87	-	-
	Batch N	3988	-	-	0.89	-	-

**29 day

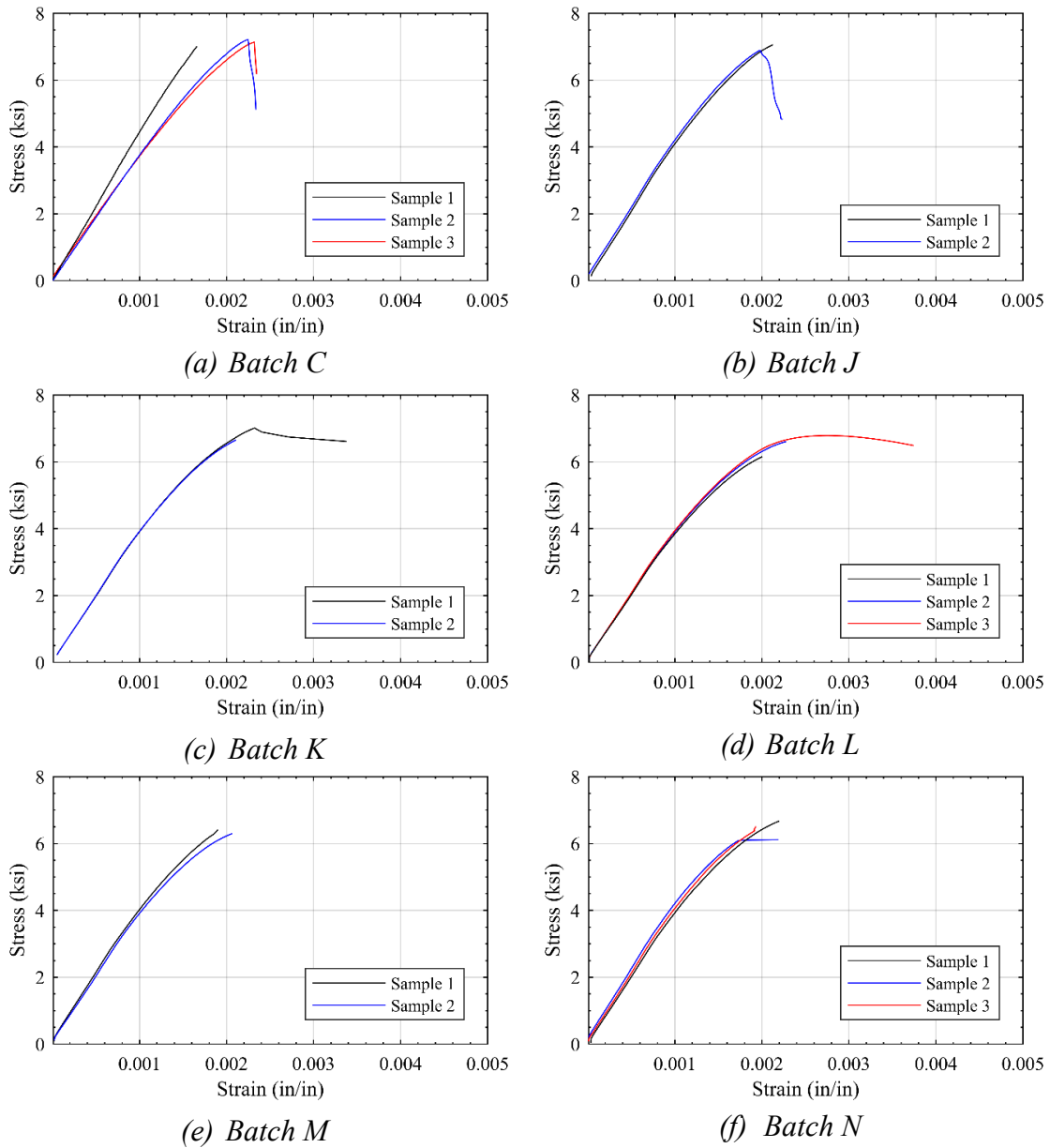


Figure 3.37. 28-Day Bent Cap Concrete Stress-Strain Curves.
 (Reprinted with permission from Birely et al. 2018a)

3.4.2. Steel Material Properties

Tensile testing of reinforcing bar specimens was conducted to determine yield strength (f_y), ultimate strength (f_u), modulus of elasticity (E_s), and yield strain (ϵ_y) of the

mild steel reinforcement used in the construction of the columns and pretensioned bent caps. Rebar specimens were sent to Applied Technical Services for testing. Tensile tests were conducted on samples of #5 transverse reinforcing bars (Phase 1 and Phase 2) and #11 dowel bars. Three specimens from each rebar type were tested, and the results for each parameter were averaged to determine the material properties of the steel. The results are summarized in Table 3.6.

Table 3.6. Steel Tensile Test Results. (Adapted with permission from Birely et al. 2018a)

Rebar	f_y (ksi)	f_u (ksi)	E_s (ksi)	ϵ_y (in/in)
#5 (Phase 1)	64	103	28,480	0.00225
#5 (Phase 2)	65	105	29,273	0.00222
#11 (Dowels)	68	106	28,147	0.00240

3.5. Experimental Testing

3.5.1. Specimen Loading

To simulate the forces of the prototype bridge, five actuators were used to apply demands to the sub-assemblages. Two vertical actuators, P1 and P2, simulated girder loads. A third vertical actuator, V, simulated shear at the inflection point. The upper horizontal actuator, HT, at the square end provided an axial load in the bent cap. The lower horizontal actuator, HB, was slaved to HT to provide equilibrium of horizontal forces on the specimen. Figure 3.38 shows the position of the actuator forces on the specimens.

All specimens were tested under multiple load patterns. The main pattern (Pattern A) generated shear and moment demands characteristic of multi-column bridge bents. Joint opening and closing were conducted to test the cap-column connection performance in Pattern C and D. Pattern B and E were selected to generate the largest moment demands permitted by the experimental test setup. Finally, Pattern F was used to fail the specimens by using large axial forces in the bent caps. Figure 3.39 shows the general moment diagrams for each load pattern. To achieve each load pattern, P1, P2, V, and HT/HB actuators were controlled through a mix of force and displacement control settings. Table 3.7 summarizes the actuator controls for each load pattern. Table 3.10 and Table 3.11 summarize actuator forces for Patterns A, B, E, and F. Patterns C and D are not included.

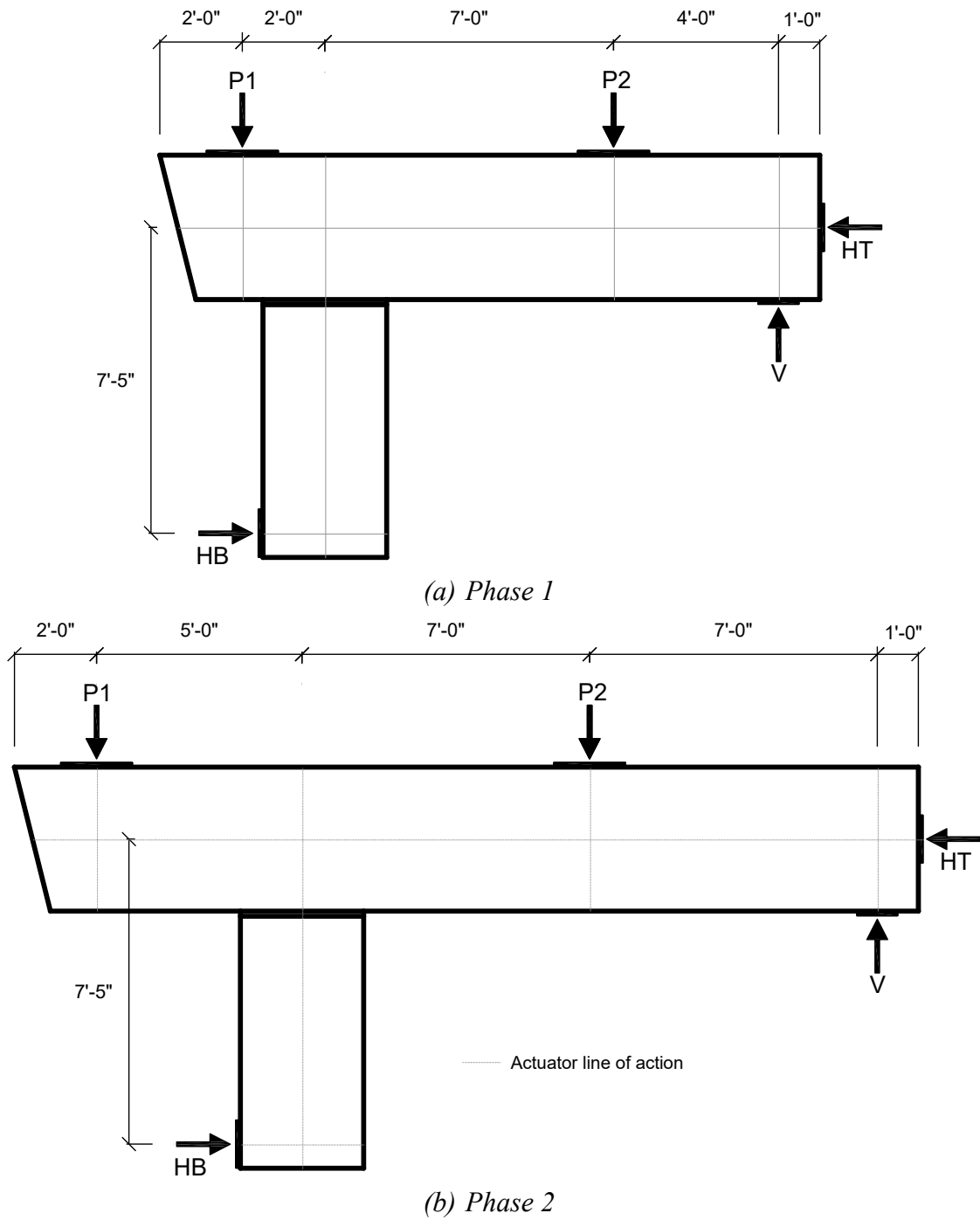


Figure 3.38. Location of Actuator Forces.
 (Reprinted with permission from Birely et al. 2018a)

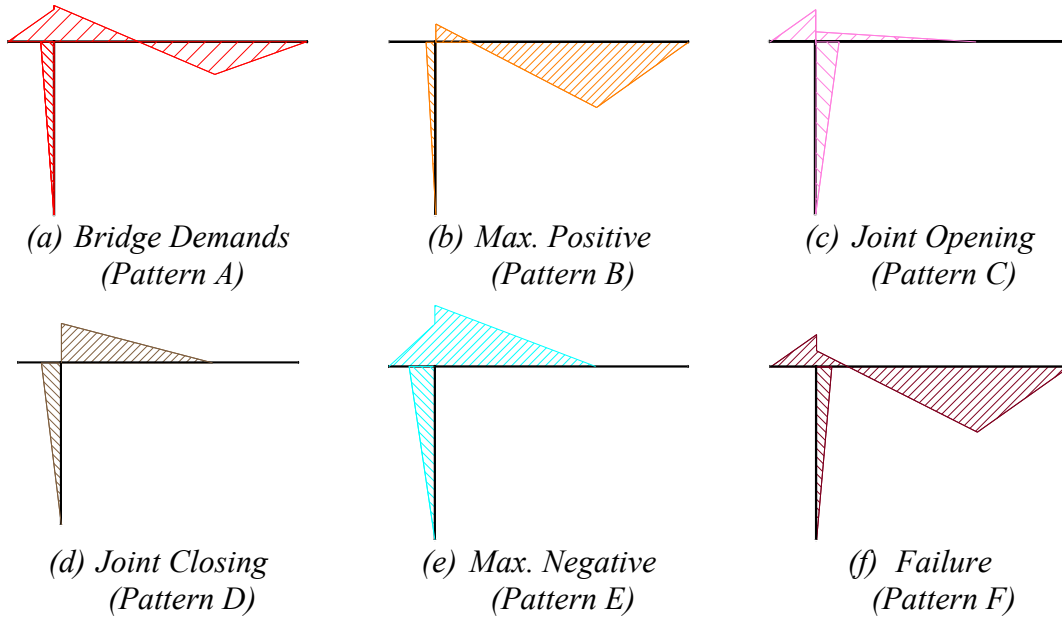


Figure 3.39. Load Pattern Moment Diagrams.
(Reprinted with permission from Birely et al. 2018a)

Table 3.7. Actuator Control Pattern. (Reprinted with permission from Birely et al. 2018a)

Load Pattern	Description	P1 (kips)	P2 (kips)	V (kips)	HT (HB) (kips)	
A	Bridge Demands	Dead	160*	160*	$\Delta = 0$	
		SLS	270*	270*		
		ULS	(262 [†]) 400* (380 [†])	(262 [†]) 400* (380 [†])		0.48P2* (0.21P2 [†])
		140% ULS	Max. Capacity	Max. Capacity		
B	Max. Positive Moment	0	Max. Capacity	0.64P2* (0.48P2 [†])	$\Delta = 0$	
C	Joint Opening	$\Delta = 0$	0	0	100 (Ten)	
D	Joint Closing	0	$\Delta = 0$	0	100 (Comp)	
E	Max. Negative Moment	Max. Capacity	$\Delta = 0$	0	100 (Comp)	
F	Failure	Max. Capacity	Max. Capacity	Max. Capacity	105 (Ten)	

*Actuator forces for Phase 1 test setup; †Actuator forces for Phase 2 test setup; Δ : Displacement Control governed by zero change in displacement; P1, P2, and V compression only.

Table 3.8. Summary of Demands Phase 1.

Specimen		Moment (Kip-ft)			Shear (Kip)			Jack Forces (Kip)			
		M _L ⁻	M _R ⁻	M ⁺	V _{OH}	V _{Span}	V _{SQ}	P1	P2	V	H ^a
Pattern A SLS	RCS-16-12	540	642	520	270	140	130	270	270	130	14
	PSS-16-12	540	598	520	270	140	130	270	270	130	8
	PSS-16-24	540	649	520	270	140	130	270	270	130	15
	PSV-16-12	540	613	520	270	140	130	270	270	130	10
Pattern A ULS	RCS-16-12	800	880	768	400	208	192	400	400	192	11
	PSS-16-12	800	829	768	400	208	192	400	400	192	4
	PSS-16-24	800	887	768	400	208	192	400	400	192	12
	PSV-16-12	800	844	768	400	208	192	400	400	192	6
Pattern A 140% ULS	RCS-16-12	1132	1219	1092	566	293	273	566	566	273	12
	PSS-16-12	1126	1126	1084	563	562	271	563	563	271	0
	PSS-16-24	1126	1162	1084	563	619	271	563	563	271	5
	PSV-16-12	1126	1133	1084	563	635	271	563	563	271	1
Pattern B Max. Pos.	RCS-16-12	0	218	1600	0	228	400	0	628	400	30
	PSS-16-12	0	160	1604	0	227	401	0	628	401	22
	PSS-16-24	0	73	1600	0	221	400	0	621	400	10
	PSV-16-12	0	138	1532	0	210	383	0	593	383	19
Pattern E Max. Neg.	RCS-16-12	1130	1855	0	565	260	0	565	260	0	100
	PSS-16-12	1120	1881	0	560	243	0	560	243	0	105
	PSS-16-24	1156	1917	0	578	255	0	578	255	0	105
	PSV-16-12	1030	1791	0	515	237	0	515	237	0	105
Pattern F Failure	RCS-16-12	1130	333	1400	565	236	350	565	586	350	-110
	PSS-16-12	1096	335	1508	548	234	377	548	611	377	-105
	PSS-16-24	1074	349	1468	537	255	367	537	622	367	-100
	PSV-16-12	970	209	1360	485	176	340	485	516	340	-105

^aBoth HT and HB; (+) = Compression; (-) = Tension

Table 3.9. Summary of Demands Phase 2.

Specimen		Moment (Kip-ft)			Shear (Kip)			Jack Forces (Kip)			
		M _L ⁻	M _R ⁻	M ⁺	V _{OH}	V _{Span}	V _{SQ}	P1	P2	V	H ^a
Pattern A SLS	PSV-28A	1783	1478	626	1170	876	294	1170	1170	294	-138
	PSV-28B	1783	1508	598	1170	890	280	1170	1170	280	-125
Pattern A ULS	PSV-28A	2576	2212	816	1690	1308	383	1690	1690	383	-165
	PSV-28B	2576	2242	788	1690	1321	369	1690	1690	369	-151
Pattern A 140% ULS	PSV-28A	3817	3266	1300	2504	2754	609	2504	2478	609	-249
	PSV-28B	3783	3075	1129	2482	2802	529	2482	2473	529	-320
Pattern B Max. Pos.	PSV-28A	0	265	2847	0	1348	1335	0	2682	1335	120
	PSV-28B	0	226	2857	0	1375	1339	0	2714	1339	102
Pattern E Max. Neg.	PSV-28A	3464	4349	0	2273	1851	0	2273	1851	0	400
	PSV-28B	4034	4034	0	2647	1704	0	2647	1704	0	0
Pattern F Failure	PSV-28A	-	-	-	-	-	-	-	-	-	-
	PSV-28B	0	295	3103	0	1214	1455	0	2669	1455	-133

^aBoth HT and HB; (+) = Compression; (-) = Tension

Pattern A generated shear and moment demands characteristic of multi-column bent caps. To generate the demands seen in Figure 3.39a, P1 and P2 increased simultaneously to simulate girder demands. Although the simultaneous loads in both actuators differs from AASHTO LRFD specifications, which has different live load

factors for exterior and interior girders, it is in accordance with TxDOT design practice. To generate the desired shear demands at the span, V was set to be a factor α of P_2 . The HT actuator was set to zero displacement. For the prototype discussed in Section 3.1.2, α was set to 0.48 and 0.21 for Phase 1 and 2 respectively. In Pattern A, P_1 and P_2 forces of 160 kips generated dead load P_D for both phases. Live load, P_L , was 110 kips and 102 kips, respectively. Service limit state (SLS) demands were the sum of dead and live loads. The ultimate limit state (ULS) demands were based on $1.25P_D + 1.75P_L$ in accordance with AASHTO LRFD 3.4.1. In both phases, calculated ULS values were rounded up slightly for simplicity, resulting in girder loads of 400 kips and 380 kips for Phase 1 and 2, respectively. The maximum capacities of the actuators corresponded to 140% and 150% ULS in Phase 1 and 2, respectively. 150% ULS demands for Phase 2 is referred to as 140% ULS for simplicity and consistency with Phase 1.

Pattern B generated the maximum positive demands in the span of the bent cap that were achievable with the current test setup. Creating the demands represented in Figure 3.39b required locking HT in displacement control, completely removing P_1 and increasing P_2 to its maximum capacity while V was set to force control at $0.64P_2$ and $0.48P_2$ for Phase 1 and 2, respectively.

Pattern C and D provided demands testing the connection between the bent cap and column by opening and closing the joint at the interior face of the column. To achieve the demands seen in Figure 4.3c, P_1 was locked in displacement control to allow a reaction at the overhang while HT was increased to its maximum tensile capacity. The P_2 and V loads were not used. The loads that generated the demands seen in Figure 3.39d were the

reverse of Pattern C; P2 was locked in displacement control and HT was increased to its maximum capacity in compression. The P1 and V loads were not used.

Pattern E generated the maximum negative moment demands achievable with the current test setup. Creating the demands represented in Figure 3.39e required lowering P2 to contact the specimen acting as a brake, and increasing P1 to its maximum capacity, HT was incrementally increased to its maximum compression capacity with V completely removed from the specimen.

Pattern F was the final load pattern and created the necessary demands to study the different failure mechanisms between the reinforced and pretensioned concrete bent cap specimens. To cause failure in each specimen, actuators P1, P2, HT (tension) were set to force control at their respective maximum load capacities while V was set to displacement control acting as a reaction. Control of V was changed to force control near the final stages of Pattern F to increase the force provided by P2.

Pattern A was applied first, with loads applied incrementally from dead to 140% ULS demands. The order of the subsequent load patterns varied, and in some instances, patterns were repeated. The details of pattern application on each specimen are available in Appendix B.

In general, Phase 1 specimens were loaded in order of 'Bridge Demands up to 140% ULS (Pattern A) → Maximum Positive Moment Demands (Pattern B) → Joint Opening (Pattern C) → Joint Closing (Pattern D) → Maximum Negative Moment Demands (Pattern E) → Failure (Pattern F)'. Creep tests were done for a few hours and

unloading to dead load or SLS was conducted to check the closure of cracks while applying Bridge Demands (Pattern A).

Phase 2 specimens were loaded by the order of ‘Bridge demands up to ULS (Pattern A) → Joint Opening (Pattern C) → Joint Closing (Pattern D) → Bridge demands up to 140% ULS (Pattern A) → Maximum Positive Moment Demands (Pattern B) → Maximum Negative Moment Demands (Pattern E)’. In Phase 2 tests, Pattern A was stopped at ULS to avoid severe damage in the overhang regions before conducting joint performance tests (Pattern C and D). For this reason, 150% ULS was applied after the joint performance tests. Unloading to dead load or ULS was also conducted during application of Pattern A, but creep test was not conducted in Phase 2.

3.5.2. *Summary of Observed Results*

During testing, the specimens were observed for signs of damage at different load stages. The outline of cracks was marked with colored permanent marker to correspond the damage with a load pattern. The cracks were measured with a metric crack comparator, and the maximum width of the cracks were recorded. Reported crack measurements have been converted from mm to inches. Photos were taken during testing to document damage. Figure 3.40 and Figure 3.41 shows the extent of the damage after the failure load case for each specimen.

All specimens exhibited the same extent of cracking under design loads; cracks were limited to hairline or 0.004-in. wide. All voided specimens (PSV-16-12, PSV-28A, and PSV-28B) displayed shear cracks along the interior void prior to reaching design loads. The solid specimens (PSS-16-12 and PSS-16-24) displayed flexure-shear failures

in the square end region. Voided specimens displayed failure by spalling of concrete in the compression zone; under P2 actuator for PSV-16-12 and at the column for PSV-28A and PSV-28B. Final cracks maps are shown in Figure 3.42.

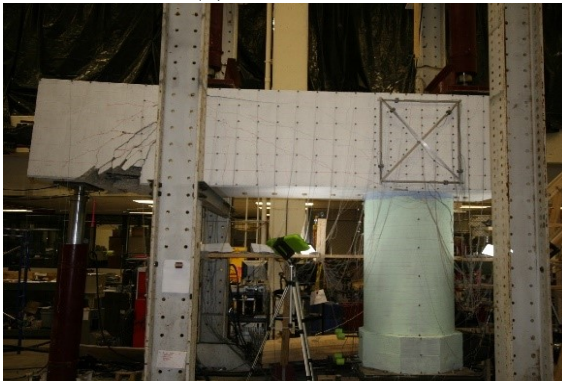
Cracks are categorized with reference to the AASHTO Standard Specifications Section C.5.7.3.4 crack width limit of 0.017-in (Class 1 exposure). Damage progression of Phase 1 and 2 specimens are presented in the following sections.



(a) PSS-16-12



(b) PSS-16-24



(c) PSV-16-12



(d) PSV-28A

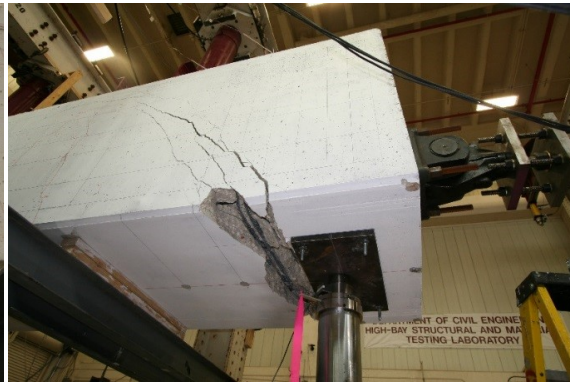


(e) PSV-28B

**Figure 3.40. Visual Observation at Failure (Back Face).
(Reprinted with permission from Birely et al. 2018a)**



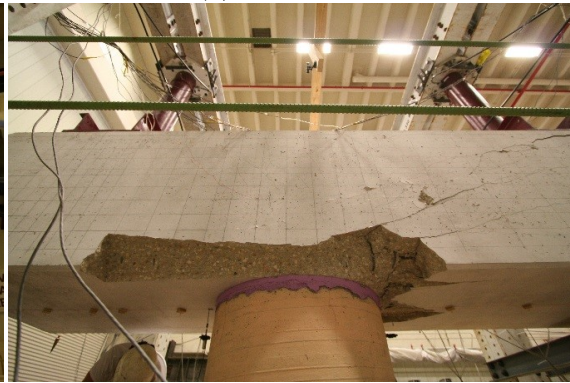
(a) PSS-16-12



(b) PSS-16-24



(c) PSV-16-12



(d) PSV-28A



(e) PSV-28B

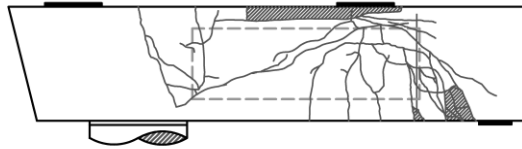
**Figure 3.41. Visual Observation at Failure (Failed region).
(Reprinted with permission from Birely et al. 2018a)**



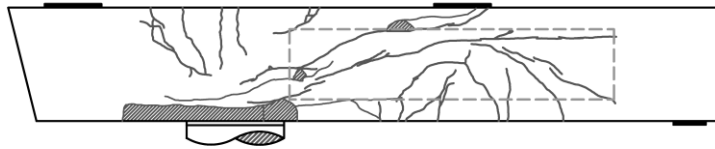
(a) PSS-16-12



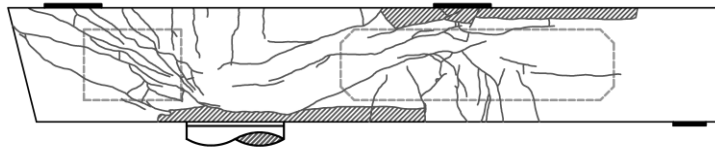
(b) PSS-16-24



(c) PSV-16-12



(d) PSV-28A



(e) PSV-28B

Figure 3.42. Cracking of Phase 1 and Phase 2 Specimens After Failure.

3.5.2.1. Phase I

All specimens had no cracks under dead load. At SLS demands (P1&P2 = 270 kips), only the negative moment region cracked in PSC bent caps; all cracks were hairline cracks. Crack maps for up to SLS are provided in Figure 3.43.

While loading to ULS demands, a diagonal shear crack appeared between the column face and P2 actuator in PSV-16-12 specimen. This type of shear crack was not observed in the other bent cap specimens with a solid section at this load stage.

Under ULS demands, crack extension and new crack formation were observed in the negative and positive moment regions in all specimens. The crack widths remained below the Class 1 Exposure limit. The shear crack of PSV-16-12 was along the interior void following the compression strut path between the column and P2 actuator.

Slight expansion or formation of new hairline crack were noted in the PSC bent caps during the creep tests.

After unloading to dead load, all cracks were closed or reduced to hairline cracks in PSS-16-24 and PSV-16-12. It is noted that PSS-16-12 was unloaded to an equivalent dead load following Pattern B, not Pattern A as in other PSC specimens, thus cracks did not close as much.

At 140% ULS demands, bent caps existing cracks lengthened/widened and new cracks formed. PSV-16-12 had shear crack extension with a horizontal crack formation below the P2 actuator. The maximum crack widths of PSC specimens ranged from 0.008-in. to 0.016-in., and those were still within the AASHTO crack limit. Crack maps for damage up to 140% ULS are provided in Figure 3.44.

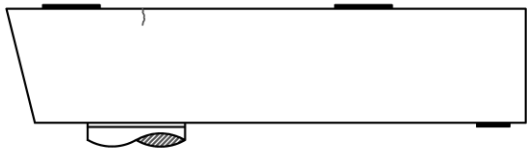
Under maximum positive moment demands, all specimens showed significant crack length and width extension with the formations of new cracks in the positive moment region. Additional diagonal cracks formed between P2 and V actuators in PSV-16-12. Maximum crack widths for all specimens exceeded AASHTO crack limit in this stage. For PSS-16-12, the load was unloaded to equivalent dead load in the span region, and all cracks were closed or reduced to hairline cracks.

Significant crack growth was noted in all specimens under maximum negative moment demands. For PSC specimens, no diagonal crack formed along the compression strut but the flexure-shear crack extended to nearly the whole bent cap depth. Measured maximum crack widths for all specimens were 0.2-in., substantially exceeding AASHTO crack limit. These large cracks showed evidence that significant yielding of longitudinal reinforcement had occurred. Crack maps for Pattern B and Pattern E are provided in Figure 3.45.

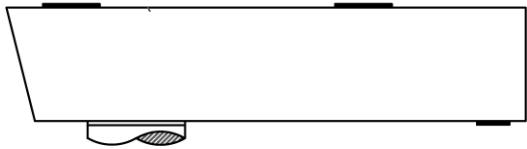
Load Pattern B and Pattern C applied joint opening and closing demands, respectively, to test the performance of the bedding layer and dowel bars in the connection of the column and the bent cap.

Joint opening demands during PSS-16-12 caused cracks in the column and the bedding layer to form with a maximum measured width of 0.004-in. Joint closing demands during PSS-16-12 caused hairline cracks to form on the exterior face of the column and the bedding layer which also propagated horizontally and vertically. No signs of pullout from the dowel bars were observed during either joint opening or joint closing

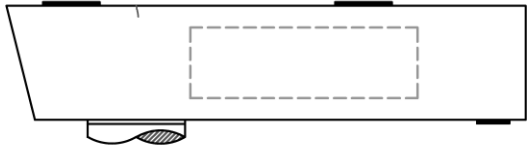
demands. Results of Joint Opening and Joint Closing tests were consistent for the subsequent specimens.



(a) PSS-16-12

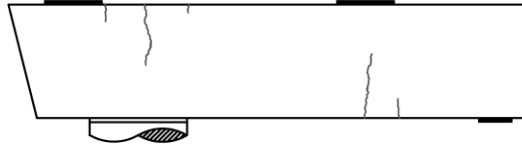


(b) PSS-16-24

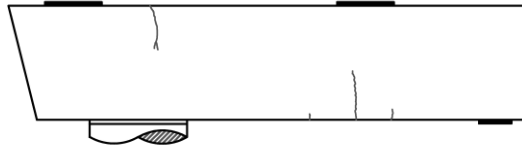


(c) PSV-16-12

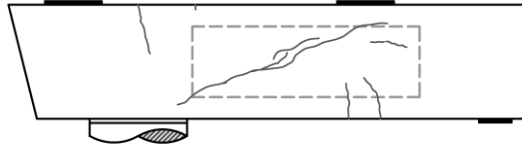
Figure 3.43. Cracking of Phase 1 Specimens under Pattern A SLS.



(a) PSS-16-12

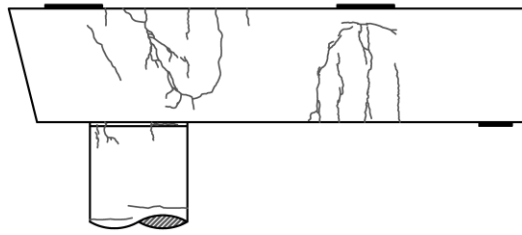


(b) PSS-16-24

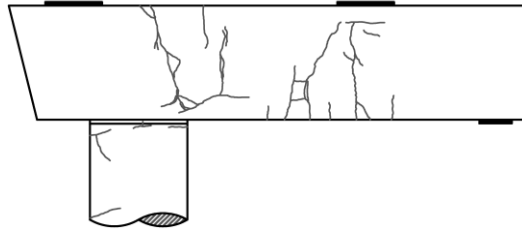


(c) PSV-16-12

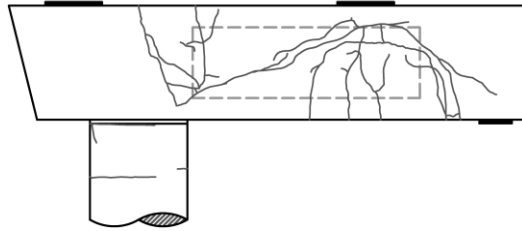
Figure 3.44. Cracking of Phase 1 Specimens under Pattern A 140% ULS.



(a) PSS-16-12



(b) PSS-16-24



(c) PSV-16-12

Figure 3.45. Cracking of Phase 1 Specimens under Pattern B (Max. Positive Moment) and Pattern E (Max. Negative Moment).

Table 3.10. Summary of Crack Formation and Widths: Phase 1. (Reprinted with permission from Birely et al. 2018a)

	PSS-16-12	PSS-16-24	PSV-16-12
Dead	• No Cracks	• No Cracks	• No Cracks
SLS	• Negative moment region cracked • Hairline cracks	• Negative moment region cracked • Hairline cracks	• Negative moment region cracked • Hairline cracks
ULS	• Negative moment cracks extended • Positive moment region cracked • New hairline crack & crack extension under creep • No unloading to dead load in this step	• Negative moment cracks extended • Positive moment region cracked • New hairline crack and crack exten. at creep • All cracks closed after unload to dead load	• Shear crack along interior void at 370 kips • Negative moment cracks extended • New cracks at the interface of the column • Positive moment region cracked • Cracks closed or reduced to hairline cracks after unloading to dead load
140% ULS	• Both region cracks extended and grew • New crack in both regions • Max width (0.008-in.) < AASHTO limit	• Flex. cracks extended with min. width growth • New crack in positive moment region • Max width (0.008-in.) < AASHTO limit	• All flex. and shear cracks extended • New cracks in both moment regions • New horiz. crack below P2 actuator • Max width (0.016-in.) < AASHTO limit
Max. Pos.	• New cracks in the positive moment region • Significant crack length and width extension • Max crack width (0.06 in.) > AASHTO limit • Equivalent dead load → All cracks closed or reduced to hairline cracks	• New flexural cracks in the positive moment region • Significant crack length and width extension • Max crack width (0.04 in.) > AASHTO limit	• New flexural cracks in the pos moment region • New shear crack between P2 and V actuators • Max crack width (0.04 in.) > AASHTO limit
J/O	• East face of the col. and bedding layer cracked	• East face of the col. and bedding layer cracked	• East face of the col. and bedding layer cracked
J/C	• West face of the col and bedding layer cracked	• West face of the col and bedding layer cracked	• West face of the col and bedding layer cracked
Max. Neg.	• New flex cracks in negative moment region • Significant crack length and width growth • Max crack width (0.2 in.) > AASHTO limit	• New flex cracks in negative moment region • Significant crack length and width growth • Max crack width (0.2 in.) > AASHTO limit	• New flex cracks in negative moment region • Significant crack length and width growth • Max crack width (0.2 in.) > AASHTO limit

Note: Bold indicates when AASHTO limit of 0.017-in. exceeded

3.5.2.2. Phase 2

No cracks were observed under dead load in both specimens. At SLS, the first hairline cracks formed in the negative moment region in both specimens. PSV-28B showed a horizontal crack in the span region which was not observed in PSV-28A. Crack maps for up to SLS are provided in Figure 3.46.

A shear crack was first observed while loading to ULS demands in both specimens. At ULS demands, negative moment cracks were extended, and additional flexure crack formations were noted in both specimens. Maximum crack widths were 0.049-in. and 0.033-in. for PSV-28A and PSV-28B, respectively, exceeding AASHTO crack limit. Additionally, shear cracks were observed in the overhang along the interior void, and horizontal cracks became prominent in PSV-28B specimen. After unloading to dead load, the majority of flexure cracks were closed or reduced to no more than 0.006-in. Crack maps for damage up to 140% ULS are provided in Figure 3.47.

Flexure cracks first occurred in the positive moment region in both specimens after applying maximum positive moment demand. This was accompanied by significant extension of existing shear cracks. A new diagonal shear crack occurred between P2 and V actuators in PSV-28A. Maximum crack width was 0.035-in. for both specimens, exceeding the AASHTO crack limit.

New flexural cracks developed in joint regions at maximum negative moment demands. While PSV-28A had no damage in overhang region, PSV-28B had significant diagonal cracks in that region. As load increased, both specimens failed by showing

spalling of concrete in negative moment region. Crack maps for Pattern B and Pattern E are provided in Figure 3.48.

After the maximum negative moment demands, PSV-28B was subjected to maximum positive moment demand again with excessive tension force on the horizontal actuator to fail the positive moment region. The specimen failed by concrete spalling beneath the P2 actuator.

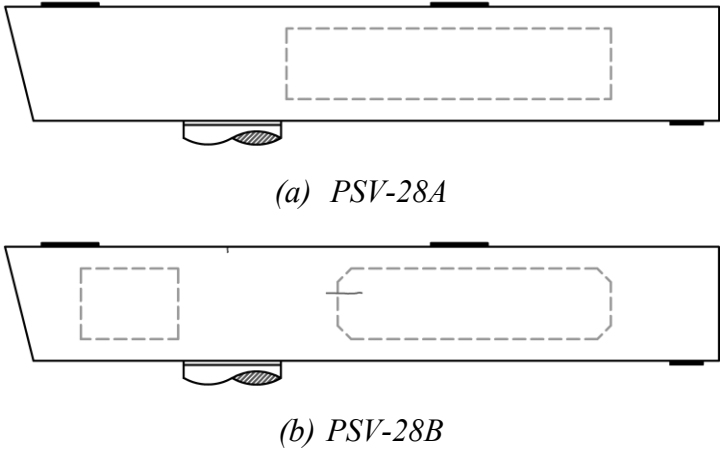
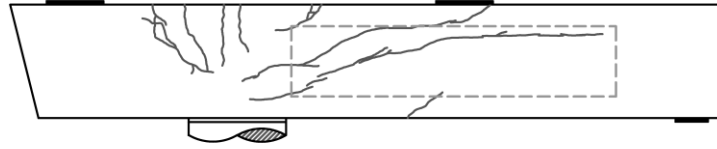
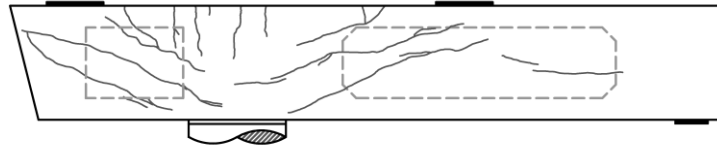


Figure 3.46. Cracking of Phase 2 Specimens under Pattern A SLS.

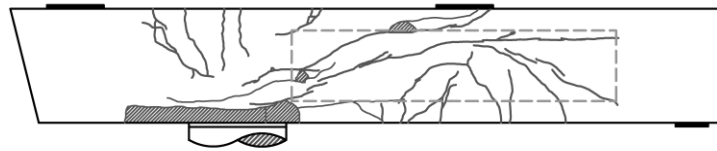


(a) *PSV-28A*

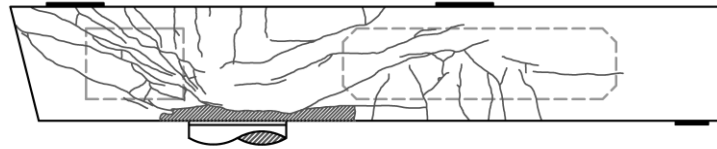


(b) *PSV-28B*

Figure 3.47. Cracking of Phase 2 Specimens under Pattern A 140% ULS.



(a) *PSV-28A*



(b) *PSV-28B*

Figure 3.48. Cracking of Phase 2 Specimens under Pattern B (Max. Positive Moment) and Pattern E (Max. Negative Moment).

Table 3.11. Summary of Crack Formation and Crack Widths: Phase 2. (Reprinted with permission from Birely et al. 2018a)

	PSV-28A	PSV-28B
Dead	<ul style="list-style-type: none"> • No Cracks 	<ul style="list-style-type: none"> • No Cracks
SLS	<ul style="list-style-type: none"> • Negative moment region cracked • Hairline crack 	<ul style="list-style-type: none"> • Negative moment region cracked • Horizontal crack observed in the span region • Hairline cracks
ULS	<ul style="list-style-type: none"> • Shear crack along the interior void at 263kips • Negative moment cracks extended • Additional flexure cracks in negative moment region • Cracks closed or reduced to hairline after unloading to dead load 	<ul style="list-style-type: none"> • Shear crack along the interior void • Negative moment cracks extended • Additional flexure cracks in negative moment region • Shear crack formed in overhang • Horizontal cracks more prominent • Flexure cracks closed or reduced to hairline after unload to dead • Horizontal cracks reduced to 0.008 in. after unload to dead load
140% ULS	<ul style="list-style-type: none"> • All flexural and shear cracks extended • New cracks formed in negative region • Additional shear crack formed • Hairline positive moment crack formed • Maximum crack width (0.049 in.) > AASHTO limit • Majority of cracks closed or reduced to hairline after unload to dead 	<ul style="list-style-type: none"> • All flexural and shear cracks extended • New cracks formed in negative region • Additional shear cracks formed in span and overhang • Hairline positive moment crack formed • Maximum crack width (0.033 in.) > AASHTO limit • Majority of cracks closed or reduced to 0.006 in. after unload to dead
Max. Pos.	<ul style="list-style-type: none"> • Extension of existing shear and flexure cracks • New flexural cracks in the positive moment region • New shear crack between P2 and V actuators • Maximum crack width (0.035 in.) > AASHTO limit 	<ul style="list-style-type: none"> • Extension of existing shear and flexure cracks • New flexural cracks in the positive moment region • Maximum crack width (0.035 in.) > AASHTO limit
J/O	<ul style="list-style-type: none"> • East face of the column and bedding layer cracked 	<ul style="list-style-type: none"> • East face of the column and bedding layer cracked
J/C	<ul style="list-style-type: none"> • West face of the column and bedding layer cracked 	<ul style="list-style-type: none"> • West face of the column and bedding layer cracked
Max. Neg.	<ul style="list-style-type: none"> • New flexural cracks in negative moment region • Significant crack length and width growth • Crushing/spalling of concrete in negative moment region 	<ul style="list-style-type: none"> • New flexural cracks in negative moment region • Significant crack length and width growth • Crushing/spalling of concrete in negative moment region and overhang

Note: Bold indicates when AASHTO limit of 0.017-in. exceeded

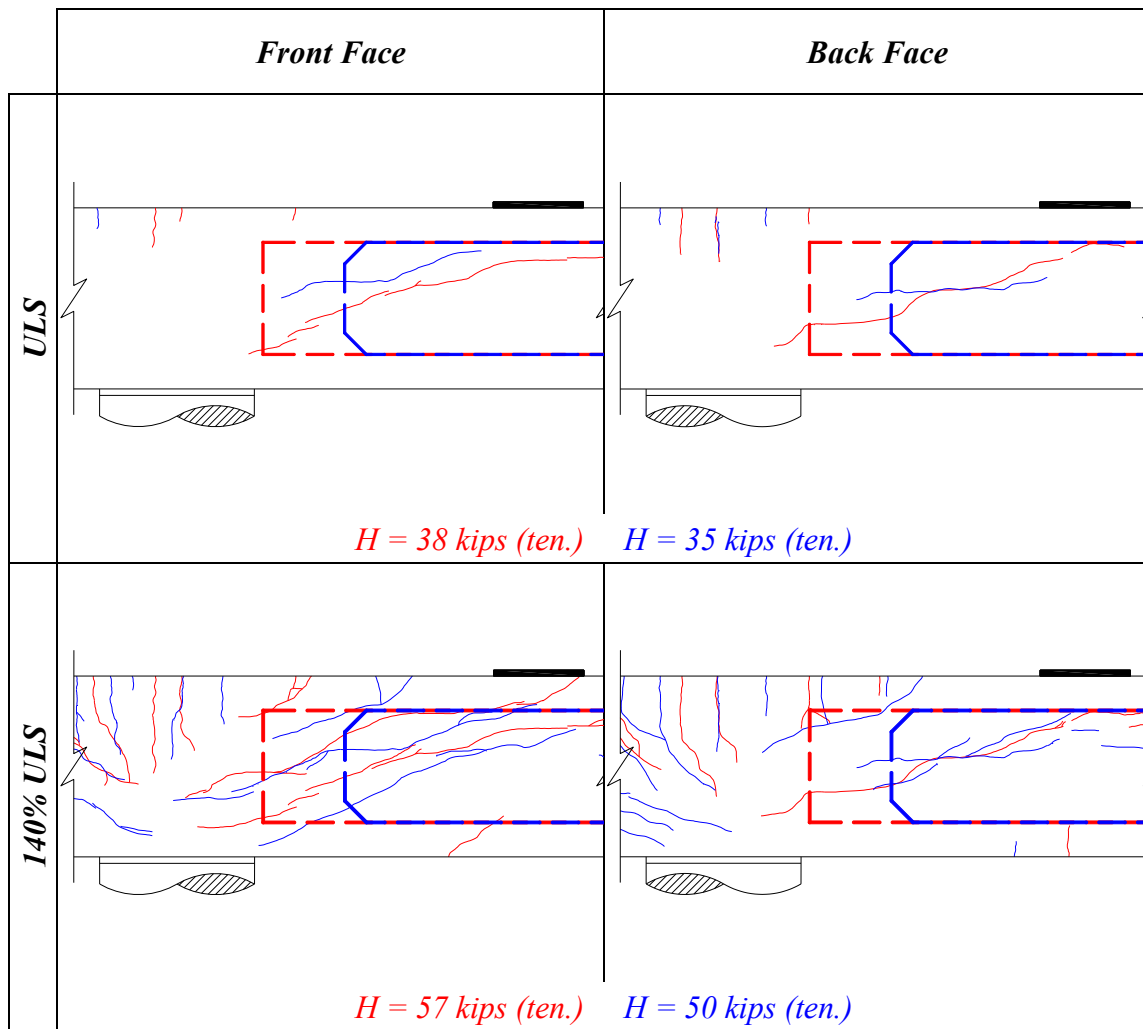
3.5.3. Impact of Design Variables

3.5.3.1. Impact of Void Details

This section discusses the results of the different interior void geometries and details investigated during Phase 2. During Phase 1, shear cracking formed along the length of the interior void (in the span region) under ULS and 140% ULS demands. Investigation of the interior void details in Phase 2 anticipated highlighting impact on the onset of shear cracking, crack angle, crack propagation, and the effect of the hollow/solid cross section in the critical shear locations.

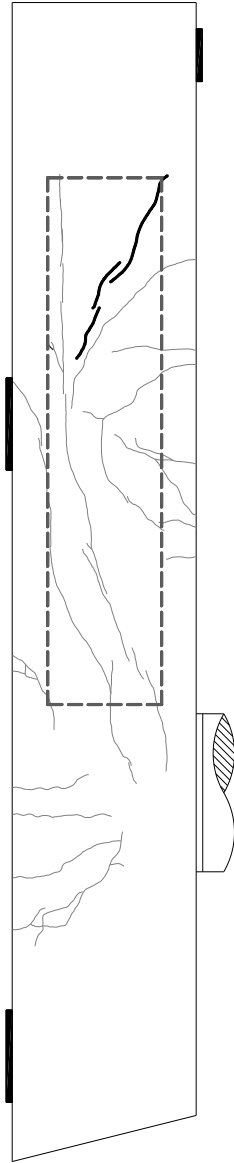
Figure 3.49 compares the cracking in the span region of PSV-28A and PSV-28B under ULS and 140% ULS demands. The cracks and interior void outlines are shown in red and blue for PSV-28A and PSV-28B, respectively. Vertical loads were nearly identical for both PSV-28A and PSV-28B during ULS and 140% ULS demands, with slight differences due to the initial position, specimen weight, and horizontal forces applied. Horizontal tension force applied by the HT/HB actuators had minor differences, these differences are noted in Figure 3.49. During ULS loading, the initial shear crack angle for PSV-28B was shallower than for PSV-28A and did not travel toward the corner of the interior void. The initial shear crack that formed on the front face of PSV-28B appeared to incorporate a preexisting horizontal crack, which was likely missed during pretesting inspection. Under 140% ULS loading, the differences in angle and direction of new shear cracks were not apparent. The extent of shear cracking in the span region on the back face of PSV-28B, even under shear and moment demands greater than 140% ULS, did not extend to the interior face of the column like that of PSV-28A.

Differences in shear cracking in the square end of PSV-28A and PSV-28B were observed under maximum shear demands (V_{max}) in the square end region. Figure 3.50 compares the formation of shear cracks under equivalent shear demands in the square ends of both specimens, noting the force in the V actuator (V_{max}) and difference in horizontal compression. PSV-28A displayed a shear crack (on both faces) that travelled to the corner of interior void, terminating at the solid region of the cross-section. This crack is highlighted with a thick line in the figure. PSV-28B did not display a shear crack of the same nature.



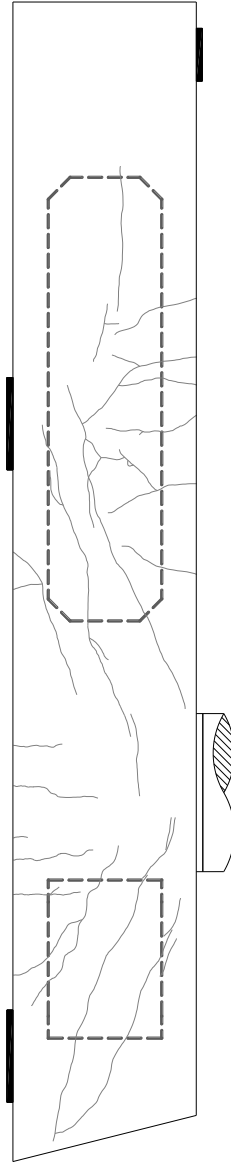
Red = PSV-28A *Blue* = PSV-28B

Figure 3.49. Comparison of Shear Cracks in Span Region of PSV-28A and PSV-28B at ULS and 140% ULS Demands. (Reprinted with permission from Birely et al. 2018a)



$V = 300$ kips $H = 27$ kips (comp.)

(a) PSV-28A



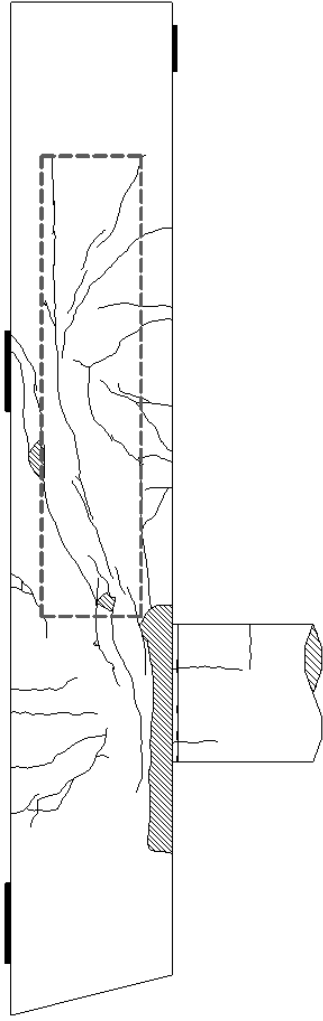
$V = 300$ kips $H = 22$ kips (comp.)

(b) PSV-28B

Note: Thick line highlights shear cracks in square end

Figure 3.50. Comparison of Formation of Shear Cracks in Square End of PSV-28A and PSV-28B under V_{max} of Square End. (Reprinted with permission from Birely et al. 2018a)

Both specimens failed in the negative moment region during Pattern E (maximum negative moment). Shown in Figure 3.51, the loss of concrete appears to be associated with the concentration of compressive stress at the corner of the interior void in both specimens. Differences in the loading conditions are noted. Although PSV-28B also had extensive shear damage in the overhang, the spalling of the concrete on the interior (span) side of the column happened first similar to the failure of PSV-28A.



$P1 = 503 \text{ kips}$ $P2 = 416 \text{ kips}$ $V = 0 \text{ kips}$ $H = 90 \text{ kips (comp.)}$

(a) PSV-28A



$P1 = 595 \text{ kips}$ $P2 = 395 \text{ kips}$ $V = 0 \text{ kips}$ $H = 0 \text{ kips}$

(b) PSV-28B

Figure 3.51. Comparison of Damage at Failure in Negative Moment Region of PSV-28A and PSV-28B.
 (Reprinted with permission from Birely et al. 2018a)

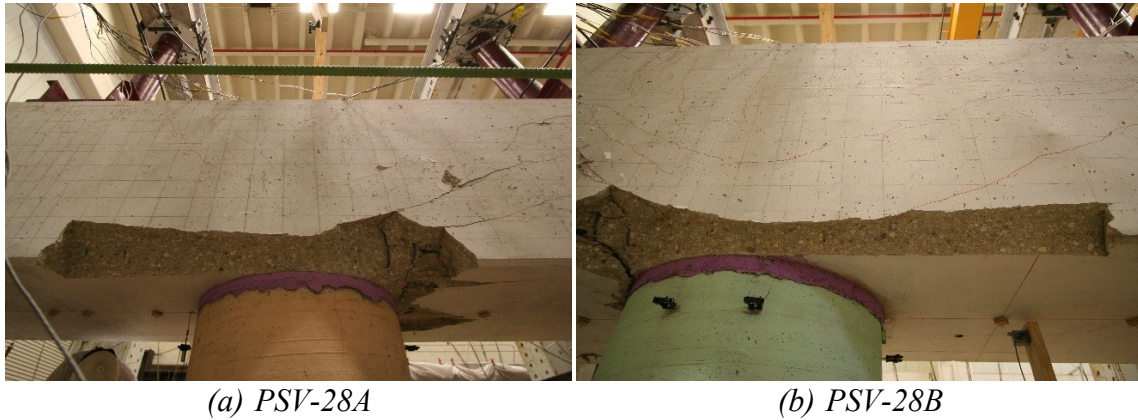
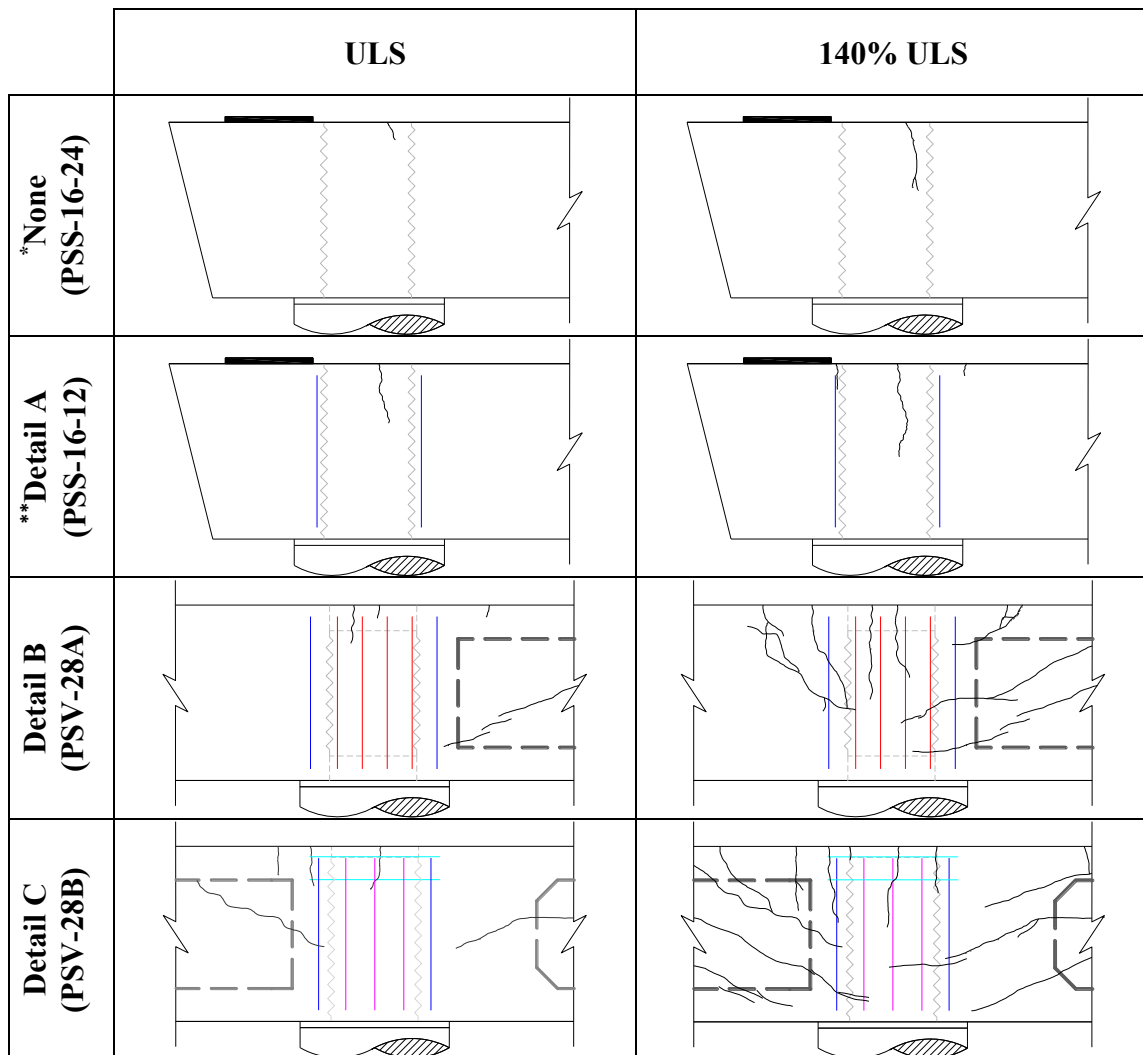


Figure 3.52. Loss of Concrete in Negative Moment Region of Phase 2 Specimens during Maximum Negative Moment Demands. (Reprinted with permission from Birely et al. 2018a)

3.5.3.2. Impact of Pocket Connection Details

Figure 3.53 shows the cracking in the negative moment region of the pretensioned specimens. While forces at ULS and 140% ULS demands are similar in both Phase 1 and Phase 2, the longer overhang of Phase 2 specimens induced a larger moment in the joint region. Due to the increased moment in the joint compared to Phase 1, a direct comparison of the damage between Phase 1 details and Phase 2 details are not feasible. However, comparisons of joint region detailing investigated in Phase 2 are possible. The maximum width of flexure cracks in the joint region of PSV-28A (0.014-inch) were larger than that of PSV-28B (0.010-inch), leading one to conclude that the additional mild steel hoops included at the top of the pocket connection were effective at limiting the expansion of flexure cracks at increased loads. No significant differences in the performance of the connection were observed with the varied corrugated pipe embedment depth. No

significant differences in the onset or propagation of cracking in the joint region was observed with the variation in shear reinforcement between Detail B and Detail C.



* Additional reinforcement also not included in RCS-16-12

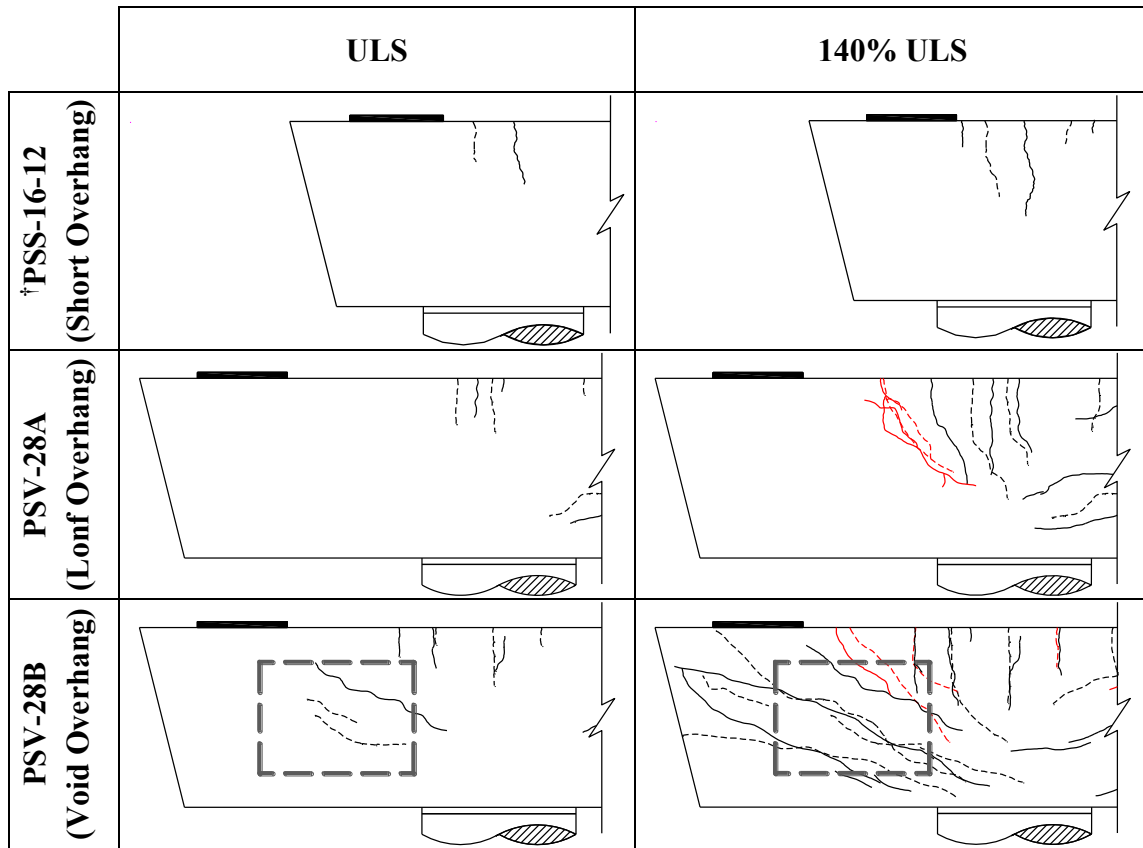
** Detail A is present in both PSS-16-12 and PSV-16-12

Figure 3.53. Comparison of Cracking in Negative Moment Region of Pretensioned Specimens with Different Pocket Connection Details under ULS and 140% ULS Demands. (Reprinted with permission from Birely et al. 2018a)

3.5.3.3. *Impact of Overhang Geometry and Details*

The geometry and detailing of the overhang region was varied in Phase 2. Figure 3.54 compares the damage that occurred in pretensioned specimens that had the standard (short, solid) overhang in Phase 1 to that of the two Phase 2 overhangs (long, with and without void). Due to similarities in damage in Phase 1 pretensioned specimens, only PSS-16-12 is represented in the figure. Under ULS demands, the solid overhangs, both short and long, showed similar results. Cracking was limited to the flexure region within the joint. However, in the voided overhang (PSV-28B) shear cracking along the interior void was observed on both faces at ULS demands. Shear cracking was expected after ULS demands ($P1$ & $P2 = 380$ kips), when $P1$ reached V_{cr} of the overhang (330 kips). These shear cracks were measured in the range of 0.002 – 0.010-in., which is below the AASHTO limit. Under 140% ULS demands, the standard overhang showed limited crack progression with the damage mainly isolated to the flexure region within the joint. Both longer overhangs showed crack propagation and the onset of additional cracking. In PSV-28A, flexure-shear cracks formed between the $P1$ actuator and the exterior face of the column, and the widths exceeded the AASHTO limits. In PSV-28B, extensive shear cracking was observed, with similar flexure-shear cracks present.

Figure 3.55 compares the damage in the solid and voided longer overhangs of PSV-28A and PSV-28B at the time of failure in the negative moment region. While failure in both specimens occurred in the compression zone of the negative moment region, PSV-28B also crushed along the compression strut from the $P1$ actuator to the exterior face of the column.



† Representative of Phase 1 specimens. Negligible differences in overhang cracking of other Phase 1 specimens

Red = Crack exceeds AASHTO limits.

--- = Cracks on back face

**Figure 3.54. Comparison of Damage in Overhangs with Different Lengths and Void Details under ULS and 140% ULS Demands.
(Reprinted with permission from Birely et al. 2018a)**

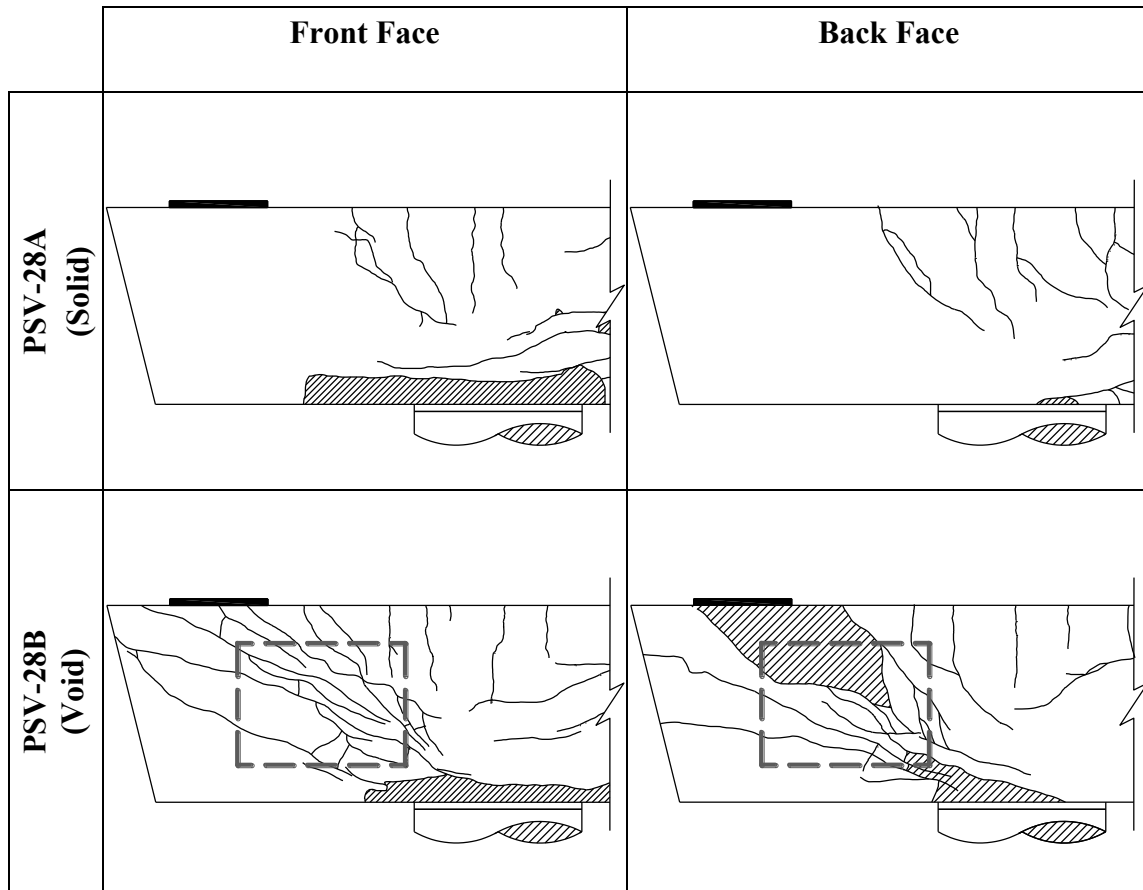


Figure 3.55. Comparison of Overhang Damage of Solid (PSV-28A) and Voided (PSV-28B) Overhang at Negative Moment Region Failure.
(Reprinted with permission from Birely et al. 2018a)

3.5.3.4. Summary

Through visual observations of damage from experimental testing, the impact of the interior void details, overhang geometry and length, and pocket connection details were examined. The detailing of the interior voids did not appear to affect the onset of shear cracking but did appear to affect the extent of cracking under design bridge demands. At loads beyond design bridge demands, the influence of interior void details was less apparent, as newly formed cracks appeared at similar angles and extent for both details.

Pocket connection details showed no significant impact on the onset or extent of cracking in Phase 1 specimens. However, the addition of the mild steel hoops at the top of the pocket connection in PSV-28B appeared to limit the expansion of flexure cracks at increased loads. No significant differences in the performance of the connection were observed with the varied corrugated pipe embedment depth. No significant differences in the onset or propagation of cracking in the joint region was observed with the variation in shear reinforcement.

Overhang geometry appeared to significantly impact the behavior of the bent caps. Under design bridge demands, the longer, solid overhang resulted in similar performance to the shorter, standard overhang. Beyond design bridge demands, additional flexure-shear cracking was observed outside of the joint region in the longer, solid overhang that was not present in the shorter, standard overhang. Inclusion of an interior void in the overhang negatively impacted the overall performance of the bent cap. Shear cracking was observed in the voided overhang under design bridge demands, which was not present in bent caps with solid overhangs. Failure occurred in the negative moment region of the Phase 2 specimens, with spalling of concrete in the compression zone. Failure was more abrupt for PSV-28B, with additional spalling of concrete along the compression strut along the voided overhang.

The impact of the design variables are investigated further with analysis of the experimental data collected with the Optotrak motion capture system, as discussed in section 4.

4. DATA ANALYSIS

4.1. Overview

Detailed data analysis was conducted using the Optotrak Certus motion capture data collected during experimental testing. This section discusses the methods used to conduct data analysis. Section 4.2 provides details on the necessary components of post-processing experimental data. Section 4.3 discusses the validation of the Optotrak Certus motion capture system measurements by comparison to string potentiometer measurements. Section 4.4 discusses the data analysis techniques performed on the experimental data and presents discussion on the presented analysis. Section 4.5 provides a summary and discussion of the data analysis.

4.2. Post-Processing

To perform analysis of the data collected during experimental testing, it was necessary to post-process the raw data into a useable form. The following sections provide details on the procedures and methods used to post-process the experimental data.

4.2.1. *Data Synchronization*

Data collection rates differed for the traditional instrumentation connected to the data acquisition unit (DAQ) and the separate Optotrak system. The DAQ sampled data at 0.5 Hz during the majority of the testing and was slowed to 0.2 Hz for the creep tests performed during Phase 1. The Optotrak collection rate remained constant at 1 Hz for the duration of testing. In addition, the starting point of the DAQ and Optotrak data files did not occur at the same point in time. To compare loading and measurement data collected

with the DAQ and the displacements measured with the Optotrak, the data files had to be synchronized.

The timestamps on the computers running the DAQ and Optotrak were often misaligned. Therefore, files timestamps could not be relied upon to provide adequate alignment of the starting points. Initially, the timestamps were used to approximately align the data and displacement versus step plots were used to better adjust the starting points. To synchronize the DAQ and Optotrak data, the time between adjacent steps in the DAQ data was determined and used to filter out the non-corresponding Optotrak data points.

4.2.2. Coordinate System Transformation

When multiple position sensors are used to collect data, the coordinate systems of each sensor are registered together into a global coordinate system. To simplify future calculations, the data for each test was transformed into the orthogonal directions by rotation and translation.

The global coordinate system varied for each test, so each data set was transformed individually. A reference plane was chosen along the face of the bent caps by selecting the outer corners of the LED marker grid. The starting coordinates of these four markers were determined by averaging the first 20 data points in the set. The entire data set was translated such that the lower left marker on the bent cap was the origin point. To rotate the data, the set was multiplied by a three-dimensional Euler rotation matrix. The rotation matrix was determined with the following equations:

$$R = R_z(\Phi) * R_{Y'}(\Theta) * R_{X''}(\Psi) \quad \text{Eq. 4-1}$$

where:

$$R_z(\Phi) = \begin{bmatrix} \cos\Phi & -\sin\Phi & 0 \\ \sin\Phi & \cos\Phi & 0 \\ 0 & 0 & 1 \end{bmatrix} \quad \text{Eq. 4-2}$$

$$R_{Y'}(\Theta) = \begin{bmatrix} \cos\Theta & 0 & -\sin\Theta \\ 0 & 1 & 0 \\ \sin\Theta & 0 & \cos\Theta \end{bmatrix} \quad \text{Eq. 4-3}$$

$$R_{X''}(\Psi) = \begin{bmatrix} 1 & 0 & 0 \\ 0 & \cos\Psi & -\sin\Psi \\ 0 & \sin\Psi & \cos\Psi \end{bmatrix} \quad \text{Eq. 4-4}$$

The Euler angles and rotation process are summarized in Figure 4.1. An example of the coordinate transformation process is shown in Figure 4.2. Placement of the position sensors was more symmetric during Phase 2, leading to less severe initial out-of-planeness of the original global coordinate system. The transformation was performed with the assumption that the bottom surface of the bent cap specimen was perfectly level. After the transformation, the average out-of-planeness of the LED marker furthest from the origin of rotation relative to the X-Y plane was 3.9 mm (0.15 in.), with the largest being 6.4 mm (0.25-in.).

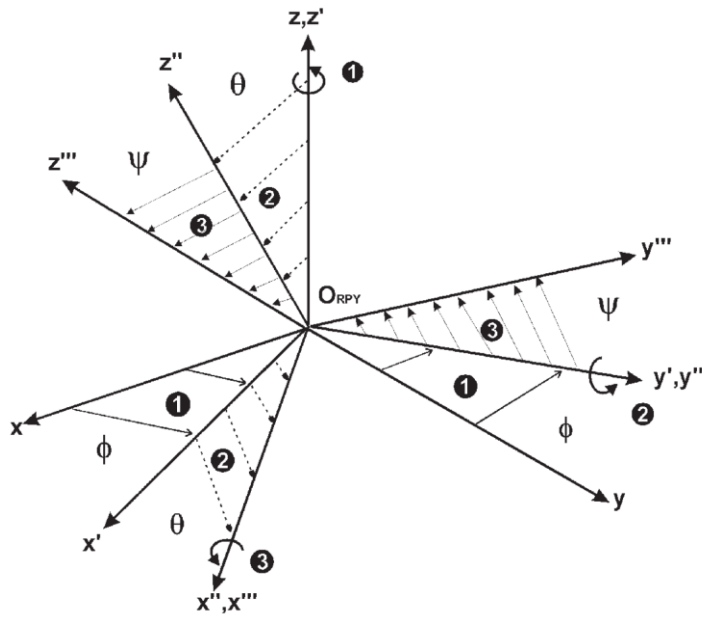


Figure 4.1. 3-D Euler Rotations. (Source: Optotrak User Manual)

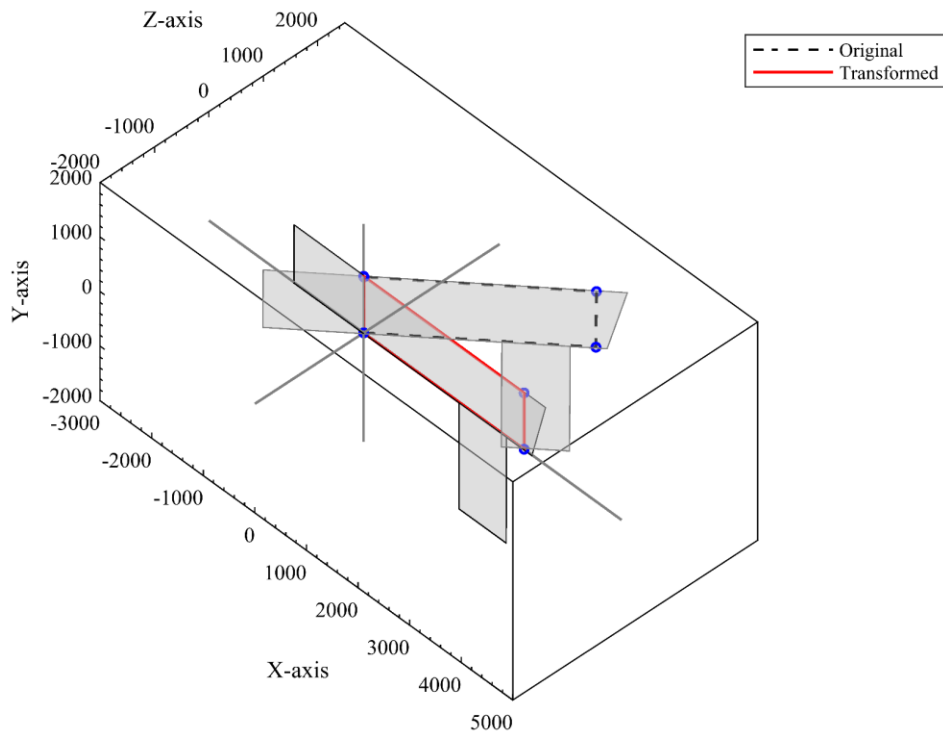


Figure 4.2. Optotrak Coordinate Rotation (units in mm) Showing Original and Transformed Position of Bent Cap Specimen.

4.2.3. *Marker Naming*

Each LED marker was given a name which identified its vertical and horizontal grid position. The naming aided in comparing data from corresponding markers. Since the LED marker layout differed for Phase 1 and Phase 2, the LED marker names do not perfectly correlate between phases. Figure 4.3 and Figure 4.4 show the general LED marker names and locations.

Data such as the original coordinate and marker name were stored with each LED marker. The original coordinates were determined from the average of the first 25 data points. The displacement data was stored as the change in position from the original coordinate, to simplify future data analysis tasks.

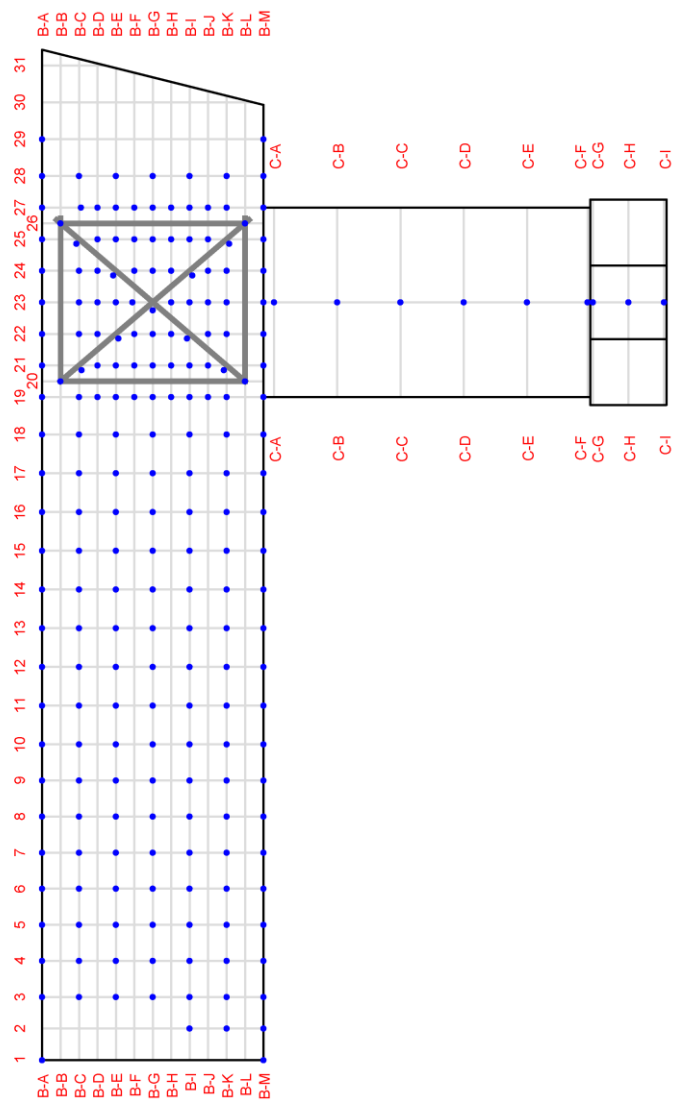


Figure 4.3. General LED Marker Naming – Phase 1.

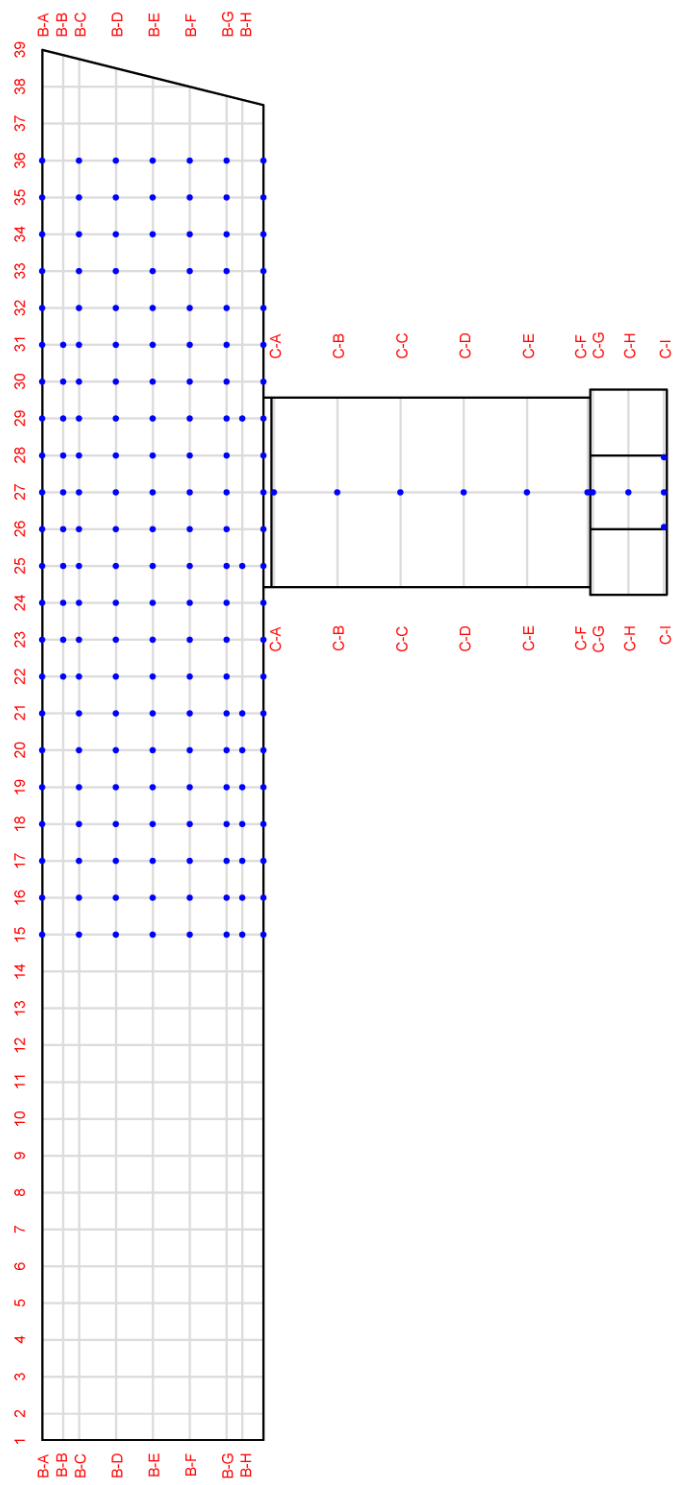


Figure 4.4. General LED Marker Naming – Phase 2.

4.3. Data Comparison

To validate the data collected with the Optotrak system, the displacements were compared to measurements from traditional methods as discussed in the following section.

At several locations along the bent cap and column, LED markers were attached close to the location of string potentiometers. The proximity allowed for the comparison of the measured displacements. Figure 4.5 and Figure 4.6 show a comparison of the vertical and horizontal displacements measured with the Optotrak and vertical/horizontal string pots during the application of Pattern A (Bridge Demands). The Optotrak data has been smoothed to remove noise using a robust local regression method using weighted linear least squares with a second-degree polynomial model.

It is important to note that due to the ability of the test setup to rotate about the rocker foundation, the vertical and horizontal displacements measured include vertical and horizontal components of the specimen rotation. This issue is illustrated in Figure 4.7. The initial vertical position of the point on the bent cap (shown in red) is indicated by Y_i . As the bent cap specimen is loaded there is deformation of the bent cap, opening or closing of the cap-column connection joint, and rotation of the test setup. As demonstrated with exaggerated deformation and rotation, the final vertical position of the point on the bent cap as measured with a string pot measurement is indicated by Y_{f_sp} and the actual vertical position is indicated by Y_{f_act} . The change in vertical position as measured with string pots does not necessarily correspond to pure Y-displacement. This issue also holds true for X-displacement measurements.

Under Pattern A, the rotation of the test setup is minimal due to locking the square end of the beams in displacement control with the HT actuator. As a result, displacement

values were similar for the Optotrak and string pots. As the deformation of the beam and column increases, such as during Patterns B-E when the square end of the beam was not locked in displacement control, the vertical and horizontal displacement values diverge. An example of this divergence is shown in Figure 4.8 by comparing the vertical displacement as measured by a string pot and a LED marker at the location highlighted in green in Figure 4.7. The close vertical and horizontal displacements under the Pattern A loading and similar displacement trends throughout the test data validate the use of the Optotrak system data for use in demonstrating additional data analysis and measurement of experimental behavior.

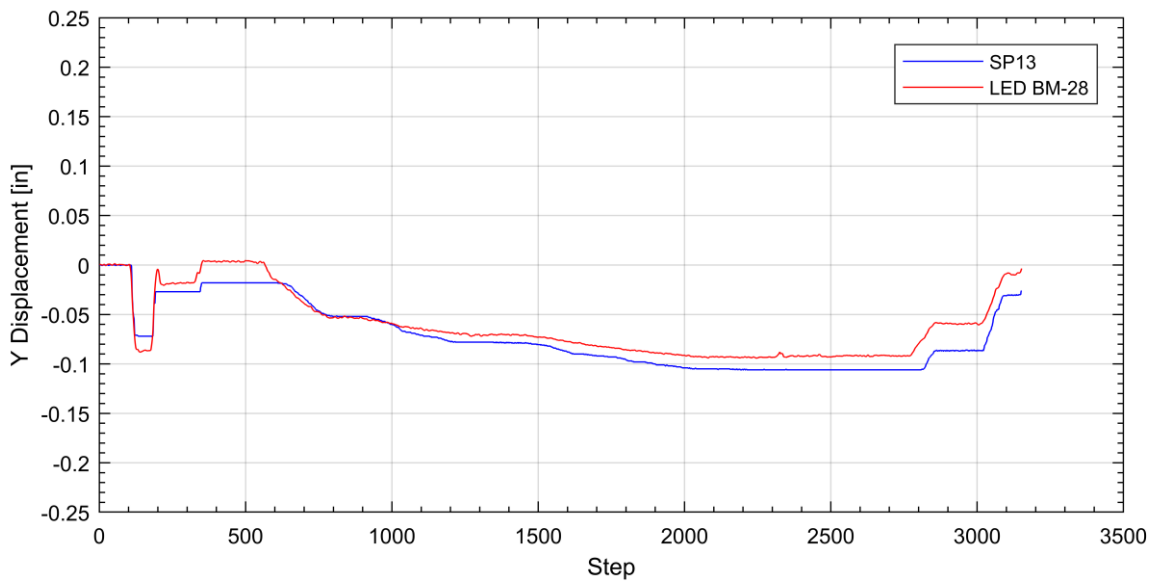


Figure 4.5. Comparison of Vertical Displacement Measured by String Pot 13 and LED Marker BM-28 During Pattern A for PSV-16-12.

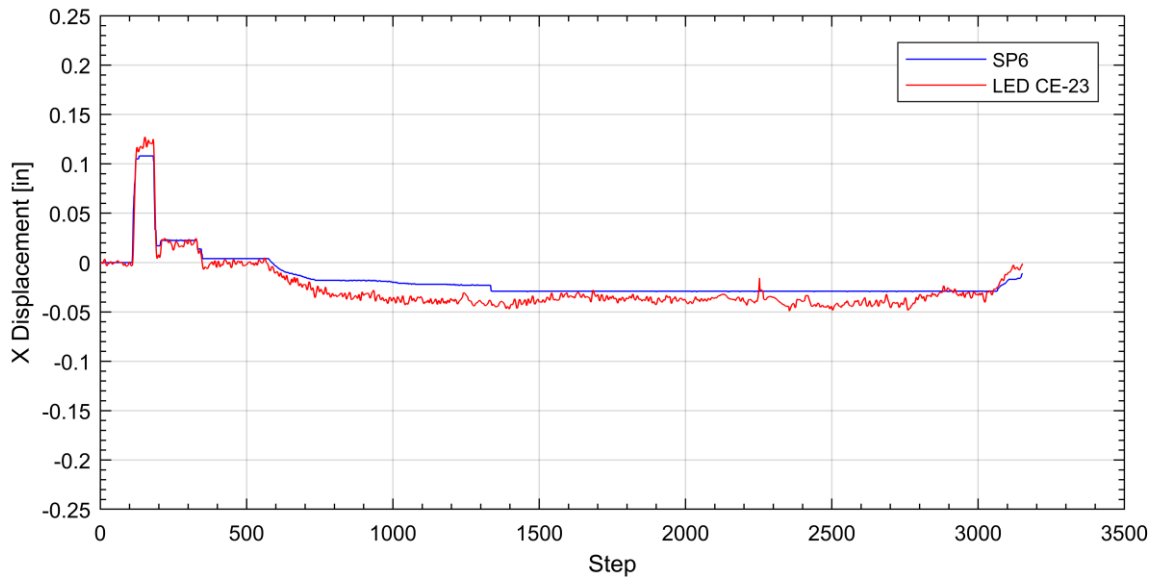


Figure 4.6. Comparison of Horizontal Displacement Measured by String Pot 6 and LED Marker CE-23 During Pattern A for PSV-16-12.

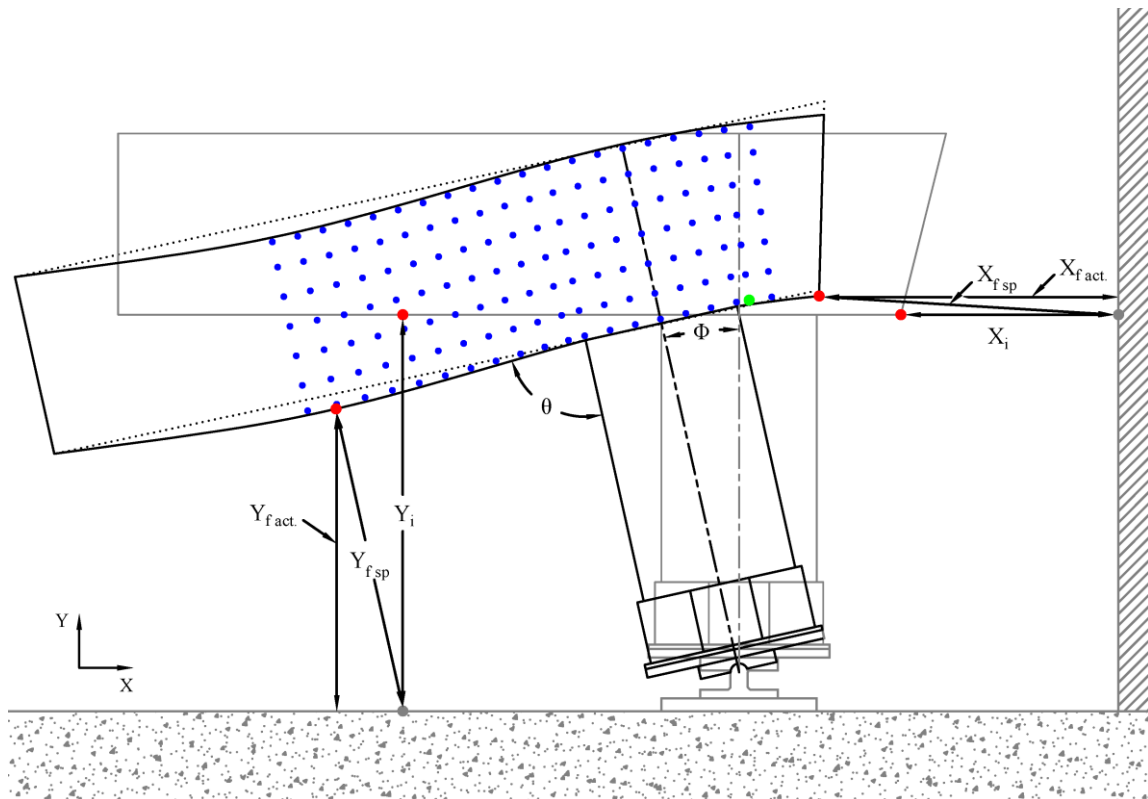


Figure 4.7. Demonstration of Specimen Rotation Influence on Vertical and Horizontal Displacement Measurements.

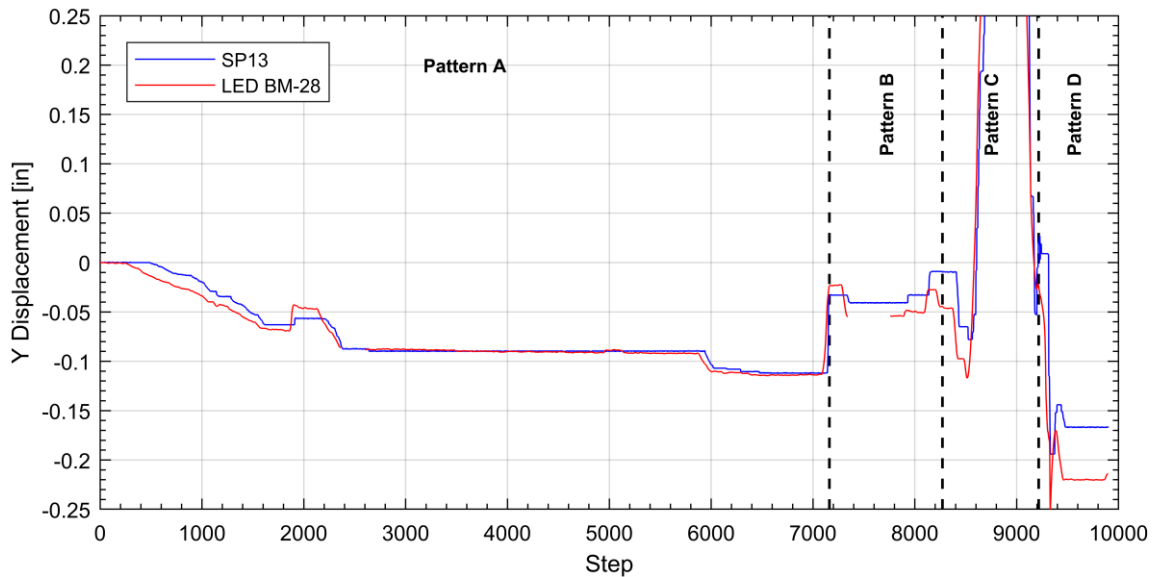


Figure 4.8. Comparison of Vertical Displacement Measured by String Pot 13 and LED Marker BM-28 During Pattern A to Pattern D for PSS-16-12. (Note: LED BM-28 Shown in Green in Figure 4.7)

4.4. Analysis of Experimental Data

To provide insight on the behavior of the pretensioned bent cap specimens, the Optotrak displacement data was analyzed. The following sections provide details on the methods used to analyze the data and present a discussion of the results of the analysis.

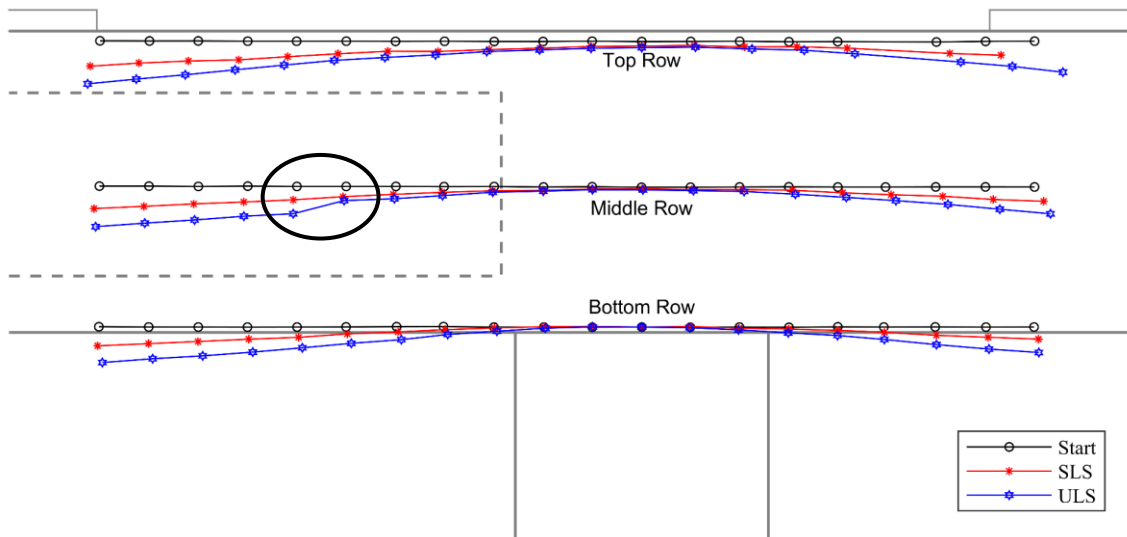
4.4.1. Deformed Shape

The deformed shapes of the bent caps were plotted to observe and compare the response and behavior of the specimens. Exaggerated vertical and horizontal displacements of rows and columns of LED markers were plotted for key loading points during the load patterns.

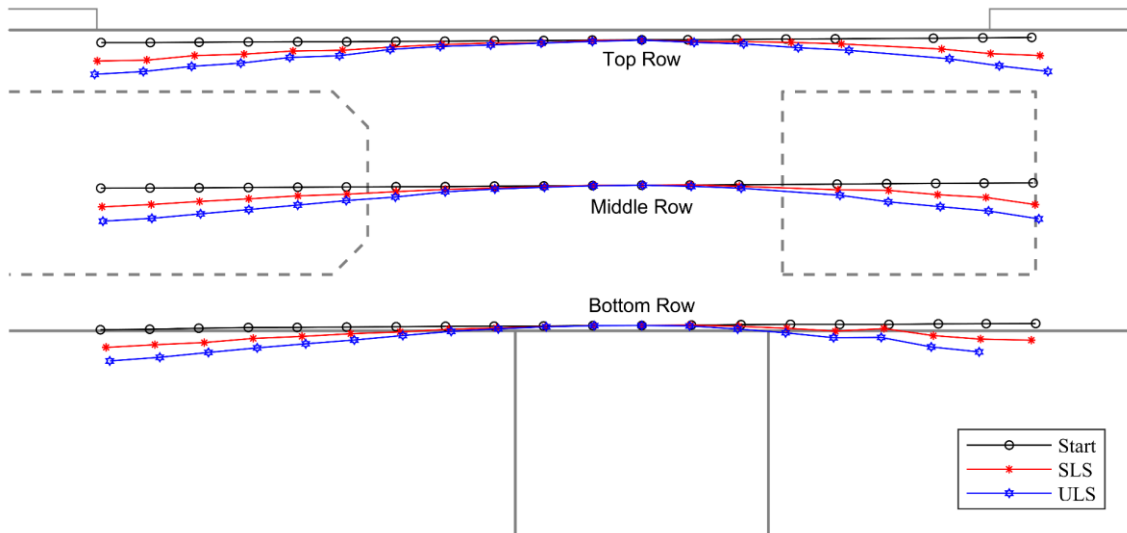
The deformed shapes of PSV-28A and PSV-28B during Pattern A demands, as displayed with rows of LED markers, are shown in Figure 4.9. Only the bottom, middle, and top row of LED markers are shown. To isolate the response of the bent caps from the

entire test setup, the displacements were normalized to a constant origin LED marker (BM-27, located at the base of the bent cap at centerline of the column) and global rotations were removed based on the rotation of the column of LED markers associated with the origin. The deformed shapes shown in Figure 4.9 match the expected deformed shape for the Pattern A load case. In the joint region, there is little vertical deformation shown. The overhang region of the bent caps shows slightly larger deformations than the locations equal distances from the face of the column in the span region. The circled region in Figure 4.9 highlights an area of significant deformation relative to adjacent LED markers for PSV-28A at ULS. The corresponding LED markers were located on either side of the shear crack that formed between SLS and ULS loads.

Figure 4.10 shows the deformation with vertical columns of LED markers under ULS demands. For clarity of the figure, not every LED marker column was included. The deformations displayed in these figures are representative of the behavior of ‘plane sections’. At the start of loading, the LED marker columns appear initially linear. At ULS demands, the deformation of the LED marker columns resemble the expected curvature response of the beams. In the joint region, there is little curvature shown. In the overhang and span region, the curvature increases as the location of the LED marker columns increases from the column centerline. The deformed shapes of the LED marker columns are significantly less linear than the initial shape. This is especially highlighted in regions where there is an interior void. This observation indicates that the ‘plane sections remain plane’ assumption may not be valid for predicting the behavior of bent caps.

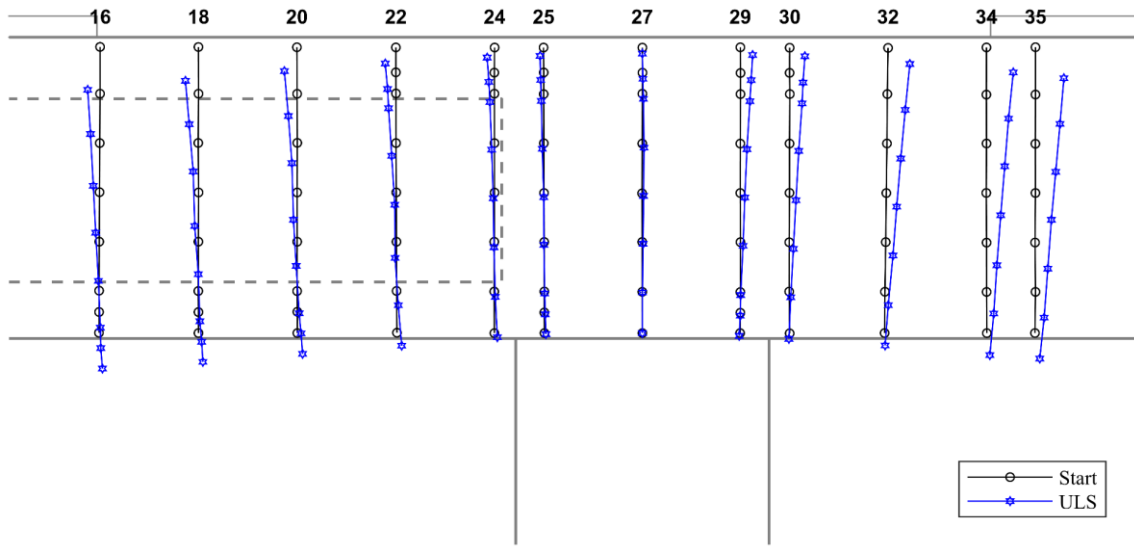


(a) PSV-28A

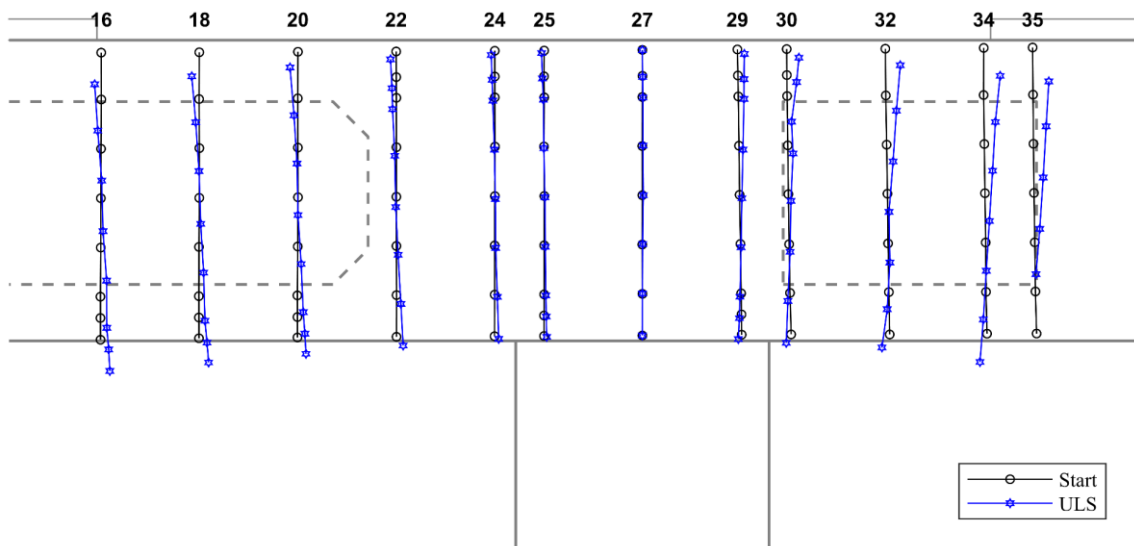


(b) PSV-28B

Figure 4.9. Comparison of Deformation of LED Marker Rows under Pattern A (SLS & ULS) Demands for PSV-28A & PSV-28B (deformation exaggerated x100).



(a) PSV-28A

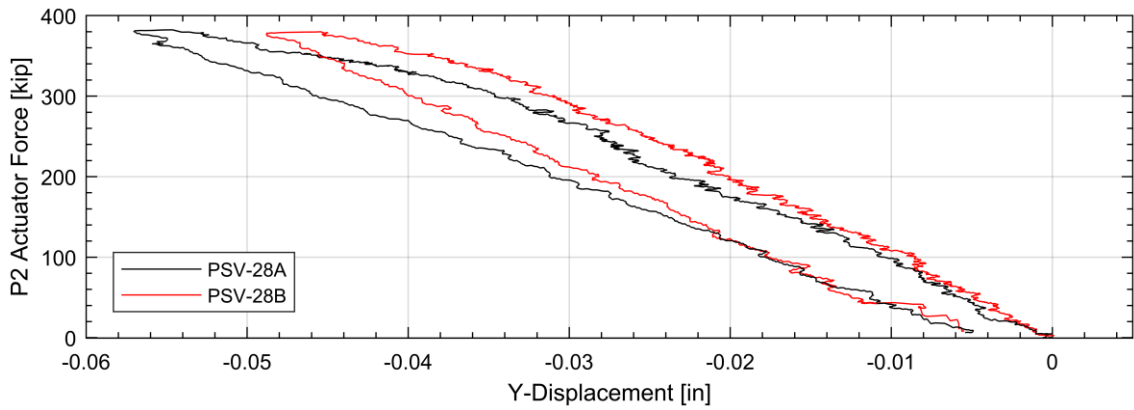


(b) PSV-28B

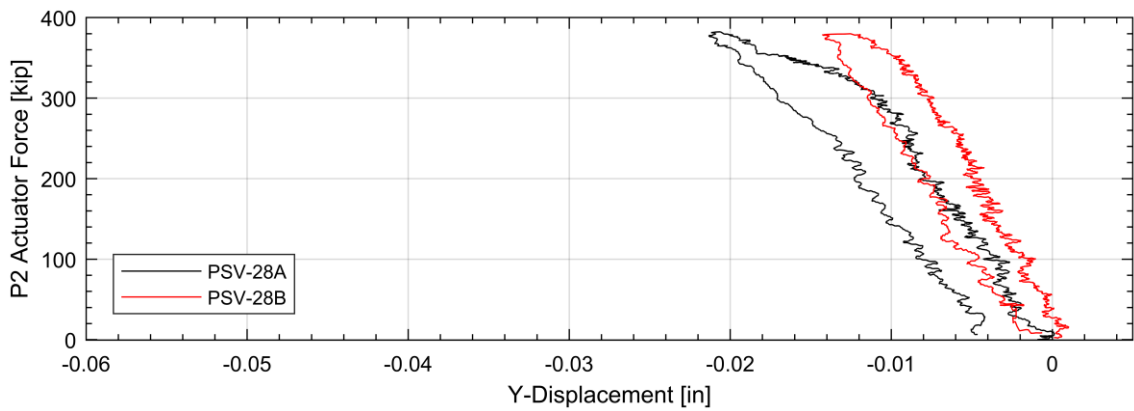
Figure 4.10. Comparison of Deformation of LED Marker Columns under Pattern A ULS Demands for PSV-28A & PSV-28B (deformation exaggerated x100).

When comparing the deformed shapes of PSV-28A and PSV-28B, differences in curvature of the bent cap appears to associate with the presence of the interior voids. To highlight this observation, vertical displacement versus applied load at key locations along

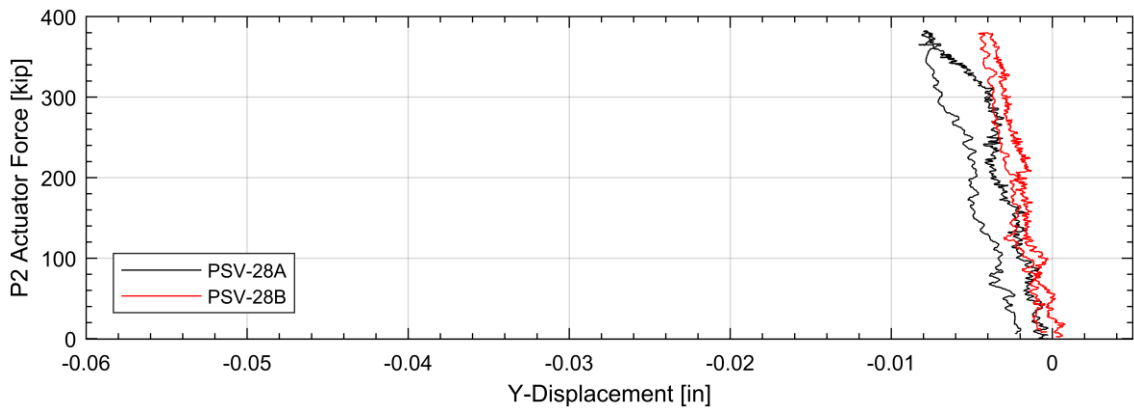
the bent caps was plotted as shown in Figure 4.11 and Figure 4.12. Figure 4.11 compares the displacement of the bent caps in the span region at the furthest point from the face of the column, the location corresponding to the start of the interior void in PSV-28B, and at the location corresponding to the start of the interior void in PSV-28A. Figure 4.12 compares the displacement of the bent caps in the overhang region at the start of the interior void in PSV-28B and at the furthest location from the face of the column. The LED marker columns are labeled in Figure 4.10. In the span region, the interior void extended to 2-in. from the face of the column in PSV-28A and $D/2$ (21-in.) from the face of the column in PSV-28B. The vertical deflection was greater in PSV-28A at each of the three locations compared in the span region. It is shown that in the overhang region, the presence of an interior void correlates with an increase in the vertical deformation of the bent cap.



(a) LED Column 16

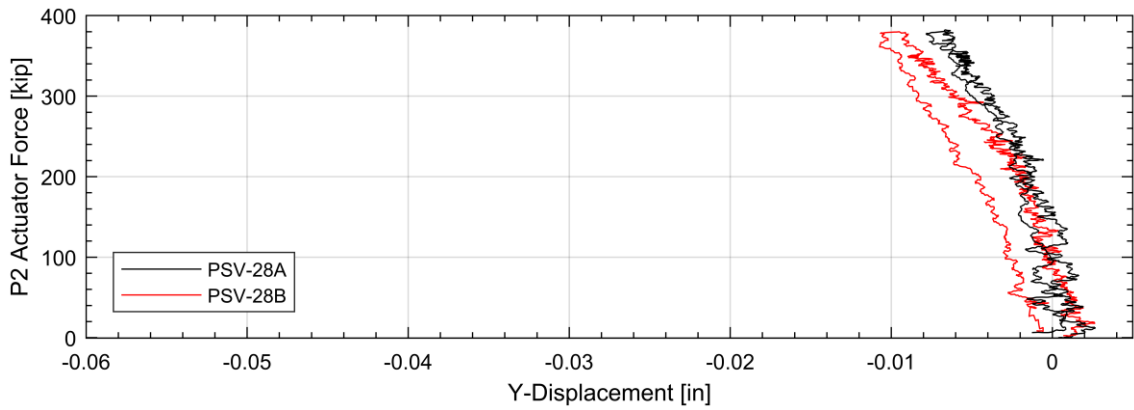


(b) LED Column 22

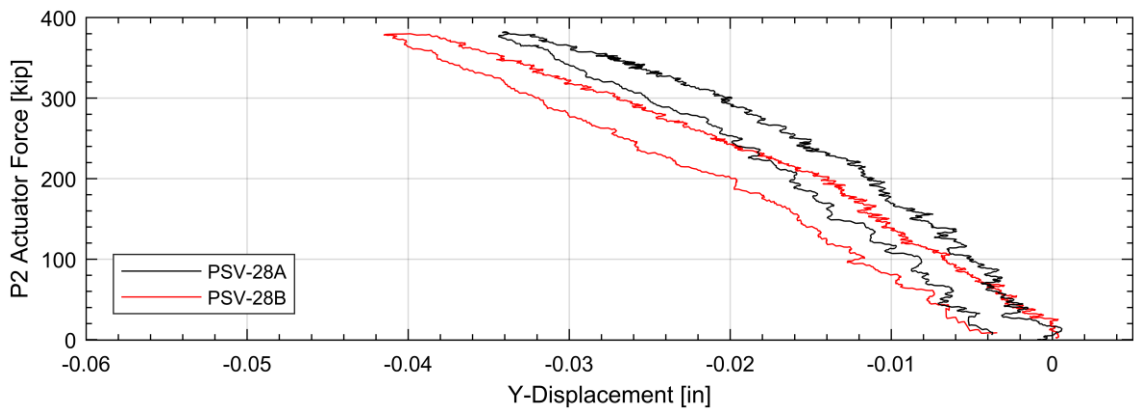


(c) LED Column 24

Figure 4.11. Vertical Displacement of the Bent Cap vs Applied Load at Key Locations along Span Region Interior Voids for PSV-28A & PSV-28B under Pattern A Demands.



(a) LED Column 30



(b) LED Column 34

Figure 4.12. Vertical Displacement of the Bent Cap vs Applied Load at Key Locations along Overhang for PSV-28A & PSV-28B under Pattern A Demands.

4.4.2. Strain Fields

Strain fields were calculated by using the grid of LED markers as a finite element mesh. LED marker displacements were used as nodal displacements of 4-node isoparametric quadrilateral elements. The displacements were used to calculate horizontal, vertical, and shear strains at the nodes of the grid layout. The finite element formulation and strain field calculations are discussed below.

The isoparametric rectangular quadrilateral element formulation allowed for the use of the non-perfect grid of LED markers. In this method, the physical layout of the LED marker grid (four-node plane element Q4) are mapped from physical space to ζ - η space which allowed for the calculation of strains, as shown in Figure 4.13. Ordinarily, the process of finite element formulation allows for the determination of nodal displacements. In this case, the nodal displacements were the measured displacements of the LED markers. The nodal coordinate vector, $\{c\}$, and the nodal displacement vector, $\{d\}$, are given as:

$$\{c\} = [x_1 \quad y_1 \quad x_2 \quad y_2 \quad x_3 \quad y_3 \quad x_4 \quad y_4]^T \quad \text{Eq. 4-5}$$

$$\{d\} = [u_1 \quad v_1 \quad u_2 \quad v_2 \quad u_3 \quad v_3 \quad u_4 \quad v_4]^T \quad \text{Eq. 4-6}$$

where x_i, y_i are the physical coordinates and u_i, v_i are the physical horizontal and vertical displacements of the LED marker.

These are mapped to ζ - η space with the following shape functions:

$$[N] = \begin{bmatrix} N_1 & 0 & N_2 & 0 & N_3 & 0 & N_4 & 0 \\ 0 & N_1 & 0 & N_2 & 0 & N_3 & 0 & N_4 \end{bmatrix} \quad \text{Eq. 4-7a}$$

$$\begin{aligned} N_1 &= \frac{1}{4}(1 - \zeta)(1 - \eta) & N_2 &= \frac{1}{4}(1 + \zeta)(1 - \eta) \\ N_3 &= \frac{1}{4}(1 + \zeta)(1 + \eta) & N_4 &= \frac{1}{4}(1 - \zeta)(1 + \eta) \end{aligned} \quad \text{Eq. 4-7b}$$

The relationship of unknown nodal strain values is provided as:

$$\begin{Bmatrix} \varepsilon_x \\ \varepsilon_x \\ 2\varepsilon_{xy} \end{Bmatrix} = \begin{Bmatrix} \varepsilon_x \\ \varepsilon_x \\ \gamma_{xy} \end{Bmatrix} = \begin{Bmatrix} \frac{\partial u}{\partial x} \\ \frac{\partial v}{\partial y} \\ \frac{\partial u}{\partial y} + \frac{\partial v}{\partial x} \end{Bmatrix} = \begin{bmatrix} 1 & 0 & 0 & 0 \\ 0 & 0 & 0 & 1 \\ 0 & 1 & 1 & 0 \end{bmatrix} \begin{Bmatrix} u_{,x} \\ u_{,y} \\ v_{,x} \\ v_{,y} \end{Bmatrix} \quad \text{Eq. 4-8}$$

where,

$$\begin{Bmatrix} u_{,x} \\ u_{,y} \\ v_{,x} \\ v_{,y} \end{Bmatrix} = \begin{bmatrix} [J]^{-1} & [0]_{2 \times 2} \\ [0]_{2 \times 2} & [J]^{-1} \end{bmatrix} \begin{Bmatrix} u_{,\zeta} \\ u_{,\eta} \\ v_{,\zeta} \\ v_{,\eta} \end{Bmatrix} \quad \text{Eq. 4-9}$$

and,

$$[J] = [N] \begin{bmatrix} u_1 & v_1 \\ u_2 & v_2 \\ u_3 & v_3 \\ u_4 & v_4 \end{bmatrix} \quad \text{Eq. 4-10}$$

$$\begin{Bmatrix} u_{,\zeta} \\ u_{,\eta} \\ v_{,\zeta} \\ v_{,\eta} \end{Bmatrix} = \begin{bmatrix} N_{1,\zeta} & 0 & N_{2,\zeta} & 0 & N_{3,\zeta} & 0 & N_{4,\zeta} & 0 \\ N_{1,\eta} & 0 & N_{2,\eta} & 0 & N_{3,\eta} & 0 & N_{4,\eta} & 0 \\ 0 & N_{1,\zeta} & 0 & N_{2,\zeta} & 0 & N_{3,\zeta} & 0 & N_{4,\zeta} \\ 0 & N_{1,\eta} & 0 & N_{2,\eta} & 0 & N_{3,\eta} & 0 & N_{4,\eta} \end{bmatrix} \{d\}_{8 \times 1} \quad \text{Eq. 4-11}$$

Prestressed concrete has an initial axial compressive strain, by nature of pretensioning. The initial horizontal strain was approximated with the following:

$$\varepsilon_{x_adjusted} = \varepsilon_{x_calc} + \varepsilon_{x_initial} \quad \text{Eq. 4-12}$$

where ε_{x_calc} is ε_x calculated from Eq. 4-8, and $\varepsilon_{x_initial}$ is approximated by the following:

$$\varepsilon_{x_initial} = \frac{F}{A_g * E_C} \quad \text{Eq. 4-13}$$

where F = the prestressing force, after losses; A_g = gross cross-sectional area; E_c = measured 28-day modulus of elasticity of concrete. For both PSV-28A and PSV-28B, $\varepsilon_{x_initial}$ was approximated to be 143 microstrain.

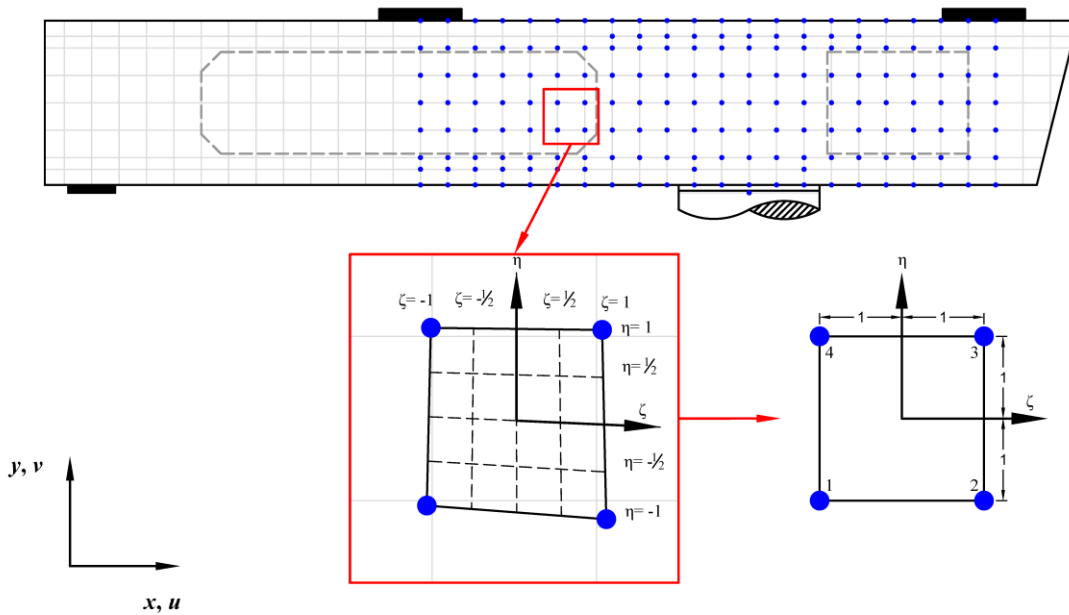


Figure 4.13. General Transformation for Mapping LED Markers from Physical Space to ζ - η Space for Isoparametric Quadrilateral (Q4) Formulation.

Principal strains were calculated using the nodal strains ε_x , ε_y , ε_{xy} , and Mohr's circle:

$$\varepsilon_1 = \frac{(\varepsilon_x + \varepsilon_y)}{2} + \sqrt{\left(\frac{(\varepsilon_x - \varepsilon_y)}{2}\right)^2 + \varepsilon_{xy}^2} \quad \text{Eq. 4-14a}$$

$$\varepsilon_2 = \frac{(\varepsilon_x + \varepsilon_y)}{2} - \sqrt{\left(\frac{(\varepsilon_x - \varepsilon_y)}{2}\right)^2 + \varepsilon_{xy}^2} \quad \text{Eq. 4-14b}$$

$$\gamma_{max} = \sqrt{\left(\frac{(\varepsilon_x - \varepsilon_y)}{2}\right)^2 + \varepsilon_{xy}^2} \quad \text{Eq. 4-14c}$$

The strains calculated for each node are influenced by the relative displacement of the other three nodes in the element. Since the LED markers acted as the nodes for 1 to 4 elements, up to four unique strains were calculated at an LED marker. When this data was plotted with a 2-D interpolating fill function, the strain fields appeared jagged, as shown in Figure 4.14. The strain fields were smoothed by averaging the elementwise nodal strains associated with each LED marker over the tributary area surrounding the node in the elements. The smoothed strain field is shown in Figure 4.15b.

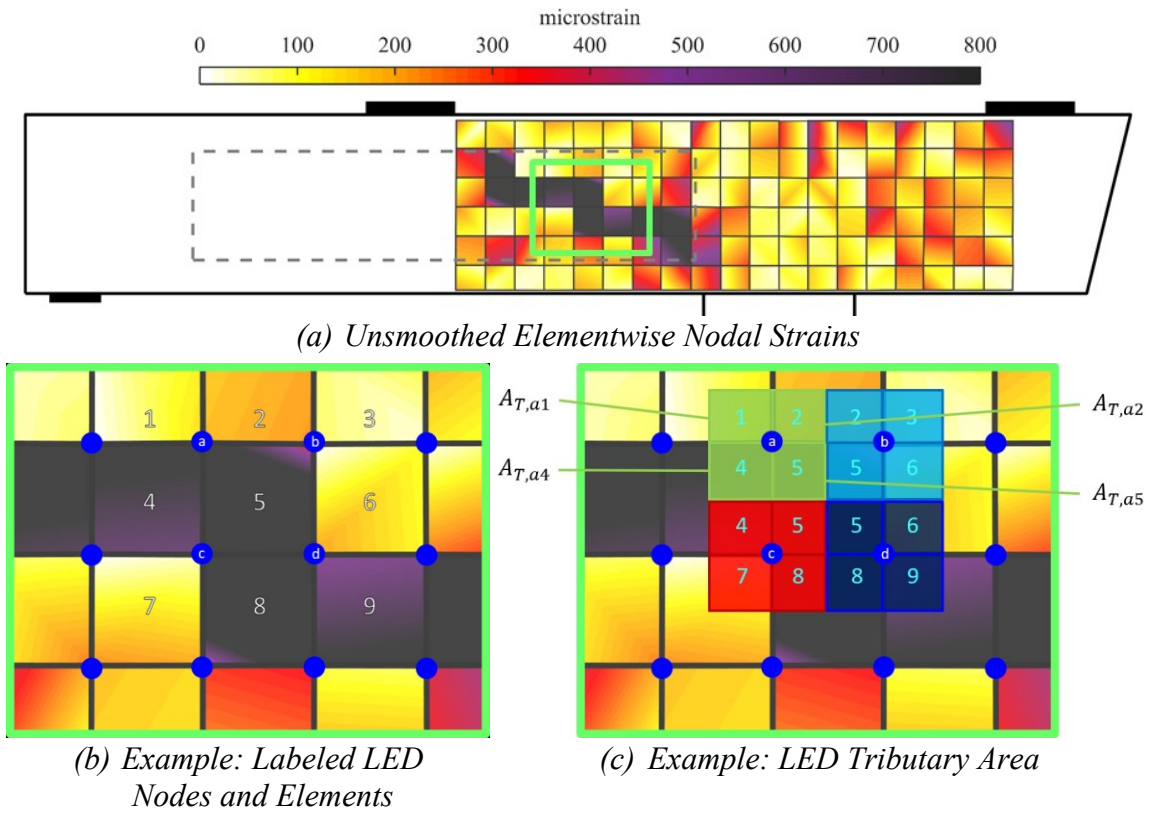


Figure 4.14. Smoothing Elementwise Nodal Strains based on LED Tributary Area.

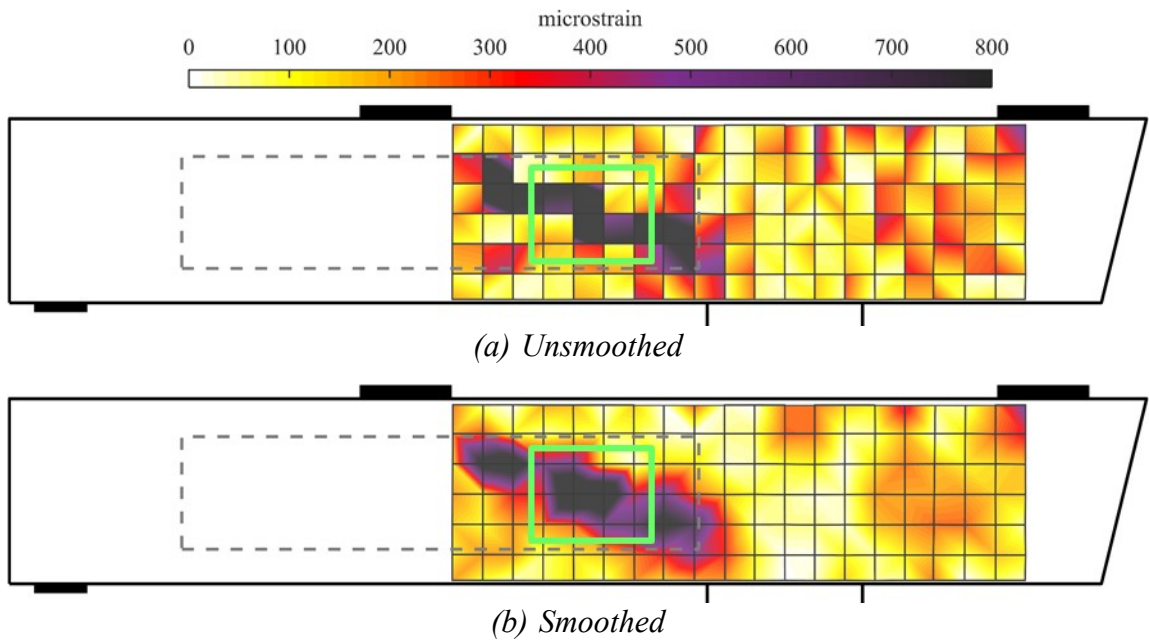


Figure 4.15. Comparison of Unsmoothed and Smoothed Shear (γ_{xy}) Strain Fields.

Smoothed strain fields were plotted for the key points of Pattern A demands for Phase 2 specimens. Figure 4.16 and Figure 4.17 show the horizontal, vertical, and shear strain fields for PSV-28A and PSV-28B for Pattern A ULS demands. The legend above the strain field plots indicate the corresponding strain value for each color. The upper and lower bound limits of the plots were chosen to allow for the visual indication of expected damage based on the strain fields.

These figures show that the strain fields correspond with the expected response of the bent caps. In the negative bending are, the horizontal strain fields show tensile strain at the top of the beam and compressive strain at the bottom of the beam. The transition from tensile (red) to compressive (blue) strain is indicated with a white fill color and relates to the location of the neutral axis. The horizontal strain fields show that for the design ULS demands, the neutral axis of the bent caps remains at just below $D/2$ through the negative bending joint region.

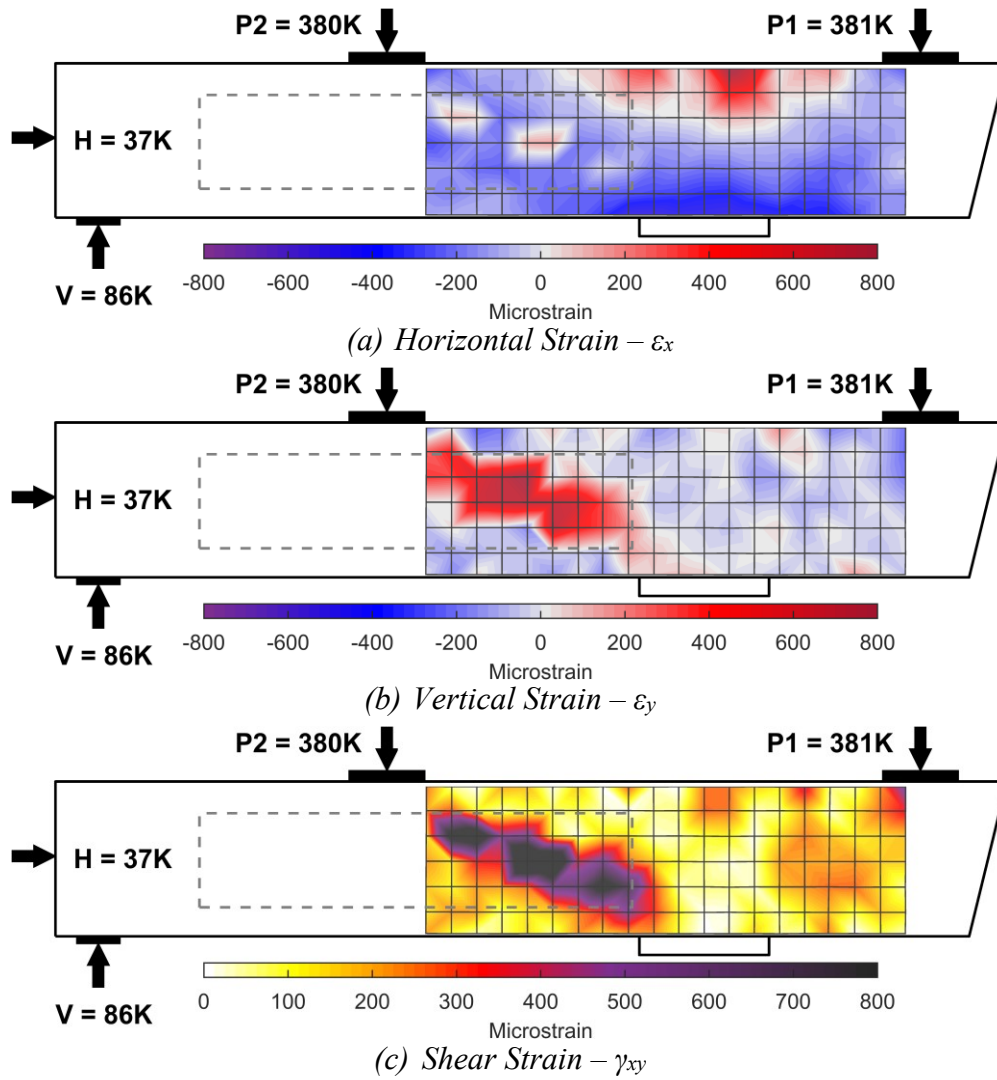


Figure 4.16. Horizontal, Vertical, & Shear Strain Fields (ϵ_x , ϵ_y , & γ_{xy}) under Pattern A ULS Demands for PSV-28A.

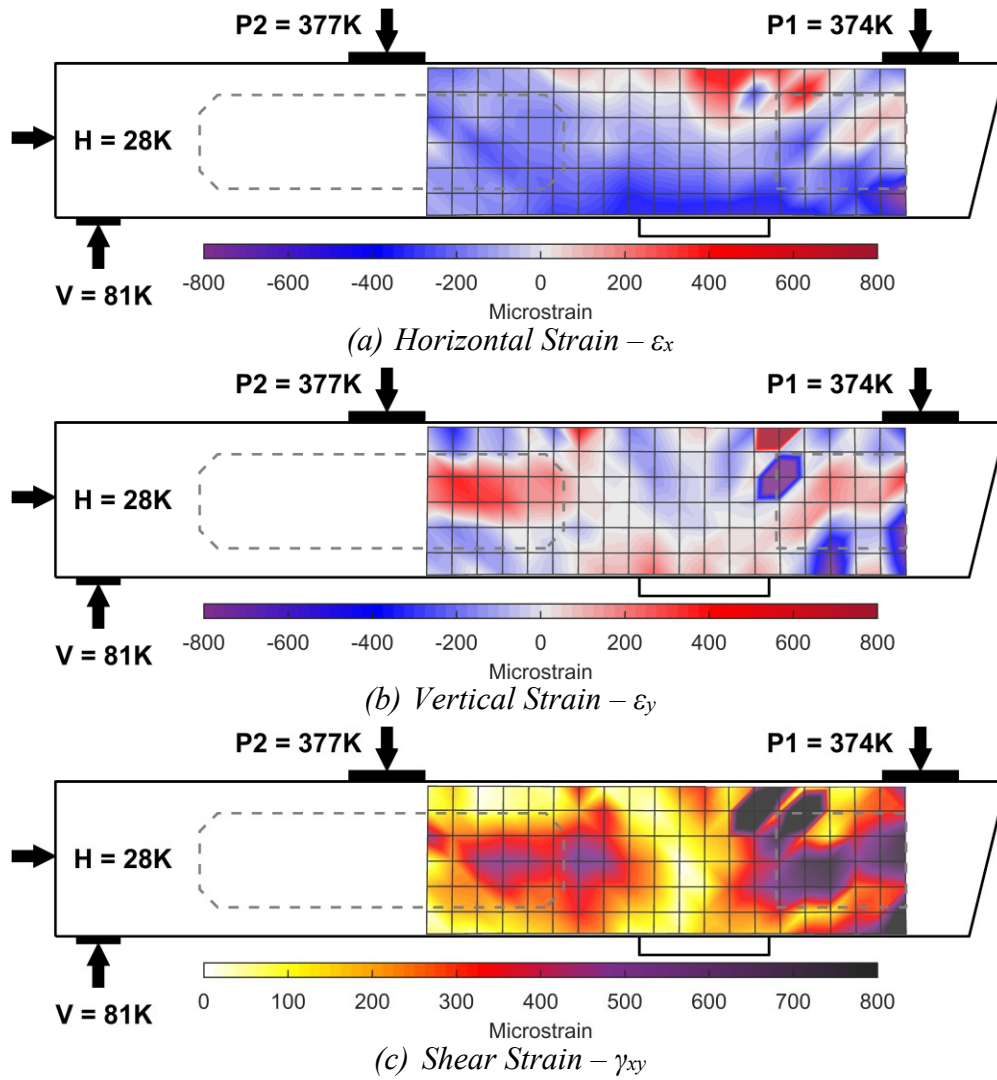


Figure 4.17. Horizontal, Vertical, & Shear Strain Fields (ϵ_x , ϵ_y , & γ_{xy}) under Pattern A ULS Demands for PSV-28B.

To gain insight on how the interaction of horizontal, vertical, and shear strain influence the overall behavior of the bent caps, the principal strain fields were plotted. Figure 4.18 and Figure 4.19 show these strains for Pattern A ULS demands. The principal strain fields isolate the principal tensile, compressive, and shear strains. Observing the locations of high principal tensile strain fields points to locations on the bent caps that may be expected to crack. Using the expected $(7.5\sqrt{f'_c})$ and measured tensile strength of concrete for Phase 2 specimens, the range of tensile strain which may correspond to cracking is 169-234 microstrain. Figure 4.18 and Figure 4.19 show that there is a concentration of tensile strains at the top of the beams in the negative bending region. This is consistent with the location of the higher horizontal strains in Figure 4.16 and Figure 4.17. It is also shown that there is a concentration of tensile strain along the interior voids, which is consistent with the location of the high vertical and shear strain components.

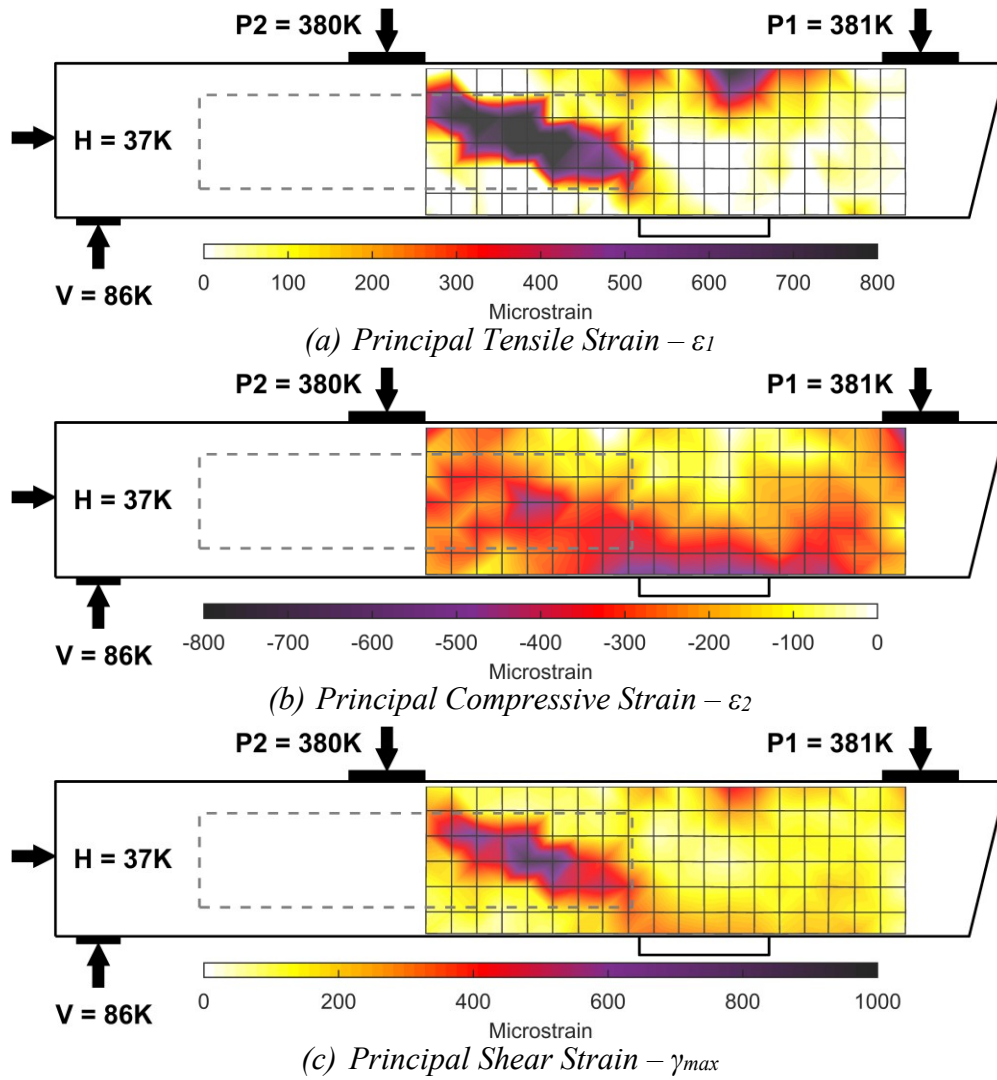


Figure 4.18. Principal Tensile, Compressive, & Shear Strain Fields (ϵ_1 , ϵ_2 , & γ_{max}) under Pattern A ULS Demands for PSV-28A.

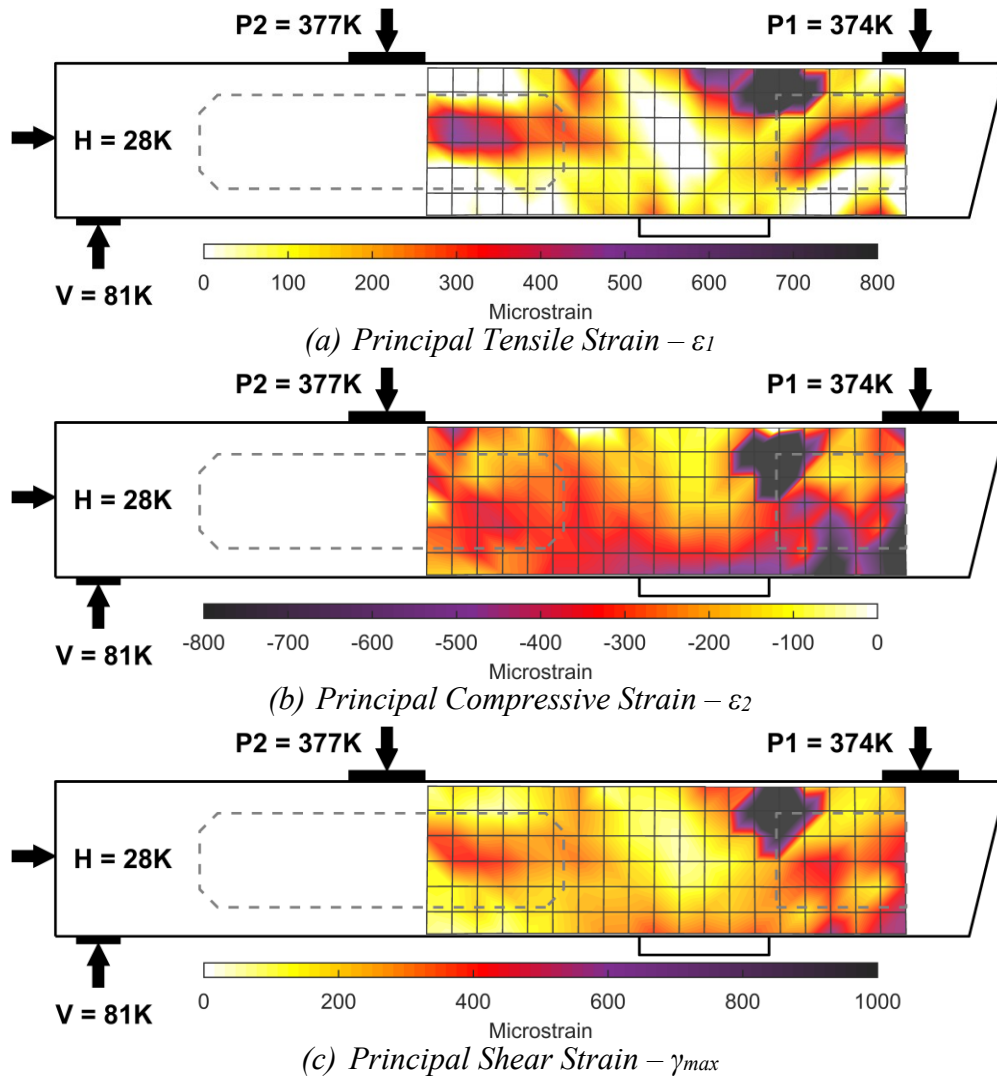


Figure 4.19. Principal Tensile, Compressive, & Shear Strain Fields (ϵ_1 , ϵ_2 , & γ_{max}) under Pattern A ULS Demands for PSV-28B.

Assessment of the strains in the bent caps provide insight to the distribution of stresses and the relationship to observed damage. Comparison of the strain fields for each specimen provides insight to the effectiveness of design variables such as interior void detailing. In this Thesis, the clean data available from the full test program is the Phase 2 tests at SLS and ULS demands. At these load levels, strain fields can provide insight to initial crack location and orientation. Thus, principal tensile strains are presented and discussed in the following discussion.

One of the observed differences in the impact of interior void detailing of PSV-28A and PSV-28B was the angle of shear crack formation, and the direction in which it propagated. Figure 4.20 and Figure 4.21 compare the observed crack damage to the principal tensile strain field plots of PSV-28A and PSV-28B under Pattern A SLS and ULS loading. It is noted that the areas of high tensile strain, as indicated with the darker colors in the figures, correspond to the locations where cracks formed. This is especially seen under ULS demands, when much of the initial cracking was first observed.

The shear crack that formed in the void region of PSV-28A followed the steep angle from the P2 actuator to the face of the column, passing through the corner of the interior void. This is also shown in the strain fields plot. The crack that formed in PSV-28B appeared to be shallower and did not travel towards the corner of the void under ULS demands. This was also indicated in the strain field plots. The locations where flexural cracks formed in the negative moment region correspond with areas of higher tensile strains in both bent caps. It is noted, however, that in areas where high tensile strains did not correspond with observed cracks under ULS loads, these locations had

crack damage observed under increased demands in future load cases. For PSV-28B, Pattern A ULS demands were applied to the bent cap twice, on separate testing days. Prior to applying the second instance of ULS loads, the voided overhang region remained uncracked. After the second application of ULS loads, the voided overhang had cracked. Figure 4.22 shows the principal tensile strain fields for PSV-28B compared to the observed crack damage for both instances of Pattern A ULS loads. Unfortunately, due to issues with continuity of Optotrak displacement data between subsequent days of experimental testing, the strain fields from both Pattern A ULS instances cannot be directly compared. Figure 4.22 shows the correlation of high tensile strains to areas of future crack formation. The damage observed during the second instance of ULS demands is the damage that was documented for the ULS load case in Section 3.5.2.

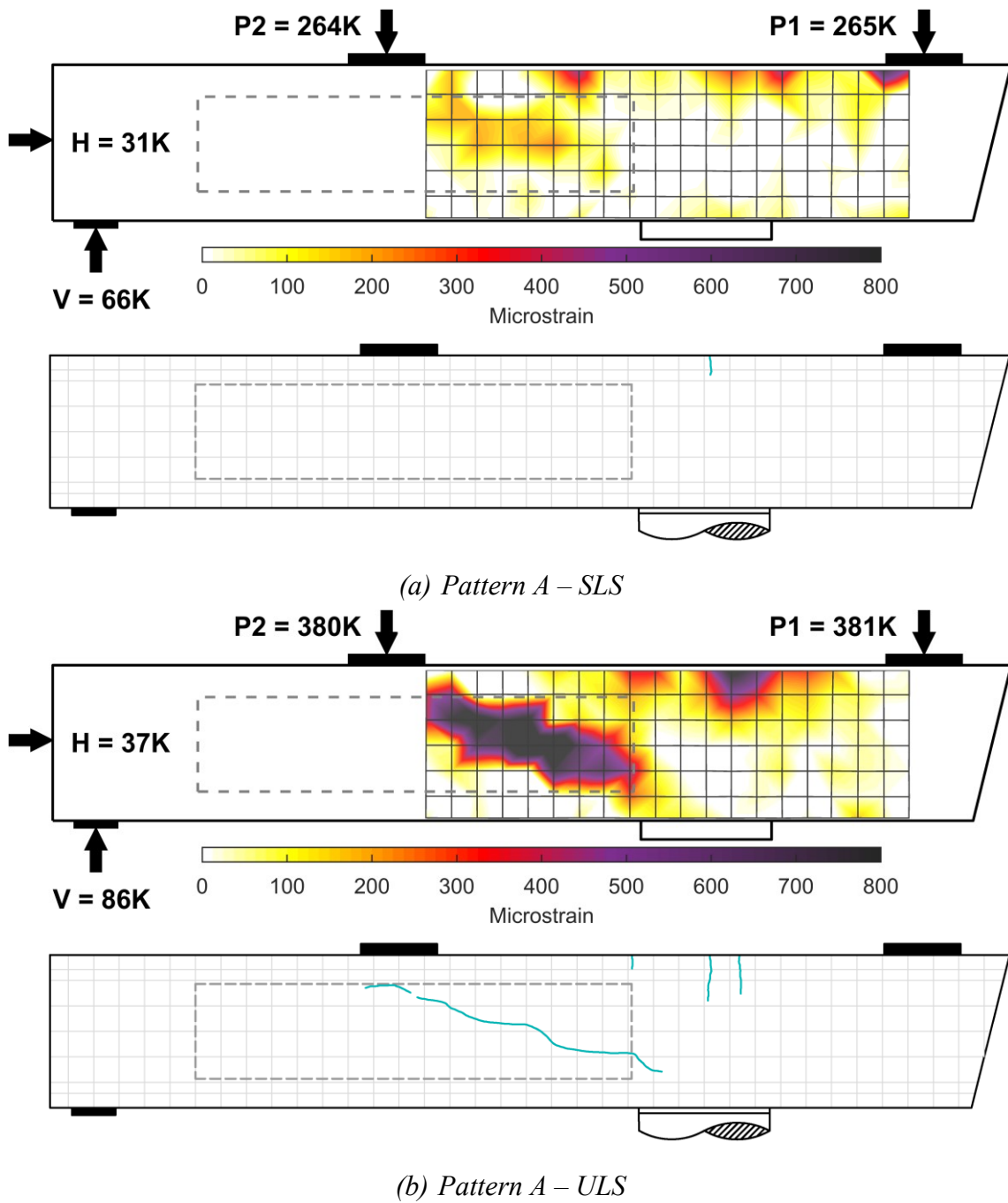
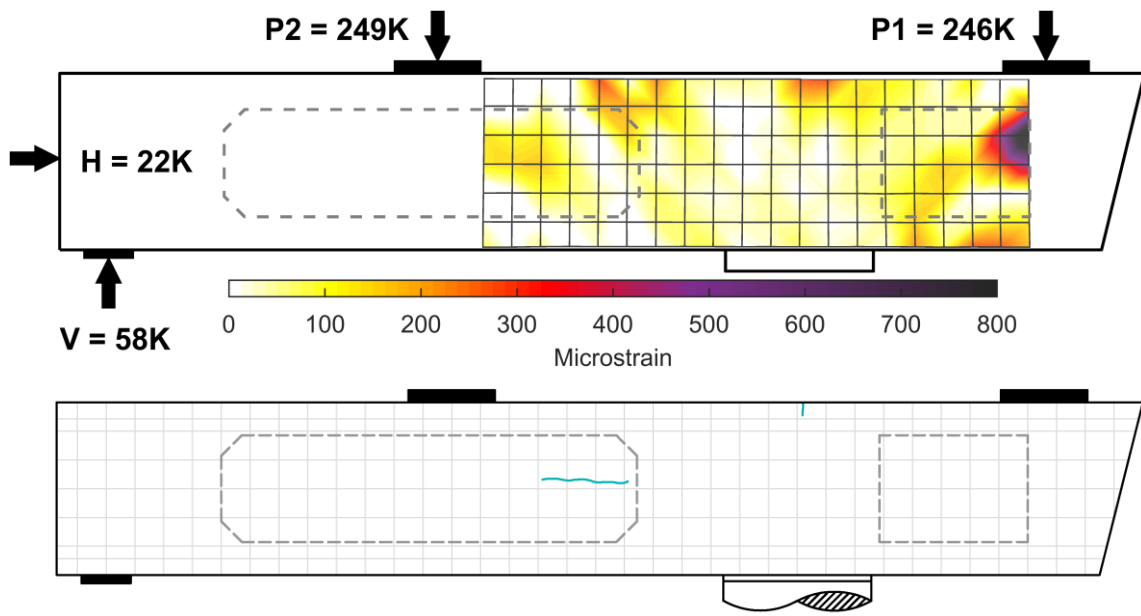
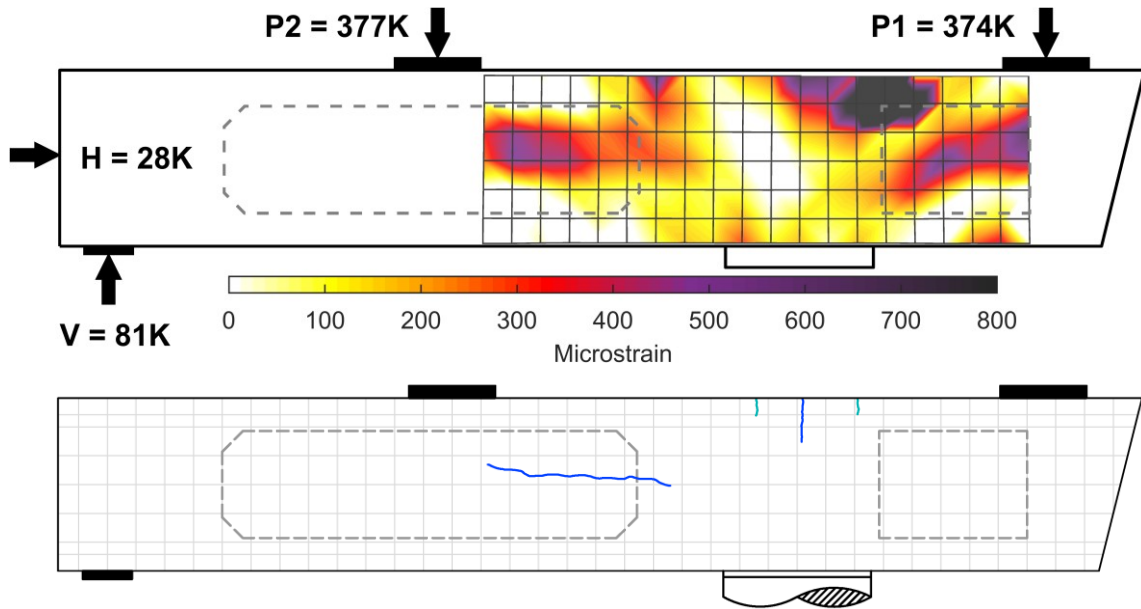


Figure 4.20. Comparison of Principal Tensile Strains and Observed Damage under Pattern A Demands for PSV-28A.

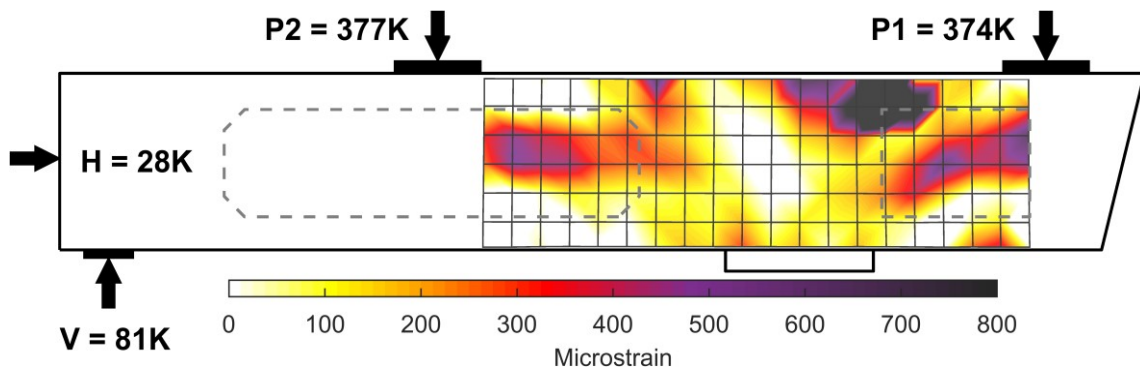


(a) Pattern A – SLS

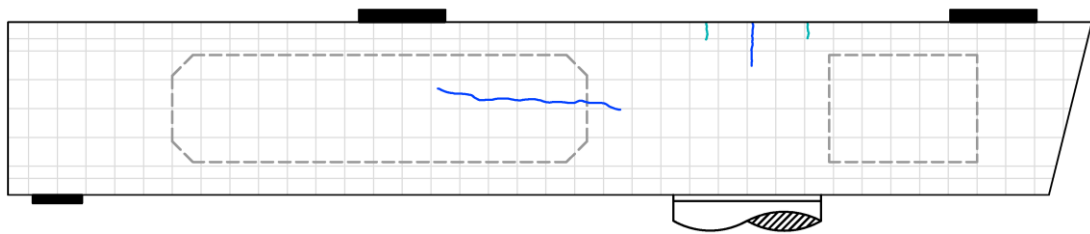


(b) Pattern A – ULS

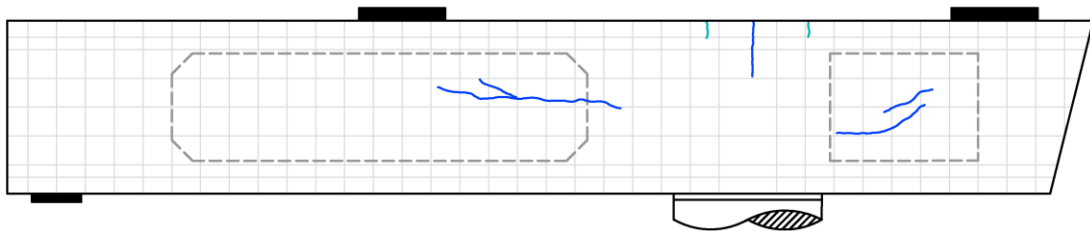
Figure 4.21. Comparison of Principal Tensile Strains and Observed Damage under Pattern A Demands for PSV-28B.



(a) 1st Instance of ULS Demands – Principal Tensile Strain Fields



(b) 1st Instance of ULS Demands – Observed Damage

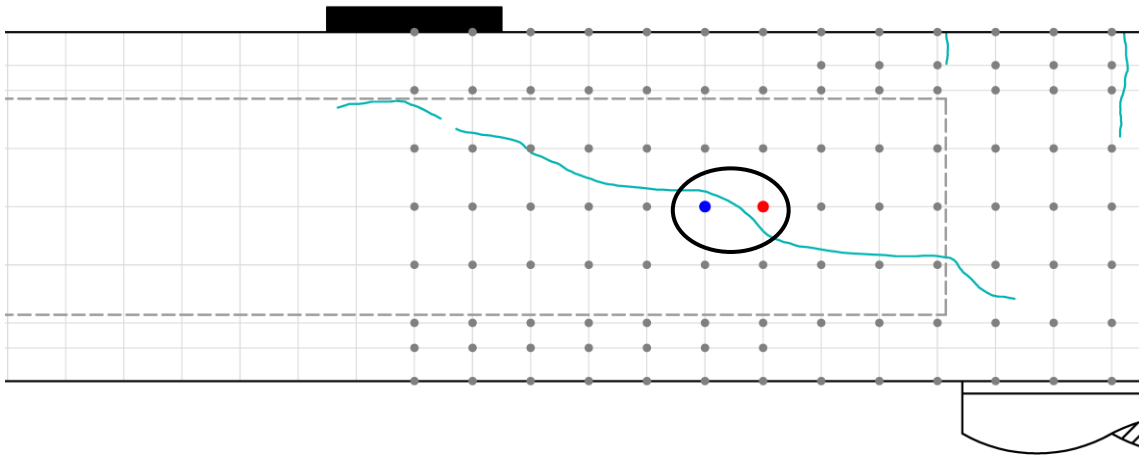


(c) 2nd Instance of ULS Demands – Observed Damage

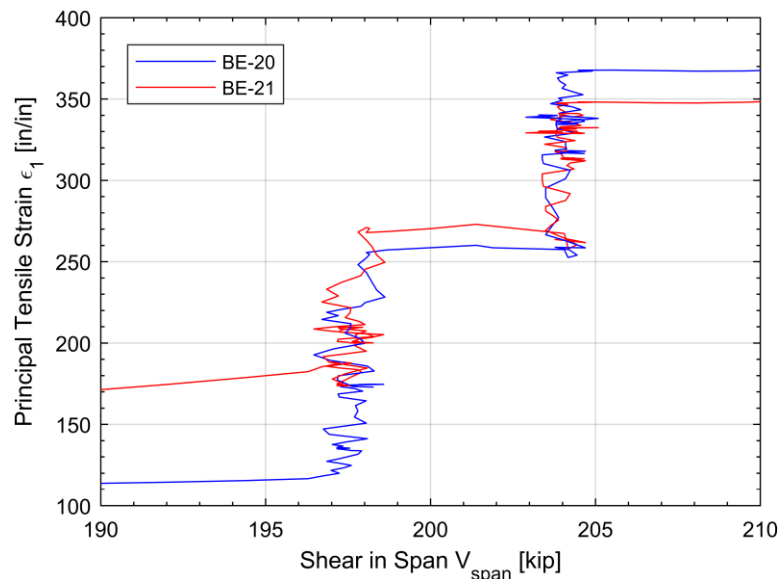
Figure 4.22. Comparison of Principal Tensile Strains and Observed Damage for PSV-28B for Both Applications of Pattern A ULS Demands.

In an effort to capture the behavior of the voided span regions of the bent caps during Pattern A (bridge demands) loading, the principal tensile strain for nodes near the location of shear cracks was plotted versus the applied shear demand in the span region (V_{span}), shown in Figure 4.23. Figure 4.23a shows the location of the LED markers plotted

in Figure 4.23b. It is noted that there appears to be significant creep of strain during times of sustained loading.



(a) Location of LED Markers in Relation to the Shear Crack Observed Between SLS and ULS Demands



(b) Principal Tensile Strain vs Applied Shear V_{span}

Figure 4.23. Principal Tensile Strain versus Applied Shear Demand at Nodes Adjacent to Observed Shear Cracks in the Voided Span Region of PSV-28A During Pattern A Loading.

4.5. Summary and Discussion of Data Analysis

This section summarizes and discusses the results of post-processing the raw experimental data, comparing the displacement measurements to traditionally collected measurements, and analyzing the experimental data collected with the Optotrak motion capture system.

4.5.1. *Post-Processing*

Post-processing of the experimental data collected with the Optotrak system was essential to permit any analysis. Optotrak data was consistently collected at the slowest possible rate (1 Hz). However, the data collected with the data acquisition unit (DAQ) was collected at a rate of 0.5 Hz for the majority of the testing and was slowed to 0.2 Hz during times of sustained loading. In addition, the starting points of the data collection for the Optotrak and DAQ varied. To adequately correlate the Optotrak data to the DAQ data, synchronization processes were necessary.

Transforming the initial arbitrary Optotrak global coordinate system to a coordinate system related to the orientation of the experimental test setup proved beneficial in providing comparisons of Optotrak measurements to traditional measurements and in simplifying the analysis of the behavior of the bent caps. The spatial coordinates of the Optotrak LED markers with the bent caps in the original position at the start of the first day of experimental was assumed as the reference point for determining displacements. The plane created by the bottom and top rows and the outermost columns of LED markers on the bent caps was assumed to be perfectly aligned with the X-Y plane for the purpose of the coordinate system transformation. The furthest LED marker from

the origin of rotation for each specimen showed little deviation from the assumed X-Y plane.

4.5.2. *Data Comparison*

To provide confidence in the data collected with the Optotrak motion capture system, the Optotrak displacements were compared to those measured with string potentiometers.

Under load patterns that produced small displacements and small rotations of the experimental test setup, Optotrak displacements matched closely to string pot measurements. As load testing continued and the bent cap specimens increasingly deformed, the X and Y displacements measured by the two methods diverged. This was attributed to a systematic limitation of accurately measuring vertical and horizontal displacements of a rotating body with string potentiometers. While the displacement values differed between the Optotrak and the string pots, the overall trends and patterns of the displacements matched for all the load patterns.

4.5.3. *Analysis of Experimental Data*

Measurements collected using the Optotrak motion capture system were shown to provide useful insight on the behavior of the bent caps under simulated bridge demands and the impact of the different interior void details.

Plotting the deformation of LED marker rows showed that the deformed shape of the bent caps matched with the expected behavior. Minimal vertical displacement was seen in the bent cap joint region at SLS and ULS loads, and the expected vertical displacement was seen in the span region and overhang. The displacement was larger in

the overhang regions than in the span regions. Comparing the vertical displacement of the bent caps at specific locations along the overhang region showed that the inclusion of an interior void corresponded with an increase in deflection.

Plotting the deformation of LED marker columns was related to the curvature behavior of the bent caps. The initial linearity of LED marker columns represented a plane section. Under ULS loading, the deformed LED marker columns no longer remained completely linear. Inclusion of an interior void and the interior void details appeared to influence the curvature behavior of the beam. These observations bring into question the applicability of the ‘plane sections remain plane’ assumption made during design.

Strain fields calculated from isoparametric quadrilateral element formulation using the LED marker displacements allowed for further comparison of the experimental behavior to the expected behavior of the bent caps. Horizontal strain fields matched the expected behavior of the negative bending region by showing tension at the top of the bent cap and compression at the bottom. The transition from tensile strain to compressive strain in the bent cap joint region can be correlated with the neutral axis.

Comparing principal tensile strain fields to the observed damage showed a correlation of locations with a higher concentration of principal tensile strain to areas that cracked. It was observed that not every location showing a higher concentration of principal tensile strains corresponded with cracks. It was noted that, especially in the case of the voided overhang in PSV-28B, locations remaining uncracked while displaying a higher concentration of principal tensile strains often cracked in subsequent applications of the same load pattern.

5. SUMMARY, CONCLUSIONS, AND RECCOMENDATIONS

5.1. Summary

The development of precast bridge substructures is an instrumental step to further the advancement and use of accelerated bridge construction techniques. Part of this advancement includes the development of precast, pretensioned bent caps. These precast, pretensioned bent caps are similar to other prestressed bridge elements in that they offer the ability for more rapid, economical, and safer construction.

The advantages from utilizing pretensioned concrete over traditional reinforced concrete allows for the construction of longer span bent caps with equal, or greater, performance. However, the construction of precast bent caps can bring forward issues related to transportation and placement. Such issues can be mitigated by including internal voids during fabrication. To implement the use of pretensioned bent caps in the State of Texas, experimental testing is necessary to understand the behavior and performance results.

The research presented in this Thesis was a subset of a Texas Department of Transportation (TxDOT) sponsored research program conducted to aid in the development of standard precast, pretensioned concrete bent cap designs for use in everyday bridges. Six full-scale experimental tests of bent cap sub-assemblages of TxDOT standard bridge designs were tested under realistic load cases. Sub-assemblages included one reinforced concrete, two solid pretensioned, and three voided pretensioned bent caps. Test specimens included design variables such as inclusion of interior voids, varied shear reinforcement detailing, increased pretensioning, longer overhangs, and different interior void details.

The objective of the research presented in this Thesis was to validate the Optotrak Certus motion capture system as a method of measuring the experimental performance of pretensioned concrete bent caps. Measurements made with traditional and non-contact systems were compared to assess the ability of the non-traditional measurements to aid in the better understanding of bent cap behavior. In addition, the influence of different design variables, including the use of interior voids and detailing options, on the overall performance of the bent caps was investigated.

A review of previous literature related to the history of concrete bent caps in the State of Texas, previous experimental research conducted on reinforced concrete and prestressed concrete bent caps, previous research related to cap-to-column connections for precast bent caps, the use of voids in concrete bridge elements, and the use of motion capture systems to measure the experimental performance of concrete structures.

An overview of the experimental test program was presented, including the construction of test specimens, instrumentation, collection and quantification of material properties, and results of experimental testing.

This research presented the analysis of experimental data collected with the Optotrak Certus motion capture system. The details and discussion of the methods and results of necessary post-processing of raw data, validation of Optotrak data by comparison with string potentiometers, and the analysis of the Optotrak data were presented.

5.2. Conclusions

This section presents the key conclusions for validating the Optotrak Certus motion capture system as a method for measuring the experimental performance of pretensioned concrete bent caps, for the influence of interior voids with different details on overall bent cap performance, and for the impact of overhang geometry on the performance.

5.2.1. Optotrak Certus Motion Capture System Measurement

The following conclusions are presented for validating the Optotrak Certus motion capture system as a method for measuring the experimental performance of pretensioned concrete bent caps:

1. The Optotrak Certus motion capture system was able to repeatably measure the small displacements experienced by the bent cap specimens under simulated bridge demands.
2. The displacements measured with the Optotrak and string potentiometers matched closely under loading conditions which produced minimal deformation and rotation of the experimental test setup, validating the Optotrak data for use in further data analysis.
3. The displacements measured with the Optotrak can provide an accurate measure of the deformation of the bent caps during load patterns which produced significant deformation of the specimen and significant rotation of the test setup. It was shown that there are probable limitations with using string potentiometers to measure vertical and horizontal displacements in applications with potential for significant rigid body rotation.

4. Displacements measured with the Optotrak can be used to analyze deformation behavior. Deformed shapes produced by the Optotrak displacements matched the expected and observed deformation shapes. Differences in deformation behavior was shown at locations of internal discontinuities, at rigid support conditions, in cracked regions, and at locations of varied sectional detailing.
5. Data collected with the Optotrak can be used to assess the validity of the design assumption that 'plane sections remain plane'. The linearity of vertical columns of Optotrak LED markers did not remain constant under the application of simulated bridge demands. This was especially highlighted in regions with internal discontinuities such as interior voids.
6. Displacements measured with the Optotrak can be used to calculate strain fields by relating the displacements of a regular grid of LED markers to isoparametric quadrilateral finite element formulation. Horizontal, vertical, and shear strain fields in the negative bending region showed tension at the top of the bent cap and compression at the bottom under simulated bridge demands. This is consistent with the expected behavior of a beam in negative bending.
7. Strain fields can be used to observe the influence of the applied demands on concentration of strains at internal discontinuities, support conditions, and damaged regions.
8. Principal strain fields can be used to locate areas that could be expected to crack. Areas of higher concentration of principal tensile strain fields correlate to observed crack damage.

5.2.2. Interior Void Details

The following conclusions are presented for the influence of interior void details on the experimental performance of pretensioned concrete bent caps:

1. Differences in interior void geometry were not shown to affect the onset of initial shear cracking, based solely on the observation of cracking.
2. The different detailing appeared to influence the orientation and extent of shear cracking under simulated bridge demands. PSV-28A displayed a steeper initial shear crack that followed the square interior void diagonally from top of the void beneath the P2 actuator to the lower corner of the void, located 2-in. from the face of the column. PSV-28B displayed a shallower initial shear crack that formed near mid-depth of the hollow section beneath the P2 actuator and remained nearly horizontal under simulated bridge demands. The location, orientation, and relative magnitude of the concentration of principal tensile strain at the location of the shear cracks in PSV-28A and PSV-28B correspond with the observed damage.
3. Regions with interior voids experienced greater vertical deformation than regions without interior voids. This is shown by comparing the vertical deflection of the solid and voided overhang in PSV-28A and PSV-28B. Comparing vertical deflection in the span region of PSV-28A and PSV-28B shows that the deflection at the start of the interior void 2-in. from the face of the column of PSV-28A is greater than the deflection of the solid section at the same location of PSV-28B.

4. At loads beyond expected bridge demands, the influence of the interior void details is less apparent. Newly formed cracks appeared at similar angles in both PSV-28A and PSV-28B. Cracks were oriented along the diagonal from the P2 actuator to the face of the column.
5. The chamfered interior void details in PSV-28B appear to reduce, relative to the square detail in PSV-28A, the effects of strains concentration at the void corners. While magnitudes of strain concentrations at the corners of both void details were similar, the chamfered corner in PSV-28B appeared to delay the onset of cracking compared to PSV-28A. Flexure cracks formed at the corner of the interior voids for both bent caps. However, the flexure crack was observed at ULS demands in PSV-28A and at 140% ULS demands in PSV-28B.

5.2.3. *Overhang Geometry*

The following conclusions are presented for the influence of overhang geometry on the experimental performance of pretensioned concrete bent caps:

1. The longer, solid overhang of PSV-28A resulted in similar performance to that of the shorter overhang of Phase 1 pretensioned specimens under ULS demands. Under 140% ULS demands, the longer overhang exhibited flexure shear cracking extending outside of the joint region that was not present within the Phase 1 specimens.
2. Inclusion of an interior void in the overhang region of PSV-28B negatively affected the performance of the bent cap. Under ULS demands, shear cracking was observed along the interior void of the overhang of PSV-28B; this cracking

did not occur in either the short or long solid overhang. At 140% ULS demands the voided overhang displayed significant shear cracking, with the extent of the cracks reaching to the end of the bent cap. Failure of both PSV-28A and PSV-28B occurred in the negative bending region with spalling of the concrete in the compression zone, with a more abrupt failure of PSV-28B due to additional spalling of concrete along the compression strut along the voided overhang from the P1 actuator to the face of the column.

5.3. Recommendations

Based on the research presented in this Thesis, the following recommendations are made for utilizing motion capture systems to measure the experimental performance of pretensioned concrete bent caps.

1. To ensure the continuity of test data, conduct uninterrupted experimental testing.
2. To simplify correlation of measurement data to loading, start data acquisition of all measurement instruments simultaneously and ensure that the sampling rate is the same.
3. Orient the position sensor appropriately to limit out-of-plane measurement. If using multiple position sensors, use a symmetric placement (in relation to orientation with the desired spatial coordinate system).

5.4. Areas of Future Work

The objectives of the research presented in this Thesis were to validate the Optotrak Certus motion capture system as a method of measuring the experimental performance of pretensioned concrete bent caps and to provide insight on the applicability

of different methods to analyze the bent cap behavior using the Optotrak data. Future work is necessary to fully realize the potential of using the Optotrak data to quantify the influence of the design variables on the overall performance of the bent caps. The following areas of necessary future work are presented:

1. Quantify and incorporate initial strains induced from fabrication, pretensioning, and curing into the analysis to provide an absolute measure of the strain behavior during loading.
2. Expand the breadth of analysis to include load patterns beyond the expected design bridge demands to provide a complete understanding of the behavior of pretensioned bent caps including joint shear deformation during joint opening & closing tests and strains leading up to failure. This includes diagnosing issues associated with the continuity of measurement data for subsequent days of testing.
3. Expand the breadth of analysis to include all six bent cap specimens, for complete comparison of the influence of design variables.
4. Utilize the knowledge learned to identify shortcomings of current design practices and recommendations.
5. Utilize the experimental behavior to validate numerical models to enable exploration of a greater number of design variables.

REFERENCES

- AASHTO Guide Specifications for LRFD Seismic Bridge Design, 1st edition (2009).
Washington, D.C. American Association of State Highway and Transportation
Officials.
- AASHTO LRFD Bridge Design Specifications, 7th edition (2014). Washington, D.C.
American Association of State Highway and Transportation Officials.
- ACI Committee 318 (2014). "Building Code Requirements for Structural Concrete
(ACI 318-14) and Commentary of Building Code Requirements for Structural
Concrete (ACI 318R-14). American Concrete Institute.
- ASTM Standard C31/C31M (2015). "Standard Practice for Making and Curing
Concrete Test Specimens in the Field" ASTM International, West
Conshohocken, PA.
- ASTM Standard C39/C39M (2015). "Standard Test Method for Compressive Strength
of Cylindrical Concrete Specimens" ASTM International, West Conshohocken,
PA.
- ASTM Standard C78/C78M (2015). "Standard Test Method for Flexural Strength of
Concrete (Using Simple Beam with Third-Point Loading)" ASTM International,
West Conshohocken, PA.
- ASTM Standard C143/C143M (2015). "Standard Test Method for Slump of
Hydraulic-Cement Concrete" ASTM International, West Conshohocken, PA.

ASTM Standard C172/C172M (2014). "Standard Practice for Sampling Freshly Mixed Concrete" ASTM International, West Conshohocken, PA.

ASTM Standard C469/C469M (2014). "Standard Test Method for Static Modulus of Elasticity and Poisson's Ration of Concrete in Compression" ASTM International, West Conshohocken, PA.

ASTM Standard C496/C496M (2011). "Standard Test Method for Splitting Tensile Strength of Cylindrical Concrete Specimens" ASTM International, West Conshohocken, PA.

Barooah, U. R. (2016). "The Flexural Design of Pretensioned Bent Caps." *Master of Science Thesis*, Texas A&M Transportation Institute, Texas A&M University, College Station, Texas.

Bechtel, A. J. (2011). "External Strengthening of Reinforced Concrete Pier Caps." *Ph.D. Dissertation*, Georgia Institute of Technology.

Birely, A. C. (2012). "Seismic Performance of Slender Reinforced Concrete Structural Walls." *Ph.D. Dissertation*, University of Washington.

Birely, A. C., Mander, J. B., Lee, J. D., McKee, C. D., Yole, K. J., and Barooah, U. R. (2018a). "Precast, Prestressed Concrete Bent Caps: Volume 1 Preliminary Design Considerations and Experimental Test Program." *Report No.* FHWA/TX-18/0-6863-1, Texas A&M Transportation Institute, Texas A&M University, College Station, Texas. Copyright 2018 Texas A&M Transportation Institute.

- Birely, A. C., Mander, J. B., McKee, C. D., and Lee, J. D. (2018b). "Precast, Prestressed Concrete Bent Caps: Volume 2 Design Recommendations and Design Examples." *Report No. FHWA/TX-18/0-6863-2*, Texas A&M Transportation Institute, Texas A&M University, College Station, Texas. Copyright 2018 Texas A&M Transportation Institute.
- Bracci, J. M., Keating, P. B., and Hueste, M. B. D. (2000). "Cracking in RC Bent Caps," Report No. FHWA/TX-01/1851-1, Texas Transportation Institute, Texas A&M University, College Station, Texas.
- Cox, R., Hohmann, D., Eskridge, A., Hyzak, M., Freeby, G., Wolf, L., Merrill, B., and Holt, J. (2007). "Concrete Bridges in Texas," *ASPIRE*, 43-45, spring. 2007.
- Hart, C. R. (2012). "Cracking of Reinforced Concrete Structural Walls Subjected to Cyclic Loading." *Ph.D. Dissertation*, University of Illinois at Urbana-Champaign, Urbana, Illinois.
- Hawkins, N. M., and Kuchma, D. A. (2007). "Application of LRFD Bridge Design Specification to High-Strength Structural Concrete: Shear Provisions." NCHRP Report No. 579, Transportation Research Board, Washington, D.C.
- Jones, K., and Vogel, J. (2001). "New Precast Bent Cap System: Saving Texas Time and Money," TR News 212, Jan-Feb. 2001.
- Lowes, L. N., Lehman D. L., Birely, A. C., Kuchma, D. A., Hart, C. R., and Marley, K. P. (2011). "Behavior, Analysis, and Design of Complex Wall Systems: Planar Wall Test Program Summary Document." *NEESR-SG*,

University of Washington, University of Illinois at Urbana-Champaign,
University of California Los Angeles.

Lowes, L. N., Lehman D. L., Birely, A. C., Kuchma, D. A., Marley, K. P., and Hart, C. R. (2012). "Earthquake Response of Slender Planar Concrete Walls with Modern Detailing." *Engineering Structures*, 43(2012), 31-47.

Mander, J. B., Mahmoodzadegan, B., Bhadra, S., and Chen, S. S. (1996). "Seismic Evaluation of a 30-Year Old Non-Ductile Highway Bridge Pier and Its Retrofit." Report No. NCEER-96-0008, National Center for Earthquake Engineering Research, State University of New York at Buffalo, Buffalo, New York.

Matsumoto, E. E., Waggoner, M. C., Sumen, G., Kreger, M. E., Wood, S. L., and Breen, J. E. (2001). "Development of a Precast Bent Cap System." *Report No.* FHWA/TX-0-1748-2, Center for Transportation Research, University of Texas at Austin, Austin, Texas.

NDI (2011). "Optotrak Certus User Guide", 5th edition. Northern Digital Incorporated.

Ralls, M. L., Ybanez, L., and Panak, J. J. (1993). "The New Texas U-Beam Bridges: An Aesthetic and Economical Design Solution," *PCI Journal*, Sept.-Oct. 1993.

Restrepo, J. I., Tobolski, M. J., and Matsumoto, E. E. (2011). "Development of a Precast Bent Cap System for Seismic Regions." NCHRP Report No. 681, Transportation Research Board, Washington, D.C.

- Schnittker, B., and Bayrak, O. (2008). "Allowable Compressive Stress at Prestress Transfer." *Report No. FHWA/TX-09/0-5197-4*, Center for Transportation Research, University of Texas at Austin.
- Valderrama, A. R. (2011). "Pretensioned Box Beams: Prestress Transfer and Shear Behavior." *Ph.D. Dissertation*, University of Texas at Austin.
- Yole, K. J. (2017). "Experimental Performance of Reinforced and Pretensioned Precast Concrete Bent Caps." *Master of Science Thesis*, Texas A&M Transportation Institute, Texas A&M University, College Station, Texas.
- Young, B. S., Bracci, J. M., Keating, P. B., and Hueste, M. B. D. (2002). "Cracking in Reinforced Concrete Bent Caps." *ACI Structural Journal*, Vol. 99(4), 488-498.

APPENDIX A – INSTRUMENTATION PLANS



ZACHRY DEPARTMENT OF
CIVIL ENGINEERING
TEXAS A&M UNIVERSITY



Phase 1
Precast Prestensioned Bent Caps
TXDOT 0-6863

PROJECT NO: 0-6863

DATE: 28-Aug-17

VERSION: V-1

DRAWN BY: J. LEE

SCALE: N.T.S.

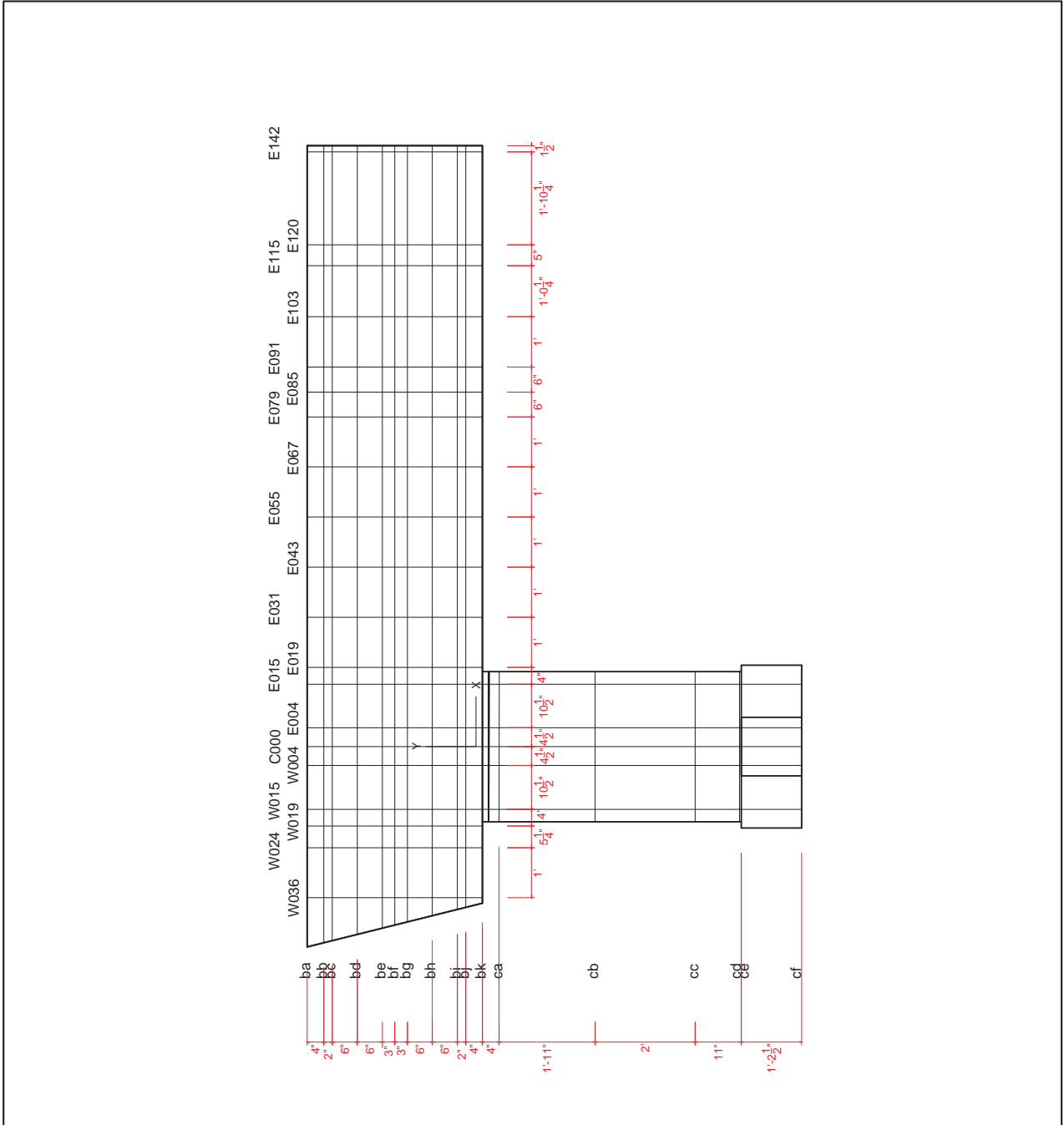
TITLE:

Phase 1
Instrumentation Plan
Grid Line

SHEET#:

1 of 11

F:\Kevin Yeibem Cap Project\Kevin Yeibem\CAD\Drawings In KY Thesis\Instrumentation 2_15_17\11x17.dwg August 28, 2017 - 4:35 PM

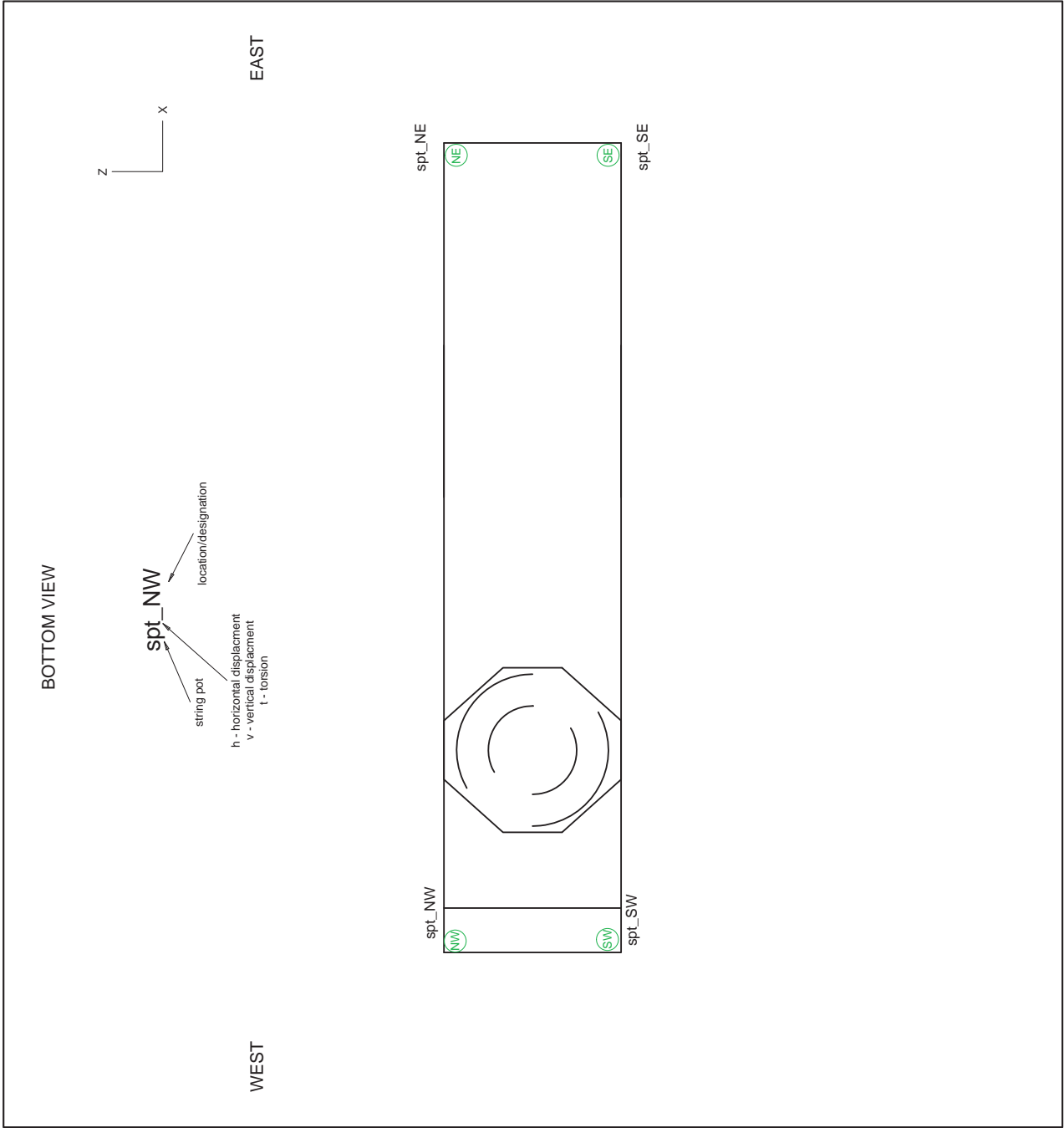






**Precast Prestensioned Bent Caps
Phase 1
TXDOT 0-6863**

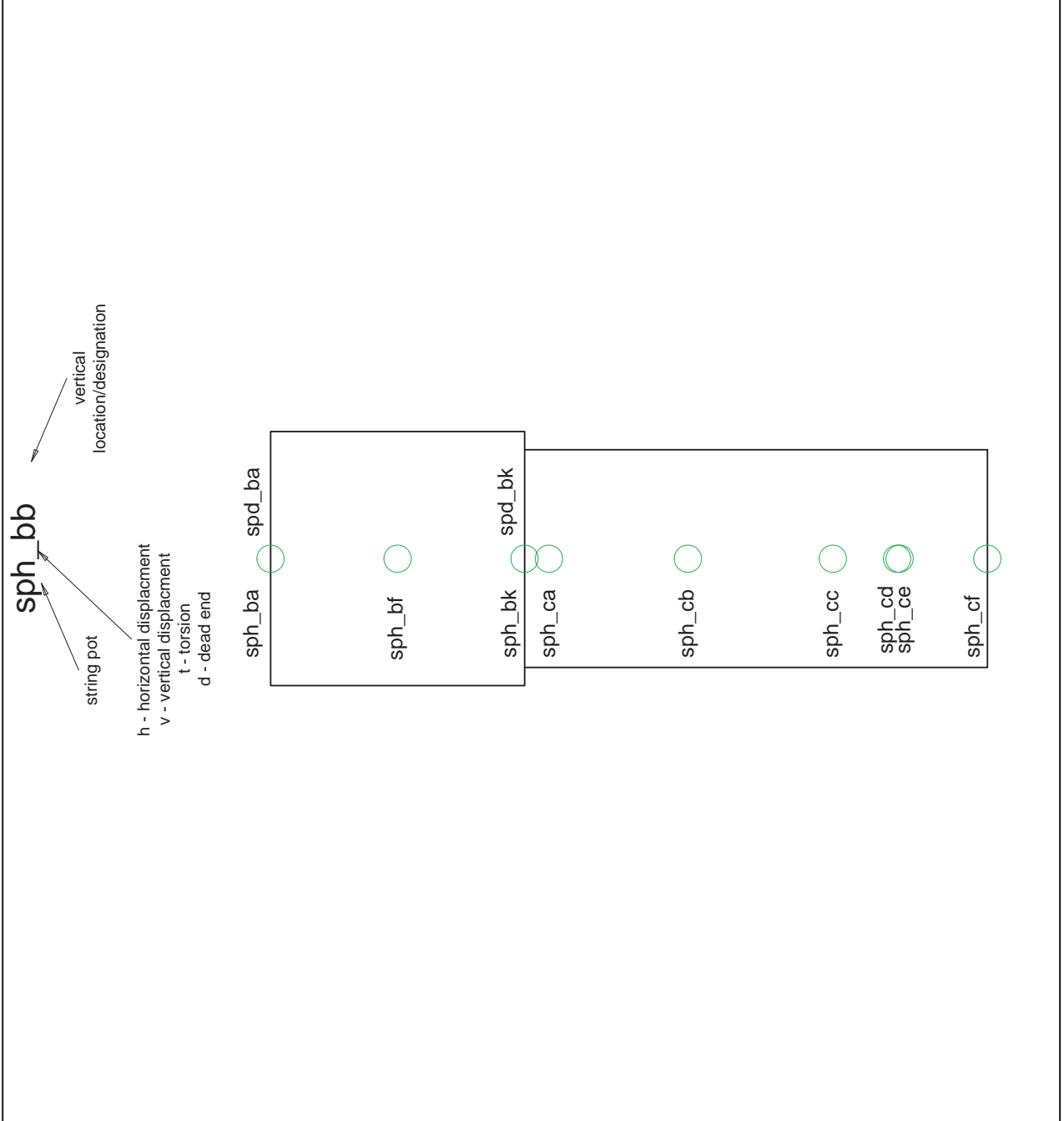
PROJECT NO:	0-6863
DATE:	28-Aug-17
VERSION:	V-1
DRAWN BY:	J. LEE
SCALE:	N.T.S.
TITLE:	Phase 1 Instrumentation Plan String Pot Bottom
SHEET#:	3 of 11

F:\Kevin Yeibrem Cap Project\Kevin Yeibrem\AEC\Drawings\in KY Thesis\Instrumentation_2_15_17\1x17.dwg August 28, 2017 - 4:35 PM



 ZACHRY DEPARTMENT OF CIVIL ENGINEERING TEXAS A&M UNIVERSITY	 Texas A&M Transportation Institute	Precast Prestensioned Bent Caps TXDOT 0-6863 Phase 1			
		PROJECT NO: 0-6863 DATE: 28-Aug-17 VERSION: V-1 DRAWN BY: J. LEE SCALE: N.T.S. TITLE:	Phase 1 Instrumentation Plan SP Battered End		

August 28, 2017 - 4:35 PM
 F:\Kevin Yoelbem Cap Project\Kevin Yoelbem\CAD\Drawings In KY Thesis\Instrumentation 2_15_17 11x17.dwg

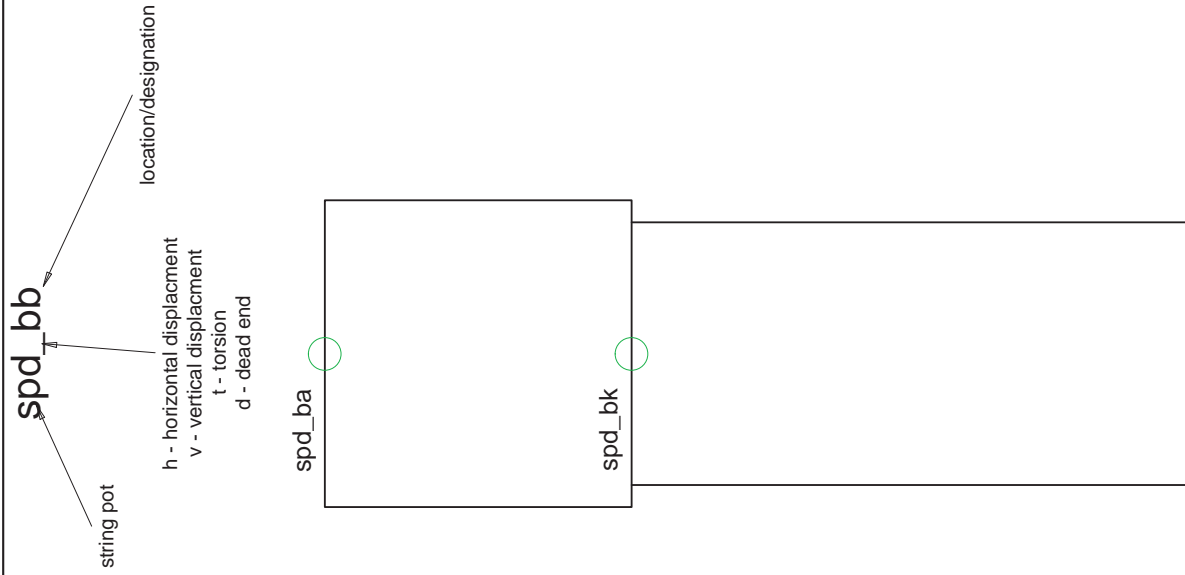




**TXDOT 0-6863
Precast Prestensioned Bent Caps
Phase 1**

PROJECT NO:	0-6863
DATE:	28-Aug-17
VERSION:	V-1
DRAWN BY:	J. LEE
SCALE:	N.T.S.
TITLE:	Phase 1 Instrumentation Plan SP Square End
SHEET#:	5 of 11

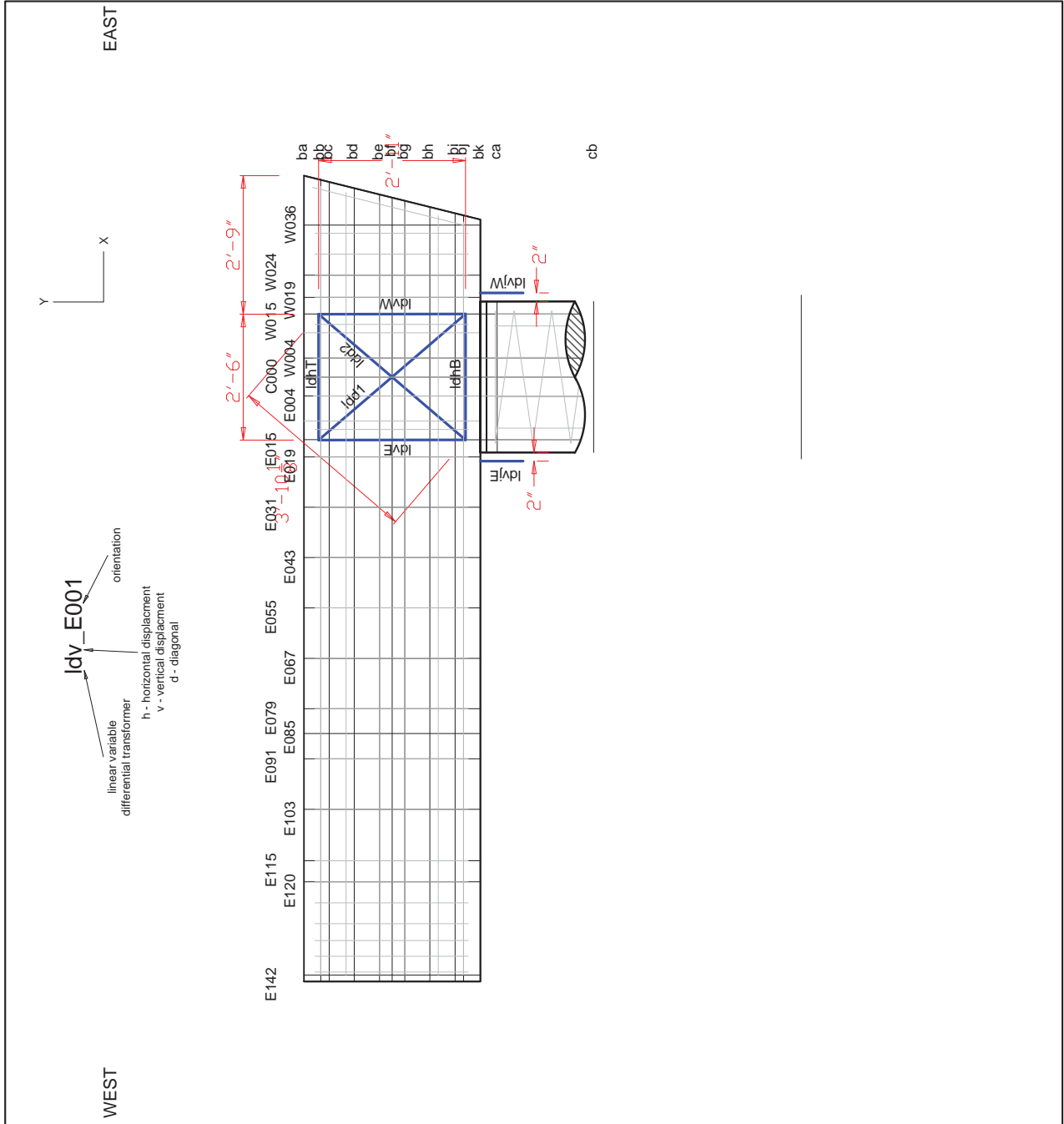
F:\Kevin Yeibem Cap Project\Kevin Yeibem\AEC\Drawings\in KY Thesis\Instrumentation_2_15_17 11x17.dwg August 28, 2017 - 4:35 PM



TXDOT 0-6863
Phase 1
Precast Prestensioned Bent Caps

PROJECT NO:	0-6863
DATE:	28-Aug-17
VERSION:	V-1
DRAWN BY:	J. LEE
SCALE:	N.T.S.
TITLE:	Phase 1 Instrumentation Plan LVDT
SHEET#:	6 of 11

F:\Kevin Yeibrem Cap Project\Kevin Yeibrem\AutoCAD\Drawings\In KY Thesis\Instrumentation 2_15_17 11x17.dwg August 28, 2017 4:35 PM



Phase 1
Precast Prestensioned Bent Caps
TXDOT 0-6863

PROJECT NO: 0-6863

DATE: 28-Aug-17

VERSION: V-1

DRAWN BY: J. LEE

SCALE: N.T.S.

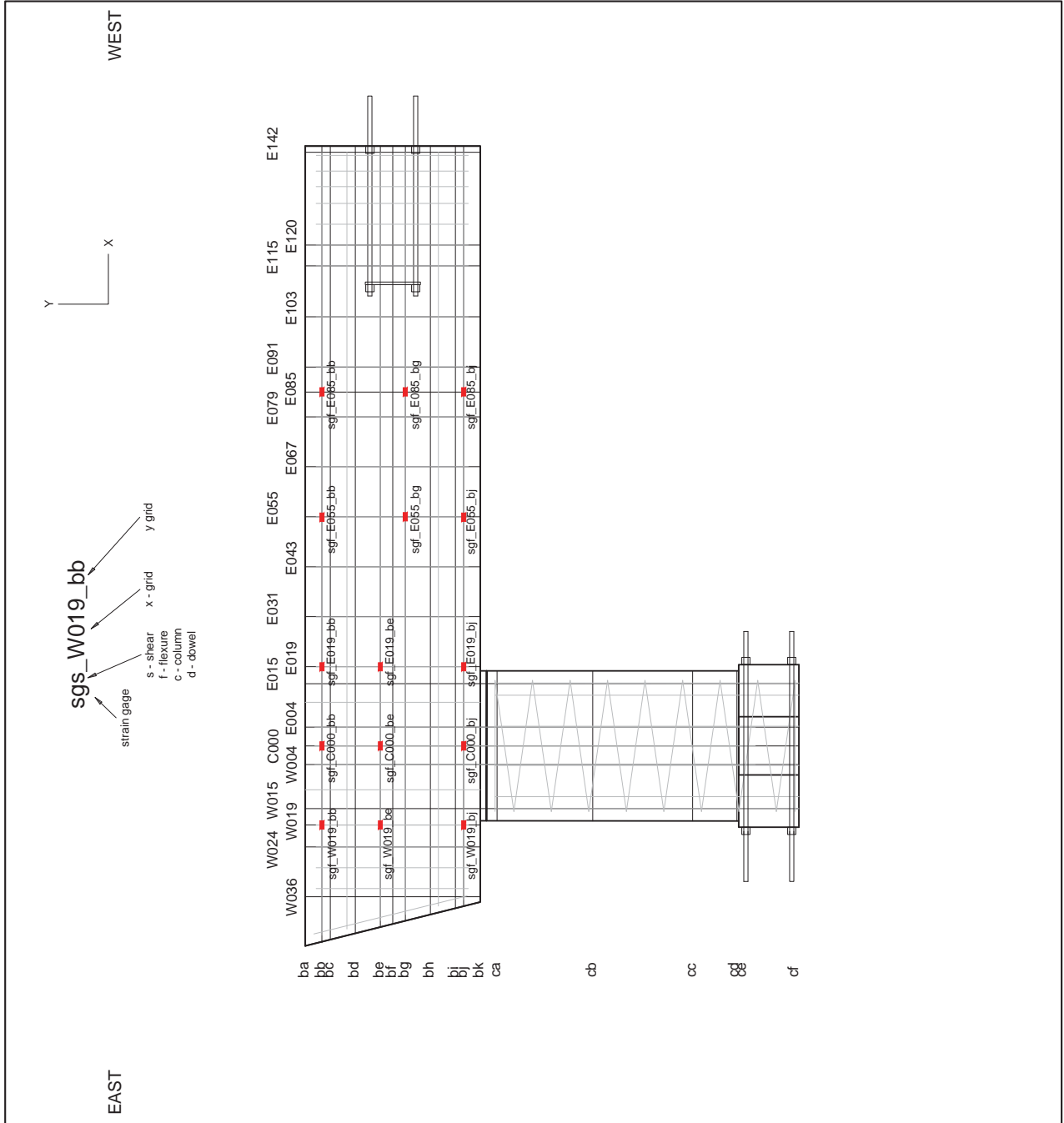
TITLE:

Phase 1
Instrumentation Plan
SG | Flex

SHEET#:

7 of 11

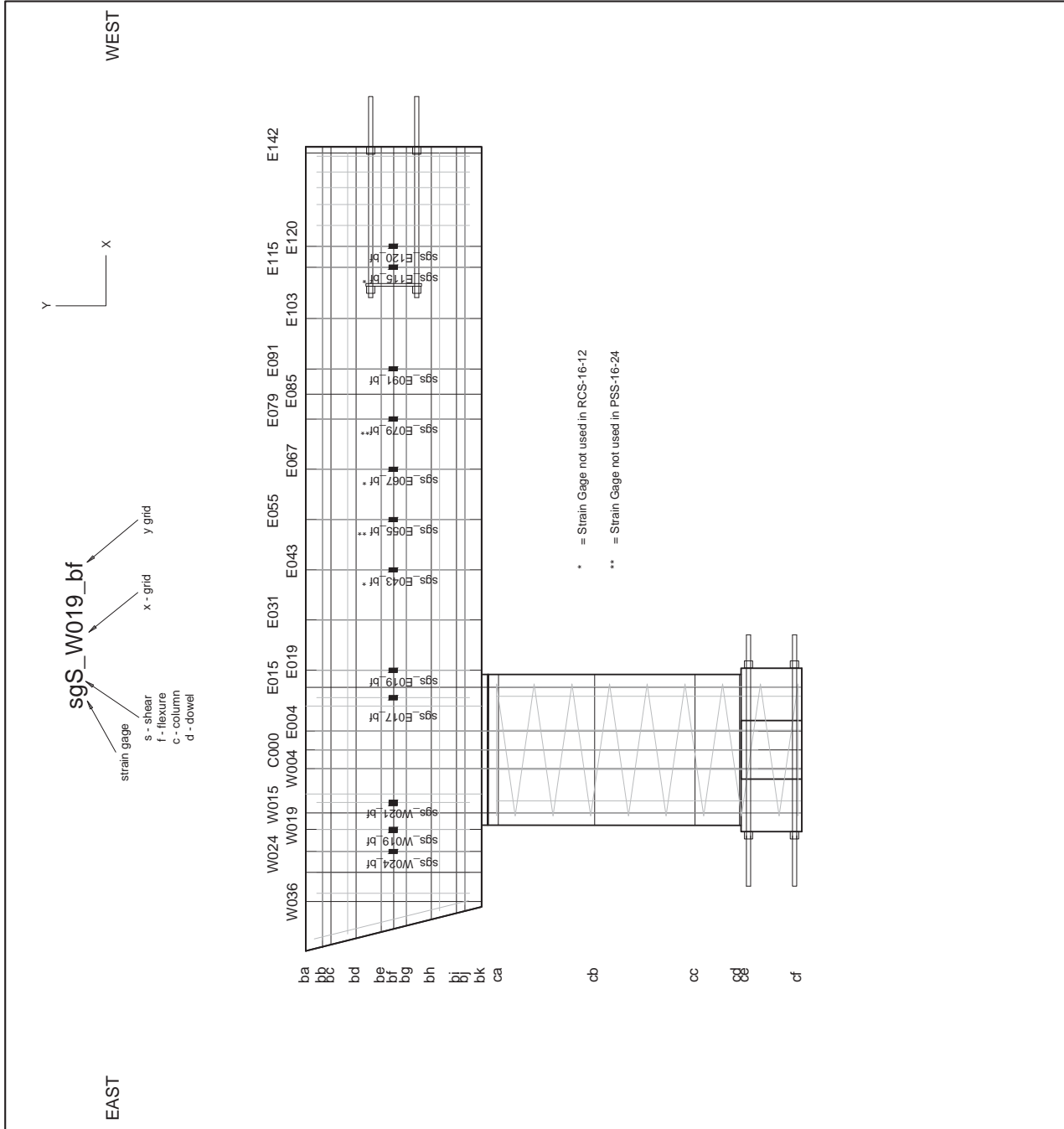
F:\Kevin Yeibem Cap Project\Kevin Yeibem\CADrawings\In KY Thesis\Instrumentation_2_15_17 11x17.dwg August 28, 2017 4:35 PM



Phase 1
Precast Prestensioned Bent Caps
TXDOT 0-6863

PROJECT NO:	0-6863
DATE:	28-Aug-17
VERSION:	V-1
DRAWN BY:	J. LEE
SCALE:	N.T.S.
TITLE:	Phase 1 Instrumentation Plan SG Shear
SHEET#:	8 of 11

August 28, 2017 - 4:35 PM
 F:\Kevin Yoelbem Cap Project\Kevin Yoelbem\CAD\Drawings In KY Thesis\Instrumentation 2_15_17 11x17.dwg





ZACHRY DEPARTMENT OF
CIVIL ENGINEERING
TEXAS A&M UNIVERSITY



Phase 1
Precast Prestensioned Bent Caps
TXDOT 0-6863

PROJECT NO: 0-6863

DATE: 28-Aug-17

VERSION: V-1

DRAWN BY: J. LEE

SCALE: N.T.S.

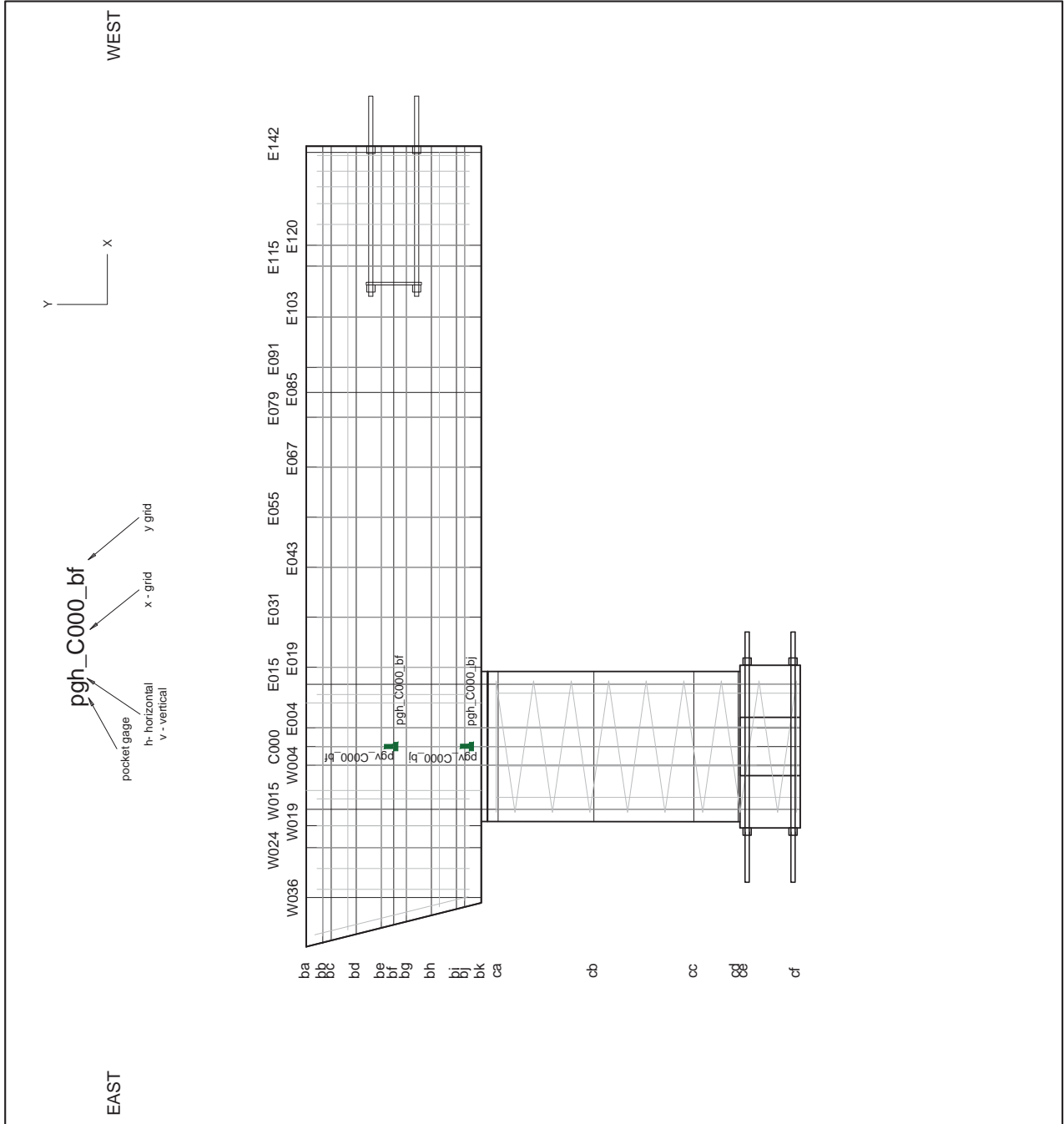
TITLE:

Phase 1
Instrumentation Plan
SG | Pocket

SHEET#:

9 of 11

F:\Kevin Yeibem Cap Project\Kevin Yeibem\CAD\Drawings In KY Thesis\Instrumentation 2_15_17 11x17.dwg August 28, 2017 - 4:35 PM





ZACHRY DEPARTMENT OF
CIVIL ENGINEERING
TEXAS A&M UNIVERSITY



Phase 1
Precast Prestensioned Bent Caps
TXDOT 0-6863

PROJECT NO: 0-6863

DATE: 28-Aug-17

VERSION: V-1

DRAWN BY: J. LEE

SCALE: N.T.S.

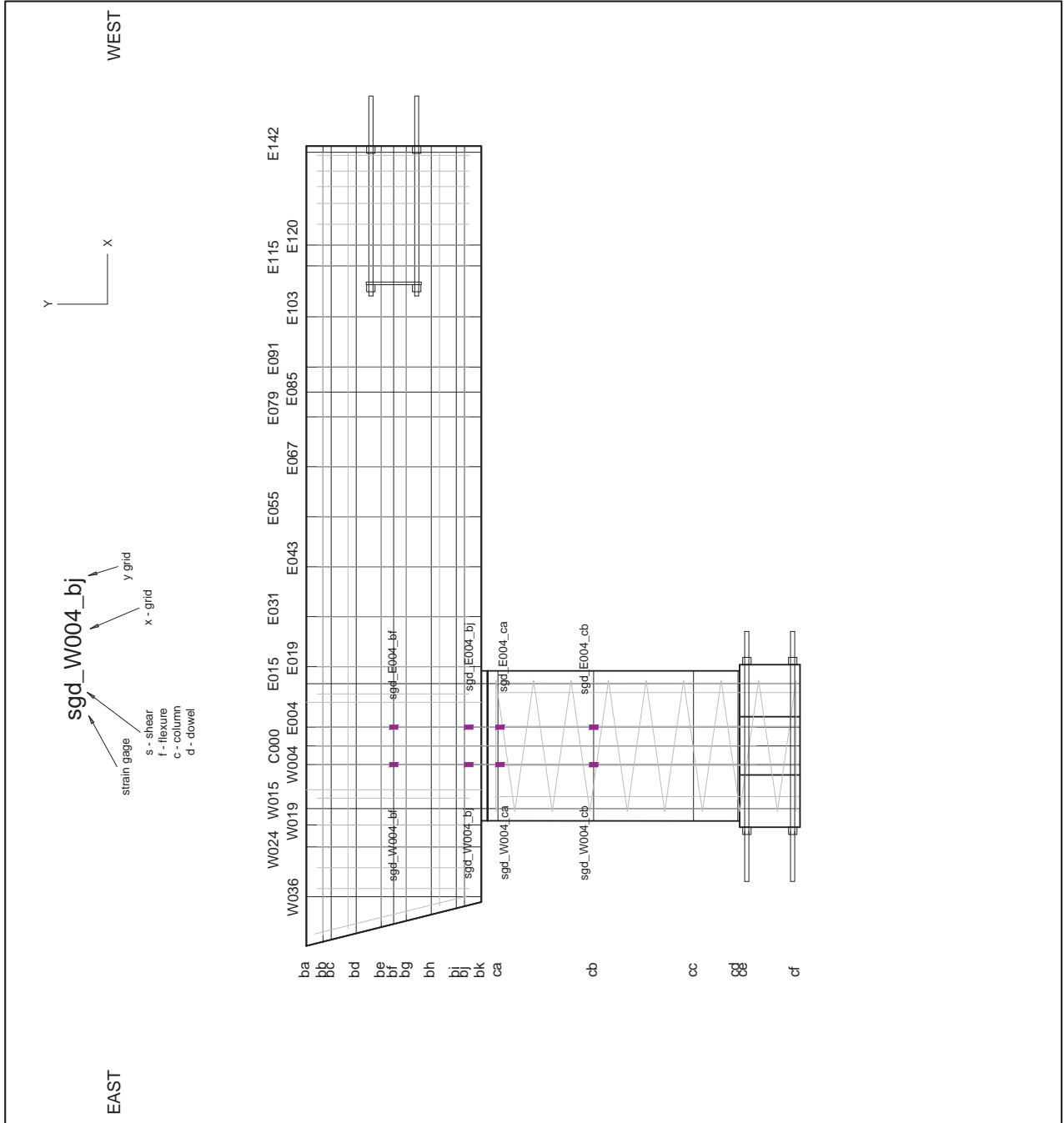
TITLE:

Phase 1
Instrumentation Plan
SG | Dowel

SHEET#:

10 of 11

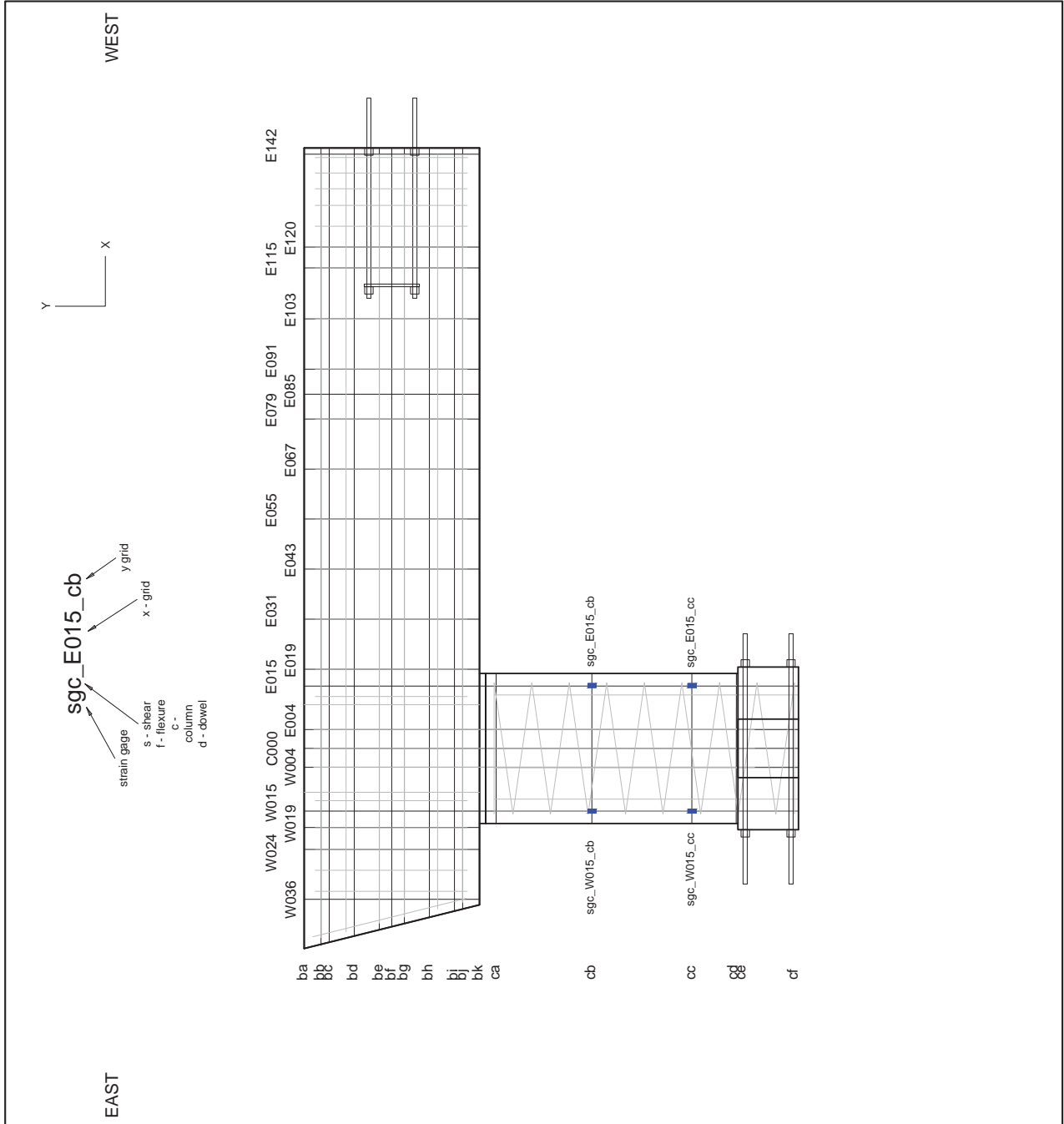
F:\Kevin Yeibem Cap Project\Kevin Yeibem\CAD\Drawings In KY Thesis\Instrumentation_2_15_17\11x17.dwg August 28, 2017 - 4:35 PM



Phase 1
Precast Prestensioned Bent Caps

PROJECT NO:	0-6863
DATE:	28-Aug-17
VERSION:	V-1
DRAWN BY:	J. LEE
SCALE:	N.T.S.
TITLE:	Phase 1 Instrumentation Plan SG Column
SHEET#:	11 of 11

F:\Kevin Yeibem Cap Project\Kevin Yeibem\CAD\Drawings\in\KT\Thesis\Instrumentation_2_15_17\11x17.dwg August 28, 2017 4:35 PM





ZACHRY DEPARTMENT OF
CIVIL ENGINEERING
TEXAS A&M UNIVERSITY



Phase 2
Precast Prestensioned Bent Caps
TXDOT 0-6863

PROJECT NO: 0-6863

DATE: 25-Aug-17

VERSION: V-1

DRAWN BY: J. LEE

SCALE: N.T.S.

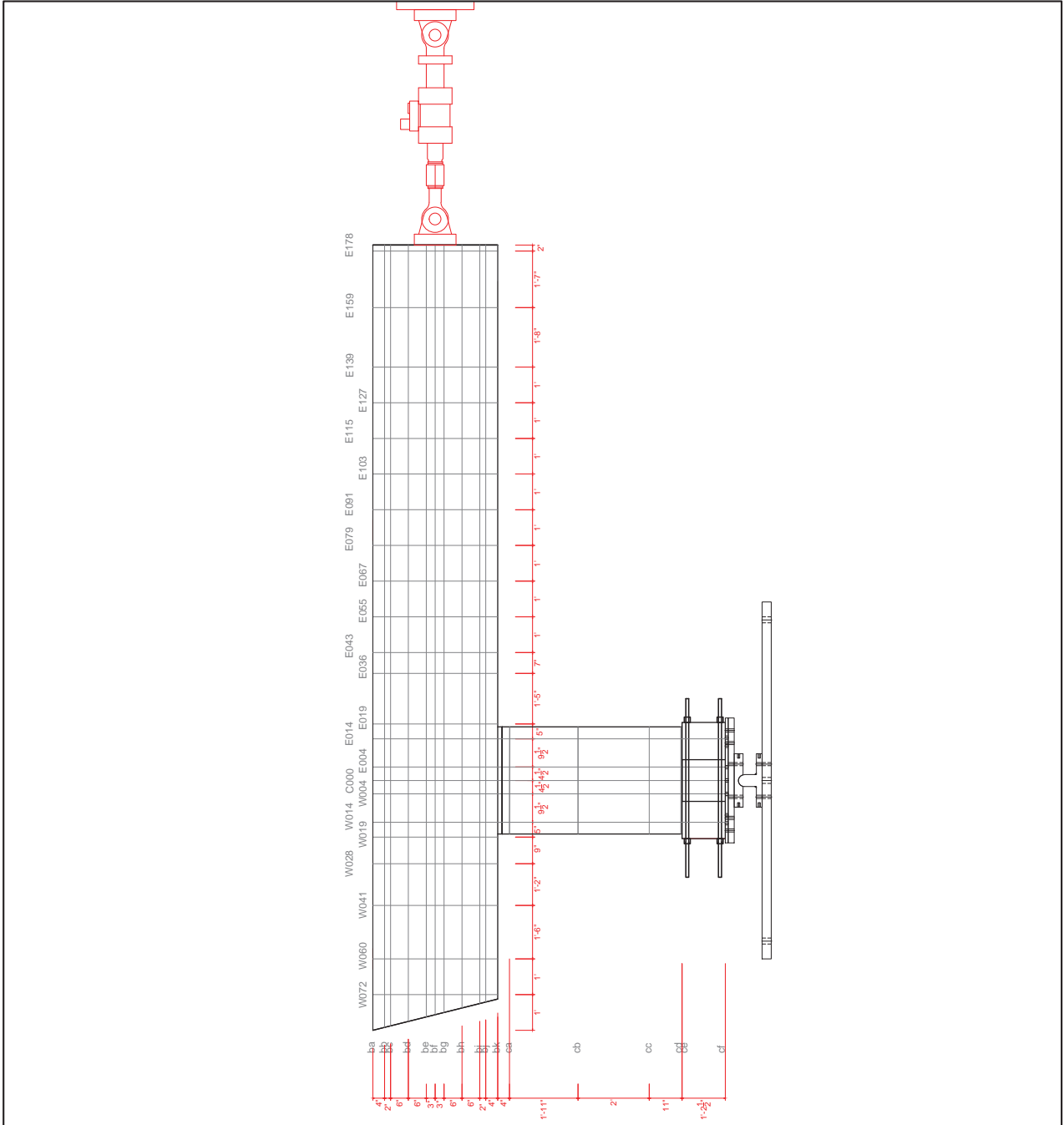
TITLE:

Phase 2
Instrumentation Plan
Grid Line

SHEET#:

1 of 9

C:\Users\mckeet\Desktop\Texas A&M\Research\0-6863 Prestressed Bent Caps\CAD Final\Instrumentation 0_13_17.dwg August 25, 2017 - 9:55 AM





ZACHRY DEPARTMENT OF
CIVIL ENGINEERING
TEXAS A&M UNIVERSITY



Phase 2 Precast Prestressed Bent Caps TXDOT 0-6863

PROJECT NO: 0-6863

DATE: 25-Aug-17

VERSION: V-1

DRAWN BY: J. LEE

SCALE: N.T.S.

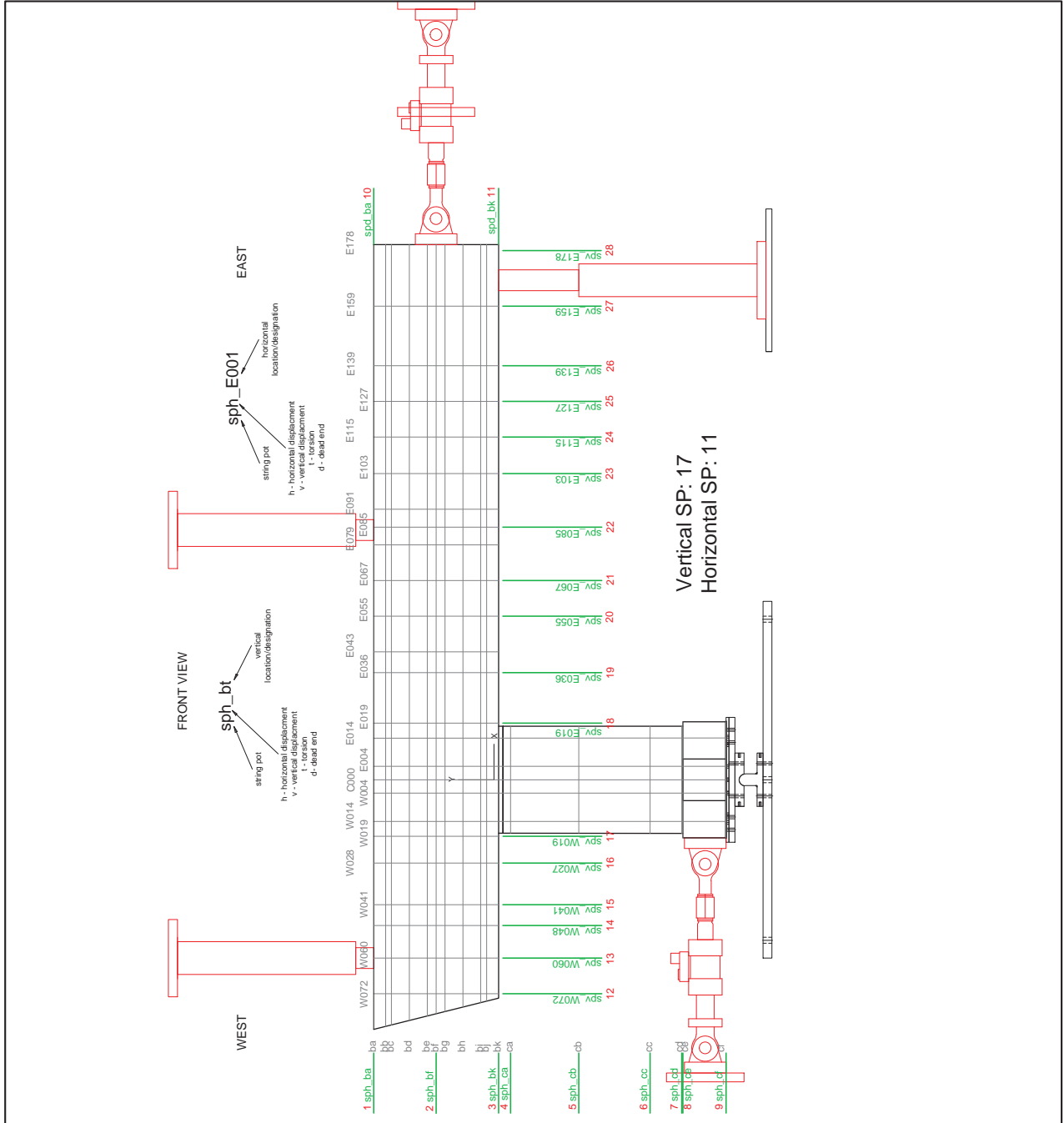
TITLE:

**Phase 2
Instrumentation Plan
String Pot | S. Elev**

SHEET#:

2 of 9

C:\Users\mckeet\Desktop\Texas A&M\Research\0-6863 Precressed Bent Caps\CAD Final\Instrumentation 0_13_17.dwg August 25, 2017 - 9:55 AM





ZACHRY DEPARTMENT OF
CIVIL ENGINEERING
TEXAS A&M UNIVERSITY



**TXDOT 0-6863
Precast Prestensioned Bent Caps
Phase 2**

PROJECT NO: 0-6863

DATE: 25-Aug-17

VERSION: V-1

DRAWN BY: J. LEE

SCALE: N.T.S.

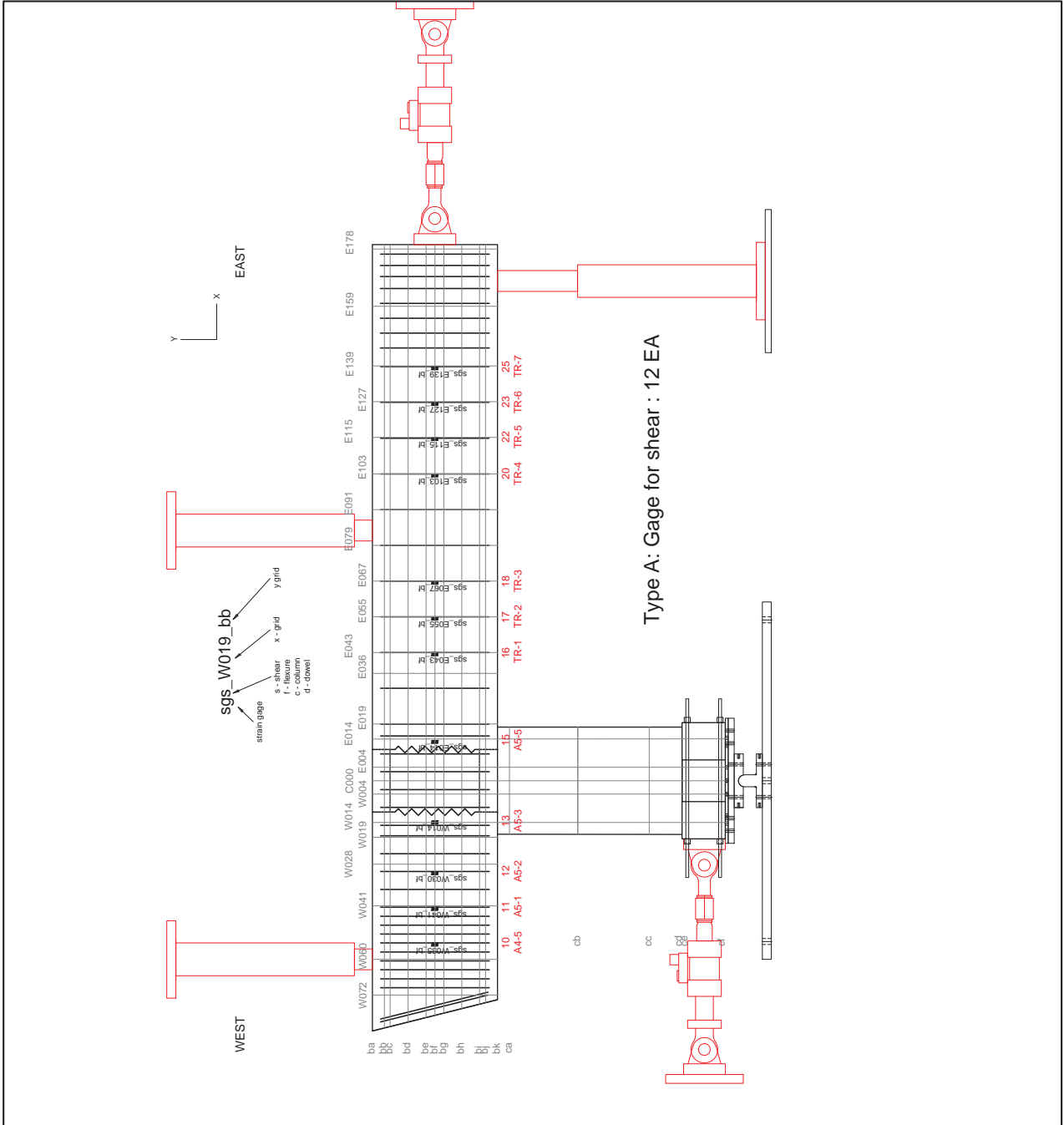
TITLE:

**Phase 2
Instrumentation Plan
PSV-28A SG Shear**

SHEET#:

3 of 9

C:\Users\mcke\Desktop\Texas A&M\Research\0-6863 Prestressed Bent Caps\CAD Final\Instrumentation 0_13_17.dwg August 25, 2017 - 9:55 AM





ZACHRY DEPARTMENT OF
CIVIL ENGINEERING
TEXAS A&M UNIVERSITY



TXDOT 0-6863 Precast Prestressed Bent Caps Phase 2

PROJECT NO: 0-6863

DATE: 25-Aug-17

VERSION: V-1

DRAWN BY: J. LEE

SCALE: N.T.S.

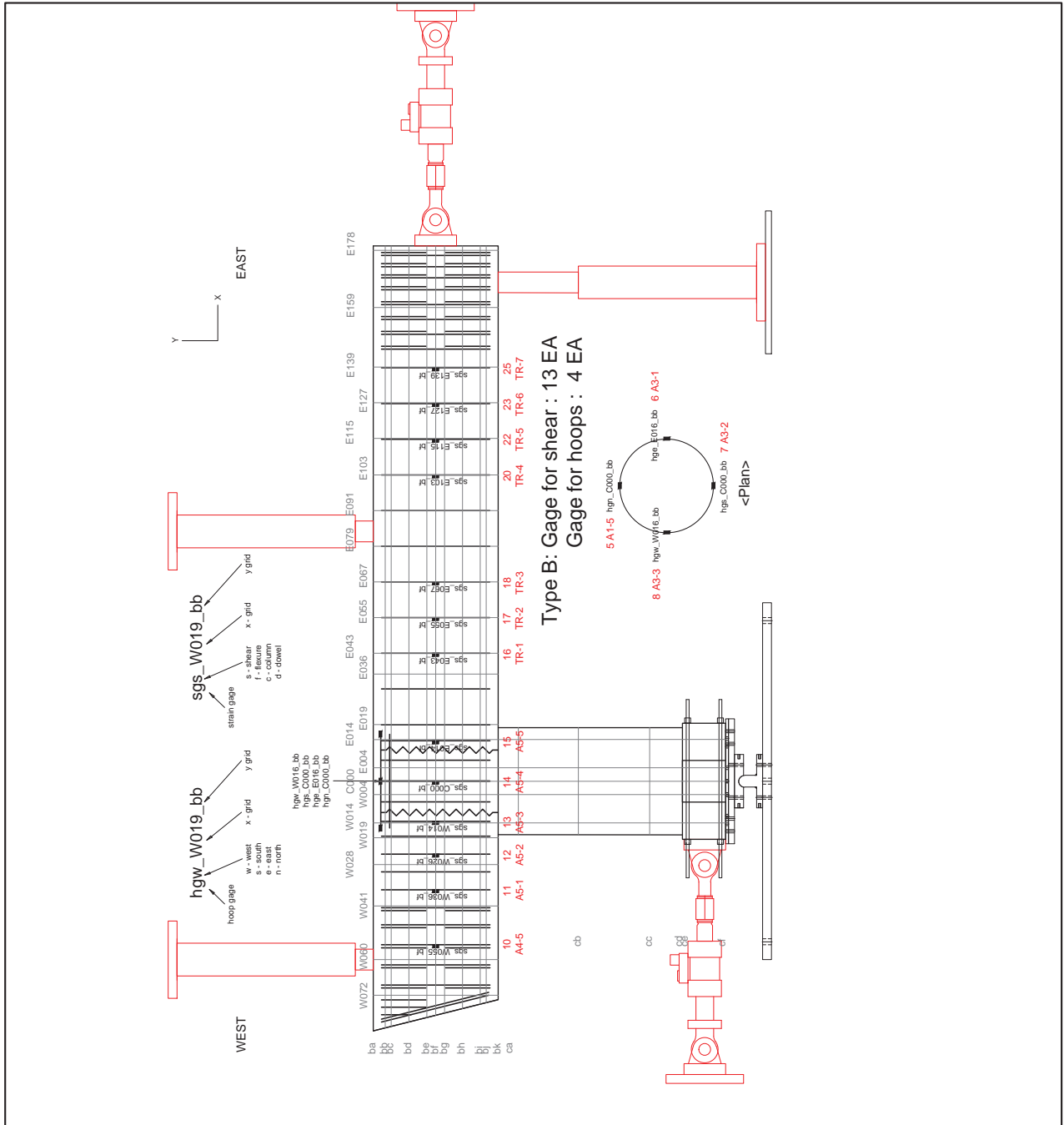
TITLE:

**Phase 2
Instrumentation Plan
PSV-28B SG Shear**

SHEET#:

4 of 9

C:\Users\mcke\Desktop\Texas A&M\Research\0-6863 Prestressed Bent Caps\CAD Final\Instrumentation 0_13_17.dwg August 25, 2017 - 9:55 AM





ZACHRY DEPARTMENT OF
CIVIL ENGINEERING
TEXAS A&M UNIVERSITY



**Precast Prestensioned Bent Caps
Phase 2
TXDOT 0-6863**

PROJECT NO: 0-6863

DATE: 25-Aug-17

VERSION: V-1

DRAWN BY: J. LEE

SCALE: N.T.S.

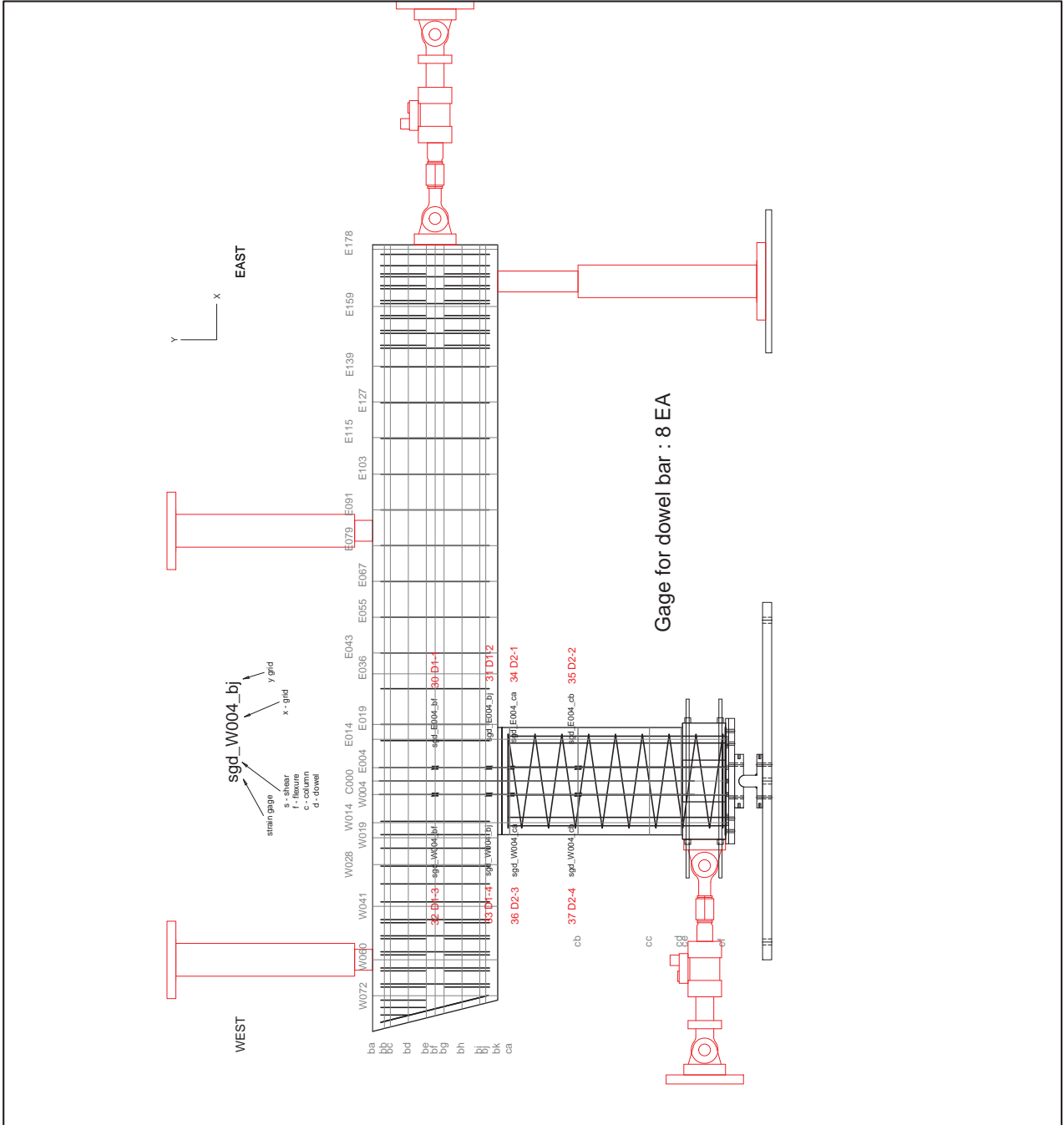
TITLE:

**Phase 2
Instrumentation Plan
SG Dowel Bars**

SHEET#:

6 of 9

C:\Users\mckee\Desktop\Texas A&M\Research\0-6863 Prestressed Bent Caps\CAD Final\Instrumentation 0_13_17.dwg August 25, 2017 - 9:55 AM





ZACHRY DEPARTMENT OF
CIVIL ENGINEERING
TEXAS A&M UNIVERSITY



**TXDOT 0-6863
Precast Prestressed Bent Caps
Phase 2**

PROJECT NO: 0-6863

DATE: 25-Aug-17

VERSION: V-1

DRAWN BY: J. LEE

SCALE: N.T.S.

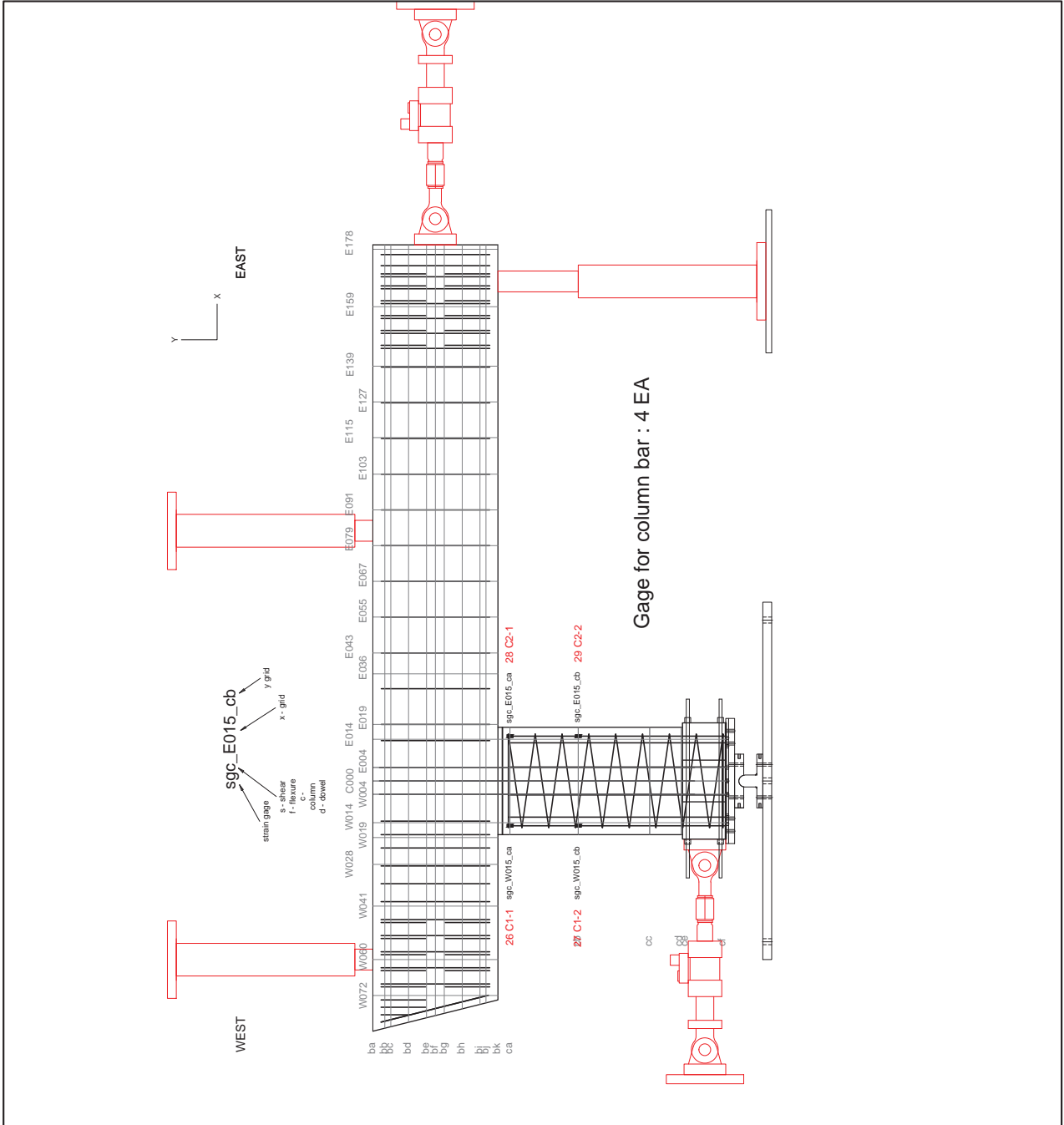
TITLE:

**Phase 2
Instrumentation Plan
SG Column**

SHEET#:

7 of 9

C:\Users\mckeet\Desktop\Texas A&M\Research\0-6863 Prestressed Bent Caps\CAD Final\Instrumentation 0_13_17.dwg August 25, 2017 - 9:55 AM



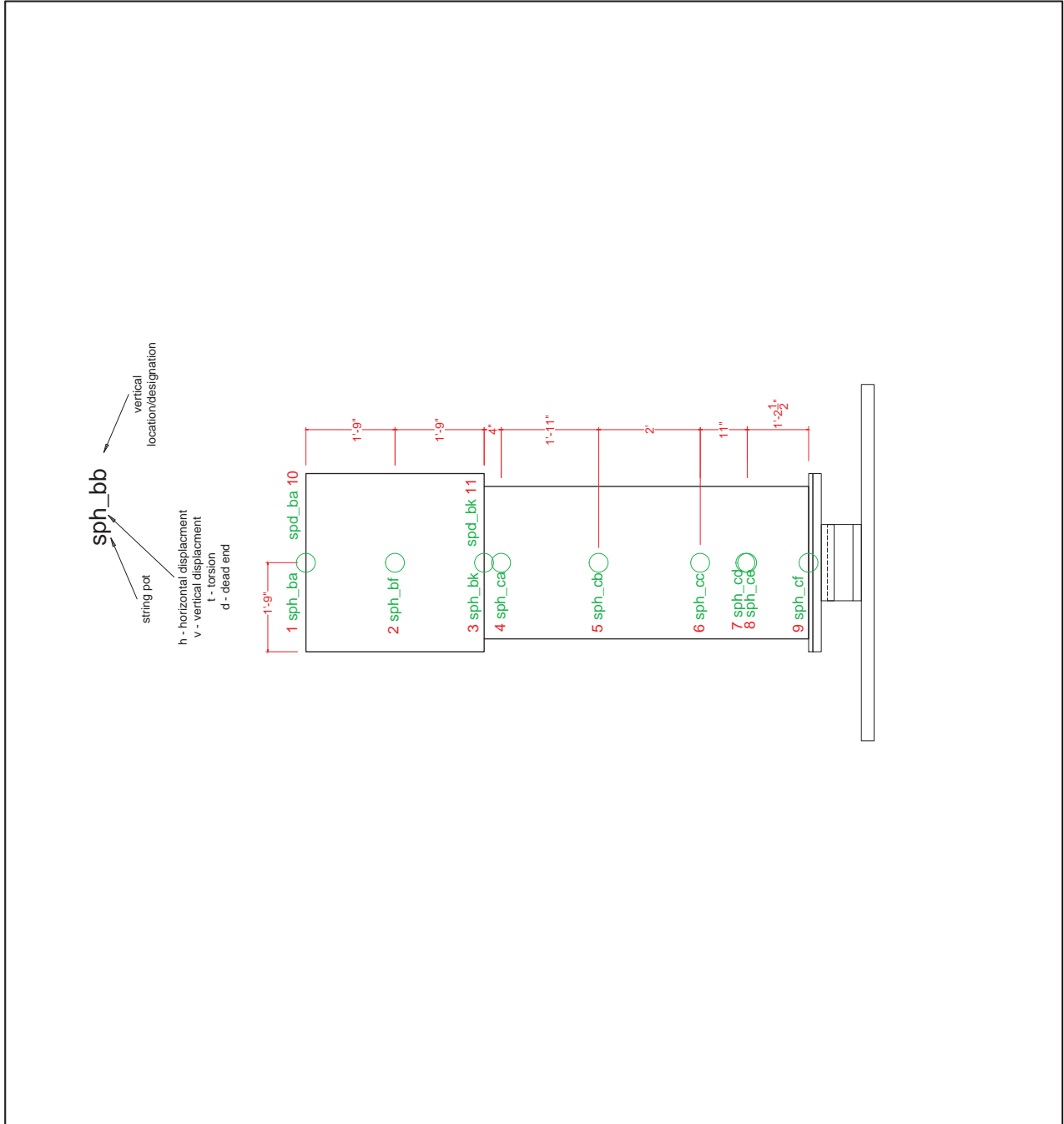
TXDOT 0-6863
Phase 2
Precast Prestressed Bent Caps

PROJECT NO:	0-6863
DATE:	25-Aug-17
VERSION:	V-1
DRAWN BY:	J. LEE
SCALE:	N.T.S.
TITLE:	

Phase 2
Instrumentation Plan
SP Battered End

SHEET#:
8 of 9

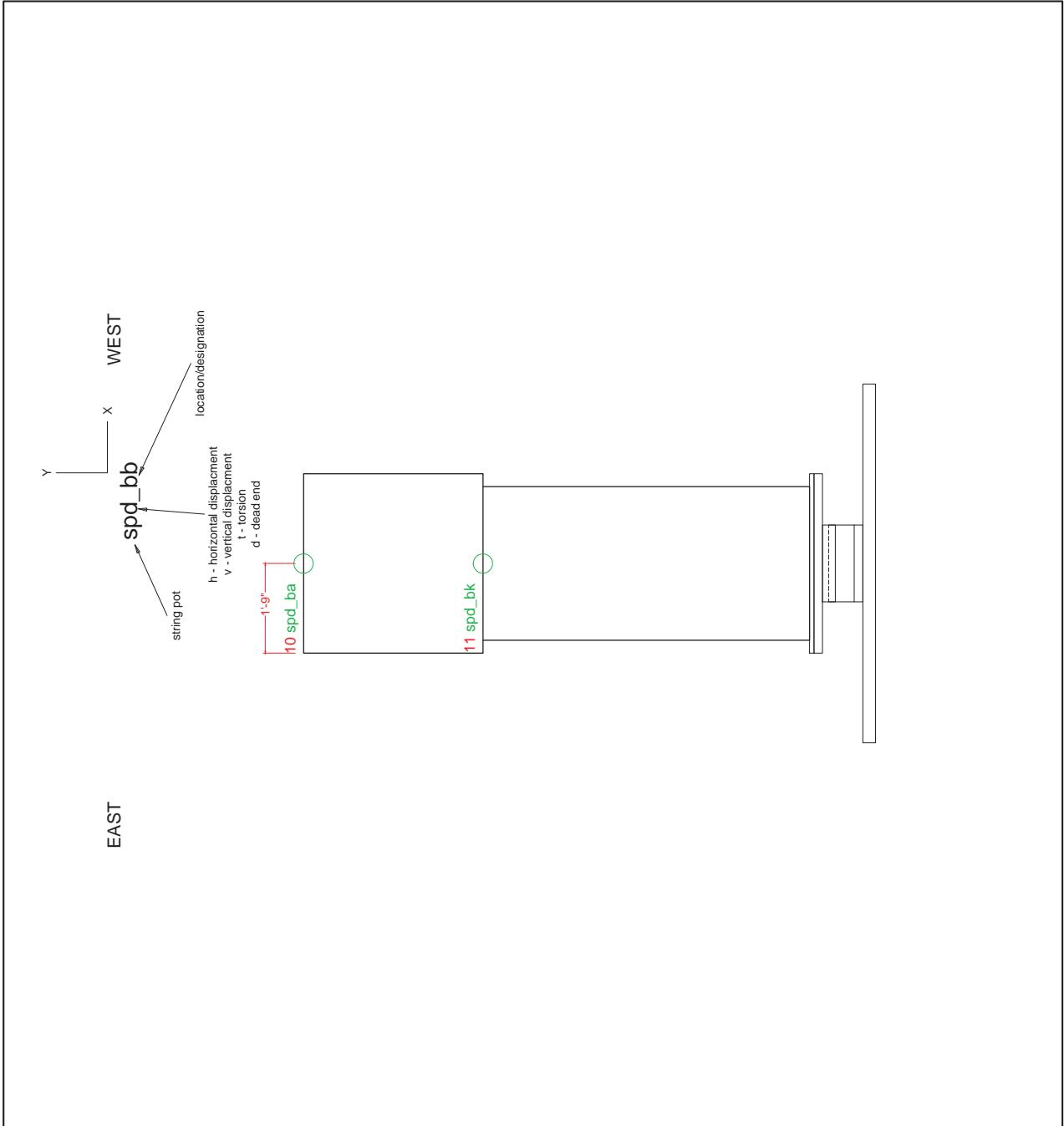
C:\Users\mckeet\Desktop\Texas A&M\Research\0-6863 Prestressed Bent Caps\CAD Final\Instrumentation 0_13_17.dwg August 25, 2017 - 9:55 AM



TXDOT 0-6863
Precast Prestensioned Bent Caps
Phase 2

PROJECT NO:	0-6863
DATE:	25-Aug-17
VERSION:	V-1
DRAWN BY:	J. LEE
SCALE:	N.T.S.
TITLE:	Phase 2 Instrumentation Plan SP Square End
SHEET#:	9 of 9

C:\Users\mckeet\Desktop\Texas A&M\Research\0-6863 Prestressed Bent Caps\CAD Final\Instrumentation 0_13_17.dwg August 25, 2017 - 9:55 AM



APPENDIX B – LOADING SEQUENCE

Table B-1. Loading Sequence – RCS-16-12.

Dates	Loads	Cracks Measured	Creep (hrs)	Unload (kips)
Day 1 10/10/2016	No loads (System check)			
Day 2 10/12/2016	Dead		1	
	SLS	✓		
	ULS	✓		0
Day 3 10/13/2016	SLS	✓		
	ULS	✓	6	270/160/0
Day 4 10/14/2016	Dead	✓		
	SLS	✓		
	ULS	✓		
	140% ULS	✓		
	Max Positive	✓		0
Day 5 10/17/2016	Joint Opening	✓		0
Day 6 10/28/2016	Joint Closing	✓		
	Max Negative	✓		0
	Joint Opening			
	Max Positive			
Day 7 10/31/2016	Failure			0

Table B-2. Loading Sequence – PSS-16-24.

Dates	Loads	Cracks Measured	Creep (hrs)	Unload (kips)
Day 1 2/22/2017	Dead			
	SLS	✓		
	ULS	✓		
	ULS	✓	2.5	160
	140% ULS	✓		
Day 2 2/27/2017	Max Positive	✓		160 / 0
	Joint Opening	✓		0
	Joint Closing	✓		0
	Max Negative	✓		
	Failure			0

Table B-3. Loading Sequence – PSS-16-12.

Dates	Loads	Cracks Measured	Creep (hrs)	Unload (kips)
Day 1 11/30/2016	Dead			
	SLS	✓		160
	ULS	✓	1	
	140% ULS	✓		
	Max Positive	✓		160/0
	Joint Opening	✓		
	Joint Closing	✓		
	Max Negative	✓		0
Day 2 12/2/2016	Dead	✓		
	SLS	✓		
	ULS	✓		
	140% ULS	✓		270/160
	Failure			0

Table B-4. Loading Sequence – PSV-16-12.

Dates	Loads	Cracks Measured	Creep (hrs)	Unload (kips)
Day 1 1/6/2017	Dead			
	SLS	✓		
	ULS	✓		160 / 0
Day 2 1/9/2017	ULS	✓	1.5	
	140% ULS	✓		270 / 160 / 0
Day 3 1/12/2017	Max Positive	✓		160 / 0
	Joint Opening	✓		
	Joint Closing	✓		
	Max Negative	✓		
	Failure			

Table B-5. Loading Sequence – PSV-28A.

Dates	Loads	Cracks Measured	Creep (hrs)	Unload (kips)
Day 1 6/29/2017	Dead			
	SLS	✓		
	ULS	✓		160 / 0
Day 2 6/30/2017	Joint Opening	✓		0
	Joint Closing	✓		0
	ULS	✓		
	140% ULS	✓		160 / 0
	Max. Positive	✓		0
	Max Negative / Failure			

Table B-6. Loading Sequence – PSV-28B.

Dates	Loads	Cracks Measured	Creep (hrs)	Unload (kips)
Day 1 7/26/2017	Dead			
	SLS	✓		
	ULS	✓		160 / 0
	Joint Opening	✓		0
	Joint Closing			0
	SLS			0
Day 2 7/27/2017	ULS	✓		
	140% ULS	✓		160 / 0
	Max. Positive	✓		80 / 0
	Max Negative / Failure			
	Max Positive / Failure			